Universidade de Aveiro
Ano 2022

JOANA LÚCIA MARTO DOS SANTOS LOPES

# MATERIAIS BASEADOS EM CARBONO PARA A FOTODEGRADAÇÃO DE POLUENTES EM ÁGUA

# CARBON-BASED MATERIALS FOR THE PHOTODEGRADATION OF POLLUTANTS IN WATER

**Universidade de Aveiro**
**Ano 2022**

**JOANA LÚCIA MARTO DOS SANTOS LOPES**

# MATERIAIS BASEADOS EM CARBONO PARA A FOTODEGRADAÇÃO DE POLUENTES EM ÁGUA

# CARBON-BASED MATERIALS FOR THE PHOTODEGRADATION OF POLLUTANTS IN WATER

Tese apresentada à Universidade de Aveiro para cumprimento dos requisitos necessários à obtenção do grau de Doutor em Química, realizada sob a orientação científica do Doutor Tito da Silva Trindade, Professor Catedrático do Departamento de Química da Universidade de Aveiro e da Doutora Ana Cristina Estrada Morais Gonçalves de Sousa, Investigadora Doutorada do Departamento de Química da Universidade de Aveiro.

Apoio financeiro da FCT através de Fundos Nacionais, FSE e União Europeia, no âmbito do POCH – Programa Operacional Capital Humano.

O autor agradece o apoio financeiro da FCT através da Bolsa de Doutoramento com a referência SFRH/BD/126241/2016.

To the wanderer souls in this world.

*“All that is gold does not glitter,*
*Not all those who wander are lost;*
*The old that is strong does not wither,*
*Deep roots are not reached by the frost.*

*From the ashes a fire shall be woken,*
*A light from the shadows shall spring;*
*Renewed shall be blade that was broken,*
*The crownless again shall be king.”*
J. R. R. Tolkien

**o júri**

presidente

Doutor Carlos Fernandes da Silva
professor catedrático da Universidade de Aveiro

Doutora Ana Cristina Moreira Freire
professora catedrática da Universidade do Porto

Doutor Vítor Jorge Pais Vilar
investigador principal da Universidade do Porto

Doutor Jorge Manuel Campos Marques
professor auxiliar da Universidade de Coimbra

Doutora Helena Isabel Seguro Nogueira
professora auxiliar da Universidade de Aveiro

Doutora Ana Cristina Estrada Morais Gonçalves de Sousa
investigadora doutorada da Universidade de Aveiro

**agradecimentos**

Primeiramente gostaria de agradecer aos meus orientadores, Professor Tito Trindade e Doutora Ana Cristina Estrada. Ao Professor Tito pelo seu conhecimento excecional, conselhos valiosos e criticismo construtivo que me fizeram crescer desde 2013 como sua aluna. À Doutora Ana, pelo seu conhecimento, disponibilidade e inesperada amizade tão próxima. Sou grata pelas novas ideias que despertaram em mim e por transformar o meu modo de vida, agora com um impacto mais positivo em tudo o que me rodeia. Por me encaminhar, nestes quatro anos de doutoramento, mas também de uma forma geral na vida.

Um agradecimento especial a algumas pessoas que me ajudaram a terminar este capítulo com sucesso. À Doutora Sara Fateixa pelos seus conhecimentos de Raman e pelos encorajamentos, especialmente nesta fase final. Aos Doutores Richard Gomes e José Gouveia pela simpatia, disponibilidade e pelos seus conhecimentos valiosos relacionados com os estudos de DFT. À professora Teresa Monteiro, o seu grupo, o Professor Luis Carlos e o Doutor Duarte Ananias agradeço pela ajuda com as medidas dos C-dots. Também quero agradecer à Doutora Violeta Girão pela sua amizade e ajuda sempre presente. Um agradecimento especial à Professora Cristina Freire pela possibilidade de colaboração com o seu grupo e ao projeto FOTOCATGRAF. Por fim, gostaria de agradecer também à Professora Magda Titirici e ao seu grupo por me terem acolhido durante a minha curta estadia na Universidade Queen Mary em Londres.

Um grande agradecimento a algumas pessoas que nunca falharam em ajudar-me, por vezes tão carinhosamente, durante o meu dia-a-dia nestes (quase!) 9 anos na Universidade de Aveiro, primeiro como estudante de mestrado, depois como bolseira de investigação e por fim enquanto jovem doutoranda. À Celeste, Rosário, Mónica, Marta, Margarete, Dona Manuela, Dona Dina e senhor Pedro, agradeço a ajuda sempre que pedi, os momentos de riso e conversa e a disponibilidade para por vezes “dobrar as regras”.

Aos meus colegas do nanoLAB, passados e presentes, por todos os momentos passados no laboratório e fora dele, pela entreajuda nas mais variadas tarefas. Não tinha conseguido sem vocês!

Aos meus amigos incríveis de Aveiro e da Margem Sul, que são a minha lembrança constante de quem sou e onde pertenço, especialmente Luísa, afilhada Catarina, Nicole, Joana, Jordão, Diogo, Andreia, Meri, Gabriela, Verita, vizinhos do 30 e as minhas italianas favoritas Cristina e Rugi. Obrigada pelas histórias partilhadas, pelas conversas noite fora e pelas saídas, pelos jantares de vizinhos (às vezes de gala!), pelos concertos e pelos WODs, pela ajuda nos momentos mais difíceis e pela companhia na celebração de (pequenas) vitórias, pelos risos, choros e desabafos. Mas, acima de tudo, por torcerem sempre por mim, por me acompanharem e relembrarem que os amigos são a família que escolhemos.

À minha família. 2020 foi um ano desafiante, que me fez recordar a importância de estar junto dos meus e que o tempo nunca o devemos dar por garantido. Obrigada por ser sempre tão bom voltar a casa.

Quero agradecer também à família do Miguel, especialmente os seus pais e irmã Marta, por me terem acolhido desde o primeiro dia.

Mas acima de tudo, ao Miguel. Obrigada por esta viagem maravilhosa de quase 9 anos. Pelo lar que criámos, agora também com a Pepper. Sou imensamente grata pela nossa cumplicidade, apoio constante, paciência nas horas mais difíceis, amizade e história de amor que partilhamos.

Por fim, aos meus pais. Pelas lições ensinadas, os esforços que fizeram. Pelo amor e apoio incondicionais.

Obrigada.

**palavras-chave**

carbono, semiconductores, fotocatálise heterogénea, poluentes, tratamento de águas.

**resumo**

A contaminação de águas é um problema à escala global que necessita de um conjunto de esforços para garantir o acesso de água às gerações futuras. Muitos desses contaminantes são resíduos de fármacos, sendo que os processos convencionais de tratamento de águas não são eficientes para a sua remoção. Assim, os processos de oxidação avançados baseados no uso de fotocatalisadores emergem como uma alternativa viável para estes poluentes persistentes.

Este trabalho de investigação aborda diferentes materiais baseados em carbono de dimensionalidades estruturais distintas entre os quais, óxido de grafeno e outros materiais baseados em grafeno, esferas micrométricas de carbono e pontos de carbono.

Os materiais baseados em grafeno e as esferas micrométricas de carbono foram usados como plataforma para o crescimento de diferentes fases cristalinas semicondutoras tais como, sulfuretos metálicos e vanadato de bismuto, com o objetivo de desenvolver fotocatalisadores heterogéneos com capacidade de serem ativados através de radiação solar.

Os materiais híbridos desenvolvidos foram testados na degradação fotocatalítica de um corante orgânico (rodamina B) e dois fármacos (sulfametoxazol e tetraciclina), tendo sido estudado o seu mecanismo de fotodegradação. Um aspeto crucial para o desenvolvimento de fotocatalisadores híbridos que conjuguem várias funcionalidades é o conhecimento da sua química de superfície. Neste trabalho, esse objetivo foi explorado através de vias químicas de modificação superficial para os diferentes materiais de carbono.

Por fim, foi realizada uma investigação preliminar relativamente às propriedades óticas e à química de superfície de pontos de carbono preparados a partir de carragenano, uma fonte de carbono renovável.

**keywords**

carbon, semiconductors, heterogenous photocatalysis, pollutants, water treatment.

**abstract**

Water contamination is a serious global problem which requires efforts to guarantee the water supply for future generations. Pharmaceutical wastes are one of the most relevant water pollutants, and conventional wastewater treatment processes are inefficient to their removal. Advanced oxidation processes based on the use of photocatalysts emerge as a viable alternative for these persistent pollutants.

This research work is focused on different carbon-based materials of distinct structural dimensionalities, including graphene oxide and other graphene-based materials, carbon microspheres and carbon dots.

Graphene-based materials and carbon microspheres were used as growth platform for different crystalline semiconductor phases, such as metal sulfides and bismuth vanadate with the main goal of developing multicomponent heterogenous photocatalysts activated by visible-light irradiation.

The developed hybrid materials were further tested in the photocatalytic degradation of an organic dye (rhodamine B) and two pharmaceutical compounds (sulfamethoxazole and tetracycline), and their photodegradation mechanism was studied. A crucial aspect in developing such hybrid photocatalysts combining distinct functionalities is understanding their surface chemistry. In this work, this objective was explored through surface chemical modification routes for different carbon materials.

Lastly, exploratory research was performed on the optical properties and surface chemistry of carbon dots prepared from carrageenan, a renewable carbon source.

# CONTENTS

# ABBREVIATIONS AND SYMBOLS

4-MPy – 4-mercaptopyridine

4-NP – 4-nitrophenol

5-HMF – 5-hydroxymethylfurfural

AFM – Atomic force microscopy

AOPs – Advanced oxidation processes

ATR – Attenuated total reflectance

BET – Brunauer-Emmett-Teller

BJH – Barret–Joyner–Halenda

CB – Conduction band

CBD – Chemical bath deposition

C-dots – Carbon dots

CIP – Ciprofloxacin

CNT – Carbon nanotube

CVD – Chemical vapor deposition

DFT – Density functional theory

DMF – Dimethylformamide

DNA - Deoxyribonucleic acid

DOS – Density of states

EDS – Energy dispersive X-ray spectroscopy

EGO – Exfoliated graphite oxide

GGA – Generalized gradient approximation

GO – Graphene oxide

$^{1}$H NMR – Proton nuclear magnetic resonance

HPLC-DAD – High-performance liquid chromatography with diode-array detection

HOMO – Highest occupied molecular orbital

HR-TEM – High resolution transmission electron microscopy

HTC – Hydrothermal carbonization

ICP – Inductively coupled plasma

$I_D/I_G$ – D-to-G intensity ratio

IR – Infrared

LDH – Layered double hydroxides

LO – Longitudinal optical mode

LSPR – Localized surface plasmon resonance

LUMO – Lowest unoccupied molecular orbital

MB – Methylene blue

MIPA – Monoisopropanolamine

MO – Methyl orange

MP – Monkhorst-Pack

*m-s* – Monoclinic scheelite

MWCNT – Multi-walled carbon nanotube

NIR – Near infrared

NMP – *N*-methyl-2-pyrrolidone

PAW – Projector-augmented wave

PDT – Photodynamic therapy

PEG – Poly(ethylene glycol)

PL – Photoluminescence

PLE – Photoluminescence excitation

rGO – Reduced graphene oxide

RhB – Rhodamine B

SAED – Selected area electron diffraction

$S_{BET}$ – BET surface area ($m^2/g$)

SEM – Scanning electron microscopy

SERS – Surface enhanced Raman scattering

S-graphene – Sulfur-doped graphene

SMX – Sulfamethoxazole

$S_P$ – Pore size (nm)

STEM - Scanning transmission electron microscopy

SWCNT – Single-wall carbon nanotube

TC – Tetracycline

TEM – Transmission electron microscopy

TO – Transverse optical mode

TRPL – Time-resolved photoluminescence

*t-s* – Tetragonal scheelite

*t-z* – Tetragonal zircon

UV – Ultraviolet

UV/VIS – Ultraviolet/visible

VASP – Vienna ab initio simulation package

VB – Valence band

$V_P$ – Pore volume ($cm^3/g$)

wt% – Weight percentage

WWTPs – Wastewater treatment processes

XPS – X-ray photoelectron spectroscopy

XRD – X-ray diffraction

ZnDTC – Zinc diethyldithiocarbamate

*a*, *b, c* – Lattice parameters (Å)

*d* – Interlayer distance (nm)

$e^-$-$h^+$ – Electron-hole pair

$E_{ads}$ – Adsorption energy (eV)

$E_g$ – Band gap energy (eV)

*k* – Kinetic rate constant ($min^{-1}$)

α – Relative amplitude of the measured lifetimes (%)

β – Lattice parameter (°)

δ – Chemical shift (ppm)

θ – X-ray diffraction angle (°)

ι-carrageenan – Iota-carrageenan

κ-carrageenan – Kappa-carrageenan

λ-carrageenan – Lambda-carrageenan

λ – Wavelength (nm)

$\lambda_{exc}$ – Excitation wavelength (nm)

$\lambda_{onset}$ – Absorption onset wavelength (nm)

$\chi^2$ – Chi-square statistic test

# LIST OF FIGURES

# LIST OF TABLES

# FRAMEWORK

## 1. Motivation and context

In 2015, all United Nations Member States agreed on 17 Sustainable Development Goals inscribed in the 2030 Agenda for Sustainable Development.[1] These goals are an urgent call for effective action by all countries to achieve peace and prosperity for all people and the planet. Several strategies have been planned to end poverty and hunger, improve health and education, fight inequality, stimulate economic growth and tackle the impact of climate change. To make the 2030 Agenda a reality in a global context, significant efforts and a strong commitment must be addressed by governments, companies, industries, universities, and society at the collective and individual levels. Specifically, the Goal 6 and Goal 14 concerning “Clean water and sanitation” and “Life below water” are important key factors for the prosocial motivation of this research work. Goal 6 aims to ensure availability and sustainable management of water and sanitation for all, whereas Goal 14 attempts the conservation and use of the oceans, seas, and marine resources for sustainable development.

Clean water is essential to human health and is a critical feedstock in a variety of key industries, however the world is being challenged to meet rising demands of clean water as the available supplies of freshwater are decreasing due to several factors, such as extended droughts, population growth and more severe health-based regulations.[2] Thus water contamination is a global problem requiring efforts at political, educational and social levels, including the scientific community which has an important role to guarantee sustainable water supplies for future generations.[3,4]

Advances in nanoscale science are offering extraordinary opportunities to develop more cost-effective and environmentally acceptable water purification processes in surface water, groundwater and industrial wastewater streams, which are contaminated by toxic metal ions, radionuclides, organic and inorganic solutes, bacteria and viruses.[2,5] Nanomaterials are typically materials with sizes below 100 nm, presenting distinct properties than those observed in bulk materials, due to size and surface effects which become relevant at the nanoscale level. These materials present attractive features such as, small size, large surface area to mass ratio, reactive surface sites, high photosensitivity and physicochemical stability, and tunable pore size and surface chemistry, which make them particularly attractive for water purification applications.[6]

A significant portion of pharmaceutical wastes contain anti-inflammatory/analgesic drugs. Although designed to target specific metabolic pathways in humans, these compounds may adversely impact aquatic ecosystems and human health.[3,4] Pharmaceutical compounds cannot be fully assimilated being only partially metabolized, and some part is excreted which enters in wastewater treatment plants (WWTPs) or the water environment. Their occurrence in surface water, groundwater and industrial wastewater streams has been detected ranging from ng/L to µg/L.[6] WWTPs processes

have been developed but in many cases these are non-effective for persistent organic pollutants.[7] Advanced oxidation processes (AOPs) based on photocatalysis stands as an important technology for degradation of such pollutants. This process involves the generation of reactive radicals, which oxidizes organic matter in the presence of light activated catalysts with possible complete mineralization of the target compounds.[8]

The photocatalytic degradation of pharmaceutical compounds under solar light has been considered as a sustainable method considering the low energy cost. However, there are important issues to be considered, such as low solar light activity, a low quantum yield efficiency and high energy consumption.[6] Photocatalysts should exhibit unique properties, such as a large surface area, abundant surface states and the feasibility of surface functionalization; therefore a crucial aspect in developing such photocatalysts has been the application of adequate surface chemistry methods aiming at efficient photodegradation mechanisms. In this research project, this scientific issue is tackled by exploring innovative surface chemical modification routes of carbon-based structures, such as graphene oxide (GO), carbon spheres and carbon dots (C-dots).

Graphene exhibits properties such as high surface area, mechanical strength, high electron mobility and high conductivity for electron capture and transport.[9] On the other hand, GO is more hydrophilic due to the presence of oxygen functionalities at the surface, resulting in a good candidate for many applications, including semiconductor heterogeneous catalysis. $TiO_2$ has been the elected photocatalyst for environmental applications due to its photostability, photoactivity and low toxicity.[10] However, pure $TiO_2$ photocatalysts also present disadvantages mainly related to strong catalytic activity only in ultraviolet (UV) region, which represents only ~4% of the solar radiation available, and visible photons are not harvested for the photocatalytic process. Although this limitation has been tackled by several strategies, there is clear interest in developing visible-light activated photocatalysts based on alternative semiconductors. Narrow band gap semiconductors, such as certain metal sulfides have been investigated as photocatalysts in the visible region that might extend to the near infrared (NIR).[11] For example, CuS has been reported to harvest photons efficiently in the visible region, which makes this semiconductor an interesting material to be explored in visible-light photocatalysis. As GO has been extensively investigated as platform to develop such hybrid materials, the understanding of the phenomena that mediates the surface chemistry of the photocatalytic materials is of great interest. Surface enhanced Raman scattering (SERS) combined with confocal Raman spectroscopy can be a useful tool to fully examine the surface of such photocatalysts.

Carbon spheres comprise other type of carbonaceous materials which present several functional oxygen groups at the surface, determinants for further chemical functionalization and to explore surface modifications in aqueous medium.[12] As such, these materials can be easily combined with other inorganic particles yielding functional composites for target applications. Bismuth vanadate ($BiVO_4$) is a prime candidate widely used for water splitting for hydrogen and oxygen evolution[13,14] as well for photocatalytic degradation of organic pollutants.

C-dots are nanoparticles less than 10 nm in average size, which recently have drawn great attention due to their optical properties, benign nature, (photo)chemical robustness, ability for surface functionalization and low-cost production by using renewable carbon sources.[15]

This research plan intends to explore several carbon-based photocatalysts that combine carbon-based materials and semiconductor phases enabling the efficient harvesting of photons in the visible region of the spectrum.

## 2. Objectives of the thesis

This research plan comprised an integrated approach in using nanostructures with distinct functionalities by considering from the very beginning the adequate surface chemistry of several nanomaterials. There was the clear objective in developing multicomponent photocatalysts whose properties are better that the expected sum of the parts, resulting from the synergy of the several functional components.

Hence, the general aim of this research plan was to investigate chemical routes that provided carbon-based materials with photocatalytic properties, foreseeing new technologies for water treatment stations. In particular, water pollutants such as antibiotic pharmaceuticals were considered here as the target pollutants. *En route* to this main objective, the following goals were specifically addressed:

1. To explore different carbon-based materials as dispersible platforms for photocatalysis and inquire about their effect on the photocatalyst performance;
2. To prepare and characterize materials based on GO or carbon microspheres decorated with distinct semiconductor phases, such metal sulfide crystals and $BiVO_4$ phases;
3. To evaluate the photocatalytic performance of the ensuing composites, first on the degradation of model pollutant rhodamine B (RhB) and then of pharmaceutical compounds, specifically sulfamethoxazole (SMX) and tetracycline (TC);
4. To understand the mechanisms involved on the photocatalytic degradation of the investigated water pollutants;
5. To characterize the photocatalysts after the photodegradation experiments evaluating their stability, morphological and optical properties, and potential for reuse;
6. To contribute for the development of Raman spectroscopic methods in the surface characterization of the photocatalysts;
7. To explore eco-friendly routes towards photoluminescent C-dots using renewable sources parallel to the photocatalysts production.

## 3. Thesis outline

This thesis is composed by seven chapters.

**Chapter I** presents an overview on carbon-based materials with distinct structural dimensionalities with potential for the development of visible-light photocatalysts. This chapter is an effort to summarize classes of carbon materials, including the properties of hybrid structures also containing metal oxides and metal sulfides, which are of interest for heterogeneous photocatalysis applied to water treatment technologies.

**Chapter II** describes original research on the *in situ* thermal decomposition of a series of metal alkyldithiocarbamate complexes aiming the production of graphene-based materials functionalized with semiconducting nanophases. In particular, the synthesis and characterization of several metal sulfide@GO hybrid nanostructures was investigated envisaging the use of selected materials for subsequent photocatalytic studies.

**Chapter III** explores CuS supported on graphene-based materials synthetized by the chemical route developed and described in the previous chapter. These materials were used for the photocatalytic removal of two target water contaminants, RhB and SMX and compared with pure GO and CuS particles.

**Chapter IV** describes the research on exploring confocal Raman microscopy combined to the SERS effect to probe the surface of photocatalysts, specifically GO decorated with nanocrystalline ZnS. These studies provide new physicochemical insights related to the SERS effect using semiconductors, namely based on Raman maps of the hybrid nanostructures, which are useful to thoroughly understand the nature of the synergy observed in such structures. Density functional theory (DFT) studies were conducted to complement such spectroscopic studies and to investigate the adsorption behaviour of a molecular probe on both ZnS and ZnS@GO substrates.

**Chapter V** introduces a hydrothermal carbonization (HTC) method as a route to prepare other class of carbon materials, specifically carbon microspheres, which can be regarded as platforms for the deposition of semiconductor photocatalysts. Specifically, $BiVO_4$ phases were grown over the carbon microspheres by thermal treatment of a chemical bath containing the respective metal coordination ions. The hybrid materials obtained were then used for the photocatalytic degradation of TC dissolved in water and their performance was compared with pure carbon spheres and $BiVO_4$ phases.

**Chapter VI** comprises exploratory research on the synthesis and optical properties of photoluminescent C-dots. This research demonstrates that in parallel with the chemical synthesis of HTC-based photocatalysts, other photoactive carbon materials can be produced, such as C-dots prepared by the HTC of carrageenan, as a renewable carbon source.

**Chapter VII** presents the overall conclusions of the research performed in these doctoral studies and some perspectives for future work in this field.

# 4. List of contributions

From this research work have resulted several publications, oral and poster communications.

*Published papers:*

Joana L. Lopes, Maria J. Martins, Helena I. S. Nogueira, Ana. C Estrada, Tito Trindade. *Carbon-based heterogeneous photocatalysts for water cleaning technologies: a review*. **2021**, Environ. Chem. Lett. 19, 643-668.

Joana L. Lopes, Sara Fateixa, Ana C. Estrada, José D. Gouveia, José R. B. Gomes, Tito Trindade. *Surface-enhanced Raman scattering due to a synergistic effect on ZnS and graphene oxide*. **2020**, J. Phys Chem C. 124, 12742-12751.

Joana L. Lopes, Ana C. Estrada, Sara Fateixa, Marta Ferro, Tito Trindade. *A general route for growing metal sulfides onto graphene oxide and exfoliated graphite oxide*. **2017**, Nanomaterials. 7, 245.

Renata Matosa, Marta S. Nunes, Iwona Kuźniarska-Biernacka, Mariana Rocha, Alexandra Guedes, Ana C. Estrada, Joana L. Lopes, Tito Trindade, Cristina Freire. *Graphene@metal sulfide/oxide nanocomposites as novel photo-Fenton-like catalysts for 4-nitrophenol degradation*. **2021**, Eur. J. Inorg. Chem. 4195-4928

*Submitted papers*:

Joana L. Lopes, Ana C. Estrada, Sara Fateixa, Ana L. Daniel-da-Silva, Tito Trindade. *Visible-light activation of carbon supported $BiVO_4$ photocatalysts*. **2021**.

*Manuscripts in preparation*:

Joana L. Lopes, Tito Trindade, Ana C. Estrada. *Copper sulfide nanoflower-like structures supported on graphene materials for photocatalytic degradation of water contaminants*. **2021**.

*Oral communications*:

Joana L. Lopes, Sara Fateixa, Ana C. Estrada, José D. Gouveia, José R. B. Gomes, Tito Trindade. *Surface studies on ZnS/graphene oxide nanostructures using 4-mercaptopyridine as molecular probe*, presented at 14º Encontro Nacional de Química Física 14 ENQF, March 29-31, 2021 (online conference).

Joana L. Lopes. *Carbon nanostructures for the photodegradation of pollutants in water*, presented at Research Summit 2019, in University of Aveiro, Portugal, July 3-5, 2019 (in the form of pitch).

*Poster contributions*:

Joana L. Lopes, Ana C. Estrada, Tito Trindade. *Hybrid nanomaterials of graphene oxide and copper sulfide for the photodegradation of sulfamethoxazole in water*, presented at VIII Iberian Meeting on Colloids and Interfaces RICI8, in Aveiro, Portugal, July 17-19, 2019.

Joana L. Lopes, Sara Fateixa, Ana C. Estrada, Tito Trindade. *Raman spectroscopy as a tool to probe surfaces of graphene oxide decorated with ZnS nanophases*, presented at XXXIV European Congress on Molecular Spectroscopy EUCMOS, in Coimbra, Portugal, August 19-24, 2018.

Joana L. Lopes, Ana C. Estrada, Tito Trindade. *Hybrid carbon nanostructures aiming at photocatalytic applications*, presented at 6$^{th}$ Portuguese Young Chemist Meeting 6PYChem, in Setúbal, Portugal, May 15-18, 2018.

Joana L. Lopes, Ana C. Estrada, Sara Fateixa, Marta Ferro, Tito Trindade. *Raman studies on graphene-based materials doped with metal sulfides*, presented at VII Iberian Meeting on Colloids and Interfaces RICI7, in Madrid, Spain, July 4-7, 2017.

Joana L. Lopes, Ana C. Estrada, Tito Trindade. *Decoration of carbon nanostructures using silver sulfide nanocrystals*, presented at Materiais 2017, in Aveiro, Portugal, April 9-12, 2017.

*Presence in scientific meetings as member of the organizing committee:*

**July 2019**: VIII Iberian Meeting on Colloids and Interfaces (RICI8), Aveiro, Portugal

**July 2018**: 5th International Conference on Nanotechnology, Nanomaterials & Thin Films for Energy Applications, Aveiro, Portugal

**April 2017:** Materiais 2017, Aveiro, Portugal

**February – March 2019:** Queen Mary University of London

Short Term Scientific Mission: *Synthesis and characterization of carbon dots (C-dots) as growth platforms for morphological well-defined particles,* funded by the European COST Action CA17120 supported by the EU Framework Programme Horizon 2020.

# CHAPTER I

## *Literature review*

This chapter presents an overview on the research involving carbon-based nanostructures for heterogeneous photocatalysis applied to water purification. In particular, this review approaches the reported literature on this topic with focus on carbon nanomaterials with distinct structural dimensionality (2D: graphene-like; 1D: carbon nanotubes; 0D: carbon dots) discussing developments in synthetic routes and surface modification of carbon nanostructures with distinct phases, such as semiconductor compounds.

# CHAPTER I | "Carbon-based heterogeneous photocatalysts for water cleaning technologies"

Clean and accessible water for all has been defined by the United Nations as a major goal to promote sustainability in a planet with improved life quality. However, the growth of population and global industry processes are having a massive impact on the water quality. The presence of organic pollutants in water and wastewater, such as pharmaceuticals, organic dyes and by-products of industrial processes, is a major issue. Conventional wastewater treatments are still limited, and, consequently, it is crucial to design innovative cleaning technologies such as heterogeneous photocatalysis comprising nanomaterials. Here the mechanisms and applications of carbon-based nanostructures for heterogeneous photocatalysis applied to water purification are reviewed. In particular, the recent developments in synthetic routes and surface modification of carbon nanostructures aiming at their use under visible-light irradiation are presented. As such, carbon-based nanostructures decorated with distinct phases have been investigated, such as semiconductor compounds. The photocatalytic efficiency of hybrid nanocomposite materials is attributed to improved light harvesting and reduced recombination of photo-generated charge carriers. Furthermore, the recovery of photocatalysts by using assisted magnetic separation is presented as a promising strategy of reusability. [1]

*Keywords*: carbon nanostructures; metal oxides; metal sulfides; semiconductors carbon nanocomposites; visible-light photocatalysts; heterogeneous photocatalysis; photodegradation; organic pollutants; water cleaning.

[1] This chapter is based on the literature review: Joana L. Lopes, Maria J. Martins, Helena I. S. Nogueira, Ana. C. Estrada, Tito Trindade. *Carbon based heterogeneous photocatalysts for water cleaning technologies: a review*. **2021**, Environ. Chem. Lett. 19, 643-668. (DOI: 10.1007/s10311-020-01092-9)

In this manuscript, Joana L. Lopes was the main author involved in all the written and literature search tasks, except the material concerning polyoxometalate chemistry which was performed by Maria J. Martins. All the authors contributed to the planning, revision and writing of the manuscript.

# 1. Introduction

Contamination of water resources is a global problem. According to the European Environmental Agency Report, only about 40% of surface waters are in good ecological status and 38% are in good chemical status.[16]

Organic pollutants, such as pesticides, pharmaceutical waste, dyes, and many other forms of industrial waste that appear from the discharge of sewage, agricultural activities, and industrial releases, are the main environmental concern due to their persistence and bioaccumulation properties. Nowadays, the development of new and efficient strategies that contemplate the elimination of emergent pollutants requires efforts from the scientific community to guarantee sustainable supplies of water for future generations.[17,18]

Wastewater treatment based on adsorption processes have been developed but in many cases these methods are non-effective for persistent organic pollutants such as certain pharmaceutic products.[7] Advanced oxidation processes (AOPs) based on photocatalysis stands as an important technology for degradation of such pollutants even when present in trace amounts.[8] This process involves the generation of reactive oxygen species, typically at the surface of suspended particles that act as photocatalysts, which then oxidize organic matter when light irradiated at specific wavelength regions.[8,19,20] A crucial aspect in developing such photocatalysts has been the application of surface chemistry methods aiming at efficient photodegradation under ultraviolet (UV) and visible-light. This scientific issue has been tackled by using different types of materials and exploring innovative surface modification routes, namely those involving carbon-based nanostructures.

Carbon nanostructures comprise a class of materials that have been central in the development of nanotechnologies. Noteworthy, scientific discoveries in this field have earned recognition with the highest scientific award, with the Nobel prizes for the discovery of fullerene (H. Kroto, R. Smalley and R. Curl: 1996 Nobel Prize in Chemistry)[21] and the production of free standing graphene monolayers (A. Geim and K. Novoselov: 2010 Nobel Prize in Physics).[22] In addition to the fundamental interest of these nanostructures, these materials have attracted the attention of the scientific community to their potential in the development of new technologies.

The allotropy of carbon is well known, and its knowledge has long allowed for a multiplicity of applications of carbon materials, such as those involving graphite, diamond and amorphous carbon. Thus, the discovery of new structural forms of carbon can be regarded as an extension of the carbon lexicon available to produce new materials and devices. For example, the distinct structural dimensionalities of carbon nanostructures can be explored to determine the final properties of carbon-based nanocomposites. These have been defined as the combination of a carbon nanomaterial with at least another distinct material whose components maintain their chemical identity. In light of this, in the next sections of this review a brief introduction to carbon nanomaterials will be firstly presented, followed by a discussion on the use of surface modified carbon materials with semiconductor nanophases, and finally the application of these materials in photocatalysis

applied to water treatment, a topic in line with the societal challenge of providing new materials for water cleaning technologies.[6]

## 2. Carbon nanostructures of distinct structural dimensionality

Carbon nanostructures are versatile materials of particular interest in environmental science (e.g. water purification/ remediation).[23] However, there is need to develop sustainable variants of conventional carbon materials.[24] The production of such carbon materials should be low cost, scalable and based on renewable and highly abundant resources.

Among the variety of carbon materials, graphite is the most common allotrope and, together with diamond, comprise the most well-known natural 3D carbon material.[25] Typical carbon nanostructures show lower structural dimensionality, 2D (graphene and other derived flat-type materials), 1D (carbon nanotubes) and 0D (fullerenes and carbon dots) (**Figure I.1**). Conceptually, these lower dimensional nanomaterials can be regarded as derived from atom carbon thick sheets of graphene.[26] Hence, a graphene sheet can be rolled up to originate a single-wall carbon nanotube (SWCNT) or, a fullerene molecule by using carbon hexagonal arrangements complemented by carbon pentagons. Other graphene-based materials can be originated by either over stacking the graphene layers or by chemical oxidation, in which case graphene oxide (GO) forms. Among the carbon-based nanomaterials reviewed here, those based on GO are the focus due to their relevance in aqueous colloidal chemistry processes such as heterogeneous photocatalysis.[27–29] The following section presents main aspects concerning the structure and chemistry of graphene-based materials.

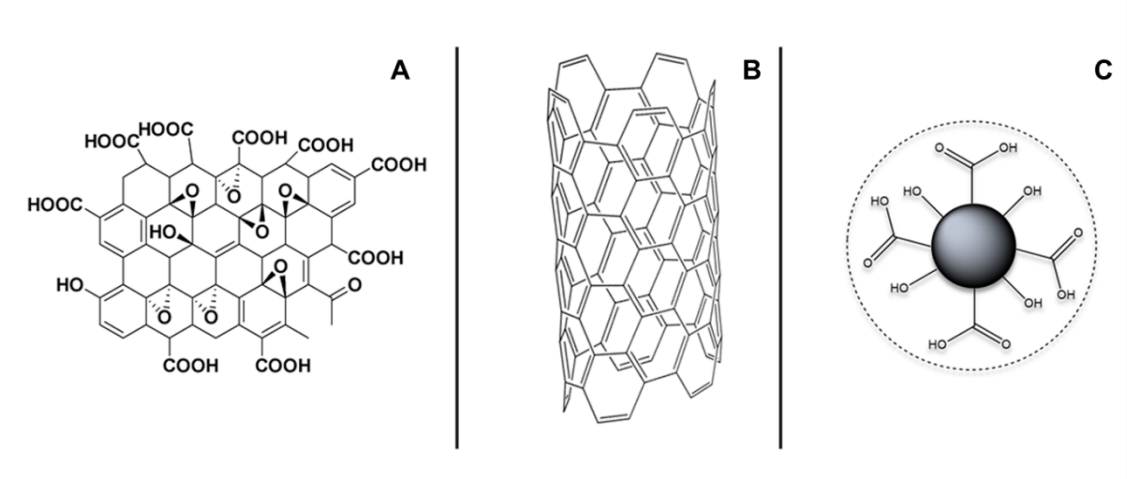


**Figure I.1:** Schematic representation of carbon nanostructures of distinct structural dimensionality: graphene oxide (A), single-wall carbon nanotube (B) and carbon dot (C).

## 2.1. 2D carbon nanostructures: graphene and graphene-based materials

Research in this field has started in 1840s, when intercalation compounds of graphite were first discovered. In the early 1930s, with the introduction of X-ray diffraction (XRD) techniques, the crystalline structures were revealed and a few years later, in 1947, theoretical analyses suggested that isolated graphene layers would present unique electrical properties. Nowadays, these predictions have been proven correct.[30] Graphene is a one atom thick planar sheet of $sp^2$-bonded carbon atoms arranged in a honeycomb lattice, exhibiting remarkable electronic, thermal and mechanical properties.[24,26] It is the building block of graphite, with the lamellar graphitic structure hold in place by the stacking of graphene sheets, spaced by a interlayer distance of 0.34 nm between the sheets, bound together through van der Waals forces.[26,31] In each sheet, the carbon atoms are covalently linked *via* overlapping of $sp^2$ orbitals with the remaining $p_z$ overlapping to form a band of filled π orbitals, valence band (VB) and a band of empty π* orbitals, conduction band (CB).[25]

Mechanical exfoliation of graphite generates single layers of graphene. Originally this was demonstrated by the sequential micromechanical cleavage of graphite using adhesive tape originating free standing graphene layers, known as the *"scotch tape method"*, reported by Novoselov and Geim in 2004 and honored with the Noble Prize in Physics, six years later.[25,32] Chemical vapor deposition (CVD) processes have also been developed and are nowadays applied for mass production of graphene with a relatively small number of defects.[24,26] Graphene layers can be produced by chemical exfoliation of bulk graphite.[30,33] These methods are cost-effective because use an inexpensive raw material and can be combined with other chemical treatments, producing a variety of graphene and graphene-based materials, such as GO or reduced graphene oxide (rGO).[34] With the direct exfoliation of graphite, the resulting graphene sheets have significant quality with good crystallinity, low defect densities and high conductivity, however, the yield is usually low.[34] Oxidation of graphite followed by exfoliation in aqueous media yield colloidal stable GO suspensions.[35]

Although water is a medium of first choice for the formation of graphene-based materials, the exfoliation process is challenging due to the hydrophobic character of pristine graphene sheets. This drawback can be overcome with surfactants which allow exfoliated sheets to remain suspended and prevent overstacking.[30,36] Atomic force microscopy (AFM) studies show that almost all the sheets were less than 5 layers thick. Overcoming the van der Waals forces is essential for the success of the exfoliation process, by increasing the distance between the layers *via* chemical intercalation. Ideal solvents should have a surface tension about 40 $mJ/m^2$ allowing a good dispersion of the material.[26,30,35] Hence, graphene can be exfoliated by ultrasonication of graphite in organic solvents, such as dimethylformamide (DMF) and N-methyl-2-pyrrolidone (NMP).[37,38] Commonly used sonication techniques consist in shear forces and cavitation (the growth and collapse of micrometer-sized bubbles) acting on the bulk material and inducing the exfoliation process.[26] Successful sonication-based exfoliation of graphite was achieved by using NMP by Hernandez *et al.*[39] The authors reported a material comprising 28% of graphene monolayer and nearly 100% graphene nanosheets less than 6 atomic layers thick. Repeated sonication and re-centrifugation of the

unexfoliated bulk material can increase the yield.[26] Other solvents commonly used include pyridine and perfluorinated compounds.[25,30] Single layered graphene can be produced by thermal annealing of silicon carbide and CVD.[25]

GO consists in $sp^2$ graphene sheets with an high density of oxygen functional groups such as epoxy, hydroxyl, carboxyl and carbonyl groups.[40] The ultraviolet/visible (UV/VIS) absorption spectrum of a GO suspension exhibits an absorption peak related to π-π* transitions of aromatic C-C bonds around 230 nm and a shoulder at 315 nm assigned to n-π* transitions of the oxygen-containing groups.[41] The polar nature of these chemical groups, coupled with the electrostatic repulsion associated with extensive proton dissociation, turn GO sheets colloidal stable in water. These suspensions are adequate for aqueous based technologies such as water cleaning using AOPs.[38] The presence of out of planar C-O covalent bonds increases the interlayer distance from 0.34 nm to 0.65 nm, thus decreasing the energy required to separate the graphene layers.[25,31,40] The hydrophilic character of oxidized graphite allows water to adsorb into the lamellar structure, further increasing the interlayer distance to 1.15 nm.[42] At slightly basic pH, the negatively charged oxygen-containing groups on GO surface contribute to the stability of the dispersions of these sheets in aqueous media due to their hydrophilic nature. Polar solvents, for instance ethanol, acetonitrile, DMF, NMP, dimethyl sulfoxide, allow stable dispersions, while dispersion in less polar solvents, such as acetone, tetrahydrofuran or toluene, led to either flocculation or aggregation.[40] Chemical modifiers and surfactants, including isocyanates, quaternary amines, diazonium salts, ionic liquids and single-stranded DNA, are known to stabilize either aqueous or organic dispersions of graphene.[43–47] Non-covalent functionalization of GO with organic compounds involves mostly van der Waals forces or π−π interactions. Usually, van der Waals forces are established between GO and organic molecules or polymers with high hydrophobic character, while π−π interactions are common between GO and molecules comprising a π system. Oxygen functional groups on the surface and edges of GO allow ionic interactions and hydrogen bonds to take place. The noncovalent interactions are extremely relevant for applications because the extended π system contributes to enhanced electric conductivity and mechanical strength.[48]

Early on 1958 Hummers and Offerman introduced a method to produce GO from graphite involving its oxidation using $KMnO_4$ as an oxidizing agent in concentrated $H_2SO_4$.[49] Graphite oxide is prepared from graphite powder and $NaNO_3$, in $H_2SO_4$ solution. The addition of $KMnO_4$ promotes the oxidation of graphite through the active species $Mn_2O_7$, which selectively oxidizes unsaturated aliphatic double bonds over aromatic double bonds. GO can be obtained by exfoliation of graphite oxide into monolayer sheets through a variety of thermal and mechanical methods.[50] Due to the disruption in the π orbital structure on oxidation with high defect density introduced, GO is a poor electrical conductor.[38,48] Due to its low production costs, GO is an affordable intermediate to graphene production if the original carbon lattice could be restored. The reduction of GO to yield rGO, can be achieved using chemical reducing agents, photoreduction, thermal annealing or microwave-assisted reduction.[51] However, the reduction process cannot remove all structural defects and restore the

charge-carrier mobility of pure graphene (250000 $cm^2/Vs$ at room temperature);[30,40] generally, the extent of reduction of oxygen groups in rGO is approximately 70%.[52] Solid GO has a brownish color but becomes darker as it is reduced.

The structure of the different graphitic materials can be monitored by powder XRD. Graphite presents a basal reflection (002) peak at 26.6º related to an interlayer distance of 0.34 nm. Oxi*d*ation or exfoliation processes increase the interlayer distance shifting the basal (002) reflection peak to at 11.2º, which corresponds to a interlayer distance of 0.79 nm, observed in GO.[25] Raman spectroscopy is a sensitive technique to symmetric covalent bonds with little or no natural dipole moment. Carbon-carbon bonds present in carbon materials such as graphene, fit this criterion thus Raman spectroscopic methods are applied to study graphene materials, such as the surface chemistry of GO. Graphitic materials are characterized by two distinct Raman bands, the G band and the 2D band, which are related with the $sp^2$ hybridized carbon atoms in the planar sheets. The existence of defects in the carbon lattice by introducing $sp^3$ hybridized carbon atoms originates an additional spectroscopic feature termed D band.[53] The features of the G and 2D Raman bands allow to differentiate between monolayer (or few-layer) graphene and graphite-based materials. The D band, also known as the disorder band, is weak in high quality graphene. The intensity of this band is directly related with the level of defects, either edges or topological defects in the sheet, therefore it is visible at around 1350 $cm^{-1}$ in the Raman spectrum of graphite and graphite-based materials.[25,38,53] The D band is also observed in GO samples due to the oxygen moieties in the carbon layers. Hence, the D-to-G bands intensity ratio ($I_D/I_G$) gives information about the level of defects that characterize the GO samples.[25] The 2D band is an overtone of the D band, resulting from a two-photon lattice vibrational process, but unlike the D band, is not related to the defects. For single layer graphene, this band is observed as a single symmetric peak below 2700 $cm^{-1}$.[38,53] Adding successive layers causes the splitting in several overlapping modes with consequent decrease in symmetry with a shift to slightly higher wavenumbers.[25] This behaviour is observed in graphite and graphite oxide substrates with a broad band around 2800 $cm^{-1}$.

In brief, the surface chemistry and structural features of GO turn this material a suitable platform for anchoring photocatalytic phases. Nevertheless, other carbon nanomaterials have been explored due to their distinct properties, as presented in the following sections.

## 2.2. 1D carbon nanostructures: single-wall- and multi-wall-carbon nanotubes

It has been reported that carbon nanotubes (CNTs) were firstly described in 1952 by Radushkevich and Lukyanovich. However, it was after Iijima's discovery in 1991 of a novel method of preparation of finite carbon structures, designated by multi-walled carbon nanotubes (MWCNTs),[54] that CNTs have gained an increasing interest in the past three decades. Two years later, a method to prepare SWCNTs was reported.[55] CNTs are rolled-up hollow cylinders of graphene sheets with fullerene-like hemispheres at the terminal ends. CNTs are classified as single-wall or multi-wall CNTs depending

on the number of concentric layers.[56,57] According to this definition, a SWCNT is a rolled-up one atom-thick sheet of graphene, whereas a MWCNT comprises an array of cylindrically nested SWCNTs.[58,59]

Arc-discharge and laser ablation methods were among the first synthetic methods used to prepare CNTs.[58] For instance, MWCNTs discovered by Iijima were produced at a temperature about 3500 $^{o}$C, by arc-discharge using graphite electrodes,[54] but current CVD processes allow much lower temperatures (700-950 $^{o}$C).[60] Materials produced by these processes have several impurities and only a small fraction corresponds to CNTs. Most common impurities are carbonaceous materials and metallic catalysts (Fe, Ni, Mo or Co). The development of efficient purification methods is crucial, where acid treatment methods are the most common ones.[61,62] CVD allows to produce relatively pure CNTs with possibility of scale-up, when compared with laser ablation methods.[63]

While SWCNTs possess diameters of 1-2 nm and lengths from 50 nm up to 1 cm, MWCNTs possess larger diameters, from 10 to 100 nm.[56] Within the graphene sheet, carbon–carbon covalent bonds are almost exclusively $sp^2$-hybridized and therefore stronger than the $sp^3$ C-C bond found in diamond, which confers unique properties to these structures.[64]

Pristine CNTs are found to be hydrophobic in nature and their high aspect ratio allows the development of interparticle van de Waals forces, with no electrostatic or steric repulsive interactions to balance this out.[64] In suspension, CNTs aggregate, and this often results in mesoscopic aggregates of fifty to hundreds of tightly entangled CNTs.[64,65] Flexible SWCNTs allow loading of multiple molecules along the length of the nanotube due to their high surface area with all atoms exposed on the surface (1300 $m^2/g$).[56] In addition, supramolecular binding of aromatic molecules can be reached by π-π stacking of such molecules onto the surface of CNTs. On other hand, due to their larger sizes, MWCNTs constitute different platforms as delivery agents of biomolecules.[66,67]

Mechanical disentanglement of CNTs is usually achieved by ultrasonication with high shear forces that promotes their efficient dispersion in the liquid medium. This process relies on surface modification using surfactants, homopolymers and block copolymers, which enhance the compatibility with the dispersing medium. In addition, repulsive forces (steric or electrostatic) between CNTs are promoted.[64] Stabilizing agents possess an anchoring component able to attach to the CNT surface by physisorption or chemisorption, and a stabilizing part which interact with the medium providing colloidal stabilization. The non-covalent functionalization takes place between the CNTs' surface and the hydrophobic domains of selected molecules.[56] In this case, the surface modifiers are adsorbed through hydrophobic forces, van der Waals forces, π–π, or cation-π interactions.[64] The chemical structure or the π network is not altered, except for shortening of the CNTs' length when sonication is applied but preserving their intrinsic physical properties. CNTs have been reported to form stable black suspensions when sonicated in a 1% aqueous solution of sodium dodecyl sulfate.[68] Chemical adsorption of these amphipathic molecules generates a distribution of charges that induces colloidal stability in water. The hydrophobic part is adsorbed on the graphitic

network by van der Waals interactions and the hydrophilic part is oriented towards the bulk of the aqueous phase.[69,70] The amphiphilic molecules should have a low critical micelle concentration so that CNTs remain stable after removal of the excess coating molecules.[56]

Covalent functionalization of CNTs occurs by chemical reactions with the sidewalls that contain reactive $sp^2$ carbon atoms at the surface (COOH or OH groups) often arising from oxidative purification processes.[56,64] A common method uses oxidizing agents such as $HNO_3$.[71] In this process, COOH and OH functional groups are formed at the end of the tubes along with defects on the sidewalls. Functionalized CNTs are not dispersed in a range of solvents but allow further grafting of polymer chains onto CNTs surface.[64] The chains can be grown from an introduced initiator or can occur at the CNT surface, by chemical reactions, including click chemistry.[72,73] On the other hand, oxidized CNTs are soluble in water, but aggregate in the presence of salts and it is not viable for certain applications. Other surface modifications include the use of hydrophilic polymers such as poly(ethylene glycol) (PEG), originating CNT-polymer conjugates that are stable in physiological medium.[74] Cycloaddition reactions are used type to functionalize CNTs, which occurs *via* covalent linkages on the aromatic sidewalls.[56] The modification of CNTs considers the chemical nature of the solvent or the polymer matrix (hydrophilic/ hydrophobic, polar/ apolar).[75] Chemical functionalization by covalent bonds can affect electrical and optical properties of CNTs by disrupting the $sp^2$ conjugation of the carbon lattice.[65] Hence, this type of chemical functionalization limits the recycling of the CNTs, whereas noncovalent approaches in principle allow recycling of CNTs.[64,76]

The application of CNTs is usually determined by their structure (number of walls, diameter, length, chiral angle, etc.), which gives them specific properties.[58] These 1D nanostructures exhibit remarkable physical, mechanical, and chemical properties. For instance, their size, shape, high surface area, rigid platform structure and good electrical conductivity, in addition to the possibility to be easily derivatized with various molecules,[56,65] brings this class of carbon materials to be widely used in many fields and applications, including composite materials,[77] sensors,[78–80] drug delivery agents,[56,81,82] field-effect transistors,[83–85] hydrogen storage[86–88] and photocatalysis.[89–92] There has been great debate about the health impact of these carbon nanomaterials and toxicological assessment is mandatory before technology implementation. Hence, negative effects were reported for nonfunctionalized hydrophobic CNTs regarding their toxicity towards cells and animals.[93–95] On the other hand, the development of biocompatible CNTs harmless to cells *in vitro*[96–100] and *in vivo*[101–104] have also been reported. This is a critical issue for the application of CNTs in water remediation technologies, which turns more relevant the exploitation of other carbon nanomaterials posing less toxicological concerns. As discussed above, GO is one of such materials, but the last years have assisted to an increasing interest for carbon quantum dots (C-dots), as described in the next section.

## 2.3. 0D carbon nanostructures: carbon dots

C-dots present size and excitation wavelength ($\lambda_{exc}$) dependent photoluminescence (PL) behavior, attracting significant attention for applications in which size, cost and bio-/eco-compatibility are critical factors.[40] C-dots were accidentally discovered by Xu *et al*. in 2004, during the separation and purification of SWCNTs where a highly luminescent material was found.[105] C-dots are regarded as small quasi-spherical nanoparticles (2-10 nm) with graphitic or turbostratic carbon, containing mostly diamond-like $sp^3$ hybridized carbon insertions.[106] Usually, C-dots possess substantial carboxylic moieties at their surfaces, and the oxygen content in the oxidized C-dots may range from 5 to 50% depending on the synthetic route.[15] These carboxylic moieties on the surface improve water solubility and offer chemically reactive groups for further functionalization and surface passivation with several chemical groups. Surface functionalization might also contribute for improved solubility in aqueous and non-aqueous media, and enhanced fluorescence.[15,107] Their well-defined, closely isotropic shape, ultrafine dimensions, tunable surface functionalities alongside with several simple, fast, and cheap synthetic routes make C-dots a promising material for a number of applications, such as bioimaging, chemical sensing, photodynamic therapy (PDT), drug delivery, photocatalysis and electrocatalysis.[107,108] However, their separation and purification procedures, functionalization methods and their low quantum yields, are issues that need to be addressed.

Top-down strategies for preparing C-dots involve breaking down larger carbon structures (e.g. graphite, nanodiamond) by methods such as arc-discharge, laser ablation and electrochemical oxidation.[109–114] Alternatively, bottom-up methods enable the synthesis of C-dots from chemical precursors, such as carbohydrates, hydroxy acids and polymer-silica nanocomposites through combustion/thermal treatments and microwave synthetic routes.[115–118] Hydrothermal (or solvothermal) treatments are elected methods to prepare these materials by using several types of precursors.[108] In a typical solvothermal treatment, an high boiling point organic solution containing the precursor (e.g. glucose, citric acid) is sealed in an autoclave which is placed in the oven, for thermal degradation, after which the product is extracted with organic solvents.[119–124] Following Li's successful attempt to prepare fluorescent green C-dots with high solubility in aqueous media, stability and sensitivity to pH,[125] other bioderived precursors have been employed, such as citrate, glucosamine, ascorbic acid, chitosan and gelatine.[126–129] The particle size distribution can be adjusted by post-synthesis methods and the surface properties can be tuned during the preparation or post-synthesis stages.[108]

The complete structural description of C-dots is still a matter of discussion. C-dots with an average particle size of 3 nm, prepared by the laser ablation technique, show the diffraction planes (111), (220), (311), (400), and (331) corresponding to a diamond-like structure.[15] In general, C-dots show two characteristic diffraction peaks at 18.26º and 23.82º, which are attributed to their amorphous and graphitic content with an interlayer distance of 0.34 nm.[106] C-dots are composed by graphitic $sp^2$ carbon atoms confirmed by the presence of C=C aromatic ring stretching mode at 1623 $cm^{-1}$, functionalized with carboxylic and/or carbonyl groups. Infrared (IR) spectroscopy data show bands

at 3442 $cm^{-1}$, 1710 $cm^{-1}$, 1244 $cm^{-1}$ which are attributed to vibrational modes of hydroxyl, carbonyl and epoxide groups, respectively [106]. The Raman spectrum ($\lambda_{exc}$ 633 nm) of C-dots shows the presence of both $sp^2$ and disordered $sp^3$ carbons. As compared with graphite, C-dots exhibit only the D (1350 $cm^{-1}$) and G (1600 $cm^{-1}$) bands. The $I_D/I_G$ ratio demonstrates that C-dots have high content of $sp^3$ carbon atoms.[106,130]

C-dots shows strong optical absorption in the UV region with a tail extending to the visible range, eventually showing absorption shoulders attributed to π-π* transitions of the C=C bonds and the n-π* transitions of C=O bonds.[108] These carbon structures are frequently referred as carbon nanolights because have strong fluorescence,[15] which is strongly dependent on the $\lambda_{exc}$.[130,131] The band gap transition can be caused by conjugated π-domains, or it can involve surface defects in C-dots.[107] Both $sp^2$ and $sp^3$ hybridized carbon atoms and functionalized surface defects present in C-dots contribute to their multicolor emissions, but with strong fluorescence in the blue green region of the visible spectrum.[132–135] Such electronic transitions display weak absorption in the near UV region but intense emission in the visible range.[136,137] C-dots also exhibit phosphorescence properties when excited by UV-light, originated from the triplet excited states or aromatic carbonyl on the surface.

Although C-dots exhibit luminescent properties, the reported low quantum yields (less than 10%) have been a major limitation for applications.[130] Surface functionalization by promoting chemical interactions at the surfaces, such as covalent bonding and π-π interactions or electrostatic interactions, are used to tune their surface properties.[121,138–140 141] Indeed, the surfaces of C-dots are rich in oxygen-containing groups, which are prone to establish covalent bonding in order to improve PL behavior.[108] Polymer diamine-terminated oligomeric poly(ethylene glycol) has been used, among other polymers, such as poly-propionylethyleneimine-co-ethyleneimine.[142] Carbon particles with an average diameter 30-50 nm were found less luminescent and with lower quantum yields, as compared to C-dots.[114] Doping with N, S and P, is also used to tune the PL properties of these materials. Noteworthy, Zhu *et al*. have reported N-doped C-dots exhibiting 80% quantum yield, which approaches the observed in organic dyes and semiconductor quantum dots.[119]

C-dots have been employed in other applications, for instance the detection of heavy metals[143–145] and in the development of dye-sensitized solar cells and light-emitting devices.[108,146,147] C-dots are also interesting as contrast agents for *in vivo* optical imaging[148,149] and as multifunctional theragnostic agents. C-dots can also act as photosensitizers in PDT, since are able to generate more reactive oxygen species,[107] and as nano-carries for tracking and delivery of drugs or genes. Biocompatibility of the functionalized C-dots is an important factor for future applications in living cells, tissues and animals, and already several cytotoxicity evaluations were performed on both raw and passivated quantum dots. Toxicity studies have been performed suggesting that C-dots appear to have low toxicity.[149–151] C-dots functionalized with PEG were found to be non-cytotoxic up to concentrations much higher than that is required for cell imaging and related applications. Furthermore, the injection into mice was assessed and no significant toxic effects *in vivo* up to 28 days.[149] Recent findings show that under light excitation C-dots exhibit PL emission in the near infrared (NIR). This is exceptionally

useful for *in vivo* biotechnology applications because of the transparency of body tissues in the NIR "water window".[130,152]

The above sections discussed properties of carbon nanostructures that allows to realize their potential for several technologies. It is clear the role of surface chemistry on the use of such materials, which is demonstrated for example by their use as heterogeneous substrates of supported photocatalysts. The surface modification of carbon nanostructures, in particular GO, using inorganic photocatalysts is the subject of the following section.

# 3. Carbon-based semiconductor nanocomposites

## 3.1. Metal oxide loaded carbon nanostructures

Metal oxide semiconductors such as $TiO_2$, ZnO, $SnO_2$, $BiVO_4$ and $Fe_3O_4$ have been combined with carbon substrates using diverse methodologies. Among the semiconducting metal oxide nanoparticles, $TiO_2$ Degussa-Evonik P25 (70:30 % anatase-rutile)[153,154] (**Figure I.2**) has been the prime choice due to its photostability, relatively low toxicity, cost effectiveness, reusability and outstanding electronic and optical characteristics.[153] Thus, Kamat and co-workers demonstrated that $TiO_2$/GO nanocomposites act as an electron-transfer medium[155,156] through the sonication of an ethanolic suspension of $TiO_2$ and GO.

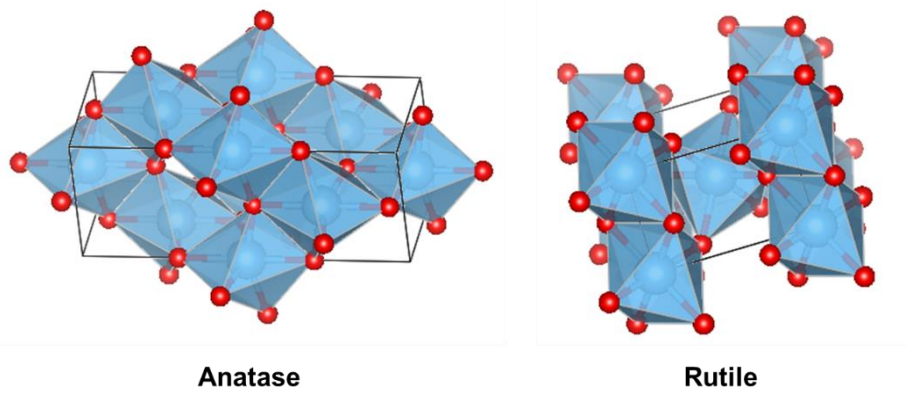


**Figure I.2:** Different crystalline strucutures of $TiO_2$, anatase phase and rutile phase. Color scheme: Ti in blue and O in red (using VESTA[157]).

Müllen and co-workers used $(NH_4)_2TiF_6$ as a precursor to sandwich-like $TiO_2$/GO nanosheets.[158] Other precursors, as $TiCl_3$ and tetrabutyl titanate, were used in the large-scale preparation of $TiO_2$/GO nanocomposite.[159,160] Polyvinylpyrrolidone it is commonly added to prevent the aggregation of $TiO_2$/GO nanocomposites and stabilize the as-prepared nanocomposites. Li *et al*. used $TiCl_4$ and titanium (IV) isopropoxide with GO in the presence of the non-ionic surfactant Pluronic P123, which also avoided the agglomeration of $TiO_2$ nanoparticles.[161] Titanium (IV) isopropoxide was also used

in the large scale preparation of $TiO_2$/GO nanorod composites through a two phases method, using oleic acid as a surfactant.[162] Recently, Ton *et al*. reported the exfoliation of graphite in the presence of titanium tetra-*n*-butoxide to obtain graphene sheets uniformly and thinly coated by a $TiO_2$ nanolayer, without using surfactants.[163] Other nanocomposite structures like $TiO_2$ nanowires/graphene nanocomposites and 3D hierarchical $TiO_2$/graphene hydrogel nanocomposites were prepared using a hydrothermal process.[164–167] Overall, $TiO_2$/GO nanocomposites show improved photocatalytic degradation of dyes, and in certain cases antibacterial activity, when compared to bare $TiO_2$ or GO materials.

Second in popularity to $TiO_2$, it is the use of ZnO in photocatalytic applications and several synthetic methodologies are reported for carbon-based ZnO systems. ZnO is a direct semiconductor (band gap ~3.4 eV) with an exciton binding energy of 60 meV; as compared with $TiO_2$ it has less quantum efficiency and poor photocatalytic stability associated to photocorrosion effects during light irradiation.[168] Several methodologies are available to prepare ZnO/carbon nanocomposites. For instance, Atchudan *et al*. reported the synthesis of ZnO/GO composites using a solvothermal method, where 15 nm ZnO nanoparticles were dispersed over the wrinkled graphene layers,[169] and Rabieh *et al*. prepared hierarchical ZnO/rGO nanocomposites *via* a green hydrothermal method as an efficient photocatalyst for the photodegradation of azure B dye.[170] Dong *et al.* have prepared ZnO nanorods/graphene nanocomposites through hydrothermal synthesis of $ZnCl_2$.[171] On the other hand, other authors have used microwave-assisted and sonochemical synthetic methods,[162,172] electrochemical deposition of ZnO nanorods onto rGO[173] and deposition of ZnO by CVD onto GO[174] or rGO.[175] Recently, Abdala and co-workers reported a new solventless route for the synthesis of ZnO/graphene nanocomposites comprising 9 nm ZnO nanoparticles dispersed on the surface of thermally reduced graphene *via* ball milling of hydrozincite and graphite oxide.[176] Overall, graphene-based ZnO nanocomposites are obtained using multistep solution-based approaches that have some drawbacks such as low productivity and production of large amounts of wastes. Other hybrid nanocomposites comprising CNTs and ZnO nanoparticles have been reported using ball milling,[177] ultrasonic spray,[178] chemical precipitation of ZnO on SWCNTs[179] and pulsed laser for ZnO deposition onto MWCNTs *via* hydrothermal synthesis.[180,181] In these cases, the acidic treatment of CNTs bundles it is an important key to create anchors points for the growth of ZnO nanoparticles.

Although less explored as compared to $TiO_2$ and ZnO, there is interest in $SnO_2$ photocatalysts because of negligible photocorrosion.[182] $SnO_2$ is an *n*-type semiconductor with a wide band gap (~3.6 eV) and a rutile-type crystal structure. Compared with pristine $SnO_2$, hybrid structures of $SnO_2$ nanoparticles onto GO or graphene, provide higher electrical conductivity and excellent photocatalytic properties. The materials are prepared by sonochemical, hydrothermal or microwave-assisted methods.[183–187] For instance, Kim *et al*. (2019) synthesized porous $SnO_2$ aerogel/rGO nanocomposites *via* an epoxide-assisted sol–gel process.[188] GO sheets were captured by the colloidal $SnO_2$ 3D network suspension, followed by the *in situ* thermal reduction of GO during the supercritical drying of the resulting nanocomposites. Liang *et al*. reported nanostructured materials

comprising SnO/$SnO_2$ nanoparticles loaded onto rGO thin flakes, after ultrasound treatment.[189] On the other hand, Zhou and co-workers attached ultra-small 2.4 nm $SnO_2$ nanoparticles onto graphene quantum dots and used them for photocatalytic removal of nitric oxide.[190] Using a different approach, Chen *et al*. (2017) prepared composites comprising two $SnO_2$ dense layers and a rGO sheet sandwiched in between.[191] The large area of contact between the $SnO_2$ nanoparticles and graphene sheets seems useful to separate electron-hole ($e^-$–$h^+$) pairs when the composite is used in photocatalysis.

**Table I.1** summarizes characteristics of the metal oxides discussed above. The use of metal oxide/ carbon hybrid nanostructures is promising in the field of photocatalysis but requires a better understanding of the interaction between metal oxide and carbon surface. Furthermore, visible-light photocatalysis is limited using such metal oxides which can be surpassed by exploring other inorganic phases, as discussed below.

**Table I.1:** Characteristic parameters of $TiO_2$, ZnO and $SnO_2$ crystalline lattices.[182,192–194]

| Phase | Space group | Lattice parameters (nm) | Volume density ($g/cm^3$) | Band gap (eV) |
|---|---|---|---|---|
| **$TiO_2$ tetragonal (rutile)** | P4/mnm | a= 0.4585, c= 0.2953 | 4.3 | 3.0 |
| **$TiO_2$ tetragonal (anatase)** | I4/amd | a=0.3784, c= 0.9515 | 3.9 | 3.2 |
| **$TiO_2$ rhombic (brookite)** | Pbca | a= 0.9184, b= 0.5447, c= 0.5145 | 4.1 | 3.3 |
| **ZnO hexagonal** | $P6_3mc$ | a= 0.3249, c= 0.5206 | 5.6 | 3.4 |
| **$SnO_2$ tetragonal (cassiterite)** | $P4_2/nmm$ | a= 0.4738, c= 0.3188 | 7.0 | 3.6 |

## 3.2. Metal sulfides loaded carbon nanostructures

Metal sulfide quantum dots are semiconductor nanocrystals exhibiting quantum size dependent optical properties.[195] These nanocrystals have typical sizes between those of molecules and micrometric crystals, displaying distinct optical behaviour in relation to their bulk counterparts (**Figure I.3**).[195] Macrocrystalline (bulk) semiconductors are characterized by a band gap energy, defined as the minimum energy necessary to excite an electron from the ground state VB into the vacant CB. In molecular terminology applied to smaller nanocrystals (nanoclusters), this corresponds to an electronic transition between the highest occupied molecular orbital (HOMO) and the lowest unoccupied molecular orbital (LUMO). The absorption of a photon with energy greater than the band gap energy, promotes an electron to the CB leaving a hole in the VB. The positively charged hole and the negatively charged electron form and $e^-$–$h^+$ pair know as exciton, with a characteristic size defined by the Bohr exciton diameter.[196–198] The charge carriers in a semiconductor nanoparticle are

weakly coupled and will migrate fast undergoing photochemical and photophysical events, like trapping and recombination.[153,199]

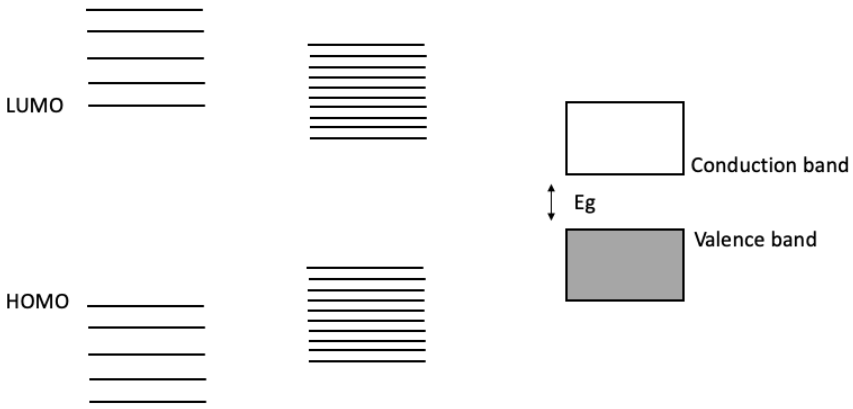


**Figure I.3:** Energy level diagrams illustrating the transition from nanoclusters (left) to nanosized particles (middle) to a bulk semiconductor (right), showing the widening of the energy gap $E_g$ (or HOMO-LUMO gap) as particle size decreases.

In semiconductor nanocrystals smaller than the bulk exciton dimensions, the optical and electronic properties are size-dependent due quantum confinement. Quantum size effects are of interest in visible photocatalysis namely by using metal sulfide quantum dots as photosensitizers.[200,201] The redox levels of the CB and VB are influenced by size quantization effects. Charge carriers formed after light absorption migrate to the surface of the particles where they participate in redox reactions. As compared to molecular photosensitizers, these systems have a large density of states and extinction coefficients with broad absorption spectra due to the strong overlap between the electron and hole wave functions in the confined structure,[196] which is critical for solar energy harvesting in photocatalytic applications. Currently, colloidal synthesis is a convenient strategy for the fabrication of nanocrystals with controlled sizes and shapes. These colloidal systems have been investigated as photocatalysts with strong absorption in visible region that might extend to NIR (**Table I.2**). However, improvements on photocatalytic activity of metal sulfides are challenging because of fast recombination of $e^-$–$h^+$ pairs, which has been achieved through the combination with inorganic substrates, such as carbon nanostructures.

Graphene constitute an alternative as electron-transport matrix for quantum dots systems due to its high conductivity.[41] Quantum dots can behave as light harvesting materials within the visible to NIR spectral regions, while graphene is the charge collector for photogenerated holes and electrons under an applied electric field.[202]

**Table I.2:** Characteristics of metal sulfides as photocatalysts.[200]

| Metal Sulfide | Wavelength (nm) | Band energy (eV) | Absorption light | Structure |
|---|---|---|---|---|
| **ZnS** | 250-380 | 3.2-4.3 | UV | Cubic, Hexagonal |
| **CdS** | 350-550 | 2.2-2.7 | Vis | Cubic; Hexagonal |
| **CuS** | 450-800 | 1.4-2.2 | Vis-NIR | Hexagonal |
| **$Ag_2S$** | 415-500 | 1.1-2.3 | Vis-NIR | Monoclinic |
| **$Bi_2S_3$** | 400-900 | 1.1-1.46 | Vis | Orthorhombic |

There are several approaches to prepare metal sulfides coupled to rGO or GO substrates, which include solid-state, sonochemical, microwave irradiation, solvothermal or hydrothermal methods.[77,201,203–217] Wei and co-workers reported the assembly of nanospheres of CdS onto GO, with the simultaneous reduction of GO.[207] Using a similar approach, Chen *et al*. used the polyelectrolyte poly(sodium-*p*-styrenesulfonate) adsorbed on the surface of rGO to prevent the aggregation of $Bi_2S_3$ particles (*ca.* 25 ± 3 nm) dispersed on the surface.[216] Chen *et al*. reported an all-solid-state *Z*-scheme system containing BiOI and $Bi_2S_3$ grown on rGO sheets using an electrostatic self-assembly method.[218] In the *Z*-scheme photocatalytic system the oxidation and reduction reactions occur separately on two different photocatalysts with an expanded light absorption spectrum, avoiding the recombination of photoinduced charge carriers.

A one-step approach to prepare a series of GO-based composites with different metal sulfides, such as $Ag_2S$, $Bi_2S_3$, PbS and CdS, using metal alkyldithiocarbamate complexes as single-molecule precursors was developed.[219] This method was inspired by the approach developed by Estrada *et al*. on the use of a sonochemical route to decorate MWCNTs, GO or graphite with CdS nanocrystallites[77] and it will be described in **Chapter II.**

Graphene-based metal sulfide nanocomposites in photocatalytic applications might result in photocorrosion of the metal sulfide and fast recombination of the photogenerated charge carriers. The formation of heterojunctions at the interface with a distinct semiconductor can overcome this issue. Hence, Liu *et al*. reported a solvothermal route to prepare tri-component $Bi_2S_3$/ZnS/GO hybrid nanocomposites, in which $Bi_2S_3$ forms heterojunctions with ZnS forming $Bi_2S_3$/ZnS rod-like composites.[220] The hybrid nanorods were grown mainly on the edges of GO sheets, which was related with the high content of oxygen groups in those regions. Wang *et al*. showed that nanoparticles of CdS form heterojunctions with $TiO_2$ and both phases were supported on rGO. The synergetic effect of the coupled structure prevented CdS photocorrosion.[221] Similarly, tri-component graphene-based composites have been reported by other authors. For example, coupled semiconducting phases with interfaces between $TiO_2$ and, CdS or $Ag_2S$, increase the capability of

light harvesting and efficiency of charge separation, also preventing the oxidation of the metal sulfides.[222,223]

This section provided several strategies to obtain metal sulfide-carbon hybrid nanostructures with interest as photocatalysts for wastewater treatment. Despite some limitations found in these systems, there are important issues to be further investigated such as solid interfaces tailoring in order to limit the photocorrosion of the sulfide. Also, quantum size effects in metal sulfides supported on carbon nanostructures are far from being explored in photocatalytic applications.

# 4. Application of carbon-based nanocomposites in heterogeneous photocatalysis

## 4.1. Metal oxides

Semiconductor photocatalysis involves photogeneration of $e^-$–$h^+$ pairs due to absorption of photons with energy higher than the band gap energy of the semiconductor.[224] Ideally, after migration to the surface, these charge carriers initiate interfacial electron transfer or participate in chemical reactions with adsorbates or with surface-bound hydroxyl groups.[153] Semiconductor photocatalysts are usually composed of particles with nano-to-submicron size, having a high density of grain boundaries, which due to insufficient $e^-$–$h^+$ pair lifetime and electron diffusion length, result that only a fraction (~5%) of these charges participate in redox reactions at the interface before they undergo recombination.[154]

In general semiconductor metal oxide photocatalysis is limited to the UV region due to its wide band gap of these photocatalysts.[225] To improve the photocatalytic performance of a semiconductor metal oxide several approaches should be considered, for instance (i) extending the photo-response of the UV-active semiconductor into the visible region by band gap tuning or introduction of photosensitizers, (ii) suppressing the excited $e^-$–$h^+$ recombination, and (iii) promoting the forward reaction through localizing the reactants adjacent to the active sites. This can be achieved by coupling narrow band gap semiconductors, metallic and non-metallic doping, dye-sensitization, deposition of noble metal nanoparticles and hybridized structures with carbonaceous materials.[18,226] Among them, carbon-based metal oxide nanocomposites have been the prime choice as visible-light-driven photocatalysts. In fact, the coupling of carbon nanostructures with metal oxide nanoparticles limits charge recombination and facilitates the hydrophobic surroundings for localization of the reactant in neighbouring active sites[227] (**Figure I.4**). Researches also showed that the graphitic carbon, when it forms an effective complex interface with semiconductor, can act as a sensitizer or as impurity energy levels to extend the absorption spectral region.[228]

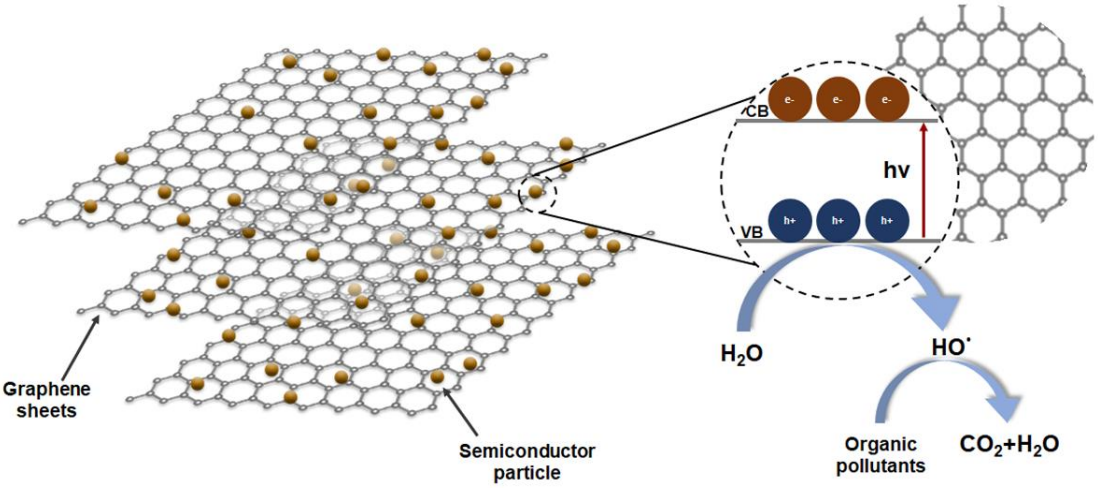


**Figure I.4:** Schematic representation of graphene sheets decorated with semiconductor particles for photocatalytic degradation of organic pollutants. VB – valence band; CB – conduction band; $e^-$ – electron; $h^+$ – hole; hv – photon energy.

Liang *et al*. reported that hybrid nanostructures composed of graphene and $TiO_2$ P25 leads to superior photocatalytic activity than $TiO_2$ P25 alone, in the degradation of rhodamine B (RhB) under UV irradiation.[229] Other authors prepared visible-light active $TiO_2$/graphene nanocomposites with significant narrowing of the band gap, exhibiting enhanced photocatalytic activity in the degradation of various dyes.[163,230,231] For instance, Chen *et al*. prepared visible-light active $TiO_2$/GO composites, with a band gap narrower than 2.43 eV, for the degradation of methyl orange (MO).[232] Also, Lin *et al*. described a $TiO_2$/GO composite as highly active photocatalyst for the degradation of MO, which reached up to 90% after 4 hours.[233] Overall, the superior photocatalytic activity of $TiO_2$/graphene hybrid materials is a consequence of the strong coupling between $TiO_2$ and graphene or GO, which enables interfacial charge-transfer and prevents $e^-$–$h^+$ recombination. In fact, the *p*-type or *n*-type semiconductor formed by GO in the hybrid material acts as a sensitizer enhancing the visible-light photocatalytic performance of nanocomposites (**Figure I.5**).

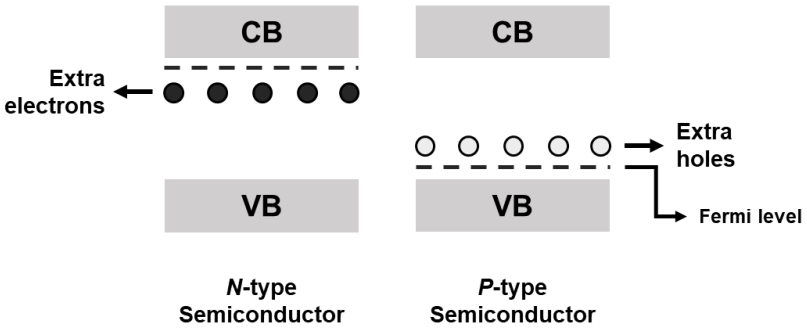


**Figure I.5:** A schematic diagram showing the formation of *n*-type and *p*-type semiconductors.

Although less explored as compared to $TiO_2$, but also widely used as a photocatalyst, ZnO-based carbon nanocomposites have been investigated in the removal of organic pollutants from water. For instance, Víctor-Román *et al*. reported ZnO/GO hybrid material with high efficiency (80%) for the degradation of methylene blue (MB) after 70 minutes even at low concentration (0.045 mg/mL).[234] In this study was described the chemistry of GO and the photo-induced charge-transfer interface interactions with ZnO, which enhanced the photocatalytic activity. Azarang *et al*. reported that GO sheets coupled to ZnO have better photocatalytic activity (92.5%) in the MB photodegradation in comparison to ZnO nanoparticles (37%). Furthermore, the photocatalysts were used over five consecutive cycles of 120 minutes, without no significant decrease of photocatalytic efficiency.[235] Other authors, prepared structured ZnO/rGO for the photodegradation of dye pollutants, showing that in the presence of hybrid nanocomposites, more than 98.5% of dye was degraded compared with less than 49% of degradation in the presence of neat ZnO.[169,170,236] On the other hand, Zhang and co-workers found that the band gap energy of ZnO/graphene hybrids decrease compared to pristine ZnO and the value of band gap energy depends greatly on the graphene loading level. Pure ZnO exhibits a gap energy of 3.4 eV, whereas ZnO/graphene composites exhibit a band gap energy between 1.77-2.37 eV.[237] Similarly, Hur *et al*. reported composites of rGO and ZnO with a narrower band gap (2.16 eV) as compared with pristine ZnO, which was attributed to the formation of Zn-O-C or Zn-C chemical bounds in the composites.[238] Overall, the combination of ZnO with GO or rGO restrains the recombination of photogenerated $e^-$–$h^+$ pairs, improving the photocatalytic activity. However, carbon loadings above 4 wt% seems to decrease the photocatalytic activity of nanocomposites, which is probably due to less light reaching the surface of ZnO particles due to strong absorption from the carbon nanomaterial.[239]

Apart from the most used $TiO_2$ and ZnO photocatalysts, $SnO_2$ is a semiconductor with promising photocatalytic properties.[184] For instance, Kim *et al*. reported the photocatalytic activity of $SnO_2$ aerogel/rGO nanocomposites in degradation of MO dye under UV-light irradiation. The authors observed that pristine $SnO_2$ aerogel has a moderate photocatalytic activity, with 56% of MO degradation after 60 minutes, while by coupling with rGO (0.1 wt%) resulted in the enhancement of photodegradation rate, reaching 84% of MO degradation for the same reaction time. In order to reduce its band gap energy and extend its application under solar radiation, several researchers have prepared $SnO_2$ carbon-based nanocomposites. Wu *et al*. have reported that the photocatalytic efficiency of $SnO_2$/GO nanocomposites for RhB degradation was 2.5 times fold than that of pure $SnO_2$, under visible-light irradiation.[186] Also, Sagadevan *et al*. investigated $SnO_2$/graphene nanocomposites for the MO and MB visible-light photodegradation achieving 100% efficiency.[185] It was found that larger amounts of graphene added to $SnO_2$ nanoparticles did not have a pronounced increase of the photocatalytic activity of the composites.[188]

Finally, $BiVO_4$ is a promising candidate for the development of semiconductor photocatalysts, which have been extensively studied for the photocatalytic degradation of organic compounds.[240–243] For instance Soltani and co-workers described the use of $BiVO_4$/rGO hybrid structures for the

photocatalytic degradation of MB under visible-light irradiation.[244] Wang *et al*. reported a tri-component material $BiVO_4$/$BiPO_4$/GO with high photocatalytic performance towards photodegradation of reactive blue 19 dye, up to 10 cycles.[245] The high photocatalytic activity was attributed to the heterojunction between $BiVO_4$ and $BiPO_4$. Liu *et al*. described a binary N-doped C-dots and $BiVO_4$ nanoheterostructures with enhanced photocatalytic performance for degradation of RhB and tetracycline (TC).[246]

In general, the coupling of metal oxide nanoparticles with nanocarbons have improved the photocatalyst efficiency under solar irradiation, but still present limitations concerning its separation after photochemical reaction and, eventual, regeneration. In this context, the development of nanocomposites with magnetic phases reveals itself with advantage regarding the recovery of the photocatalyst and its subsequent reuse, as discussed below. Due to their low cost and availability, magnetic iron oxides coupled with carbon nanomaterials are interesting photocatalysts for wastewater treatment. Among the magnetic materials available, those containing magnetite ($Fe_3O_4$) nanoparticles appear as particularly relevant due to their tunable magnetic properties and eco-friendly nature.[247–249]

$Fe_3O_4$ is an inverse spinel of structural formula $Fe^{3+}[Fe^{2+}Fe^{3+}]O_4$ that consists of a cubic close packed array of oxide ions, where all of the $Fe^{2+}$ ions occupy half of the octahedral sites and the $Fe^{3+}$ are split evenly across the remaining octahedral sites and the tetrahedral sites.[250,251] The Fe(III) ions are paired off in opposite directions, producing no external magnetic field, but the Fe(II) ions are all aligned in the same direction, accounting for the external magnetism. This antiparallel ordering occurs because of exchange interactions due to the overlapping of the 3*d* electron orbital wave functions of the Fe ions with the 2*p* electron orbital wave function of the O ion. The magnitudes of these exchange interactions are dependent on the distance between Fe and O ions and their bond angles (Fe-O-Fe); and these, in turn, are determined by the positions of the $Fe^{3+}$ and $Fe^{2+}$ ions in the spinel structure.[250] $Fe_3O_4$ particles should have a high magnetic susceptibility to facilitate a fast separation under a moderate magnetic field, and this may be achieved by controlling the morphological characteristics and surface chemistry.[252]

There are numerous examples of research work describing the coupling of magnetite with carbon-based materials envisaging the development of multifunctional materials with photocatalytic activity. Magnetic chitosan grafted GO nanocomposite for the removal of ciprofloxacin (CIP) from water were developed by Wang *et al*.[253] Mishra and co-workers reported the synthesis of $Fe_3O_4$/rGO with biomolecules acting as capping agents and simultaneously preventing agglomeration and promoting stabilization of nanoparticles.[254] Recently, Nazari *et al*. prepared magnetic composites based on $Fe_3O_4$ and $TiO_2$ core/shell nanoparticles linked to rGO using a sol-gel technique.[255] Using GO sheets, Yu *et al*. synthesized $Fe_3O_4$/GO nanocomposites as an effective heterogeneous photo-Fenton catalyst for the degradation of phenol under UV-light irradiation.[186] The coupling of $Fe_3O_4$ with GO promotes the photo-Fenton reaction *via* three roles: increasing adsorption capacity, offering more

active sites and accelerating the $Fe^{3+}/Fe^{2+}$ cycle under UV-light irradiation showing high photocatalytic activity after five cycles.

The following examples illustrate the use of $Fe_3O_4$ to confer multifunctionality to nanocarbons, namely the ability for magnetic separation and strong optical absorption in the visible. Mishra and his group reported the use of biomolecules as capping agents for the preparation of $Fe_3O_4$/rGO nanocomposites which showed higher photocatalytic efficiency, 76% of phenol (10mg/L) photodegradation, after 2 hours under visible-light illumination.[254] Ma and co-workers described the loading of $Fe_3O_4$@$TiO_2$ core/shell nanocomposites on the surface of rGO as an efficient multifunctional photocatalyst for the degradation of MO.[256] Other authors have noted that the introduction of $Fe_3O_4$ decreases the photocatalytic activity of the system due to the surface defects of $Fe_3O_4$ that act as electron traps.[257] Nada *et al*. reported the synthesis of a tri-component system, $TiO_2$/$Fe_3O_4$/rGO photocatalyst which demonstrated visible-light photocatalytic activity on the degradation of tartrazine, showing higher photocatalytic activity than $Fe_3O_4$/rGO or $TiO_2$.[258] The photocatalysts were recovered and reused still showing good degradation rate (90%). Similarly, Nazari *et al*. prepared magnetic composites based on $Fe_3O_4$ and $TiO_2$ core/shell nanoparticles linked to rGO as photocatalysts for solar light degradation of MB, demonstrating excellent recovery of composites without losing the original activity and stability.[255] Other works have reported the synthesis of $TiO_2$/$Fe_3O_4$/rGO or GO composites with significant magnetic properties and photocatalytic activity for removal of several organic dyes.[259–261] In order to avoid oxidation of the magnetite nanoparticles, Tang *et al*. have prepared silica encapsulated $Fe_3O_4$ particles coated in $TiO_2$ anchored to rGO sheets. This composite exhibits high adsorption capacity and strong light absorption in the visible region, enabling the photocatalytic degradation of the herbicide 2,4-dichlorophenoxyaceticacid.[262]

Overall, the coupling of carbon materials with metal oxide semiconductors increases the photo-efficiency of nanoparticles, overcoming the various drawbacks of bare metal oxide nanoparticles. The development of photocatalysts containing magnetic nanoparticles is a valuable advancement in this field, because it allows to explore magnetic assisted separation techniques. This aspect deserves further research namely by considering the implementation of pilot scale units that use such multifunctional photocatalysts.

## 4.2. Metal sulfides

Metal sulfide semiconductors such as CdS, $Ag_2S$, CuS, and $Bi_2S_3$ can efficiently harvest photons in the visible region,[263] and supported on graphitic substrates exhibit excellent conductivity for electron capture and transport.

Although CdS presents severe limitations for practical applications due to its well-known toxicity, there are many reports highlighting photocatalytic research on CdS and CdS-based nanomaterials,

due to their excellent photocatalytic properties and visible-light response.[264] Several studies reported CdS/rGO and CdS/GO visible-light active heterostructures for the photocatalytic degradation of organic dyes.[203,205,207] The photocatalytic efficiency of heterostructures was higher than pristine CdS and could be used up to 4 cycles, without loss of activity. Also, Zhang *et al.* prepared a series of visible-light CdS/graphene nanocomposites for photocatalytic oxidation of alcohols and reduction of Cr(VI) species in water.[265] Ternary materials composed of $TiO_2$/CdS/rGO, present slightly higher photocatalytic activity than $TiO_2$/rGO nanocomposite for the visible-light photodegradation of RhB, MB and *p*-chlorophenol.[221,222]

$Bi_2S_3$ absorbs visible and NIR radiation efficiently and, unlike CdS, does not pose such concerns in terms of toxicity. For instance, Wang and co-workers reported that $Bi_2S_3$/C-dots nanohybrids showed higher photocatalytic efficiency for degradation of MB or TC under UV, visible and NIR light irradiation, as compared with the bare components.[266] Khalid *et.al*. reported $Bi_2S_3$ nanorods with photocatalytic efficiency of 87% for degradation of congo red within 90 minutes under UV-light.[267] On the other hand, Chen *et al*. reported that $Bi_2S_3$/rGO composites exhibits a significant enhancement in the photodegradation of 2,4-dichlorophenol under visible-light irradiation.[216] Moreover, the authors concluded that there is an optimal ratio between carbon substrate and $Bi_2S_3$ phases observing that higher contents of rGO lead to lower photocatalytic efficiency. In fact, the same was also observed for $Ag_2S$/graphene nanostructures with different graphene content (wt%: 2, 4 and 6), achieving higher photodegradation of RhB, under visible-light irradiation, using 4 wt% of graphene.[268]

CuS is a *p*-type semiconductor relevant in photocatalysis because of its stoichiometry-dependent band gap.[269–273] There is a variety of stable and metastable phases at room temperature, from copper-rich chalcocite ($Cu_2S$) to the highest oxidized form covellite (CuS), with some non-stoichiometric phases ($Cu_{2-x}S$) in between those two compositions.[274] The hybrid nanostructures comprising CuS nanocrystals and graphene derivatives have engaged successfully as efficient heterogeneous photocatalysts for dyes degradation. For instance, several studies showed that CuS/rGO nanostructures improved the photocatalytic activity for organic dyes photodegradation under visible-light[210,275–277] or UV-light irradiation,[278] in comparison to pure CuS nanoparticles. El-Hout *et al*. reported a highly efficient sunlight-driven photocatalyst based on rGO supported CuS particles.[279] For the first time, this material was used for the complete degradation of malachite green within 90 minutes. Similarly, to other carbon-based semiconductor nanomaterials there is an optimal loading for carbon substrates. For example, Shi *et al*. reported that samples containing 20% of rGO holds better photocatalytic activity, than samples containing 10% or 30% of rGO.[210] In fact, several other works showed that, higher carbon loadings (rGO or graphene) leads to staking of graphene sheets and particle aggregation.[277] Wang *et al*. stated that the elevated stability and photoactivity of CuS/graphene were attributed to the high electronic conductivity of graphene and its effect on the morphology of the CuS/graphene nanocomposite, which consequently affect the synergistic interaction between graphene and nanoparticles.[280]

ZnS has a wide band gap energy of 3.66 eV (blende type) or 3.77 eV (wurtzite type) which results in a non-absorbing material in the visible region.[281,282] Nevertheless, it has been demonstrated that by coupling ZnS to carbon materials, the resulting nanocomposites might show enhanced photocatalytic activity in the photodegradation of various organic pollutants using visible-light irradiation.[206,212,214] For instance, Ming *et al*. showed that ZnS/C-dots hybrid materials revealed enhanced photocatalytic decomposition of MB and RhB, and CIP under simulated sunlight irradiation.[283] Chen and Chakraborty showed that ZnS/graphene or ZnS/rGO nanocomposites exhibit superior photocatalytic activity in the degradation of MO and RhB, respectively, under UV-light irradiation, rather than pure ZnS.[215,284]

As mentioned before, the photocatalytic properties of nanostructures combining metal oxides and chalcogenides have been studied and are known to improve light absorption.[200,223,285,286] For instance, Lonkar *et al.* reported the preparation of ZnS/ZnO/graphene tri-component nanostructures, which exhibited almost 100% degradation of dye pollutants under visible-light as compared with ZnS (47-59%) during 5 runs without loss the efficiency.[287] Similar results were performed by Khavar *et al*. which used tri-component $Ag_2S$-ZnO@rGO core-shell microspheres for the degradation of acetaminophen under visible-light irradiation.[288] The quantum efficacy of ZnO was enhanced by narrowing its band gap through the resulting synergy with narrow band gap metal sulfides, as is the case of $Ag_2S$.[289]

Within the scope of this section, it was concluded that most published works used graphene derivatives as platforms to graft semiconductors with photocatalytic properties, offering an alternative for water treatment applications. However, the chemical interaction between the various components is still unclear. Much efforts are still needed to understand the integration between metal sulfide or metal oxide and carbonaceous materials, which in turn will offer new perspectives for the discovery of suitable photocatalytic materials for the cutting-edge applications in photocatalysis.

## 5. Final remarks

In this first chapter, it was presented an overview of carbon-based materials with potential to be applied as photocatalysts in the field of wastewater treatment. The outstanding physical and chemical properties of carbonaceous materials have endorsed exceptional research in advanced water purification technologies.

Due to the various drawbacks of bare semiconductors metal oxide or metal sulfide nanoparticles, particularly in the absorption of a small fraction of photons in the visible region, low photocatalytic quantum yield and rapid $e^-$–$h^+$ recombination, several strategies have been employed to improve photo efficiency and performance of nanoparticles as photocatalysts. The coupling of graphene with other nanomaterials, like metal oxide or metal sulfide semiconductors, synergistically increases the efficiency of nanoparticles under visible-light irradiation. Moreover, the studies showed that there

was an optimal carbon content in the hybrid nanostructure system for what the degradation of the target pollutant is maximum. Several studies showed that the increasing of graphene or graphene derivative content above a value in the hybrid nanostructure, the degradation efficiency found to be decreased.

This review proposes a contribution to understand the basic photocatalytic properties of metal oxide or metal sulfide/graphene-based nanocomposites for water treatment. In particular, the use of graphene nanocomposites at large scale with cost effective production, high photostability, high photocatalytic efficiency, is most desirable and challenging as well. Therefore, this issue needs to be addressed by the researchers to guarantee its future commercialization at large scale for environmental applications.

# CHAPTER II

## *A general route for growing metal sulfides onto graphene oxide and exfoliated graphite oxide*

Herein, a general wet chemistry method to prepare graphene oxide sheets decorated with nanophases of semiconductor metal sulfides is described. This approach can be applied to other graphene-based materials as well, such as graphite and exfoliated graphite oxide.

# CHAPTER II | "A general route for growing metal sulfides onto graphene oxide and exfoliated graphite oxide"

Graphene-based materials are elective materials for a number of technologies due to their unique properties. Also, semiconductor nanocrystals have been extensively explored due to their size-dependent properties that make them useful for several applications. By coupling both types of materials, new applications are envisaged that explore the synergistic properties in such hybrid nanostructures. This research reports a general wet chemistry method to prepare graphene oxide (GO) sheets decorated with nanophases of semiconductor metal sulfides. This method allows the *in situ* growth of metal sulfides onto GO by using metal alkyldithiocarbamate complexes as single-molecule precursors. In particular, the role of GO as heterogeneous substrate for the growth of semiconductor nanocrystals was investigated by using Raman spectroscopic and imaging methods. This method was further extended to other graphene-based materials, which are easily prepared in a larger scale, such as exfoliated graphite oxide (EGO). [2]

*Keywords*: graphene oxide; metal sulfide nanocrystals; Raman spectroscopy; exfoliated graphite oxide; metal alkyldithiocarbamate.

[2] This chapter is based on the work: Joana L. Lopes, Ana C. Estrada, Sara Fateixa, Marta Ferro, Tito Trindade. *A general route for growing metal sulfides onto graphene oxide and exfoliated graphite oxide*. **2017**, Nanomaterials. 7, 245. (DOI: 10.3390/nano7090245)

Joana L. Lopes performed the laboratorial work, including the synthesis and general characterization of the materials. Sara Fateixa performed the Raman experiments. Marta Ferro performed the (HR)TEM analysis of the materials. Ana C. Estrada and Tito Trindade conceived and designed the experiments and supervised the research. All the authors have analysed the data and made contributions for writing of the paper.

This research was funded through the FCT Project UTAP-ICDT/CTMNAN/0025/2014.

# 1. Introduction

Graphene is a one-atom-thick layer of $sp^2$ bonded carbon atoms arranged in a two-dimensional honeycomb lattice structure.[106] Due to their electronic, thermal and mechanical properties, graphene is of great interest in numerous applications such as water treatment, gas separation,[24] catalysis,[290] electronics[291] and energy storage in batteries and supercapacitors.[292,293] For certain applications there has been more interest to explore the chemistry of GO, which can be regarded as a single-layer of graphite oxide. In this case, the presence of structural defects due to oxygen functional groups bound to the two-dimensional carbon monolayer has a detrimental effect on the electronic behavior of pristine graphene. Nevertheless, these oxygen moieties confer to GO layers a hydrophilic character, which makes this material particularly useful for subsequent surface chemical modifications and water compatible applications. An interesting example is the development of hybrid nanostructures that combine GO sheets as the chemical platforms to attach other distinct functional nanophases.

Semiconductor nanocrystals are important nanomaterials whose interest to associate to GO substrates relies in some extent on the exploitation of synergistic effects by coupling both components. For example, nanosized metal sulfides have attracted great attention because of their size-tunable optical properties.[294] The hydrophilic nature of GO allows the preparation of colloidal stable suspensions that favors the *in situ* synthesis of such metal sulfides onto GO surfaces. Some synthetic strategies have been developed for decoration of GO with semiconductor nanocrystals such as CdS, $Bi_2S_3$, and PbS.[203,265,295–308] Unlike CdS, which has been extensively investigated in association to GO,[203,265,295–297,301–308] just a few reports were found involving other sulfides such as $Bi_2S_3$ and PbS.[297–299] Gao *et al*. described GO/CdS composites obtained by a two-phase mixing method.[296,309] The preparation of GO nanosheets decorated with CdS nanorods by the pyrolysis of cadmium precursors has been described by Zhang *et al.*.[306] There are several reports of solvothermal routes for the production of metal sulfides onto GO.[203,265,297,302,305,307] GO surfaces have been decorated with PbS into a semi-core/shell structure using a solution-based hot-injection method.[299]

There has been great interest in using GO as a scaffold to develop visible-light photocatalysts, because it is relatively inexpensive, environmental friendly and can enhance the semiconductor photocatalytic properties by extending the light absorption range and improving charge carrier separation and transport.[203,296,297,304,307,308,310,311] Thus far, however, it has not been reported a single-source method for the production of metal sulfides onto GO, with potential for up-scale production of nanocomposite photocatalysts. This gap has been bridged in this study by describing the use of metal alkyldithiocarbamate as precursors to metal sulfides generated *in situ* in the presence of GO. This research follows the interest in exploring this chemical route using chemically and structurally distinct substrates, such as amorphous $SiO_2$ nanoparticles and carbon nanotubes (CNTs).[77,312] The simplicity of this method relies on the use of single-molecule precursors to produce the required nanocomposites without segregated phases. This is possible without adding additional sources of

sulfur to the reacting system, such as thiourea[203,303,307] or $CS_2$.[308] Also, the method does not require extra polymeric linkers to anchor the metal sulfides to the substrates, such as polyvinylpyrrolidone or polyacrylic acid.[295,302,307] Hence, this is a general and alternative method to produce several metal sulfides onto GO sheets, at temperatures typically less than 100 $^oC$ and relatively short reaction times (less than 1 hour). Furthermore, the method reported here is easily applied to other graphene-based materials, including less expensive substrates as illustrated by using suspensions containing EGO.

# 2. Experimental section

## 2.1. Chemicals and methods

Ethylenediamine ($C_2H_8N_2$, Sigma-Aldrich, 99%), dimethylformamide (Carlo Erba, 100%), ethanol absolute (Fisher Chemical), graphite (GK), GO aqueous solution (2.5 mg/mL, Nanocs) and sodium diethyldithiocarbamate trihydrate ($Na(S_2CN(C_2H_5)_2.3H_2O$, Sigma, 100%) were used as received. Ethanol was dried with molecular sieves (3 Å, Fluka).

The following metal diethyldithiocarbamates were used as single-molecule precursors $M[S_2CN(C_2H_5)_2]x$, where M = Ag, Bi, Cd and Pb.[77] All the compounds were prepared by the stoichiometric reaction of $Na(S_2CN(C_2H_5)_2)$ (4 mmol) and the respective metal nitrate (2 mmol), in water. The solid obtained, was thoroughly washed with water and ethanol and then collected by filtration.

## 2.2. Sonochemical treatment of graphite flakes

EGO was produced by the sonochemical exfoliation of graphite in a high boiling point solvent DMF, in accordance with the literature.[38] In a typical experiment, a DMF dispersion (100 mL) of graphite flakes (50 mg/mL) was submitted to a sonochemical reaction (Sonics Vibra Cell Sonicator, VC70, 130 W, 20 kHz) during 5 hours. The resulting suspension was centrifuged (500 rpm, 45 minutes) using a Eba 20 Hettich centrifuge, and filtered under reduced pressure using 0.2 µm pore size nylon membranes. The final powder obtained was washed with ethanol and left to dry at 40 $^oC$.

## 2.3. Synthesis of hybrid carbon nanostructures

All procedures were performed in a well-ventilated fume cupboard. The GO sheets were decorated with metal sulfides by the addition of ethylenediamine (9 mmol) to a dry ethanol suspension of GO (20 mg, 25 mL) containing the respective metal precursor (58 µmol). The mixture was then stirred at reflux until a color change of the reaction mixture was clearly observed. The hybrid nanostructures were then collected by centrifugation (6000 rpm, 15 minutes) using a Eba 20 Hettich centrifuge and

thoroughly washed with ethanol. Finally, the powders were dried at room temperature and kept under $N_2$.

The metal sulfides@EGO and metal sulfides@graphite hybrid materials were prepared by the procedure described above, using EGO or graphite as carbon substrates.

## 2.4. Instrumentation

The ultraviolet/visible (UV/VIS) spectra were recorded using a Jasco V-560 spectrometer. The powder X-ray diffraction (XRD) data were collected using a PAN analytical Empyrean X-ray diffractometer equipped with Cu-Kα monochromatic radiation source at 45 kV/40 mA. The samples were prepared by deposition of aliquots of the ethanolic suspensions in hybrid nanostructures on a silicon holder. Powder XRD patterns of the metal sulfide@GO nanocomposites with the internal reference (Si) were recorded similarly. For transmission electron microscopy (TEM) analysis, a drop of the suspension under analysis was placed on a carbon-coated Cu grid and the solvent was left to evaporate at room temperature. TEM was performed using a transmission electron microscope Hitachi H-9000 operating at 300 kV. The high-resolution TEM (HR-TEM) images were acquired by using a JEOL 2200FS HR-TEM instrument. Scanning electron microscopy (SEM) analysis was performed using a scanning electron microscope Hitachi SU-70 operating at an accelerating voltage of 15 kV. Energy dispersive X-ray spectroscopy (EDS) analysis was performed using an EDS Bruker Esprit. Raman spectral imaging was performed in a combined Raman-AFM-SNOM confocal microscope WITec alpha300 RAS+. A Nd:YAG laser operating at 532 nm was used as excitation source with the power set at 1 mW. The Raman confocal microscope was calibrated by acquiring the spectrum of a silicon wafer (532 nm laser source, 0.5 s, 10 acquisitions, 40 mW laser power). The Gaussian function was fitted to the Raman band at 521 $cm^{-1}$ and an error of 0.08 $cm^{-1}$ was obtained. The intensity values and associated errors of the Raman bands of pristine GO and the nanocomposites were obtained by multi-peaks fitting using the Lorentz function[313] in Origin 8 (**Figure II.S1**). Raman imaging experiments were performed by raster-scanning the laser beam over the samples and accumulating a full Raman spectrum at each pixel. The WITec software, WITec Project 2.0 (WITec, Ulm, Germany), was used to create the Raman images. The Raman images showing a color scale have been created using band integrals, in which the value of the absolute area underneath a band (e.g. at 1586 $cm^{-1}$) corresponds to color intensity in the scale, shown in the image at the respective pixels. The Raman spectra of the semiconductor and the GO were used as the basis set in the analysis using the software tool of WITec Project, providing the color-coded combined Raman images.

# 3. Results and Discussion

## 3.1. Synthesis and characterization of metal sulfide@GO hybrid nanostructures

The hybrid nanostructures were obtained after generating the metal sulfide nanophases *in situ*, in the presence of GO sheets, following the reflux of ethanolic suspensions containing the respective metal alkyldithiocarbamate complex. **Figure II.1** shows the powder XRD patterns of GO and the hybrid nanostructures reported here. As expected, the GO sample shows a powder XRD pattern dominated by a strong peak centered at $2\theta \approx 10.3^{o}$ corresponding to the (001) plane and to a 0.86 nm interlayer distance (*d*).[314] Therefore, it was estimate that the GO sample is composed of seven over stacked layers, as deduced from peak broadening and by applying the Debye-Scherrer equation.[315] The intensity of the diffraction peak at $10.3^{o}$ decreases significantly after decorating the GO with distinct metal sulfide nanophases (**Figure II.1**). It has been reported that the attachment of nanoparticles onto GO may prevent the restacking of suspended graphene sheets, which might explain these observations.[316,317] In addition, the higher crystallinity of the metal sulfides in relation to the GO, thus resulting in sharper and more intense reflection peaks for the latter (**Figure II.S2**), can also contribute for these observations. Nonetheless, all diffraction peaks for the hybrid nanostructures were ascribed to the Bragg reflections of the respective metal sulfide, which are in good agreement with the $Ag_2S$ monoclinic phase (ICDDPDF No. 00-014-0072), CdS hexagonal phase (ICDDPDF No. 00-006-0314) and PbS cubic phase (ICDDPDF No. 01-072-4873), which clearly confirms the presence of the metal sulfides on GO. The respective ICDDPDF files are attached in **Appendix D**, **Annex 1-3,** respectively. Note that peak broadening observed for the CdS sample has been extensively reported as consequence of nanocrystalline diffracting domains.[77] In accordance with the XRD analysis, the EDS measurements performed on all hybrid nanostructures showed the peaks for S and the metal (Ag, Pb, or Cd) of the respective metal sulfide phase (**Figure II.S3**). The Cu, C and O peaks observed in the spectrum are attributed to the Cu grid and graphene substrate.

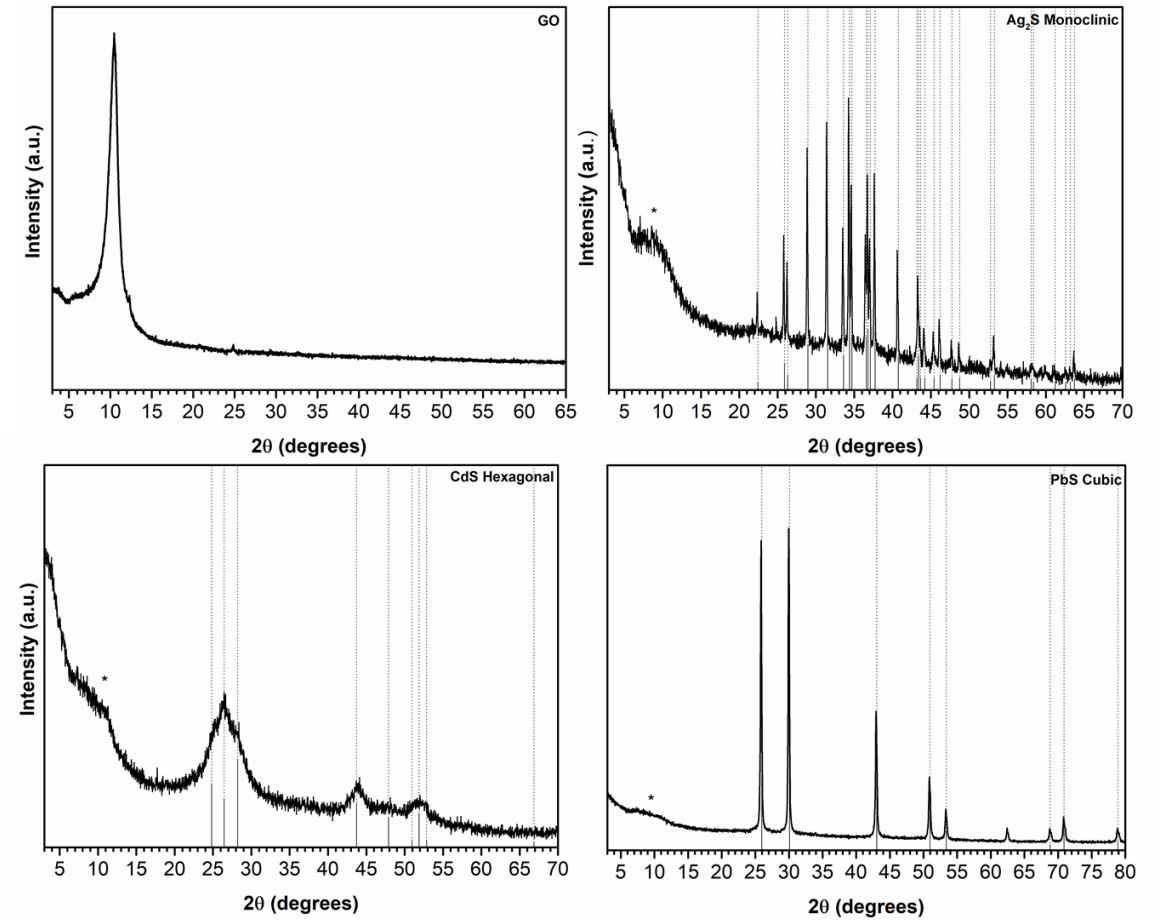


**Figure II.1:** Powder XRD patterns for GO, $Ag_2S$@GO, CdS@GO and PbS@GO nanostructures. The vertical lines correspond to the standard diffractions peaks attributed to the respective metal sulfide (ICDDPDF No. 00-014-0072; No. 00-006-0314; No. 01-072-4873, respectively). The diffraction peak of GO is marked with *.

The optical absorption spectra of the hybrid nanostructures (ethanolic suspensions) reported here are shown in **Figure II.2**. For comparative purposes, the spectra of ethanolic suspensions containing neat GO flakes are also shown. These samples appear macroscopically uniform and the respective digital photographs (**Figure II.S4**) show colloidal stable suspensions with distinct colours depending on the metal sulfide obtained. The UV/VIS spectrum of GO exhibits an absorption band peaked at 230 nm corresponding to π-π* electronic transitions in the aromatic C-C bonds, and a shoulder at 315 nm ascribed to n-π* transitions in the oxygen functional groups.[318] After growing the metal sulfide phases onto GO sheets, the absorption band at 230 nm for the π-plasmon in the graphitic network was blue-shifted to lower wavelengths, suggesting strong coupling between graphene sheets and metal sulfide phases.[303,319–321] In fact, it has been reported that an increase in the number of functional groups or defects in the graphene structure causes the decrease of the π-conjugated domain size, thus resulting in the shift to lower wavelengths of the bands associated to the polyaromatic structure.[319,322] Although the presence of oxygen moieties in GO causes disruption of

the graphene delocalized system, similarly the blue-shift observed in the π-π* optical spectrum of the metal sulfide@GO was attributed due to the contribution of metal sulfide-GO interactions. Also, note that for all the hybrids, the absorption band at 315 nm corresponding to the C-O linkages was shifted to lower values.

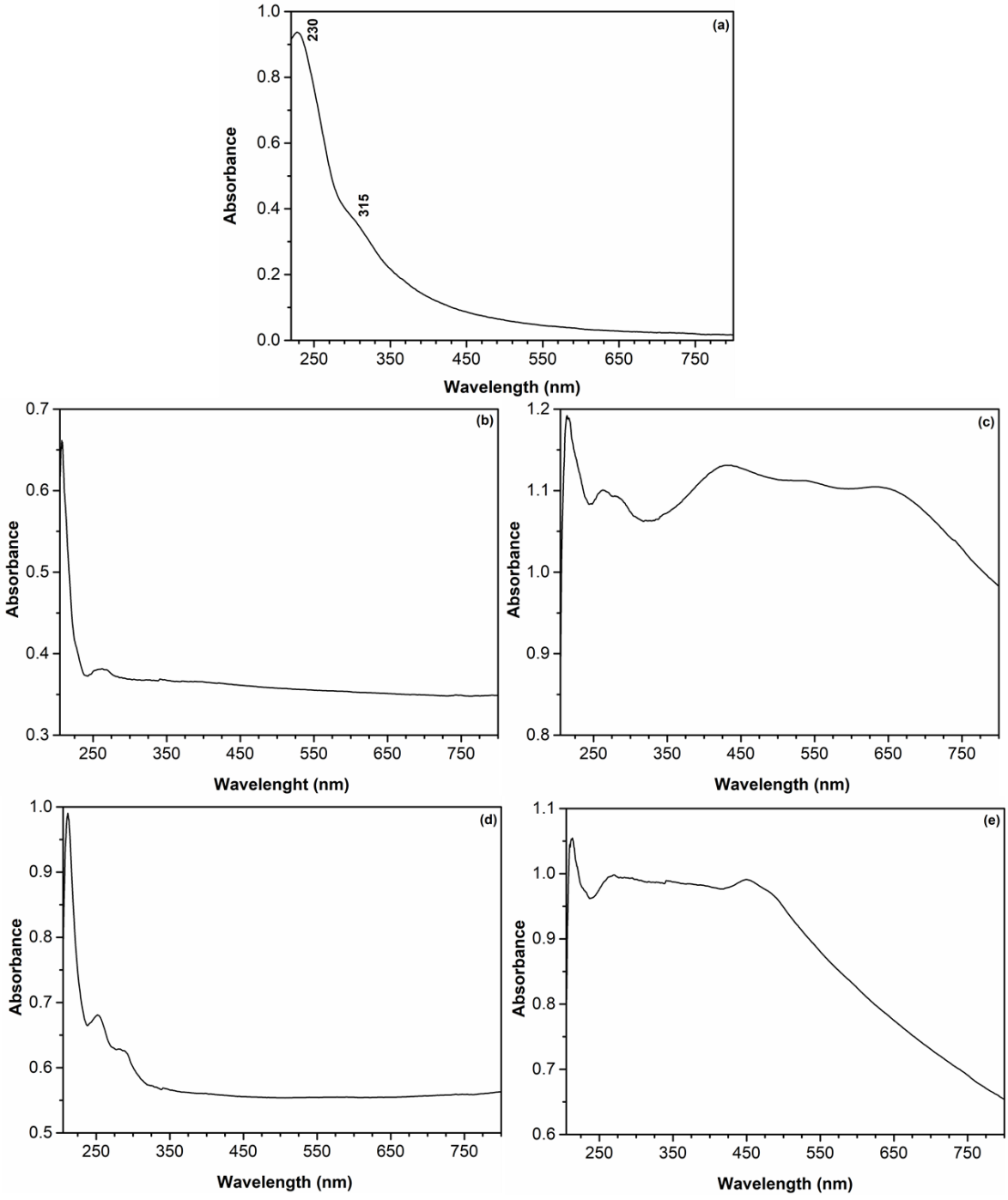


**Figure II.2:** UV/VIS absorption spectra of ethanolic suspensions (0.05 mg/mL) of GO (a) and hybrid nanostructures with $Ag_2S$ (b), $Bi_2S_3$ (c), PbS (d) and CdS (e) nanophases.

**Figure II.2** indicates that all the hybrid nanostructures absorb stronger in the visible region of the spectrum (390-700 nm). These results confirm the presence of the metal sulfides in the GO sheets, as expected by taking into consideration the reported band gap energies for the respective bulk semiconductor: $Ag_2S$ ($E_g$ = 1.0 eV, $\lambda_{onset}$ = 1240 nm), PbS ($E_g$ = 0.41 eV, $\lambda_{onset}$ = 3024 nm), CdS ($E_g$ = 2.42 eV, $\lambda_{onset}$ = 512 nm) and $Bi_2S_3$ ($E_g$ = 1.3 eV, $\lambda_{onset}$ = 953 nm). Additionally, the CdS@GO sample shows an absorption peak at 460 nm, suggesting the presence of small nanocrystallites showing quantum-sized behaviour. These smaller nanocrystallites can be present in the GO substrate, namely by clustering into larger nanostructures but retaining their crystallite size domain, as will be shown below.[312] This size-dependent optical behaviour has been well documented for diverse semiconductors with particle dimensions comparable or below the corresponding Bohr radius of the exciton in the macrocrystalline material.[323,324] The PbS@GO hybrid shows a broad absorption band that extends to the IR region, whereas the $Bi_2S_3$@GO hybrid material shows two absorption peaks in the visible, at 430 nm and 650 nm, which might be due to the presence of distinctly sized crystallites.

**Figure II.3** and **Figure II.4**-left panel show respectively the TEM and SEM images of the hybrid samples. The TEM images display a number of darker spots dispersed over a background composed of GO sheets. These images prove that the metal sulfides are present in these samples as nanophases decorating the GO sheets. The nanophases distributed over the GO surfaces retain their morphological identity although size polydispersity occurs in some extent. The SEM images are in line with these findings and the respective EDS mappings confirm the presence of the respective metal sulfide elements onto the GO substrates (**Figure II.4**-right panel). The inspection of several samples did not show evidence for the presence of semiconductor particles scattered out of the GO substrate. Indeed, further experiments involving the sonication of hybrid nanostructures suspensions did not result in a significant number of free metal sulfide particles. The inspection of the HR-TEM images confirms the presence of crystalline particles onto GO, as illustrated in **Figure II.5** for PbS and CdS, by the presence of the lattice fringes of the respective metal sulfides. These results are consistent with a surface mediated mechanism in which the metal sulfide particulates nucleate and grow on the GO sheets. The metal sulfide is formed due to the degradation of the metal alkyldithiocarbamate precursor, which is a single-source for sulfide species and metal ions, according to a mechanism previously proposed.[325]

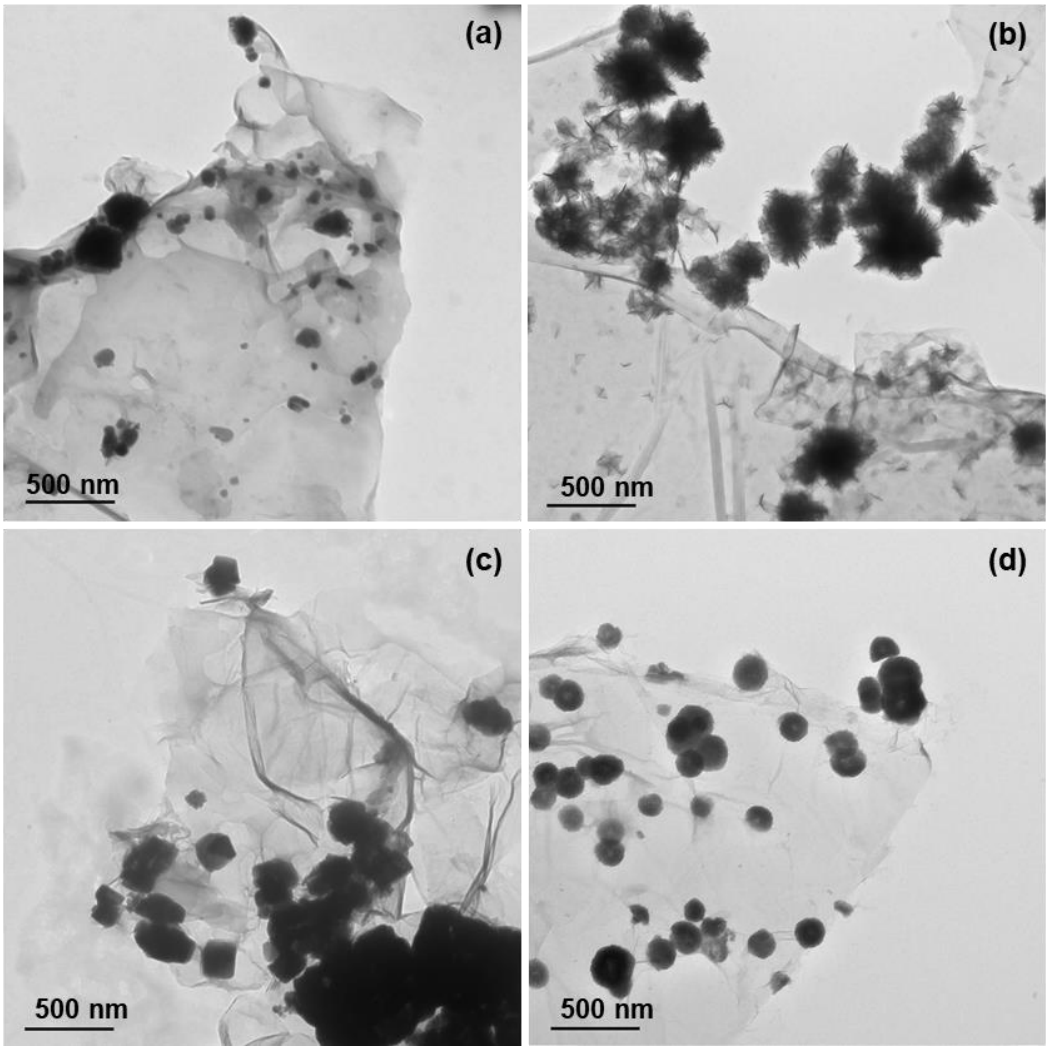


**Figure II.3:** TEM images of GO hybrid nanostructures containing metal sulfide nanophases, $Ag_2S$@GO (a), $Bi_2S_3$@GO (b), PbS@GO (c) and CdS@GO (d).

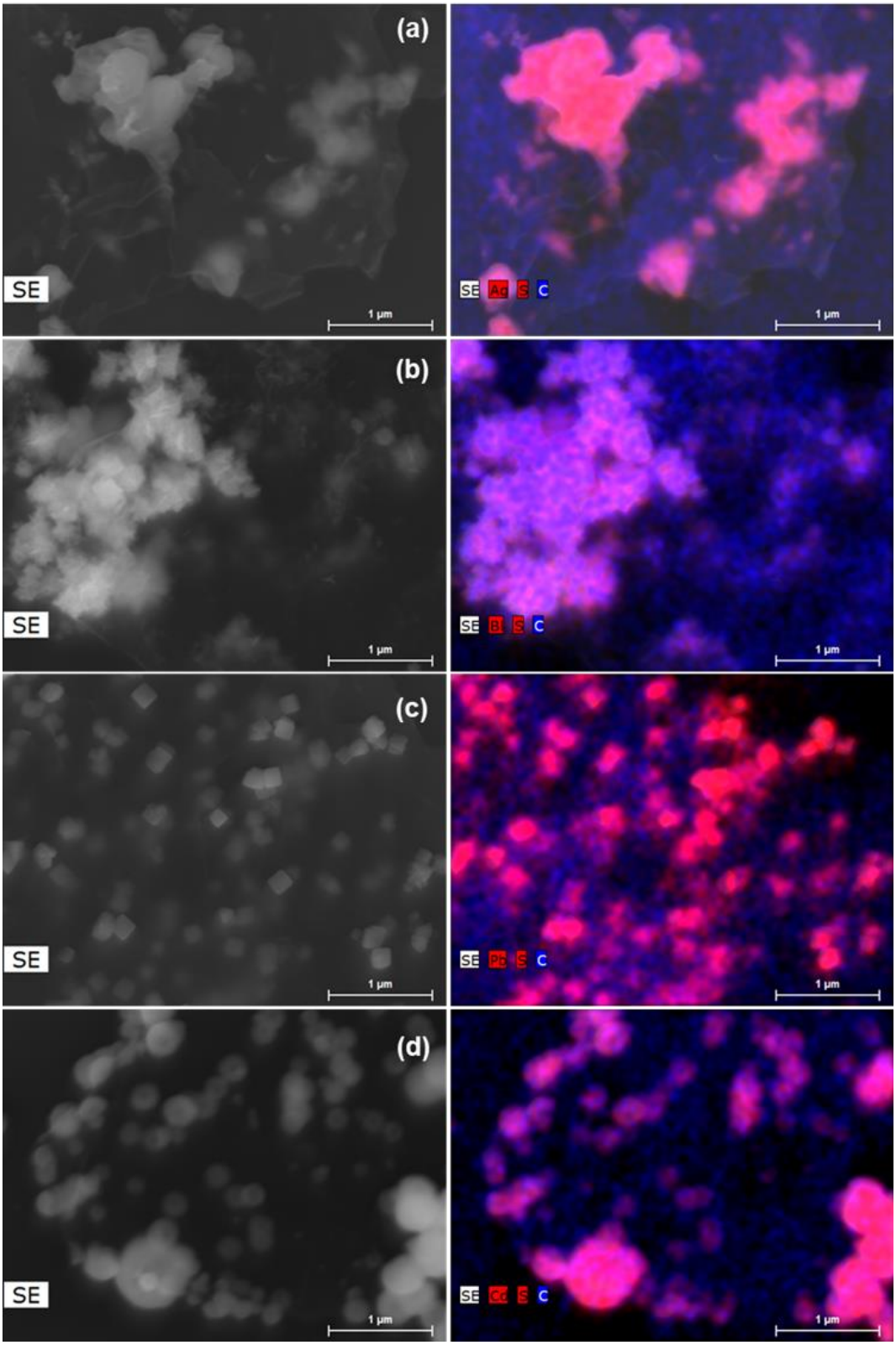


**Figure II.4:** SEM images (left panel) and EDS mapping (right panel) of GO hybrid nanostructures containing metal sulfide nanophases, $Ag_2S$@GO (a), $Bi_2S_3$@GO (b), PbS@GO (c) and CdS@GO (d) (respective metal sulfide – red; C – blue).

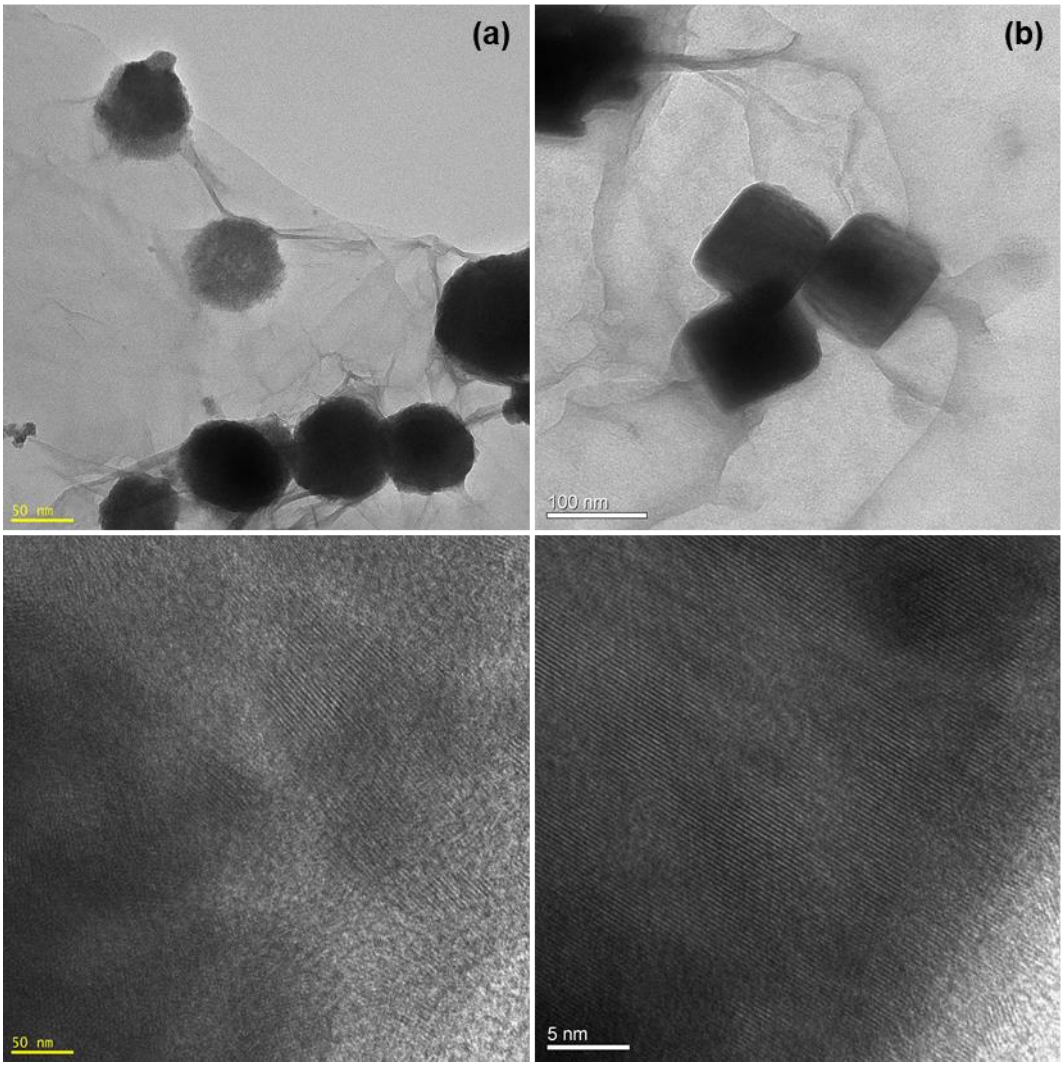


**Figure II.5:** TEM (top) and HR-TEM (bottom) images of GO sheets decorated with CdS (a) and PbS (b) nanophases.

Raman spectroscopic methods have been successfully employed in the characterization of a number of carbon nanostructures, including graphene-based materials.[326] The results discussed above suggest that the metal sulfides grown over the GO sheets have impact on the structural features of the carbon layers. As such, Raman methods were used to investigate in more detail these effects, in particular by taking into consideration that conjugated carbon-carbon bonds in graphene materials result into distinct Raman signatures. **Figure II.6** shows the Raman spectra for the hybrid nanostructures and pure GO, used as substrate. The two bands observed are characteristic of graphitic materials, corresponding to the vibration of bonded $sp^2$-carbons of the two-dimensional hexagonal lattice (G band at 1580 $cm^{-1}$) and to $sp^3$-carbon containing moieties that act as defects introduced in the graphene lattice (D1 band at 1350 $cm^{-1}$).[326–331] **Table II.1** summarizes relevant Raman data collected from the spectroscopic measurements performed on GO and hybrid nanostructures. In comparison to the Raman spectrum of GO, the G and D1 bands in the Raman

spectrum of each hybrid nanostructure are slightly shifted to lower wavenumbers. These shifts can be related to structural modifications occurring in the GO sheets during the synthesis, which are eventually mediated by interactions with the metal sulfide. Although using distinct materials, Zhu *et al*. have reported ZnO/graphene composites whose Raman spectra showed shifts to lower wavenumbers for the D band and shifts to higher wavenumbers for the G band.[328] Here, both G and D1 bands in the Raman spectrum of each hybrid material are shifted to lower wavenumbers. These shifts for lower wavenumbers can also be associated to the formation of reduced GO (rGO).[331] However, in the case of rGO formation, an increase of the $I_D/I_G$ ratio was also expected.[331] In fact, **Table II.1** indicates a slight increase of the Raman $I_D/I_G$ ratio, suggesting an increase of the number of defects in the hybrids as compared to pristine GO. The origin of such defects could be traced to the treatment of the GO flakes during the synthesis. The broad band at ~2680 $cm^{-1}$ (2D band) is the second order of the D band, that result from a two phonon lattice vibrational process, but that does not need to be activated by the proximity of defects.[330] Unlike monolayer graphene, whose Raman spectrum shows a sharp 2D band with stronger intensity than the G band, the materials reported here show broad and less intense Raman 2D bands as expected for a multilayered GO.[332]

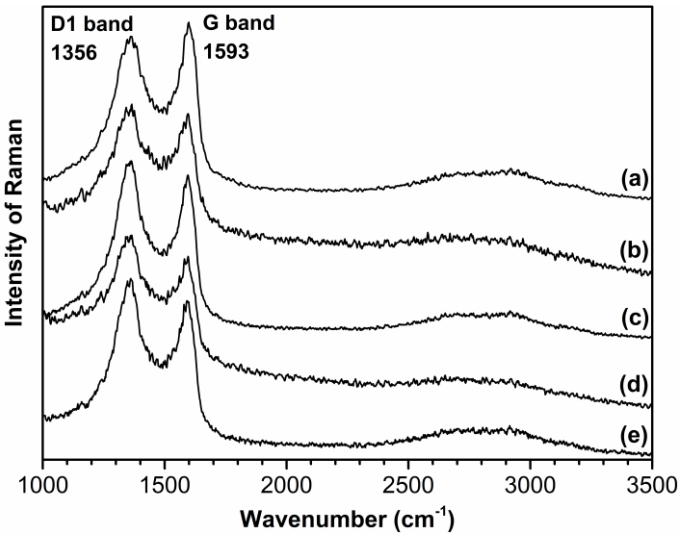


**Figure II.6:** Raman spectra of GO (a) and derived hybrid nanostructures $Ag_2S$@GO (b), $Bi_2S_3$@GO (c), CdS@GO (d) and PbS@GO (e) (1000-3500 $cm^{-1}$ region).

**Table II.1:** Raman shifts ($cm^{-1}$) for D1 and G bands with the respective intensities ratio ($I_D/I_G$) of GO and derived hybrid nanostructures $Ag_2S$@GO, $Bi_2S_3$@GO, CdS@GO and PbS@GO.

| Sample | Band Positions ($cm^{-1}$) | | |
|---|---|---|---|
| | **D1** | **G** | **$I_D/I_G$** |
| **GO** | 1356.8 ± 0.4 | 1593.6 ± 0.9 | 1.32 |
| **$Bi_2S_3$@GO** | 1353.9 ± 0.4 | 1587.2 ± 1.3 | 1.48 |
| **$Ag_2S$@GO** | 1351.7 ± 1.2 | 1566.4 ± 4.6 | 2.22 |
| **CdS@GO** | 1352.5 ± 0.8 | 1589.3 ± 1.3 | 1.46 |
| **PbS@GO** | 1353.1 ± 0.5 | 1585.7 ± 1.5 | 1.51 |

Raman mapping has been a less exploited tool in the characterization of decorated graphene-based materials, such as the hybrid nanostructures reported in this research. Taking advantage of the Raman signature assigned to the presence of $sp^3$-carbon defects, at about 1350 $cm^{-1}$, Raman imaging studies for neat GO and GO hybrid nanostructures were performed. These screening experiments show micrometric regions enriched in defects distributed over the GO sheets (**Figure II.7**-left panel). On the other hand, the metal sulfides deposited on GO show characteristic Raman shifts at wavenumbers lower than the G band, as shown **Figure II.S5**. These Raman bands are characteristic of each metal sulfide and were used for screening the regions of GO coated with the respective semiconductor nanophase (**Figure II.7**-middle panel). The combined Raman images (**Figure II.7**-right panel) for the GO sheets and the corresponding hybrid samples, give a fair agreement with the assertion that the metal sulfides are mainly located in GO regions enriched in defects. The Raman mapping of the hybrid samples also corroborate the presence of metal sulfide nanophases distributed over the GO sheets, as discussed above for the TEM analysis.

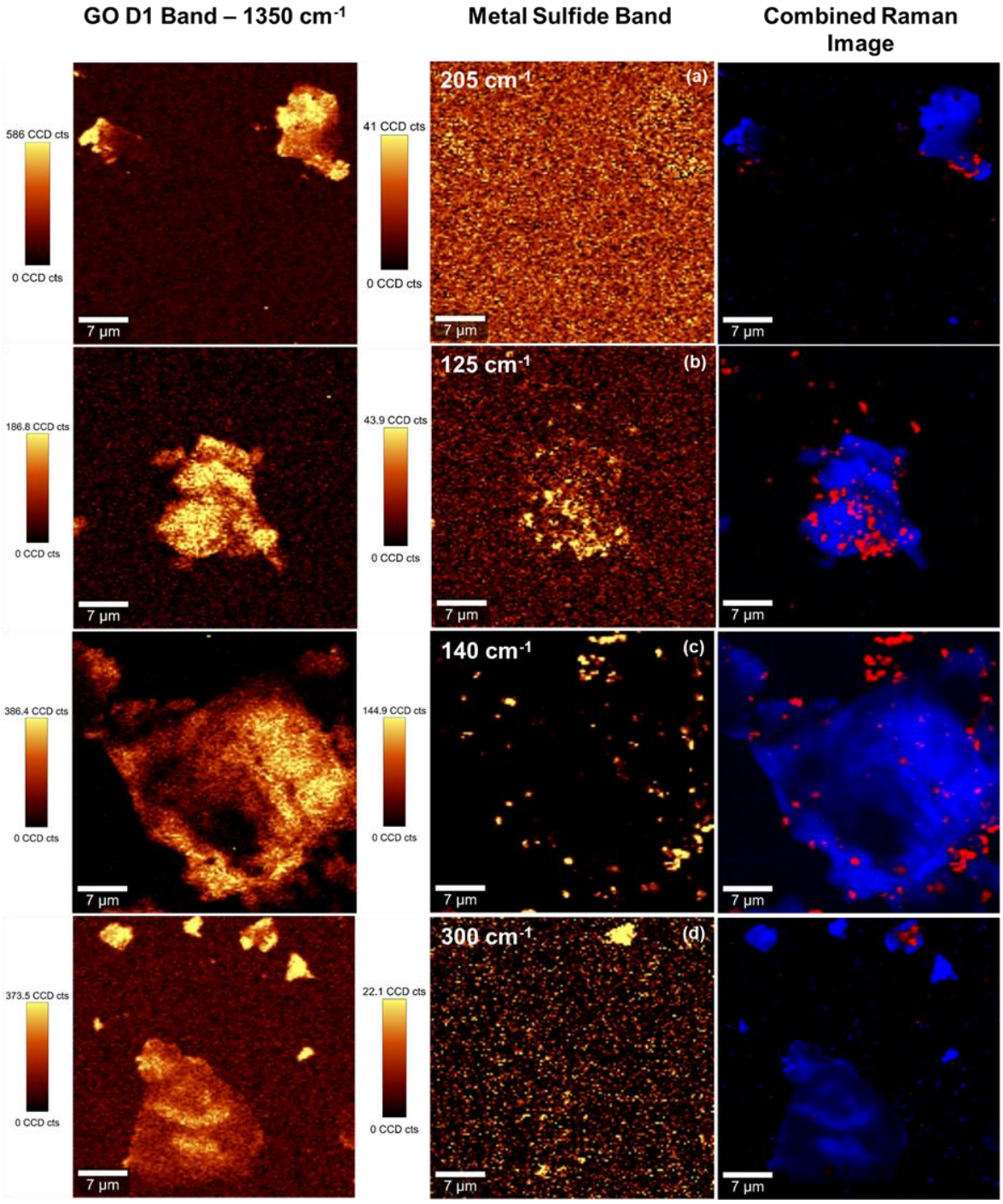


**Figure II.7:** Raman images of GO and GO decorated with metal sulfides, $Ag_2S$ (a), $Bi_2S_3$ (b), PbS (c) and CdS (d). The Raman images were obtained by using the integrated intensity of the Raman band at 1350 $cm^{-1}$ (left panel) and the characteristic Raman band of the metal sulfide as indicated (middle panel) – excitation line at 532 nm, 1 mW laser power, 150 × 150 points per grid in a 40 × 40 µm area. The vertical bar shows the color profile in the Raman images, with the relative intensity scale. The combined Raman images of the GO substrate and metal sulfides are also shown (right panel).

## 3.2. Synthesis and characterization of metal sulfide@EGO hybrid nanostructures

The method described here for decorating GO sheets can be easily applied to other carbon materials or by exploring other thermal treatment methods.[77,333,334] For example, it would be of great interest to apply this synthesis using less expensive carbon substrates, which also allow large-scale production. As illustrative cases, a similar synthetic methodology, but using suspensions of graphite and EGO instead of GO were applied.

Graphite flakes were further exfoliated through an ultrasonication process originating a graphite-based material, which was denominated EGO. These materials were characterized by powder XRD and Raman (**Figure II.8**). Powder XRD patterns show the diffraction peaks for these carbon materials, the peak located at $2\theta \approx 26.6^{o}$ is related with the (002) reflection of graphitic structures corresponding to a reported *d* of 0.34 nm.[31] EGO sample presents an additional peak at $19.5^{o}$ related to the oxidation process of the graphite flakes which promotes the increase of the interlayer distance between the sheets (*d* = 0.45 nm). Raman spectra presents the typical D1 and G bands observed in graphene-based materials, centered at 1350 and 1585 $cm^{-1}$.

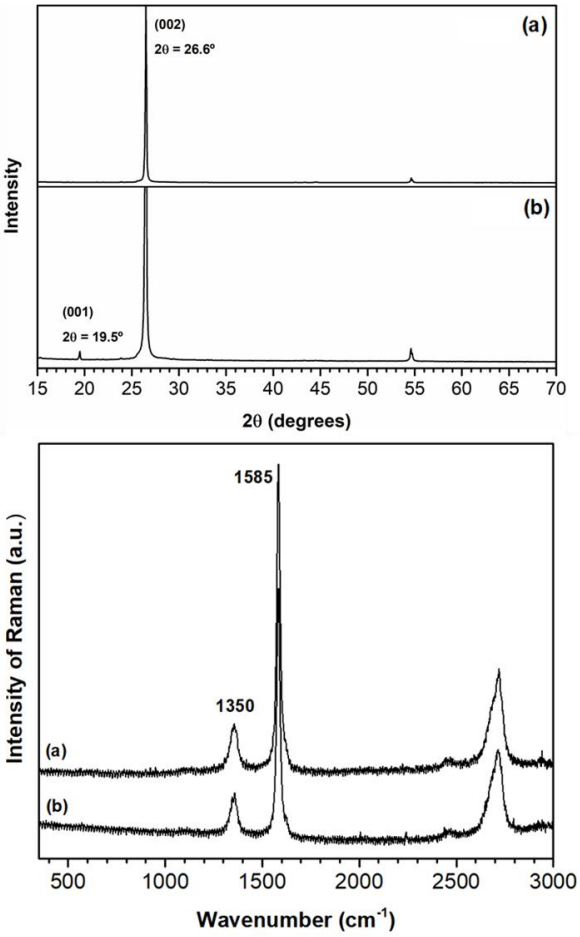


**Figure II.8**: Powder XRD patterns and Raman spectra of graphite flakes (a) and EGO (b) materials.

**Figure II.9** shows the TEM images and powder XRD patterns for EGO materials decorated with $Ag_2S$, PbS and CdS nanophases, in good agreement with the $Ag_2S$ monoclinic phase (ICDDPDF No. 00-014-0072), PbS cubic phase (ICDDPDF No. 01-072-4873) and CdS hexagonal phase (ICDDPDF No. 00-006-0314). **Figure II.10** shows the comparison between TEM images for graphite flakes and hybrid material with $Ag_2S$ nanophases deposited on the surface. Although the TEM results suggest that there is a higher population of discrete metal sulfide phases over the surfaces of graphite and EGO hybrid materials overall, the morphological features of such hybrids resemble those of the GO analogues.

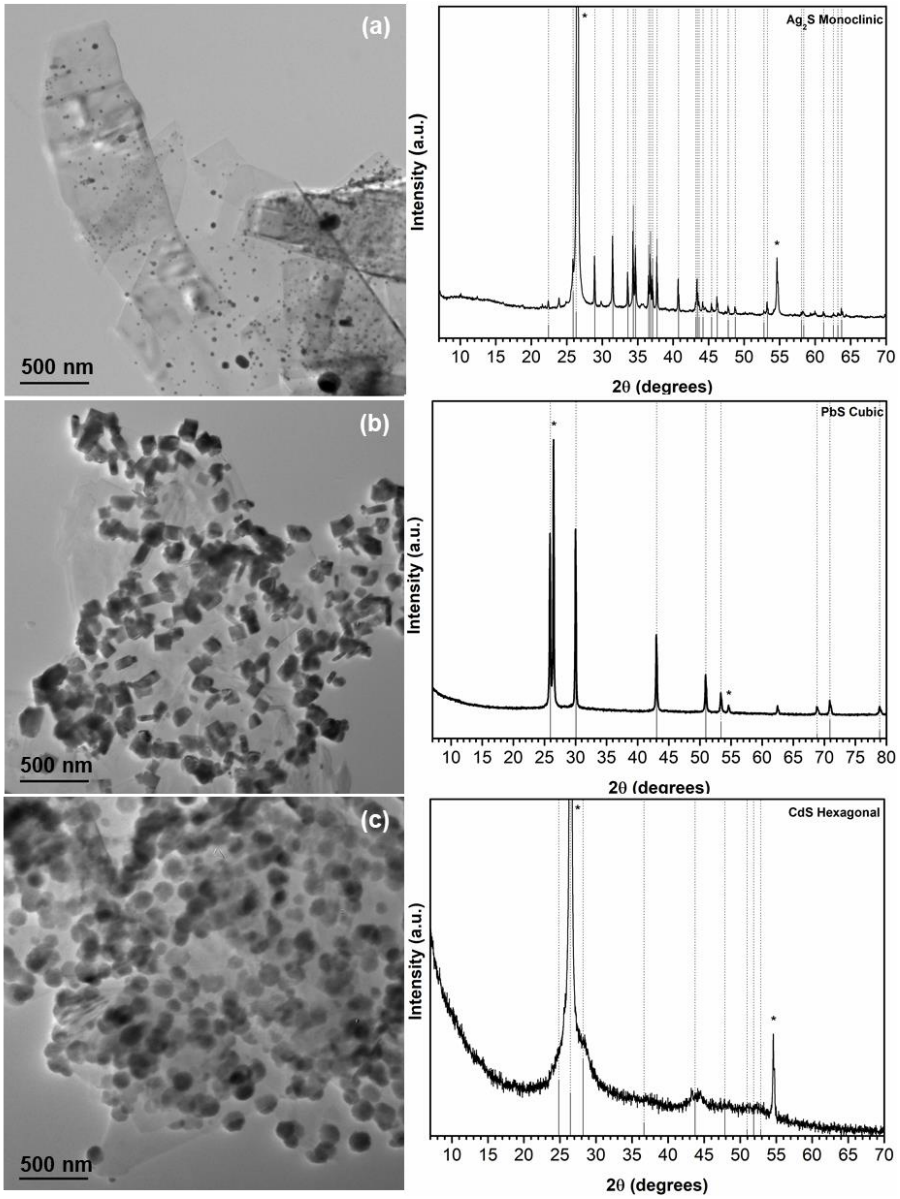


**Figure II.9:** TEM images of EGO sheets decorated with $Ag_2S$ (a), PbS (b) and CdS (c) nanophases and respective powder XRD patterns of the hybrid nanostructures. The vertical lines correspond to the standard diffractions peaks attributed to the respective metal sulfide. The diffraction peaks assigned to EGO are marked with *.

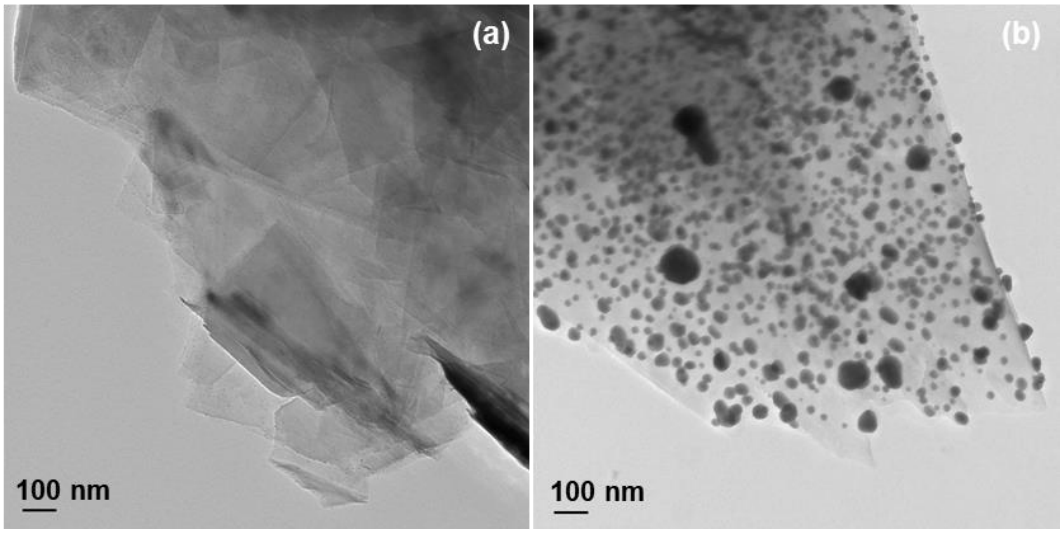


**Figure II.10**: TEM images of graphite flakes (a) and graphite decorated with $Ag_2S$ nanophases (b).

## 4. Conclusions

Metal sulfide@GO hybrid nanostructures have been successfully produced by *in situ* thermal decomposition of the respective metal alkyldithiocarbamate complexes. This one-step method is scalable for producing hybrid GO materials with negligible phase segregation and might be extended to other graphene-based materials. This method produces GO materials decorated with metal sulfides, whose absorption in the visible can be tuned by the deposited semiconducting nanophase. This approach can be explored to trigger photon harvesting in water compatible photocatalysts that perform efficiently in the visible spectral region.

# CHAPTER III

## *Copper sulfide nanoflower-like structures supported on graphene materials for photocatalytic degradation of water contaminants*

Here, graphene-based materials decorated with CuS particles synthetized by the chemical route described in the previous chapter are explored. The hybrid materials show photocatalytic activity to the degradation of the target water contaminants, rhodamine B, sulfamethoxazole and 4-nitrophenol.

# CHAPTER III | “Copper sulfide nanoflower-like structures supported on graphene materials for photocatalytic degradation of water contaminants”

Copper sulfide (CuS) nanomaterials have been investigated here for the decontamination of aqueous samples, due to their attractive properties such as large specific surface area, adsorption capacity and photocatalytic activity, including the ability to harvest photons in the visible spectral region. Additionally, graphene oxide (GO), has been of particular interest for heterogeneous catalysis due to its high specific surface area and ability for surface functionalization. Hence, the development of strategic and efficient chemical routes that combine these two classes of materials is an appealing technology for wastewater treatment processes. Thereupon, an efficient one-step synthesis is described to prepare hybrid structures comprising CuS nanoflowers supported on GO sheets, which follows the strategy detailed in **Chapter II** for the synthesis of metal sulfides. The photocatalytic performance of this material was investigated towards the degradation of rhodamine B (RhB) and sulfamethoxazole (SMX) dissolved in water, under visible-light irradiation. The above synthetic route was further explored using sulfur-doped graphene (S-graphene) as the substrate for the deposition of CuS particles. In order to conceive a photocatalyst with the ability for recovery from the reaction medium and with potential for reusability in subsequent photocatalytic cycles, tri-component photocatalysts containing both CuS and magnetic magnetite ($Fe_3O_4$) nanoparticles deposited over the S-graphene flakes were developed and used in the photocatalytic degradation of 4-nitrophenol (4-NP). [3]

*Keywords*: copper sulfide; graphene-based materials; magnetite; photocatalysis; wastewater treatment.

---

[3] This chapter is based on a research manuscript currently in preparation and partially on the work: Renata Matosa, Marta S. Nunes, Iwona Kuźniarska-Biernacka, Mariana Rocha, Alexandra Guedes, Ana C. Estrada, Joana L. Lopes, Tito Trindade, Cristina Freire. *Graphene@metal sulfide/oxide nanocomposites as novel photo-Fenton-like catalysts for 4-nitrophenol degradation*. **2021**, Eur. J. Inorg. Chem. (DOI: 10.1002/ejic.202100700)

Joana L. Lopes performed the main experimental and written tasks concerning the synthesis, characterization and photocatalytic studies on the degradation of RhB and SMX. Ana C. Estrada and Tito Trindade supervised the research performed in Aveiro. The deposition of the CuS particles on the S-graphene material and part of the characterization study of the as-prepared materials (XRD and TEM) were performed at the University of Aveiro. The S-doped graphene, deposition of $Fe_3O_4$ nanoparticles and further photocatalytic studies on the degradation of 4-NP were performed by the team of the University of Porto.

The research using S-doped graphene substrates was a collaborative initiative in the scope of the FOTOCATGRAF project (UTAP-ICDT/CTM-NAN/0025/2014).

# 1. Introduction

According to the World Health Organization and UNICEF report,[335] approximately 30% of the global population are currently without access to safe drinking water. As such, affordable and safe water treatment systems are needed to meet the United Nations Sustainable Development Goals, specifically Goal 6 to "ensure availability and sustainable management of water and sanitation for all" by 2030. Currently, to achieve this goal, a variety of wastewater treatments have been used to remove organic and inorganic contaminants from wastewater effluents.[336] Among them, advanced oxidation processes (AOPs) have been considered as an economically and ecologically safe option to solve many water pollution challenges. In particular, semiconductor photocatalysis stands as one of the most efficient AOPs for the degradation of organic pollutants.[337,338] These processes are based on the generation of highly reactive hydroxyl radicals (•OH), which ideally will mineralize organic matter in the presence of other oxidants, and are promoted by UV or solar light irradiation.[339] So far, titanium dioxide ($TiO_2$) and in a lesser extent zinc oxide (ZnO) have been the most used semiconductor photocatalysts to degrade organic pollutants from wastewater under UV-light irradiation.[154,168]

However, due to their wide band gap ($E_g$= 3.0-3.2 eV for $TiO_2$ and $E_g$= 3.4 eV for ZnO), these semiconductors are only activated by UV irradiation, which represents 4% of the entire solar spectrum.[340] Hence, the search of visible-light responsive semiconductor photocatalysts have gained more attention in the recent years. Narrow band gap semiconductors, such as certain metal sulfides, have been investigated as photocatalysts with strong absorption in the visible that might extend to the near-infrared (NIR) spectral region.[263] These metal sulfides harvest photons in the visible spectral region and can be prepared as nanosized particles showing quantum-size effects, hence displaying optical properties distinct from those of their bulk analogues.[341] CuS particles have been investigated as a non-toxic sorbent and photocatalyst of great interest due to its large specific surface area and ability to harvest photons efficiently in the visible spectral region, exhibiting a band gap ($E_g$= 1.2-2.2 eV), which is dependent on the crystalline phase present.[9,274]

Graphene-based materials have attracted great interest due to their exclusive mechanical, physical and chemical properties.[342] Moreover, graphene-based materials have already been used as adsorbents, showing high efficiency in removing vestiges of pharmaceutical compounds from water.[343,344] In particular, the implementation of chemical routes aiming to combine GO and other inorganic phases offers new possibilities for the development of innovative photocatalytic technologies. For example, the combination of GO with CuS particles has been reported to result in efficient hybrid photocatalysts towards the degradation of organic pollutants under solar irradiation. For instance, Shi *et al*. prepared CuS/rGO photocatalysts by a sonochemical method for the photodegradation of methylene blue (MB).[210] Also, Hu *et al*. prepared flower-like CuS/rGO nanocomposites through a one-step solvothermal procedure for the degradation of MB.[276] In general, these type of studies indicate that the coupling of CuS phases with carbon materials have improved

the photocatalytic activity of CuS, under visible-light irradiation. However, these systems still present limitations concerning its separation after photochemical reaction and, eventual, regeneration. In this context, the development of nanophotocatalysts with magnetic properties emerge as an advantage regarding the recovery of the photocatalyst and its subsequent reuse, as will be discussed below. Due to their low cost and availability, magnetic iron oxides, in particular $Fe_3O_4$ particles, are useful materials to confer the required magnetic properties to the photocatalysts applied to wastewater treatment,[247–249] namely they show fast separation under an external magnetic field due to its high magnetic susceptibility.[252]

Herein, following the interest in the synthesis and application of metal sulfide semiconductor nanostructures as visible-light photocatalysts for wastewater treatment,[77,219,274] the growth of CuS nanoflowers on GO sheets was investigated by a one-step synthesis method, as detailed in the previous chapter for other metal sulfides. The photocatalytic performance of the ensuing materials was evaluated in the degradation of RhB and SMX in aqueous solutions (**Figure III.1**), under visible-light irradiation. In a second stage, a magnetic carbon substrate ($Fe_3O_4$@GO) was prepared and decorated with CuS nanoflowers, to develop photocatalysts that enable their recovery and subsequent reuse. Finally, the one-step synthesis of CuS was explored in the presence of other graphene-based materials, such as S-graphene flakes decorated with $Fe_3O_4$ and used as photo-Fenton catalysts for the degradation of 4-NP (**Figure III.1**).

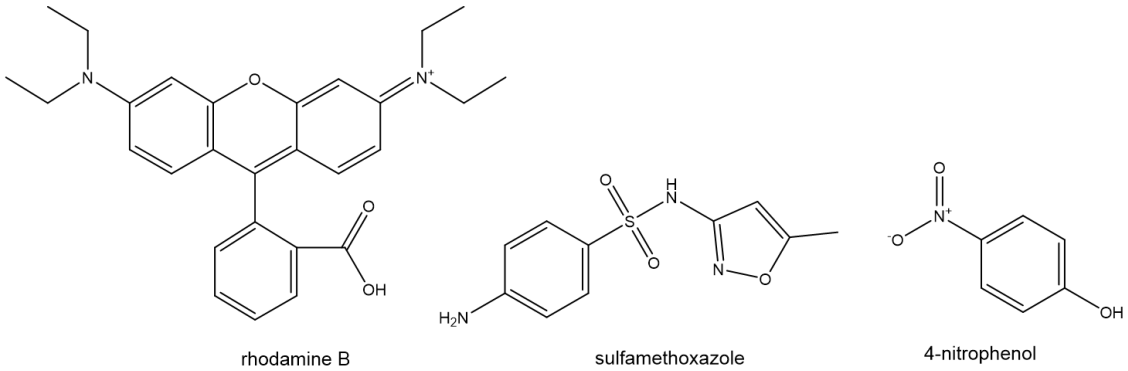


**Figure III.1**: Chemical structures of rhodamine B (RhB), sulfamethoxazole (SMX) and 4-nitrophenol (4-NP).

# 2. Experimental section

## 2.1. Materials

Acetone (Sigma-Aldrich, 99.98 %), copper nitrate hydrate ($Cu(NO_3)_2.3H_2O$, Aldrich, 99%), ethanol absolute (Fisher Chemical), ethylenediamine ($C_2H_8N_2$, Sigma-Aldrich, 99%), ferrous sulfate heptahydrate ($FeSO_4.7H_2O$, Panreac, 99%), graphene oxide (Graphenea), nitric acid ($HNO_3$, Sigma, 65%), potassium hydroxide (KOH, Pronolab, >86%), potassium nitrate ($KNO_3$, Sigma-Aldrich, >99%), rhodamine B ($C_{28}H_{31}N_2O_3Cl$, Sigma, 97%), S-graphene flakes (supplied by U. Porto, C. Freire

research group[345]), sodium diethyldithiocarbamate trihydrate ($(C_2H_5)_2NCS_2Na.3H_2O$, Aldrich, 100%) and sulfamethoxazole ($C_{10}H_{11}N_3O_3S$, Fluka Chemie) were used as received. Ethanol was dried with molecular sieves (3 Å, Fluka). Milli-Q water was obtained from the Synergy equipment from Millipore with a 0.22 µm filter.

## 2.2. Synthesis of graphene oxide-supported CuS photocatalysts

### *2.2.1. Synthesis of nanoflower-like CuS particles*

Pure CuS nanoflowers were synthesized through the thermolysis of copper(II) bisdiethyldithiocarbamate precursor, $Cu[S_2CN(C_2H_5)_2]_2$, according to previously described procedures.[77,219] In a typical procedure, ethylenediamine (9 mmol) was added to a dry ethanolic solution (25 mL) containing $Cu[S_2CN(C_2H_5)_2]_2$ (58 µmol), and the mixture was refluxed for 1 hour, under vigorous stirring and a $N_2$ stream, in a ventilated fume-hood. The dark solid formed was isolated by centrifugation (6000 rpm, 15 minutes), washed with ethanol, and after drying at room temperature was kept under $N_2$.

CuS: Analysis (wt.%): Found: Cu, 59.0. Calculated: 66.4.

$Cu[S_2CN(C_2H_5)_2]_2$ was used as a single-molecule precursor for CuS particles and was prepared by an adaptation of a literature method.[274] In a typical procedure, an aqueous solution of $Cu(NO_3)_2$ (10 mmol, 2.4 g) was treated, under stirring, with an excess of aqueous $Na[S_2CN(C_2H_5)_2]$. The brown solid obtained, $Cu[S_2CN(C_2H_5)_2]_2$, was collected by filtration and the final product recrystallized from hot acetone.

$Cu[S_2CN(C_2H_5)_2]_2$: Microanalysis (wt.%): Found: C, 33.5; H, 4.98; N, 7.6; S, 35.4. Calculated: C, 33.4; H, 5.6; N, 7.8; S, 35.6.

### *2.2.2. Synthesis of the CuS@GO hybrid material*

GO sheets were decorated with CuS particles according to the synthesis above (**section 2.2.1.**) but in the presence of GO. Typically, ethylenediamine (9 mmol) was added to a dry ethanolic suspension of GO (20 mg, 25 mL) containing the copper precursor (58 µmol). The mixture was then stirred at reflux until a color change of the reaction mixture was clearly observed. The materials were collected by centrifugation (6000 rpm, 15 minutes), washed with ethanol, dried at room temperature and kept under $N_2$.

CuS@GO: Analysis (wt.%): Found: Cu, 13.10. Average loading, 2.10 mmol/g.

## 2.3. Synthesis of magnetic graphene oxide-supported CuS materials

### *2.3.1. Synthesis of $Fe_3O_4$ nanoparticles*

Magnetic nanoparticles of $Fe_3O_4$ were synthesized by oxidative hydrolysis of $FeSO_4.7H_2O$ in alkaline conditions.[346] Milli-Q water was first deoxygenated under a $N_2$ stream under vigorous stirring for 2 hours. Then, 25 ml of deoxygenated water were added to a 250 ml round flask with KOH (1.90 g) and $KNO_3$ (1.52 g). The resulting mixture was heated at 60 ºC under a $N_2$ stream and mechanically stirred at 500 rpm. After salt dissolution, 25 ml of an aqueous solution containing $FeSO_4.7H_2O$ (4.75 g) were added dropwise and then the stirring was increased to 700 rpm. After the complete addition of the $Fe^{2+}$ salt, the resulting solution, with a dark green color, was left at 60 ºC for 30 minutes. Then, the round flask was transferred to a hot bath at 90 ºC and left under a $N_2$ stream, without stirring, for 4 hours. Finally, the resulting black solid was washed several times with deoxygenated water, collected with a laboratorial NdFeB magnet and dried at 40ºC.

### *2.3.2. Synthesis of magnetic GO flakes*

GO with magnetic properties, $Fe_3O_4$@GO, was prepared by an adaptation of a literature method.[347] Typically, $Fe_3O_4$ particles (100 mg) synthesized as above (**section 2.3.1.**) were suspended in a 0.1 M $HNO_3$ solution (100 mL). In parallel, GO flakes (50 mg) were dispersed in Milli-Q (10 ml) and then added to the $Fe_3O_4$ suspension, using an ultrasonic bath to promote stirring during 30 minutes. The $Fe_3O_4$@GO flakes were collected using a laboratorial NdFeB magnet, washed thoroughly with Milli-Q water and ethanol and dried at 40 °C.

### *2.3.3. Synthesis of CuS-$Fe_3O_4$@GO structures*

$Fe_3O_4$@GO flakes were decorated with CuS particles according to the method described in **section 2.2.2**. Thus, ethylenediamine (9 mmol) was added to a dry ethanolic suspension of $Fe_3O_4$@GO (40 mg, 50 mL) containing the copper precursor (58 µmol). The reaction was kept under mechanical stirring (400 rpm) for at least 1 hour at reflux. The CuS-$Fe_3O_4$@GO structures were collected using a laboratorial NdFeB magnet, washed with ethanol, dried at room temperature and kept under $N_2$.

CuS-$Fe_3O_4$@GO: Analysis (wt.%): Found: Cu, 11.0; Fe, 44.0. Average loading, 1.75 mmol/g.

## 2.4. Synthesis of S-doped graphene-supported CuS photocatalysts

### *2.4.1. Synthesis of CuS@S-graphene hybrid material*

The S-graphene sheets were decorated with CuS particles according to the procedure described in **section 2.2.2.** but in the presence of S-graphene sheets.[219] In a typical experiment, ethylenediamine

(9 mmol) was added to a dry ethanolic suspension containing the S-graphene (20 mg, 25 mL) and the metal precursor $Cu[S_2CN(C_2H_5)_2]_2$ (58 µmol). The mixture was stirred under reflux until a color change of the reaction mixture was clearly observed. The hybrid materials were collected by centrifugation (6000 rpm, 15 minutes), washed with ethanol, dried at room temperature and kept under $N_2$.

## 2.5. Photocatalytic screening studies

### *2.5.1. Graphene oxide-supported CuS photocatalysts*

The photocatalytic performance of as-prepared materials (GO, CuS particles and CuS@GO hybrid material) was evaluated in the degradation of RhB (20 mg/L) and SMX (5 mg/L) dissolved in water, at pH = 6 and 5, respectively. The photocatalytic reactions were performed at room temperature in a glass microreactor placed at 6 cm from a blue LED light covering the range of 410-480 nm (**Figure III.2**). The average intensity of irradiation was 1.5-2 mW/cm$^2$, as measured with a Laser Ophir Start Lite coupled with an Ophir 12A-V1 Power Laser Sensor 12A-V1.

In order to establish the adsorption capacity, all-prepared materials were dispersed in 20 mL of aqueous solution containing RhB (0.1 mg/mL) or SMX (0.2 mg/mL), and kept in the dark, under vigorous stirring. After the adsorption/desorption equilibrium time was established, the photocatalytic activity of the materials was then assessed. In a typical photocatalytic run, the catalysts were dispersed into 20 mL of aqueous solutions of RhB (0.1 mg/mL) or SMX (0.2 mg/mL) and stirred in the dark for 30 and 120 minutes, respectively, to ensure the adsorption/desorption equilibrium. Afterward, these suspensions were irradiated with the LED lamp, under vigorous stirring. The reaction was monitored at regular intervals; thus aliquots of the reaction mixture were withdrawn, immediately centrifuged (13000 rpm, 5 minutes) to remove the catalyst and the concentration of RhB and SMX was monitored by ultraviolet/visible (UV/VIS) spectroscopy at 554 nm and high-performance liquid chromatography with diode-array detection (HPLC-DAD) at 265 nm, respectively. The term of reaction was considered when the concentration of pollutant remained constant after two subsequent analyses. The photocatalytic reactions were also performed in the presence of 1% of $H_2O_2$ (30% v/v), keeping the same reaction conditions.

The photodegradation rate was calculated according to the **Equation III.1**, where $C_t$ and $C_0$ are the concentration of RhB or SMX at time t and t = 0 (after adsorption/desorption equilibrium period), respectively.

$$R = \frac{C_0 - C_t}{C_0} \times 100\% \qquad Eq.III.1$$

The RhB and SMX removal was assumed to be a pseudo-first order reaction, and the rate constant values, $k$ (min$^{-1}$), were estimated from the slopes of the linear ranges of the $ln(C_t/C_0)$ according to the **Equation III.2**.

$$ln(C_t/C_0) = -kt \qquad Eq.III.2$$

The CuS particles, GO sheets and CuS@GO material were separated from the reaction mixture by centrifugation (6000 rpm, 15 minutes), washed with $H_2O$ and ethanol, to remove the remaining pollutants and $H_2O_2$, and dried under vacuum at room temperature.

**Figure III.2**: Digital photograph of the blue LED light used in the experiments of the photocatalytic degradation of aqueous solutions of RhB and SMX.

### *2.5.2. S-doped graphene-supported CuS photocatalysts*

The photocatalytic activity of S-doped graphene-based CuS photocatalysts as well as their components was evaluated for the degradation of aqueous solutions of 4-NP (0.05 mM). The photocatalytic reactions were performed in a quartz reactor (PRL 3312 from Photochemical Reactors), irradiated with UV-A radiation (15 W mercury lamp). Due to the presence of materials with magnetic properties, the stirring was carried out using a pumping air through the reactor membrane.

In a typical photocatalytic reaction, 20 mg of catalyst were dispersed in 100 mL of aqueous solution containing 4-NP and transferred to the photocatalytic reactor. After stirring in the dark (typically during 30 minutes) to ensure the adsorption/desorption equilibrium, 2 mL of $H_2O_2$ (30% w/w) were added and the lamp was turned on for 180 minutes, maintaining a vigorous stirring. The reaction progress was monitored by UV/VIS, collecting 1.5 mL aliquots at defined interval times, which were centrifuged (13400 rpm, 2 minutes) to remove the catalyst. NaOH pearls were added to all aliquots immediately before UV/VIS analysis to promote the formation of the 4-nitrophenolate ion, which exhibit a maximum absorption at 400 nm.[348] Note that, in a first step, the 4-NP adsorption capacity of all materials was evaluated, using the same experimental procedure but keeping the mixture in the dark for 120 minutes without $H_2O_2$ addition, under vigorous stirring. The percentage of removed/degraded 4-NP was calculated through **Equation III.1**, previously described, where $C_t$ and $C_0$ are the

concentration of 4-NP at time t and t = 0, respectively. The 4-NP removal was assumed to be a pseudo-first order reaction, and the rate constant values, $k$ ($min^{-1}$), were estimated from the slopes of the linear ranges of the $ln(C_t/C_0)$, according to the **Equation III.2.** The stability of the most promising photocatalyst was evaluated in a second photocatalytic cycle, applying similar experimental conditions as those of the first cycle. At the end of each reaction cycle, the catalyst was magnetically recovered, washed, and dried at room temperature.

## 2.6. Instrumentation

The powder X-ray power diffraction (XRD) data were collected using a PANanalytical Empyrean X-ray diffractometer equipped with Cu-K$\alpha$ monochromatic radiation source at 45 kV/40 mA. The samples were prepared by deposition of aliquots of the ethanolic suspensions of the samples on a silicon holder. X-ray photoelectron spectroscopy (XPS) measurements were performed at Centro de Materiais da Universidade do Porto (CEMUP), Portugal, on a Kratos Axis Ultra HSA spectrometer with monochromatized Al Kα radiation (1486.7 eV) operating at 15 kV (90 W). The materials were pressed into pellets prior to the XPS analyses. The binding energies were calibrated using the C 1s peak at 285 eV as internal reference. The CasaXPS software was used to deconvolute the XPS spectra, employing a non-linear least squares fitting routine after a Shirley-type background subtraction. For transmission electron microscopy (TEM) analysis, a drop of the suspension under analysis was placed on a carbon-coated Cu grid and the solvent was left to evaporate at room temperature. TEM images and the selected area electron diffraction (SAED) pattern were acquired using a transmission electron microscope Hitachi H-9000 operating at 300 kV. Scanning transmission electron microscopy (STEM) was performed using a Hitachi HD-2700 STEM microscope operating at 200 kV. Scanning electron microscopy (SEM) analysis was performed using a scanning electron microscope Hitachi SU-70 operating at an accelerating voltage of 15 kV. The analysis of TEM images to build the particle size histograms was performed using the software ImageJ version 1.46. Energy dispersive X-ray spectroscopy (EDS) analysis was performed using an EDS Bruker Esprit. Raman spectral imaging was performed in a combined Raman-AFM-SNOM confocal microscope WITec alpha300 RAS+ at CICECO, in the Chemistry Department of the University of Aveiro. A Nd:YAG laser operating at 532 nm was used as excitation source with the power set at 1 mW. The intensity values and associated errors of the Raman bands of the GO sample was obtained by multi-peaks fitting using the Lorentz function in Origin 2016. The UV/VIS spectra and the measurements of the RhB degradation were recorded using a Jasco V-560 spectrometer. The UV/VIS measurements of the 4-NP degradation were performed in a Varian Cary 50 Bio spectrophotometer in the range 200-500 nm, using a quartz cuvette with an optical pass of 1 cm. The samples collected during the photocatalytic experiments with SMX were analysed by HPLC-DAD (ThermoScientific Ultimate 3000 equipped with Ultimate 3000 DAD) at 265 nm. The HPLC system comprised a column Kromasil 100-5-C18 (250 mm of length and 4.6 mm of i.d.) coupled to

a precolumn holder (imChem). The column was maintained at 30 ºC and the mobile phase consisted of acetic acid 1M (70%) and methanol (30%) with a flow rate of 0.8 ml/min. ChromeleonTM chromatography data system was used to quantify the peak areas. The elemental analysis of carbon and sulfur was obtained on a Leco Truspec-Micro CHNS 630-200-200. The elemental analysis of Cu was performed by inductively coupled plasma (ICP) spectroscopy using a Jobin-Yvon JY70 Plus spectrometer. The surface charge of the nanoparticles was given by zeta potential that was determined through electrophoretic light scattering performed in aqueous solutions of the particles, in a Zetasizer Nano ZS equipment from Malvern Instruments (Malvern, UK).

# 3. Results and discussion

## 3.1. Graphene oxide-supported CuS photocatalysts

### *3.1.1. Synthesis and characterization of the materials*

The CuS@GO hybrid material was obtained after generating the CuS particles *in situ*, in the presence of GO sheets, following the reflux of a ethanolic suspension containing the copper(II) bisdiethyldithiocarbamate complex, used here as a single-molecule source for sulfide species and metal ions.[219]

The powder XRD patterns of CuS@GO, GO and pristine CuS are shown in **Figure III.3**. The peak centered at $2\theta \approx 10.5°$ corresponds to the (001) reflection of GO with an interlayer distance $d$ = 0.86 nm. The XRD pattern of the CuS@GO material show broad diffraction peaks at $2\theta \approx 27.7°$, 29.3°, 31.8°, 38.8°, 47.9°, 52.7° and 59.3° assigned to the (101), (102), (103), (105), (110), (108) and (116) crystal planes of covellite, the hexagonal phase of CuS (ICDDPDF nº 00-006-0464 in **Appendix D**, **Annex 4**), thus confirming the presence of CuS particles on the GO sheets. Compared with the powder XRD patterns reported for covellite phase of CuS[349], the (103) and (006) reflections of the CuS@GO sample are broad and overlap with each other, which might indicate size and shape effects owing to the restrained growth of certain crystal facets.[350,351] In fact, the TEM images (**Figure III.4**-a, b) of the same sample shows spheroidal CuS particles with a flower-like morphology, with average particle diameter of (800 ± 262) nm. The close inspection of the TEM images show that each single CuS nanoflower is in turn composed of smaller needle-like nanocrystallites (**Figure III.4**-b1). The selected area electron diffraction (SAED) pattern (**Figure III.4**-d) confirmed the crystalline nature of the structures, and the calculated *d*-values are in good agreement with the XRD data. Hence, despite the micrometer-size of the nanoflower-like CuS particles, each single particle is in turn composed of smaller nanocrystallites that have clustered on the carbon substrates. In the absence of GO, this method also led to hexagonal-type CuS particles (**Figure III.4**-c) but of larger dimensions, (1308 ± 182) nm. In fact, the mean crystallite size of the pure CuS sample and CuS particles on GO sheets, were 5 and 7 nm, respectively, as estimated by the Scherrer equation using for each case the respective (102) reflection observed in the powder XRD patterns. The latter did not show XRD peaks

that could be ascribed to crystalline impurities. The nanoflower-like CuS particles were found mostly distributed at the edges of the GO sheets, which is probably associated to the existence of oxygen-containing groups on GO that act as nucleating centres for CuS formation. The SEM image and the respective EDS mapping are in line with these findings, confirming the presence of Cu and S on the GO substrate (**Figure III.5**).

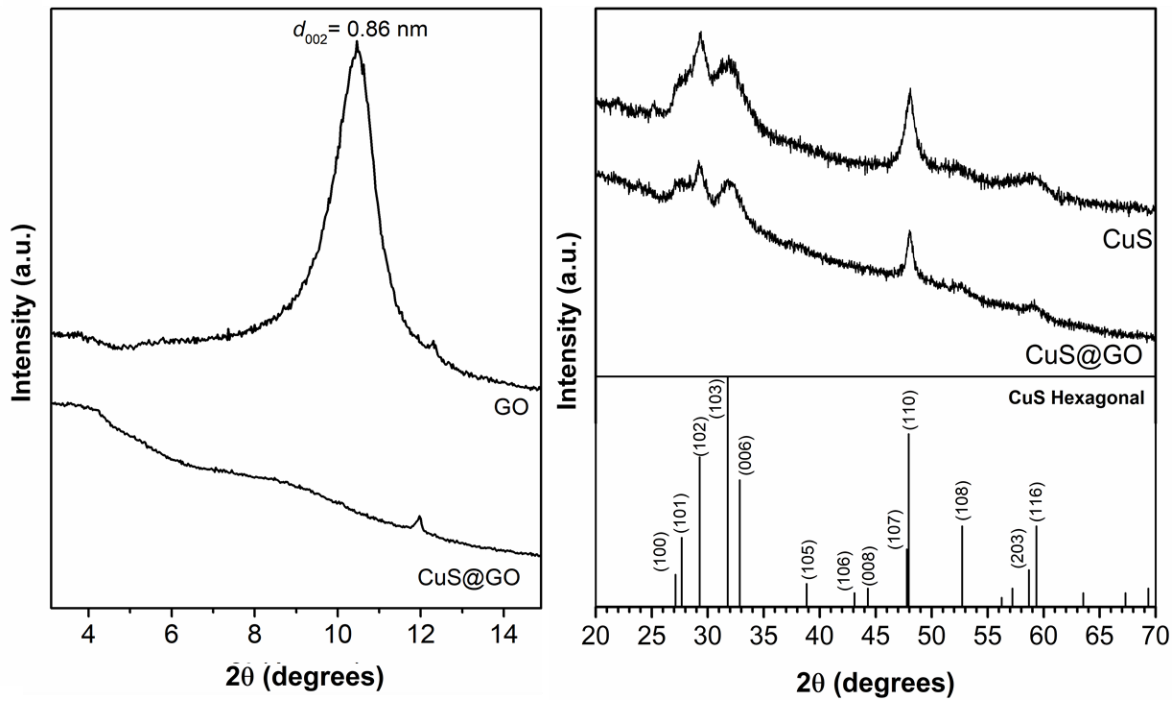


**Figure III.3**: Powder XRD patterns of CuS@GO, GO flakes and pure CuS samples. The vertical lines correspond to the standard diffraction peaks attributed to the CuS hexagonal phase (ICDDPDF nº 00-006-0464).

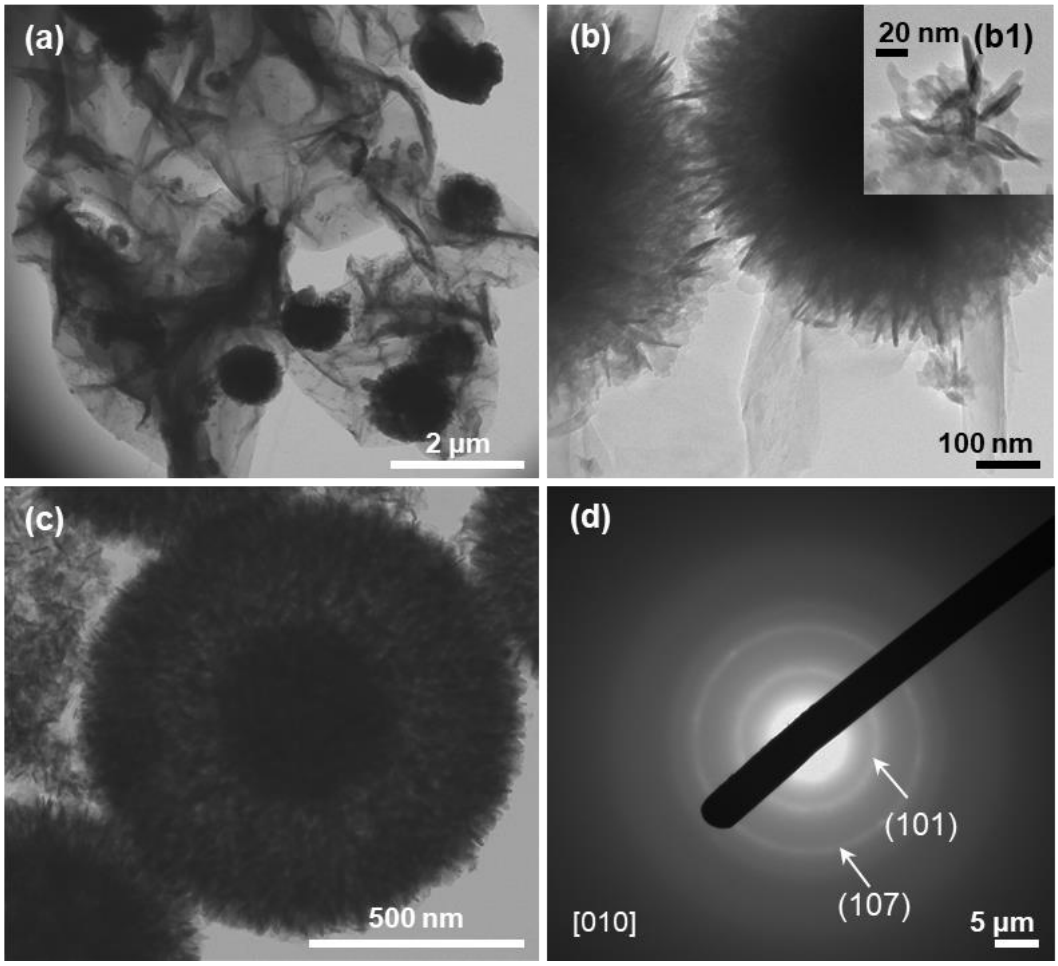


**Figure III.4**: TEM images of CuS@GO (a, b) and CuS (c) samples. SEAD of the pure CuS particles (d).

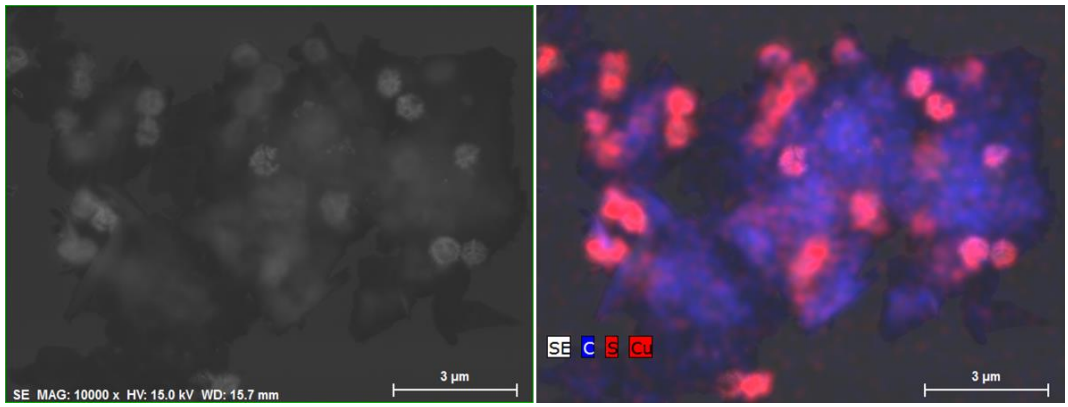


**Figure III.5**: SEM image and corresponding EDS mapping of the CuS@GO sample (C – blue; CuS - red).

The Raman spectrum (**Figure III.6**) of CuS@GO shows a band at 262 $cm^{-1}$ due to the $A_{1g}$ transverse optical (TO) mode of CuS, and a strong and sharp band at 473 $cm^{-1}$ related to the S-S stretching vibration of the $A_{1g}$ longitudinal optical (LO) mode observed in dimers at the 4e sites of CuS.[349]

Comparing the Raman spectrum of the CuS@GO sample with that one of neat CuS particles (476 $cm^{-1}$ and 272 $cm^{-1}$), the former show a small shift for lower wavenumbers, particularly observed in the TO mode, which may be associated to vacancies in the CuS lattice, induced during the growth of the CuS particles.[352] The D and G bands of GO were deconvoluted into five components, which were assigned to aryl-alkyl ether (D4; 1136 $cm^{-1}$), graphene edges (D1; 1358 $cm^{-1}$), amorphous carbon structures (D3; 1536 $cm^{-1}$), graphitic carbon (G; 1581 $cm^{-1}$), and graphene sheets (D2; 1622 $cm^{-1}$) (**Figure III.7**).[353] Moreover, the bands at 1352 $cm^{-1}$ and 1594 $cm^{-1}$ in the Raman spectrum of the CuS@GO sample correspond to the D1 and G bands of graphene-based structures, respectively.[354] The intensity ratio of these two bands ($I_D/I_G$) affords a sensitive information about the disorder and crystallite size of the graphitic layers. In this case, the $I_D/I_G$ ratio for CuS@GO was estimated as 1.46, which is slightly higher than that calculated for GO sheets (1.32), indicating an increase of the defects on the GO sheets during the growth of the CuS particles at their surface. Also, the G band in the Raman spectrum of the hybrid material is shifted in comparison with the G band in GO, which suggests the formation of Cu-S-C bonds between CuS particles and GO sheets.[355]

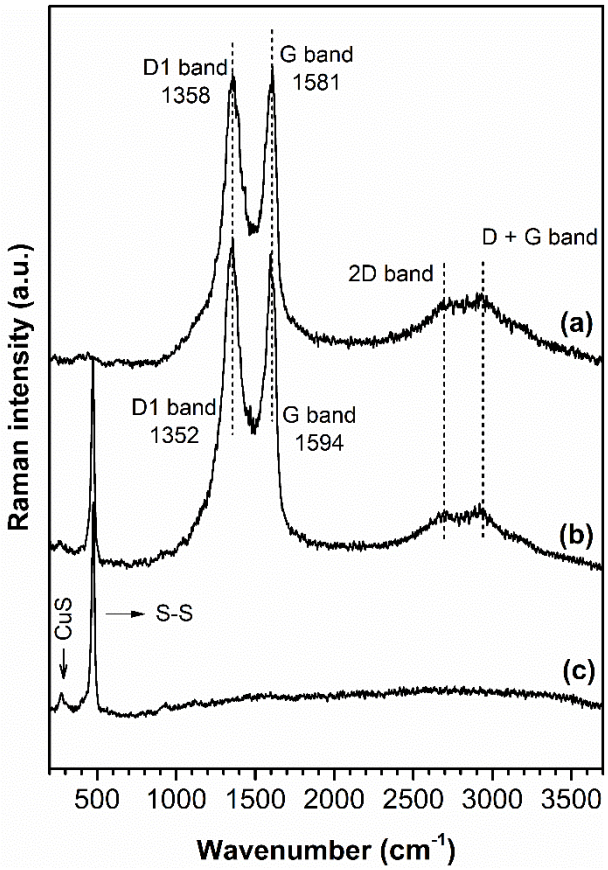


**Figure III.6**: Raman spectra of pristine GO flakes (a), CuS@GO (b) and pristine CuS (c) samples.

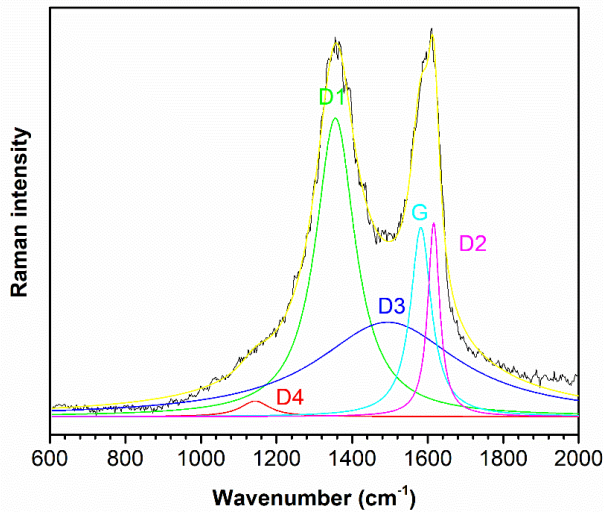


**Figure III.7**: Raman spectrum of GO showing the deconvolution evidencing the characteristic D and G bands, using the Lorentz function.

**Figure III.8** shows the C 1s core level XPS spectra for GO and CuS@GO. The C 1s core level XPS spectrum for GO, shows three peaks at 285.0, 287.0 and 288.6 eV, which are attributed to the C=C, C-OH and O–C=O bonds, in good agreement with the published data.[356] For the CuS@GO sample, the C 1s core level XPS spectrum shows the peaks at 285.0, 286.8, 288.4 and 288.6 eV; however the peak areas ascribed to the C-OH and O-C=O groups decreased significantly as compared to the XPS spectrum of GO, which suggests that the CuS particles were successfully attached to the GO sheets. The Cu 2p core level XPS spectrum (**Figure III.9**) for CuS@GO shows two peaks at 932.2 eV (2p3/2) and 952.0 eV (2p1/2), and a shakeup satellite peak at 943.6 eV, in accordance with the paramagnetic chemical state of $Cu^{2+}$. The gap of 19.8 eV for the Cu 2p doublet suggests that the chemical states of Cu on the CuS@GO are in fact +2, as expected due to the presence of Cu−S bonds.[356]

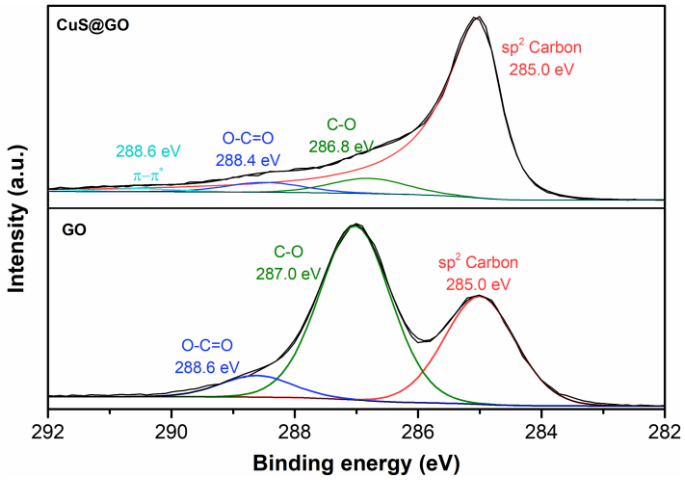


**Figure III.8**: High-resolution fitted C 1s XPS spectra of CuS@GO and GO sheets.

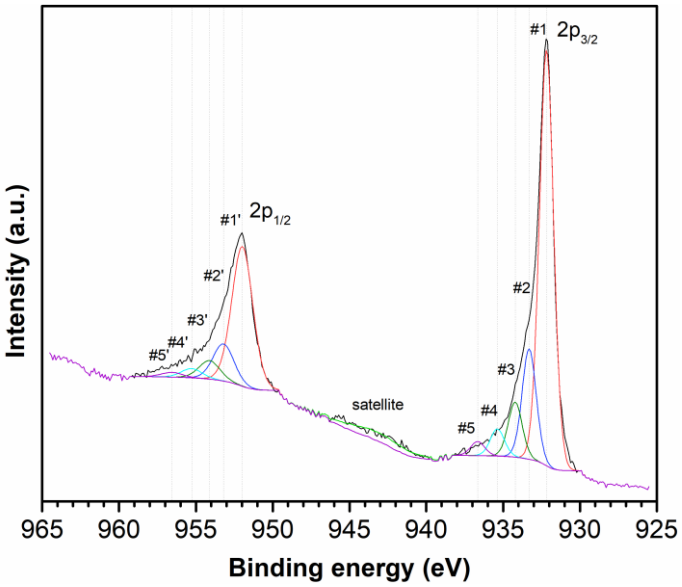


**Figure III.9**: High-resolution fitted Cu 2p XPS spectrum of CuS@GO sample. Peaks: #1 = 932.2 eV; #2 = 933.3 eV; #3 = 934.2 eV; #4 = 935.4 eV; #5 = 936.7 eV; #1' = 952.0 eV; #2' = 953.2 eV; #3' = 954.1 eV; #4' = 955.3 eV; #5' = 956.6 eV.

The UV/VIS absorption spectra of aqueous suspensions of CuS@GO, pure GO and CuS particles are shown in **Figure III.10**. The UV/VIS spectrum of GO exhibits an absorption band at *ca*. 238 nm, which corresponds to the π-π* electronic transition of aromatic C–C bonds. The band ascribed to the n-π* transition of the carbonyl groups, which usually appears at 315 nm, was not observed. The neat CuS particles have a broad absorption in the visible ($E_g$ = 1.87 eV) and in the NIR regions. In fact, colloidal CuS with covellite structure have emerged as plasmonic materials since their discovery by Zhao *et al*.[342] Their localized surface plasmon resonance (LSPR) band is located in the NIR region and has its origin in the high density of free charge carries, in this case positive holes, induced by the Cu vacancies.[357–359] However, it is interesting to note that the LSPR band of CuS was weakened by GO, which is a light-absorbing material.[360] CuS@GO presents an optical feature at 600 nm due to the d–d transition of $Cu^{2+}$ ions in CuS, whose direct band gap energy was found to be 1.58 eV.

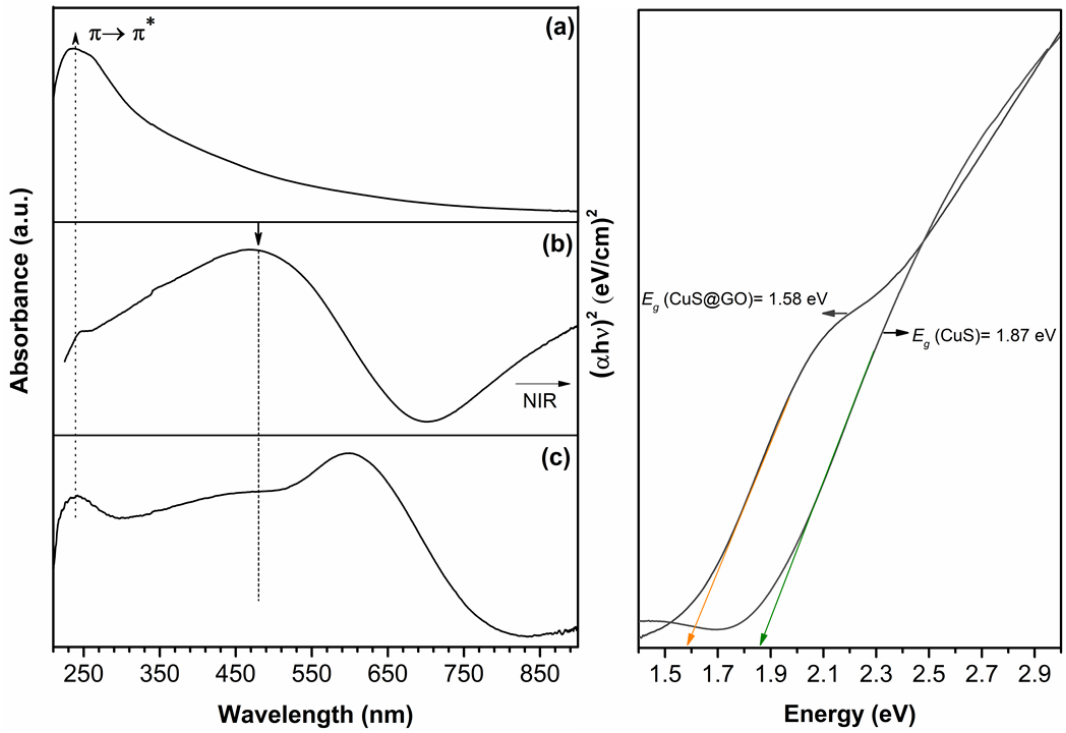


**Figure III.10**: UV/VIS spectra (left) of aqueous suspensions of pristine GO (a), CuS (b) and CuS@GO (c) and the Tauc plot for CuS present in both materials (right).

### *3.1.2. Photocatalytic performance of graphene oxide-supported CuS photocatalysts*

The photocatalytic performance of the CuS@GO materials was investigated through the degradation, under visible-light irradiation, of two organic compounds that might be found as water contaminants, a dye and an antibiotic compound - RhB and SMX, respectively, (**Figure III.1**). **Figure III.11** shows the adsorption capacity of GO sheets, pure CuS particles and CuS@GO hybrid material, under dark conditions. It was found that the CuS@GO material and CuS particles have higher adsorption capacity for RhB and SMX, as compared to the GO sheets. In fact, the presence of GO sheets resulted in negligible adsorption values of RhB and SMX, 10% and 20%, respectively. The CuS particles had moderate adsorption performance for RhB (60%), but high adsorption capacity for SMX (90%). On the other hand, in the presence of CuS@GO, the adsorption of RhB was 88% (1 hour of contact time) and for SMX was 80% (4 hours of contact time). For SMX, the adsorption/desorption equilibrium was established after 120 minutes, while for RhB no further adsorption was observed after 30 minutes.

To understand the role of GO in the hybrid material, the surface area ($S_{BET}$) and porosity of pure CuS particles, GO sheets and CuS@GO were investigated (**Table III.1**). The $S_{BET}$ of CuS@GO was 9.3 $m^2/g$, which was slightly smaller than that of pure CuS (10.4 $m^2/g$) and GO (12.7 $m^2/g$). This decrease can be associated with changes in the micropore size distribution for the CuS@GO (15.3 nm) compared with that of GO sheets (8.1 nm). Moreover, the zeta potential measurements revealed a

negative surface charge for all the materials. At pH 5-6, the measured zeta potential values were -2.1 ± 3.1 mV, -3.2 ± 3.5 mV and -45.9 ± 4.5 mV for CuS, CuS@GO and GO, respectively. The less negative zeta potential for the CuS@GO, in comparison with GO, is consistent with the presence of $Cu^{2+}$ ions over the surface of GO sheets. At working pH, RhB molecules are deprotonated (pKa 4.2)[361] and SMX is in its zwitterionic form (pKa 1.39; 5.7)[343]. These conditions favoured the adsorption of the contaminants' molecules at the surface of the less negatively charged CuS and CuS@GO materials, in comparison with the highly negatively charged GO. Probably the interaction between the contaminant molecular adsorbates and the photocatalysts' surfaces are favoured *via* electrostatic forces, thus explaining the enhancement of the adsorption capacities. Alternatively, in the presence of GO, the electric repulsion that occurs between the organic compounds and the negatively charged surface becomes more relevant and only π-π interactions may occur, although in lesser extension.[343]

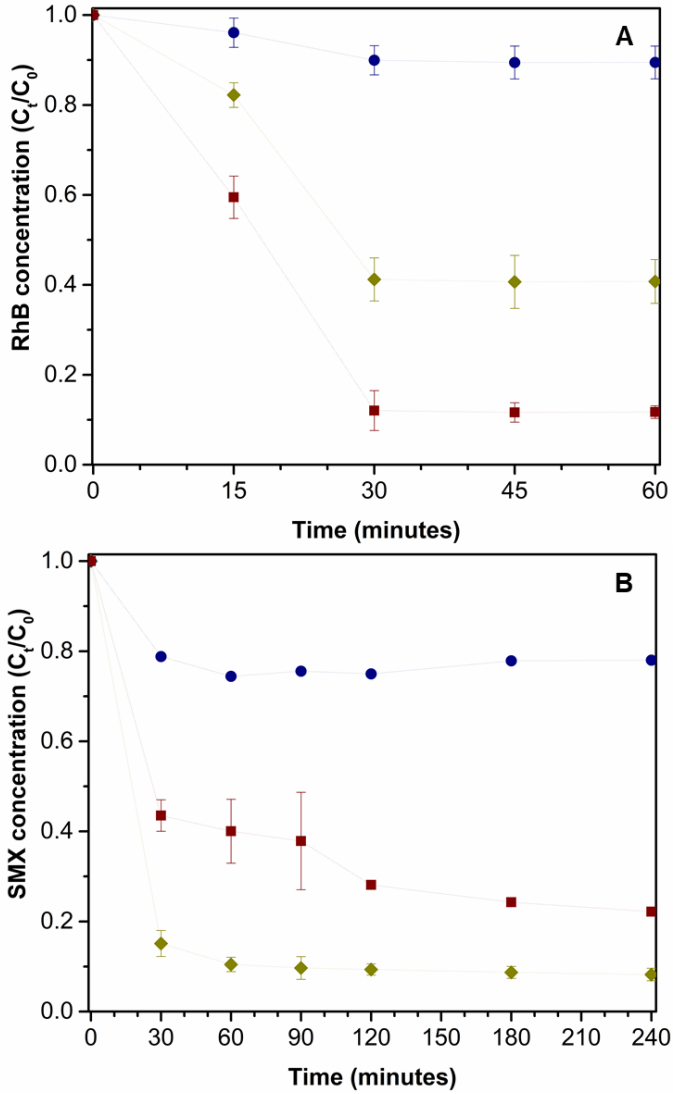


**Figure III.11**: Concentration of RhB (A) and SMX (B) as function of contact time with GO (●), CuS (◆), CuS@GO (■). Conditions: 20 mL of aqueous solution of RhB 20 mg/L and SMX 5 mg/L; 25 ºC.

**Table III.1**: Surface properties (BET surface area ($S_{BET}$), pore volume ($V_P$) and pore size ($S_P$)) of pure CuS, GO sheets and CuS@GO material.

| Sample | $S_{BET}$ ($m^2/g$) | $V_p$ ($cm^3/g$) | $S_p$ (nm) |
|---|---|---|---|
| **GO** | 12.7 | 0.025 | 8.1 |
| **CuS** | 10.4 | 0.042 | 15.3 |
| **CuS@GO** | 9.3 | 0.019 | 8.0 |

**Figure III.12** shows the concentration of RhB and SMX as function of light irradiation time in the presence and absence of GO, CuS and CuS@GO. The degradation of RhB and SMX in the presence of GO was very low; less than 10% of RhB and SMX were removed after 210 and 240 minutes of irradiation, respectively. In the presence of pure CuS, it was attained only 20% of removal for both organic compounds. In the presence of CuS@GO material, moderate degradation values of RhB (40%) and SMX (50%) were observed, after 180 minutes of irradiation.

However, the photocatalytic efficiency of the system was significantly improved with the addition of a small amount (1%) of $H_2O_2$, as already described for the photodegradation of other pollutants in aqueous solutions under similar conditions.[362–365] In fact, the photocatalysts under visible-light irradiation and in the presence of $H_2O_2$ seems to be more effective in the photocatalytic degradation of both RhB and SMX contaminants due to a positive synergistic effect. For these conditions, almost complete removal of RhB was achieved with CuS and CuS@GO materials, after 180 minutes of irradiation; as well for SMX, higher than 95% of degradation, after only 90 minutes of irradiation. Moreover, $H_2O_2$ has a negligible effect in the photolysis of RhB and SMX in the absence of the photocatalysts. Therefore, the improved oxidation of the contaminants was derived from the photocatalysts in the presence of $H_2O_2$, which acted as an electron acceptor, suppressing the recombination of photoinduced electrons and holes, and thus enhancing the photodegradation efficiency.

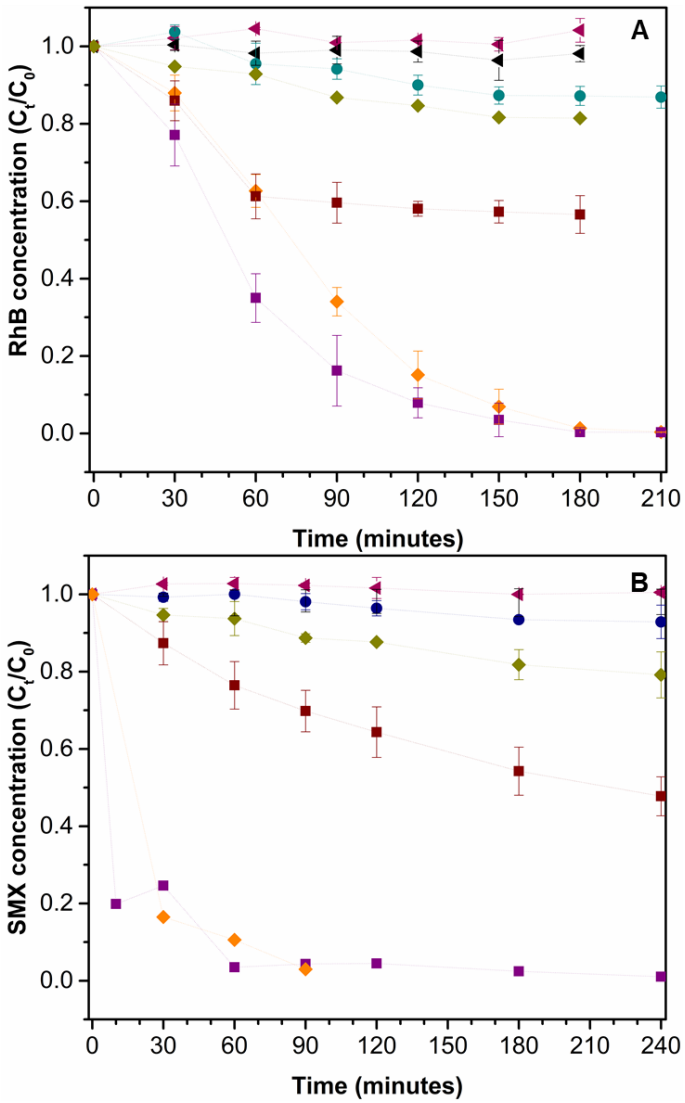


**Figure III.12**: Concentration of RhB (A) and SMX (B) as function of light irradiation time with GO (●), CuS (◆), CuS@GO (■) in absence of $H_2O_2$; GO (●), CuS particles (◆), CuS@GO (■) with 1% of $H_2O_2$; in the absence of catalyst (◀); in the absence of catalyst with 1% $H_2O_2$ (◀). Conditions: 20 mL of aqueous solution of RhB 20 mg/L and SMX 5 mg/L; 25 ºC.

The plots of the pseudo-first order kinetics which were obtained by the slopes of the linear representations of $ln(C_t/C_0)$ as function of irradiation time, are shown in **Figure III.13** and **Table III.2**. The *k* values for the photocatalytic degradation of RhB, using CuS and CuS@GO as the photocatalysts, were found 0.0013 and 0.0064 $min^{-1}$, respectively. On the other hand, using similar conditions but in the presence of $H_2O_2$, the *k* values were 0.022 and 0.026 $min^{-1}$, using CuS and CuS@GO, respectively. The *k* values for the photocatalytic removal of SMX were 0.0011 and 0.0034 $min^{-1}$ for CuS and CuS@GO, respectively. In the presence of $H_2O_2$, the photocatalytic removal increased significantly, for which the *k* values for CuS and CuS@GO were 0.04 and 0.043 $min^{-1}$, respectively. Overall, in both systems, it was observed a synergist effect resultant from the presence

of $H_2O_2$ with the photocatalysts, achieving almost complete degradation of RhB and SMX sooner. Moreover, the rate constant *k* using CuS particles or CuS@GO hybrid material was about 2 times higher for SMX than RhB.

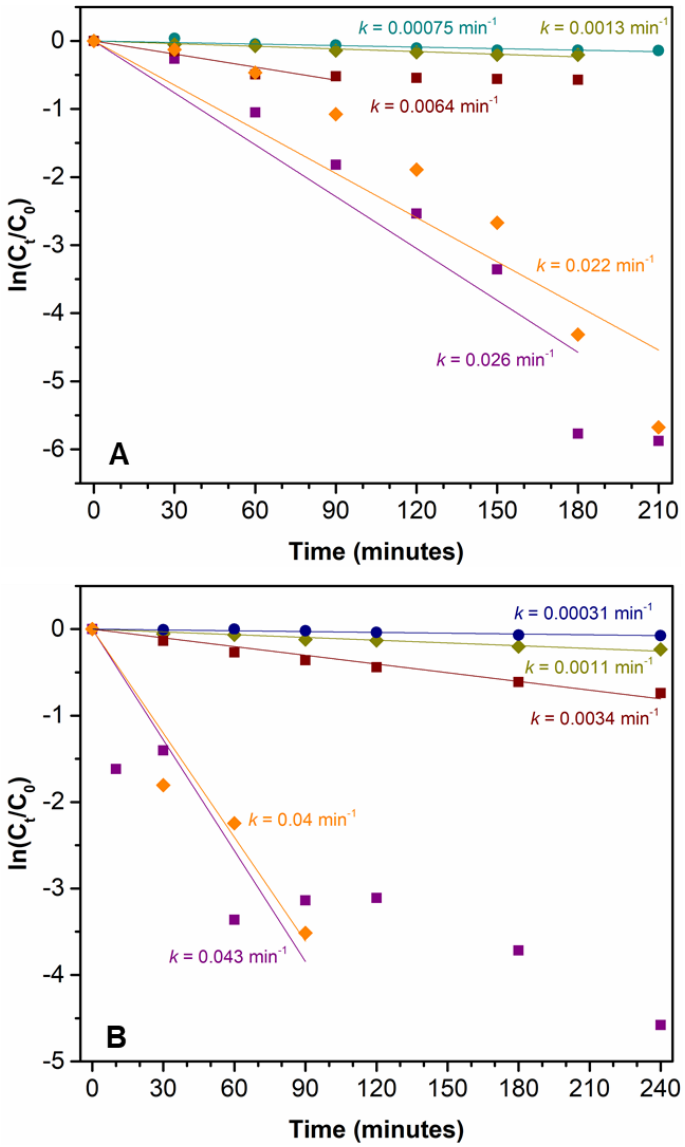


**Figure III.13**: Pseudo-first-order kinetic fitting plots for the photocatalytic removal of RhB (A) and SMX (B) with GO (●), CuS particles (◆) and CuS@GO (■) in absence of $H_2O_2$; GO (●), CuS particles (◆) and CuS@GO (■) with 1% of $H_2O_2$.

**Table III.2**: RhB and SMX degradation (%) obtained after 210 and 240 minutes of photocatalytic reaction (calculated by **Equation III.1**) and determined kinetic rate constant ($k$ – $min^{-1}$) of pseudo-first order with the respective $r^2$ values.

| Material | RhB degradation (%) | $k$ ($min^{-1}$) ($r^2$) | SMX degradation (%) | $k$ ($min^{-1}$) ($r^2$) |
|---|---|---|---|---|
| **CuS** | 19 | 0.0013 (±0.987) | 21 | 0.011 (±0.987) |
| **CuS@GO** | 43 | 0.0064 (±0.969) | 52 | 0.0034 (±0.989) |
| **CuS (w/ 1% $H_2O_2$)** | 99 | 0.022 (±0.936) | 97 | 0.04 (±0.981) |
| **CuS@GO (w/ 1% $H_2O_2$)** | 99 | 0.026 (±0.953) | 99 | 0.043 (±0.901) |

The inspection of the UV/VIS spectra (**Figure III.14**) of the supernatant solutions from RhB photocatalytic reactions in the presence of CuS@GO photocatalyst, in absence and presence of $H_2O_2$, show that the maximum absorption at 554 nm decreased in both cases with increasing irradiation time. In the absence of $H_2O_2$ (**Figure III.14**-A), the decrease of the corresponding maximum absorption was much lower without appearance of other absorption features. Nevertheless, in the presence of $H_2O_2$ (**Figure III.14**-B), the characteristic absorption band of RhB was slightly blue-shifted from 554 nm to 545 nm, along with a significant decrease in the absorbance in the first 90 minutes, being almost vanished after 180 minutes of visible-light irradiation.

A similar blue-shift was reported for the oxidation of RhB using similar photocatalysts, which was associated to the removal of the *N*-ethyl group in the degradation of RhB (*N*,*N*,*N*',*N*'– tetra-ethylated rhodamine).[274] These results indicate that the CuS@GO/LED/$H_2O_2$ system comprise the optimal conditions for the photodegradation of RhB, among those investigated here.

The photodegradation mechanism was found to occur through $^{\bullet}OH$ formation, as observed previously in similar conditions.[274] When the photocatalytic reaction was performed in the presence of *tert*-butanol, a $^{\bullet}OH$ scavenger, only 15% of RhB was removed, suggesting that the photodegradation proceed mainly *via* a $^{\bullet}OH$ mechanism. In general, the first step involves the generation of $^{\bullet}OH$ due to the presence of $Cu^{2+}$ ions through a Fenton-like process.

In summary, both CuS@GO and CuS particles demonstrated excellent adsorption and photocatalysis performance, and it is proposed that the amount of RhB and SMX decreases in a first stage due to adsorption on the suspended particulates and then the photodegradation occurs according to the process and in the conditions described above.

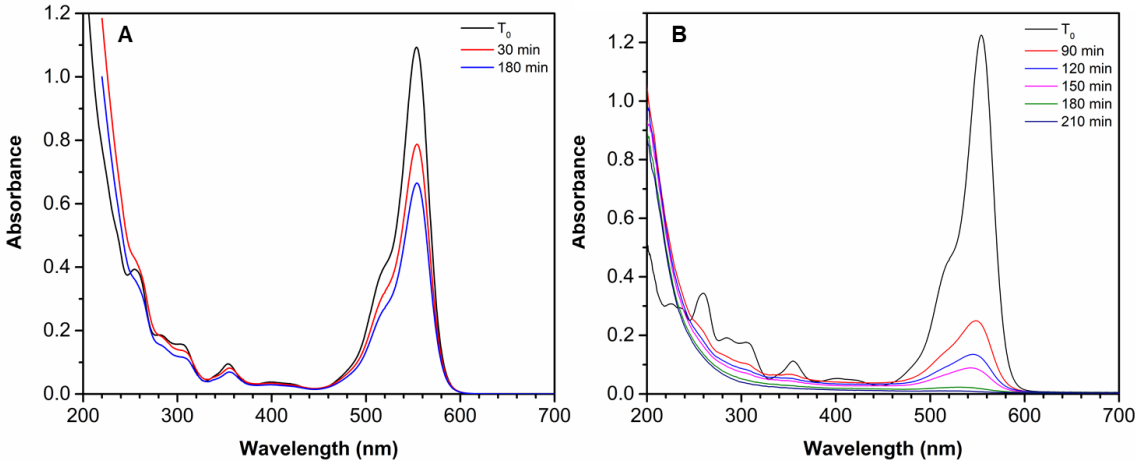


**Figure III.14**: UV/VIS absorption spectra of the RhB 20 mg/L in the presence of CuS@GO photocatalyst, in absence of $H_2O_2$ (A) and presence of $H_2O_2$ (B).

### *3.1.3. Magnetic graphene oxide-supported CuS materials*

The separation and recovery of CuS-based photocatalysts after water treatment might be a difficult task, involving laborious and high costs in real applications. Among the methods of separation of the photocatalysts from the reacting medium, the coupling of CuS-based photocatalysts with $Fe_3O_4$ nanoparticles appear as particularly relevant due to their tunable magnetic properties and eco-friendly nature.[247–249] The magnetic photocatalysts can be easily recovered from the treated water by applying an external magnetic gradient, in principle with no need for further downstream treatment processes. Having this in mind, in this research, surface-modified GO flakes with magnetic properties were first produced and then decorated with CuS particles. In a first step, ferrimagnetic nanoparticles of $Fe_3O_4$ were produced by the oxidative hydrolysis of iron(II) sulfate under alkaline conditions.[346] The particles obtained by this method present spheroidal shape with an average size of (37.5 ± 7.5) nm, as indicated by the TEM image and respective particle size histogram (**Figure III.15**-a). Herein, the ensuing colloidal $Fe_3O_4$ nanoparticles were used to produce GO flakes with magnetic properties ($Fe_3O_4$@GO) using an electrostatic assembly method. Hence, the $Fe_3O_4$ nanoparticles were treated with $HNO_3$ to generate a positive surface charge over the colloidal particles, that promote the electrostatic interaction with GO flakes having a negative surface charge due to the presence of ionizable oxygen functional groups. The attached $Fe_3O_4$ nanoparticles maintained their spherical morphology but with a slight increase on the average particle size, (43.4 ± 7.3) nm after their coupling to the GO flakes by using the respective colloidal aqueous suspensions (**Figure III.15**-b).

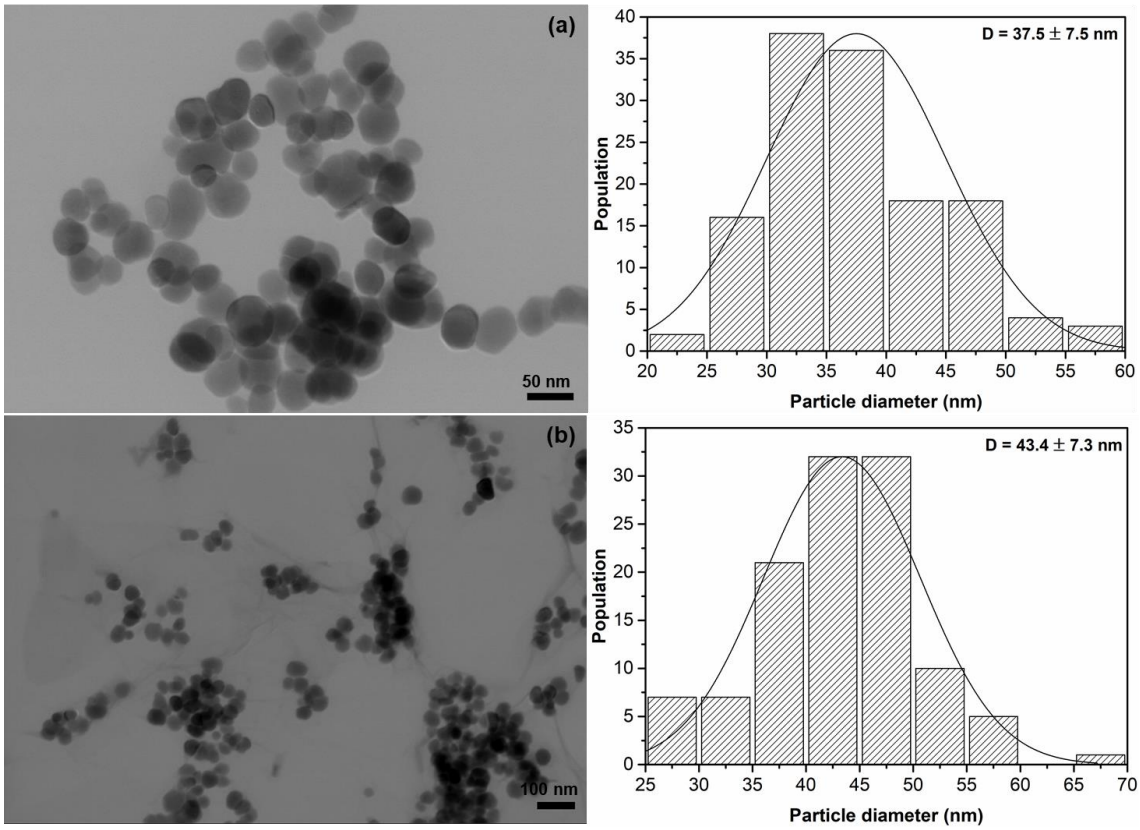


**Figure III.15**: TEM images of $Fe_3O_4$ nanoparticles (a) and $Fe_3O_4$@GO flakes (b) with the respective particle size histograms for $Fe_3O_4$ nanoparticles shown on the right.

The Raman spectrum of the $Fe_3O_4$@GO flakes (**Figure III.16**) shows the G and D1 bands characteristics of GO at 1590 and 1350 $cm^{-1}$, respectively. In addition, the intense band at 670 $cm^{-1}$ is related to the symmetric stretching of the Fe-O bond of the $Fe_3O_4$ particles.[366,367] However, the two bands at 345 $cm^{-1}$ and 715 $cm^{-1}$ suggest the presence of maghemite ($Fe_2O_3$) particles, which can be the result of the partial oxidation of the $Fe_3O_4$ particles due to the laser power used during the analysis.[368,369]

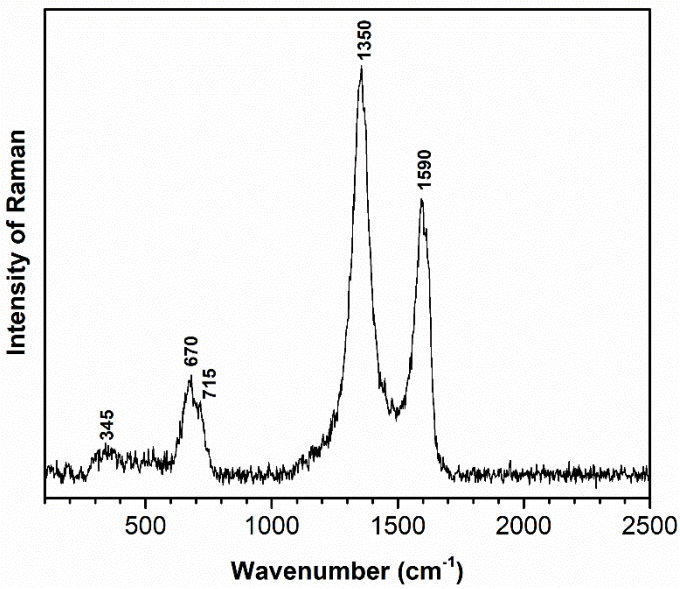


**Figure III.16**: Raman spectrum of a solid sample containing $Fe_3O_4$@GO flakes.

The $Fe_3O_4$@GO flakes were used here as substrates for the growth of the CuS particles through the single-source chemical route described above. The powder XRD patterns of the $Fe_3O_4$@GO and CuS-$Fe_3O_4$@GO are shown in **Figure III.17**. The broad peak centred at $2\theta \approx 10.3^o$ corresponds to the (001) reflection with a 0.86 nm interlayer distance of the GO sheets. The powder XRD patterns of the $Fe_3O_4$@GO flakes and the CuS-$Fe_3O_4$@GO material clearly show $2\theta$ peaks at 30.2°, 35.6°, 37.2°, 43.3°, 53.7°, 57.2°, 62.8° and 90.1° matching the crystalline planes (220), (311), (222), (400), (422), (511), (440) and (731) of the cubic spinel structure of $Fe_3O_4$ and in good agreement with the ICDDPDF No. 01-084-2782 (**Appendix D**, **Annex 5**). For the CuS-$Fe_3O_4$@GO, the powder XRD patterns assigned to the CuS appear broad, in agreement with the presence of nanosized particles. Consequently, the CuS-$Fe_3O_4$@GO material shows a broad feature at $2\theta$ = 26-34° related to (100), (101), (102), (103), (006) reflections, and a broad peak at $2\theta$ = 47-48° assigned to (107) and (110) reflections of the CuS hexagonal phase (**Appendix D**, **Annex 4**). After deposition of the CuS particles, the intensity of the GO peak at $2\theta \approx 10.3^o$ decreases drastically due to the attachment of particles onto GO.[316]

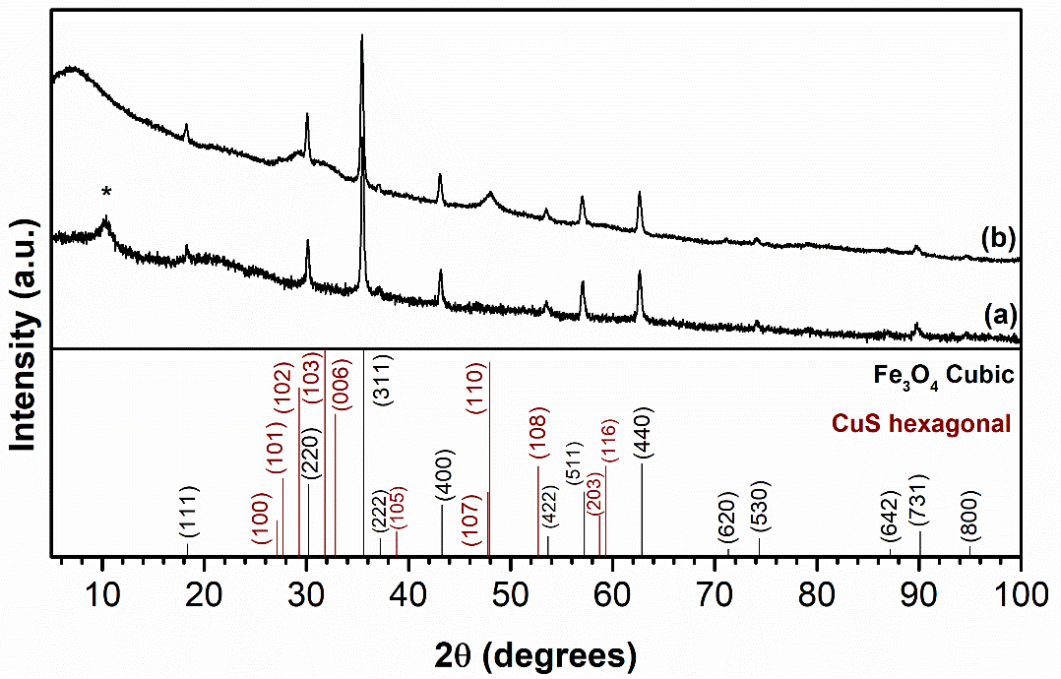


**Figure III.17**: Powder XRD patterns of $Fe_3O_4$@GO (a) and CuS-$Fe_3O_4$@GO (b). The vertical lines correspond to the standard diffraction peaks attributed to the cubic phase of $Fe_3O_4$ (ICDDPDF No. 01-084-2782) and the hexagonal phase of CuS (ICDDPDF No 00-006-0464). The diffraction peak assigned to GO are marked with *.

The powder XRD pattern of the CuS-$Fe_3O_4$@GO sample pose some difficulty in clearly stating the presence of CuS particles at the surface of the $Fe_3O_4$@GO flakes, namely due to peak broadening as consequence of nanosized crystallites (CuS needle-like nanoparticles) and also because of the higher crystallinity of the $Fe_3O_4$ phase, also present in the same material. Nevertheless, the presence of CuS particles in the tri-component structures was further confirmed by TEM. **Figure III.18** shows the TEM image in which the CuS particles appear with the expected flower-like morphology and the $Fe_3O_4$ nanoparticles retain their spheroidal-like morphology and the average particle size. In brief, the synthesis of the tri-component CuS-$Fe_3O_4$@GO did not result in significant morphological changes on the metal sulfide and metal oxide particles, as compared to the synthesis of the respective single and binary components.

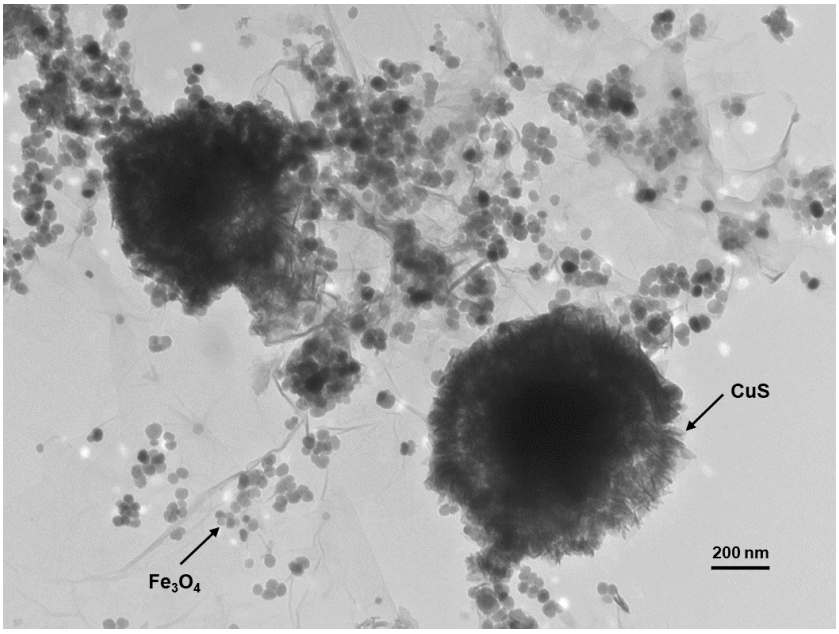


**Figure III.18**: TEM image of the tri-component material CuS-$Fe_3O_4$@GO, evidencing the spheroidal $Fe_3O_4$ particles and the flower-like CuS particles, over the GO sheets.

Although preliminary photocatalytic studies were performed using these magnetic tri-component materials for the photodegradation of SMX, there was a systematic discrepancy in the adsorption and photocatalytic removal values between several replicate experiments. The nature of the material requires mechanical stirring to ensure the dispersibility of the particles in the reaction medium. In addition, the loading of CuS particles in the CuS-$Fe_3O_4$@GO (1.75 mmol/g) is lower than the CuS@GO material (2.10 mmol/g), which might have influenced the quality of the results. Having this in mind, further studies should be performed using these materials, ensuring the adequate experimental conditions.

## 3.2. S-doped graphene-supported CuS photocatalysts

### *3.2.1. Synthesis and characterization of the materials*

To overcome limitations associated with the aggregation and photo-oxidation of metal sulfide phases, an alternative strategy was developed that comprises the doping of graphene with non-metals atoms, such as sulfur. Several studies have demonstrated that by doping graphene with heteroatoms with distinct electronegativity with respect to carbon atoms into $sp^2$-hybridized carbon frameworks, the physical and chemical properties can be modified.[370–372] Furthermore, this research allows to demonstrate the versatility of the method developed for the CuS photocatalysts by applying it to other types of graphene-based materials.

Herein, the S-graphene was prepared through the mechanochemical method - *ball milling* - using a dopant agent without any solvent, which allowed a green doping process and typically has the additional advantage of introducing defects in graphene lattice, which can act also as active sites for pollutant adsorption.[373]

The crystalline structure of the investigated materials was analysed by powder XRD (**Figure III.19**). The powder XRD pattern of S-graphene shows three peaks at 26.1°, 42.7° and 53.9°, which are characteristic of graphene and ascribed to the refractive Miller indices (002), (100) and (004), respectively (ICDDPDF No. 04-013-0293 in **Appendix D**, **Annex 6**).[374] The interlayer spacing was determined by applying Bragg's law to the (002) plane, giving 0.34 nm both for S-graphene and pristine graphene, proving the preservation of the original graphene structure during the doping process.

The powder XRD patterns of $Fe_3O_4$, $Fe_3O_4$@S-graphene and CuS-$Fe_3O_4$@S-graphene nanocomposites show reflections at $2\theta \approx 30.2°$, 35.5°, 43.3°, 53.7°, 57.2° and 62.8°, which are attributed to the (220), (311), (400), (422), (511) and (440) diffraction planes of $Fe_3O_4$, respectively (**Appendix D**, **Annex 5**). The powder XRD patterns indicate a crystalline cubic inverse spinel structure for the $Fe_3O_4$ nanoparticles, which is preserved in the nanocomposites. The XRD patterns of CuS and CuS@S-graphene show peaks at $2\theta \approx 29.3°$, 32.1°, 47.9° and 58.8°, which are ascribed to the diffraction planes (102), (103), (110) and (116) of covellite (**Appendix D**, **Annex 4**). These peaks are not noticed in the XRD pattern of CuS-$Fe_3O_4$@S-graphene, perhaps due to the overlapping of the $Fe_3O_4$ peaks. The intensity of the diffraction peak at 26° (attributed to S-graphene) decreases significantly after deposition of the metal oxide/sulfide, due to the attachment of nanoparticles onto S-graphene which may avoid the restacking of suspended graphene sheets.[219]

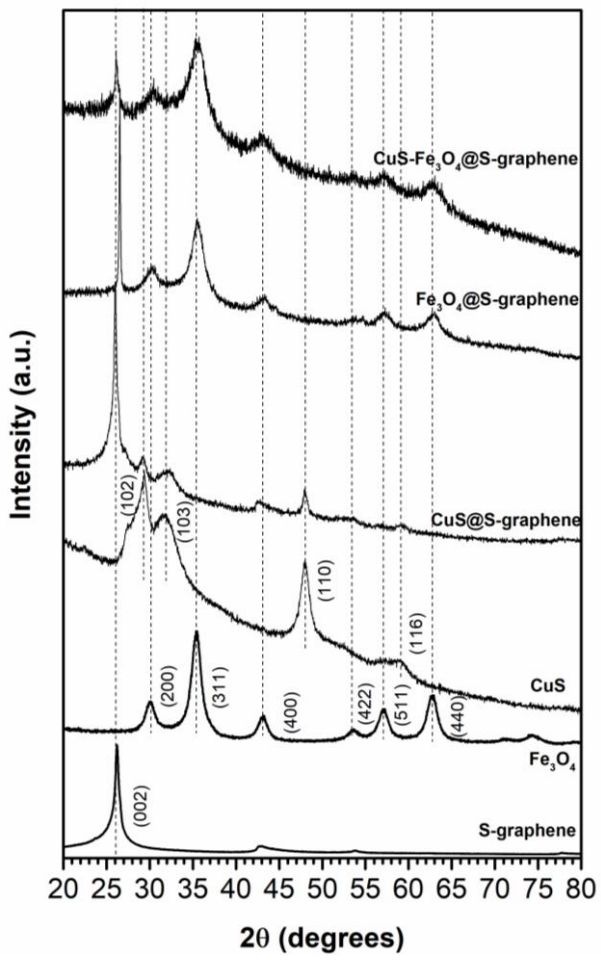


**Figure III.19**: Powder XRD patterns of the prepared materials, S-graphene, pure $Fe_3O_4$ and CuS particles, CuS@S-graphene, $Fe_3O_4$@S-graohene and CuS-$Fe_3O_4$@S-graphene. The vertical lines correspond to the standard diffraction peaks attributed to the hexagonal phase of graphite (ICDDPDF No. 04-013-0293), to the cubic phase of $Fe_3O_4$ (ICDDPDF No. 01-084-2782) and to the hexagonal phase of CuS (ICDDPDF No 00-006-0464).

The mean crystallite size of the $Fe_3O_4$ nanoparticles calculated from the half-width of the diffraction peaks and according to the Scherrer equation[375] was 9.9 nm and decreased to 5.6 and 5.1 nm for the $Fe_3O_4$ nanoparticles incorporated on the $Fe_3O_4$@S-graphene and CuS-$Fe_3O_4$@S-graphene, respectively. For pristine CuS particles, the mean crystallite size of 7.4 nm was determined, which slightly decreased for 6.7 nm for CuS on CuS@S-graphene. These values are calculated for the (311) reflection for $Fe_3O_4$, and (110) crystalline plane for CuS. These results suggest that the use of S-graphene (and CuS@S-graphene) as support, combined with the monoisopropanolamine (MIPA) mediated $Fe_3O_4$ co-precipitation method, is a valuable strategy to limit the nanoparticles growth and to avoid the aggregation of the structures.

The morphology of the pristine S-graphene sheets, CuS@S-graphene and CuS-$Fe_3O_4$@S-graphene was evaluated by TEM (**Figure III.20**).

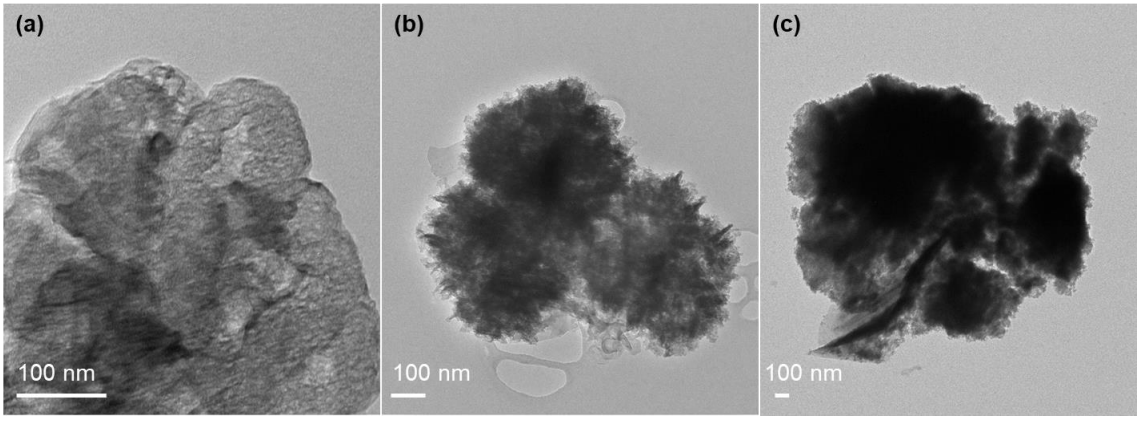


**Figure III.20**: TEM images of S-graphene (a), CuS@S-graphene (b) and CuS-$Fe_3O_4$@S-graphene (c).

The TEM image of the S-graphene sample (**Figure III.20**-a) shows graphene sheets, whose size is in the range of hundreds of nanometers to few micrometers, similarly to pristine graphene.[376] The TEM image of the CuS@S-graphene (**Figure III.20**-b) shows spheroidal particles of about 250 nm, with an acicular surface texture, dispersed over the S-graphene sheets. The image of the CuS-$Fe_3O_4$@S-graphene nanocomposite (**Figure III.20**-c) shows the respective nanoparticles loaded on the graphene sheets, especially on the more reactive graphene edges. Although the CuS particles were not detected by powder XRD, their presence is confirmed by the typical flower-like morphology observed in the TEM images.

### *3.2.2. Photocatalytic performance of S-doped graphene-supported CuS photocatalysts*

The photocatalytic activity of the as-prepared materials was evaluated towards the removal of 4-NP. 4-NP is widely used in the production of pesticides and dyes and can be commonly found in wastewaters of agricultural and industrial zones.[377,378] According to the Environmental Protection Agency[379], 4-NP was classified as a priority pollutant due to its high toxicity (even at low concentrations) and persistence in the environment (due to its high stability, water solubility and resistance to the conventional treatment methods), allied to its carcinogenic and mutagenic potential effects to human and wildlife.[378,380–382] It was found that only 2% and 12% of 4-NP was degraded/removed in the presence of either $H_2O_2$ alone or UV-light (photolysis), respectively, after 180 minutes (**Figure III.21**). However, was observed a slight synergy effect between $H_2O_2$ and the UV-light, which leads to slightly higher values of 4-NP degradation/removal (24%).

The photocatalytic degradation of 4-NP using the as-prepared materials are depicted in **Figure III.22**-A. Overall, the nanocomposites exhibited higher photocatalytic performances than the individual counterparts, which suggest a positive synergistic effect between the several components. This effect is distinctly clear for the CuS-$Fe_3O_4$@S-graphene photocatalyst, showing 20% and 32%

increase in the 4-NP degradation when compared with the CuS@S-graphene and $Fe_3O_4$@S-graphene structures, respectively, and 41% and 55% increase in comparison with the pristine $Fe_3O_4$ nanoparticles and S-graphene, respectively. The synergistic effect of Cu and Fe species for organic pollutant degradation by Fenton-like heterogeneous processes is well-known[383–388], as well as the interaction between graphene and $Fe_3O_4$ nanoparticles[389–391] or graphene and CuS.[280] According with these results, the presence of CuS particles seems to have a significant role in the 4-NP degradation, improving the catalyst performance when compared with the $Fe_3O_4$ nanoparticles, as revealed by the comparison of the CuS@S-graphene and $Fe_3O_4$@S-graphene photocatalytic activities (77% vs. 63%, respectively).

The kinetic profiles of the 4-NP degradation using the prepared photocatalysts are shown in **Figure III.22**-B. In the experimental conditions used, the $H_2O_2$ was in large excess in the reaction medium compared with 4-NP, whereby it was assumed that its concentration remained constant through all the reaction. Therefore, the 4-NP photocatalytic degradation was assumed to be a pseudo-first order reaction,[392,393] and the kinetic rate constant values, *k*, (**Table III.3**) were calculated from the slopes of the plots $ln(C_{4\text{-NP},t} / C_{4\text{-NP},t0})$, where $C_{4\text{-NP},0}$ and $C_{4\text{-NP},t}$ are the initial and remaining concentrations of 4-NP, at different irradiation time (t), respectively. All the photocatalysts presented a good linear relation confirming that the experimental data match a pseudo-first order kinetics.[394] The determined *k* values increased as follows: S-graphene (0.0006 $min^{-1}$) < CuS@S-graphene (0.003 $min^{-1}$) < $Fe_3O_4$ (0.004 $min^{-1}$) < $Fe_3O_4$@S-graphene (0.005 $min^{-1}$) < CuS-$Fe_3O_4$@S-graphene (0.016 $min^{-1}$), which indicates that the tri-component photocatalyst results in an improved photocatalytic performance under the studied conditions.

The stability of the most promising catalyst, CuS-$Fe_3O_4$ @S-graphene was assessed in a second photocatalytic cycle (**Figure III.22**-C). The catalyst did not lose photocatalytic activity during the second cycle, suggesting a good stability. The 4-NP degradation obtained after 180 minutes in the second cycle was 96% vs. 95% obtained in the first cycle. The obtained profiles indicated that the catalyst could have a slower performance at the beginning of the reutilization cycles probably due to an activation step, but this is recovered over the progress of the reaction.

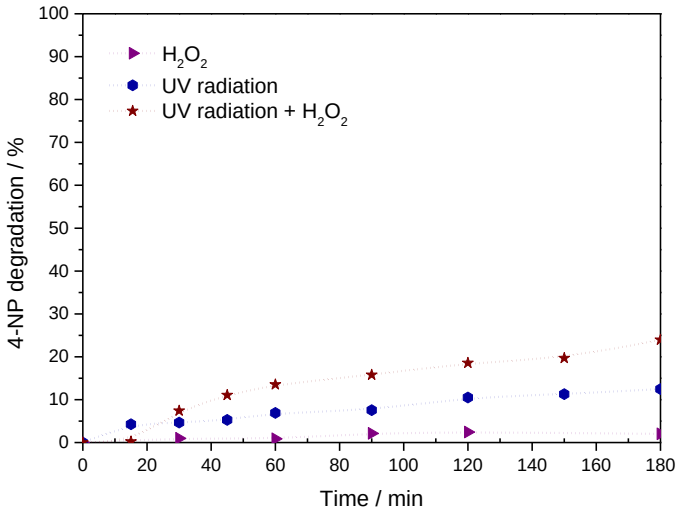


**Figure III.21**: Control assays for 4-NP degradation using UV radiation and UV radiation with $H_2O_2$ in the absence of catalyst. (Courtesy of Prof. Cristina Freire research group[345]).

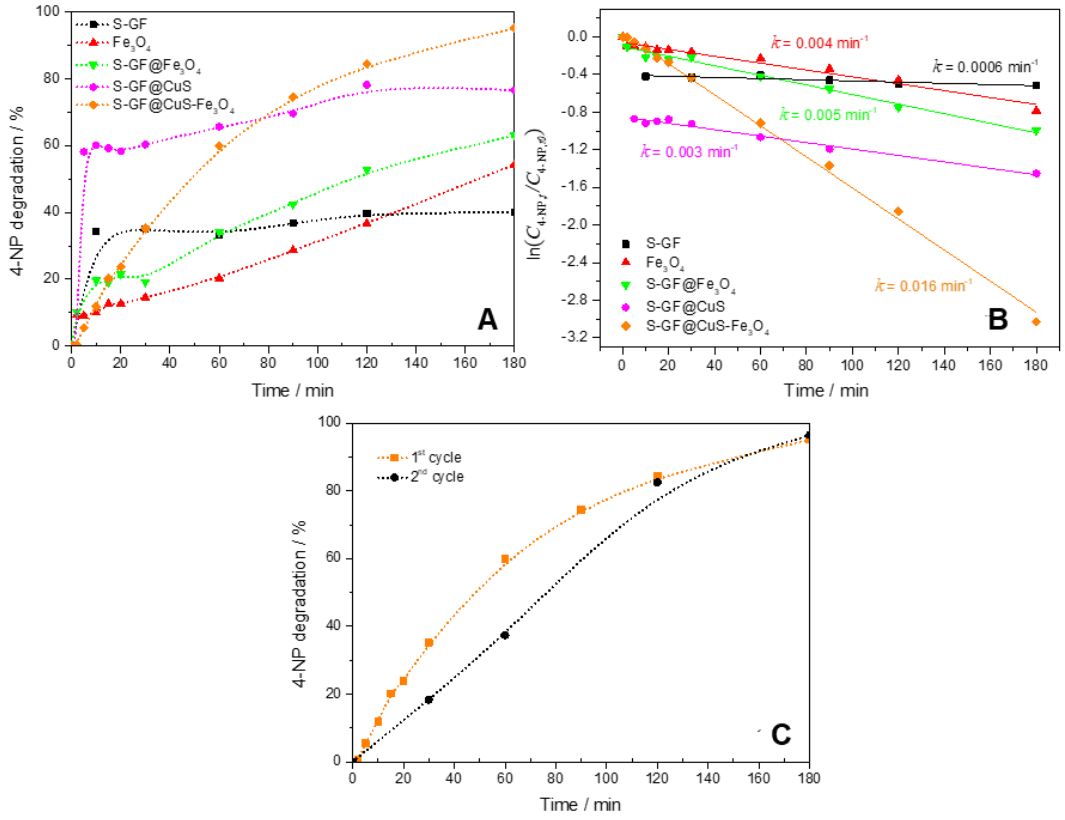


**Figure III.22**: Concentration of 4-NP as function of light irradiation time (A) and respective pseudo-first-order kinetic fitting plots (B), 4-NP concentration as function of light irradiation time after two consecutive cycles using CuS-$Fe_3O_4$@S-graphene photocatalyst. Conditions: 20 mg of catalyst, 4-NP 0.05 mM, $H_2O_2$ 0.25 M. (Courtesy of Prof. Cristina Freire research group[345]).

**Table III.3**: 4-NP degradation (%) obtained after 180 minutes of photo-Fenton catalytic reaction and determined kinetic rate constant ($k$ – $min^{-1}$) of pseudo-first order with the respective $r^2$ values. (Courtesy of Prof. Cristina Freire research group[345]).

| Material | 4-NP degradation (%) | $k$ ($min^{-1}$) ($r^2$) |
|---|---|---|
| **S-graphene** | 40.0 | 0.0006 (±0.713) |
| **$Fe_3O_4$** | 54.4 | 0.004 (±0.964) |
| **$Fe_3O_4$@S-graphene** | 63.0 | 0.005 (±0.972) |
| **CuS@S-graphene** | 76.6 | 0.003 (±0.979) |
| **CuS-$Fe_3O_4$@S-graphene** | 95.2 | 0.016 (±0.997) |

# 4. Conclusions

In summary, CuS nanoflower-like structures supported on GO sheets were successfully prepared *via* a one-step synthesis using a single-molecule source for the CuS particles. The CuS particles have the hexagonal crystalline structure of covellite and were found as pure phases evenly distributed on the GO sheets.

The as-prepared pure CuS particles and CuS@GO materials have proved to be efficient adsorbents and photocatalysts towards the photodegradation of RhB and SMX dissolved in aqueous solutions. Nevertheless, the photocatalytic activity was significantly improved in the presence of $H_2O_2$, with almost complete degradation of RhB (after 180 minutes of irradiation) and SMX (after 90 minutes of irradiation) using both CuS and CuS@GO photocatalysts. The synergy between the presence of $H_2O_2$ and visible-light irradiation should be responsible for the higher photocatalytic performance of both materials.

As a strategy to improve the recovery and reusability of the prepared photocatalysts, magnetic GO flakes were prepared. This material, $Fe_3O_4$@GO, was further used for the deposition of CuS particles by the same chemical route established, originating a tri-component material, CuS-$Fe_3O_4$@GO with both CuS and $Fe_3O_4$ particles dispersed over the GO sheets. However, further studies involving the photocatalytic performance of this material need to be addressed.

The one-step synthesis established can be applied to other graphene-based materials. Thereupon, CuS particles were deposited on S-graphene flakes. The combination of CuS and/or $Fe_3O_4$ nanoparticles with S-graphene resulted in a positive synergistic effect, leading to an improved catalytic activity. The photocatalyst demonstrated to be active and reusable; in fact, after the first catalytic cycle was registered almost complete mineralization of 4-NP and a stable catalytic performance after a second cycle.

# CHAPTER IV

## *Surface enhanced Raman scattering due to a synergistic effect in ZnS and graphene oxide*

In this work, it is demonstrated that surface enhanced Raman scattering can be easily explored to probe a semiconductor (ZnS) dispersed over graphene oxide sheets, using a Raman reporter, such as 4-mercaptopyridine.

# CHAPTER IV | "Surface enhanced Raman scattering due to a synergistic effect in ZnS and graphene oxide"

Graphene oxide (GO) has been widely explored as a platform for producing hybrid materials exhibiting synergistic properties of interest in heterogeneous (photo)catalysis. However, there has been less emphasis in demonstrating that such properties are intrinsic to the nature of the hybrid material, which in some extent can be attributed to the lack of straightforward screening techniques. In this work, surface enhanced Raman scattering (SERS) can be easily explored to probe certain regions of GO sheets decorated with a semiconductor (ZnS). In particular, these studies reveal an enhancement of the Raman signal of 4-mercaptopyridine (4-MPy), which was used as a molecular probe, upon adsorption on ZnS@GO materials when compared to adsorption on the separated parent ZnS powders or GO flakes. The GO sheets in the composite play an important role for the enhancement of the Raman signal observed for this molecular probe because they create resonant energy levels within the ZnS gap. This hypothesis was further confirmed by electronic density functional theory (DFT) calculations employed to investigate the adsorption mechanism of 4-MPy on both ZnS and ZnS@GO substrates. The calculated results are in accordance with the experimental data, predicting the adsorption mode on both S and Zn surface sites, with preference towards the sulfur atom due to the influence of GO. [4]

*Keywords*: zinc sulfide nanoparticles; graphene oxide; Raman spectroscopy; SERS; DFT.

[4] This chapter is based on the work: Joana L. Lopes, Sara Fateixa, Ana C. Estrada, José D. Gouveia, José R. B. Gomes, Tito Trindade*. Surface-enhanced Raman scattering due to a synergistic effect on ZnS and graphene oxide*. **2020**, J. Phys Chem C. 124, 12742-12751. (DOI: 10.1021/acs.jpcc.0c02135)

Joana L. Lopes performed the main experimental tasks concerning the synthesis and characterization of the materials. Sara Fateixa provided assistance to Raman imaging. Ana C. Estrada contributed to material characterization and supervised the laboratorial work. José D. Gouveia and José R. B. Gomes were involved with the DFT calculations and with the analyses of the calculated data. Tito Trindade planned and supervised all the research. All authors wrote the main manuscript text and prepared the figures.

# 1. Introduction

Hybrid nanostructures exhibiting photocatalytic properties and *in situ* sensing capabilities have been of recent great interest.[155,395–397] These multifunctional materials are not only of intrinsic concern for fundamental studies of photo-driven mechanisms but might also find application in environmental remediation nanotechnologies, such as the one-step detection-photodegradation of organic contaminants dissolved in water supplies. The design of such hybrid nanostructures has been accomplished using distinct materials but generally relies on the use of a semiconducting nanophotocatalyst and a plasmonic nanometal.[398] While the former provides a surface for the catalytic process, the latter allows the detection of metal adsorbates through SERS. The application of this concept to other types of hybrid nanostructures has been less explored, which can be explained to some extent by the difficulty in studying both functionalities using other classes of materials.

GO has been investigated as an heterogeneous substrate in a number of applications, including solar cell applications,[396,399] sensors,[400] drug delivery[401–403] and tissue engineering.[404–406] Also, its versatility as a scaffold for the development of supported catalysts has to be highlighted, which is due to its high specific surface area, good mechanical strength, potential chemical functionalization and straightforward dispersion in aqueous medium.[106] These features are particularly relevant for the development of solar light photocatalysts based on GO sheets decorated with semiconductor nanophases, such as metal oxides[397,407–410] and metal chalcogenides[203,296–298,304,308] Despite these prospects, there is a general lack of understanding of the surface phenomena that mediate the photocatalytic process using such hybrid materials. In this regard, the development of spectroscopic tools that allow to probe local environments over GO photocatalysts appears as a step forward to obtain new insights about the surface of these materials.

SERS has been extensively used to probe the adsorption behaviour of organic compounds over nanoscale roughened metal surfaces, metal-based composites or metal nanojunctions.[411–413] This is because the Raman signals due to very diluted organic adsorbates are strongly enhanced at the vicinity of such metal surfaces, thus allowing to obtain spectroscopic information that otherwise would not be collected in the absence of the metal due to relatively low Raman signal intensity. Silver and gold substrates have been the elected materials for these purposes, due to concomitant strong SERS signals that arise as a combination of plasmonic and surface charge-transfer complex effects.[414,415] Although less explored, the observation of semiconductor SERS substrates might provide a wealth of information concerning the adsorbed species.[416–418] In addition, provided adequate substrates are employed, the SERS effect can be explored together with Raman confocal microscopy to investigate the surface of the substrate by imaging areas in which molecules of a selected probe are adsorbed.[419–422] In this research, the SERS effect observed in GO substrates decorated with semiconducting nanophases was determinant for imaging the surface of such hybrid materials. Aligned with this objective, to the best of our knowledge, this was the first report of surface imaging

of a GO-based photocatalyst using as tool the combination of Raman confocal microscopy and SERS over a semiconductor.

# 2. Experimental

## 2.1. Chemicals

Ethylenediamine ($C_2H_8N_2$, Sigma-Aldrich, 99%), ethanol absolute (Fisher Chemical), GO aqueous suspension 2-5 mg/mL (Nanocs), 4-mercaptopyridine ($C_5H_5NS$, TCI, 97%), methanol (Fisher Chemical), sodium diethyldithiocarbamate trihydrate (($Na(S_2CN(C_2H_5)_2)\cdot 3H_2O$, Aldrich, 100%) and zinc nitrate hexahydrate ($Zn(NO_3)_2\cdot 6H_2O$, Sigma-Aldrich, 99%) were used as received. Ethanol was dried with molecular sieves (3 Å, Fluka).

## 2.2. Synthesis of ZnS nanocrystals and ZnS supported materials

First, zinc diethyldithiocarbamate ($Zn[S_2CN(C_2H_5)_2]_2$, ZnDTC) was prepared by direct precipitation from an aqueous solution containing stoichiometric amounts of $Na(S_2CN(C_2H_5)_2)\cdot 3H_2O$ (4 mmol, 0.90 g) and $Zn(NO_3)_2.6H_2O$ (2 mmol, 0.60 g). The white precipitate obtained was thoroughly washed with ethanol and collected by filtration and dried at room temperature. The identity and purity of the compound was assessed by proton nuclear magnetic resonance ($^1$H NMR) spectroscopy: ($CDCL_3$) δ (ppm): 1.33 (t, 3H, $CH_2CH_3$); 3.87 (q, 2H, $CH_2CH_3$) and elemental microanalysis (C: 33.19%; H: 5.46%; N: 7.78%; S: 50.05%).

ZnDTC was used here as a single-molecule precursor to produce either pure ZnS and GO-supported ZnS (ZnS@GO). Hence, ethylenediamine (1.5 mmol, 100 µL) was added to an ethanolic suspension (25 mL) of ZnDTC (58 µmol, 21 mg) and the resulting mixture was stirred at reflux for 3 hours. The obtained suspended powder was then collected by centrifugation (6000 rpm, 15 minutes) using an Eba 20 Hettich centrifuge and thoroughly washed with ethanol. Finally, the powder was dried at room temperature and kept under $N_2$ atmosphere.[77,219] The hybrid nanostructures ZnS@GO were prepared similarly but in the presence of GO (10 mg, 25 mL).

## 2.3. Adsorption of 4-mercaptopyridine onto ZnS materials

The different substrates (ZnS or ZnS@GO, 1 mg) were dispersed, respectively, in 1 mL of methanolic solutions containing 4-MPy at distinct concentration ($10^{-1}$ M to $10^{-5}$ M). The mixtures were stirred for 30 minutes, then the particulates were collected by centrifugation (13000 rpm, 5 minutes) and washed three times with methanol. The final powder was redispersed in 500 µL of methanol. To record the Raman spectra of 4-MPy ($10^{-1}$ to $10^{-5}$ M) adsorbed on different substrates, an aliquot (10

μL) of the respective suspension, which was prepared as above, was placed onto a glass slide. After the evaporation of the solvent, the samples were analysed by Raman spectroscopy/ Raman imaging.

## 2.4. Instrumentation

The ultraviolet/visible (UV/VIS) spectra of the ethanolic suspensions of ZnS nanocrystals, ZnS@GO were recorded using a Jasco V-560 spectrometer (Jasco Inc., Easton, MD, USA). The powder X-ray diffraction (XRD) data were collected using a PANanalytical Empyrean X-ray diffractometer (PANanalytical, Almelo, The Netherlands) equipped with Cu-Ka monochromatic radiation source at 45 kV/40 mA. The samples were prepared by the deposition of aliquots of the ethanolic suspensions of the hybrid nanostructures on a silicon holder. Elemental analysis of carbon, nitrogen and hydrogen was obtained on a Leco Truspec-Micro CHNS 630-200-200. $^{1}$H NMR spectra of zinc diethyldithiocarbamate precursor was recorded on Bruker AMX 300 spectrometer at 300.13 MHz. Chloroform ($CDCl_3$) was used as solvent and the chemical shifts are expressed in δ (ppm). For transmission electron microscopy (TEM) analysis, a drop of the suspension under analysis was placed on a carbon-coated Cu grid and the solvent was left to evaporate at room temperature. TEM was performed using a transmission electron microscope Hitachi H-9000 (Hitachi, Tokyo, Japan) operating at 300 kV. Raman spectral imaging was performed in a combined Raman-AFM confocal microscope WITec alpha300 RAS+ (WITec, Ulm, Germany) Five Raman spectra of each sample were acquired using a Nd:YAG laser operating at 532 nm as excitation source with the power set at 1 mW, with an acquisition time of 0.5s, 10 acquisitions. The objective used for Raman measurements was 100× for better laser spot area (~350 nm). The average Raman spectra were obtained for the average of the five spectra. The Raman map experiments were performed by raster-scanning the laser beam over the samples and accumulating a full Raman spectrum at each pixel. The combined Raman image was constructed with 150 × 150 points per grid in a 2500 μm$^2$, using WITec software for data evaluation and processing. The WITec software, WITec Project 5, was used to create the combined Raman image. The Raman spectra of GO and 4-MPy were used as the basis set in the analysis using the command True Component Analysis, providing the color-coded combined Raman image. The Raman images showing a color scale have been created using band integrals, in which the value of the absolute area underneath a band (e.g. 1353 cm$^{-1}$ for GO) corresponds to a color intensity in the scale, shown in the image at the respective pixels. This measurement was repeated thrice and for all the Raman maps, the same results were achieved.

## 2.5. Computational details

The bare and 4-MPy covered ZnS(110) and ZnS(110)@GO surfaces were modeled with the periodic slab approach. For the ZnS surface, it was assumed the (110) Miller index, as ZnS(110) is the most likely morphology of the surface of ZnS particles.[423] The GO sheet was modeled with a $C_2O$

stoichiometry (equivalent to 67%/ 33% carbon/ oxygen percentages) for simplicity, as it is very close to the 70%/30% ratio of the GO used in the experiments. DFT calculations were performed with the Vienna ab initio simulation package (VASP) code,[424–427] using the PBE-D3 approach,[428,429] plane-wave basis sets with a cut-off of 415 eV for the valence electrons, and projector-augmented wave (PAW) potentials[430] for the inner electrons. The HSE06 functional[431,432] was used to refine band gaps and densities of states using the PBE-D3 geometries. Additional computational details are provided in **Appendix B**.

# 3. Results and Discussion

## 3.1. Material synthesis and characterization

Nanocrystals of metal sulfides have been of great interest in semiconductor heterogeneous photocatalysis and their association to GO substrates relies in some extent on exploring synergistic effects by coupling both components.[201,310] A one-step method to produce a range of GO-based materials decorated with nanophases of metal sulfides is described in **Chapter II**.[219] This method allows the *in situ* growth of metal sulfide nanophases onto GO by using metal alkyldithiocarbamate complexes as single-molecule precursors.

For the purposes of the Raman studies reported here, ZnS was selected as the semiconducting nanophase, whose optical band gap is blue-shifted in relation to the excitation lines thus precluding fluorescence emission. **Figure IV.1** shows TEM images of GO sheets decorated with ZnS nanophases as obtained by the above method. TEM shows that at the nanoscale, the ZnS particles are distributed over the surface of GO, topped with clustered particulates in some regions of the sample, that appear as bigger structures. For comparative purposes, TEM images of ZnS powder and GO are also shown (**Figure IV.2**).

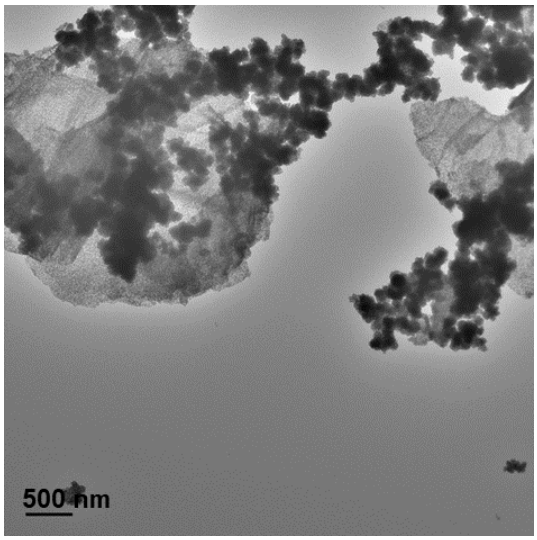


**Figure IV.1:** TEM image of ZnS@GO hybrid material.

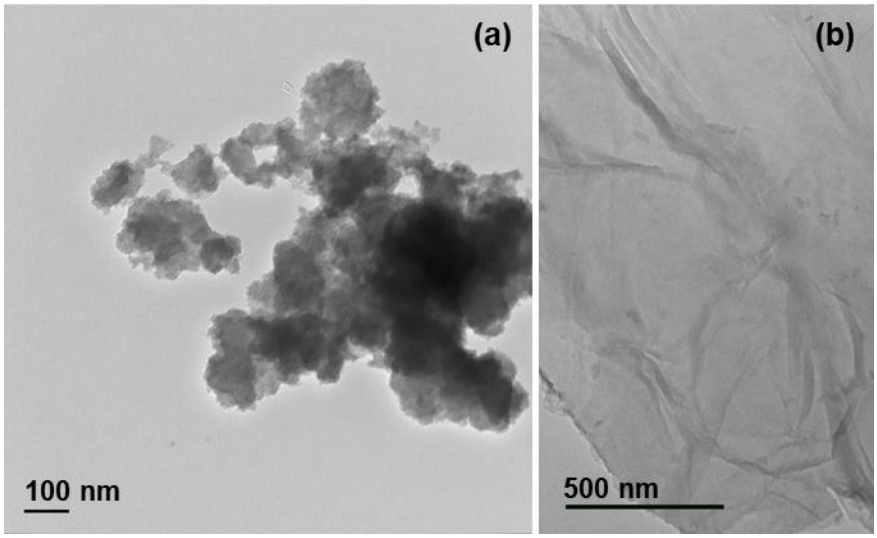


**Figure IV.2:** TEM images of pure ZnS (a) and GO flakes (b).

Powder XRD patterns confirmed the presence of cubic ZnS as the only polycrystalline phase present onto the GO substrates (**Figure IV.3**), while EDS measurements, performed on both types of particulates, showed peaks for Zn and S (**Figure IV.S1**). The diffraction peaks observed at 28.6°, 47.8° and 56.3° are in good agreement with the Bragg reflections due to the (111), (220) and (311) crystalline planes of ZnS of blende type ((ICDDPDF No. 01-071-5971 in **Appendix D**, **Annex 7**).[281] Note that the peak broadening observed in the powder XRD is consequence of the presence of very small ZnS crystallites. The optical absorption spectrum of the ZnS@GO hybrid material shows a bandgap ($E_g$ = 3.7 eV) that agrees with the reported value for macrocrystalline cubic ZnS at room temperature, thus with ZnS nanophases but not showing quantum size effects (**Figure IV.4**).[209,395]

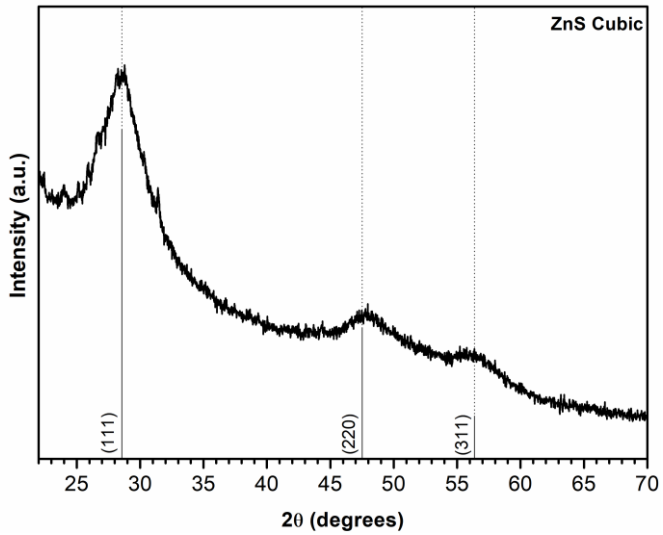


**Figure IV.3**: Powder XRD pattern of ZnS@GO hybrid material. The vertical lines correspond to the standard diffraction peaks attributed to the cubic phase of ZnS (ICDDPDF No. 01-071-5971).

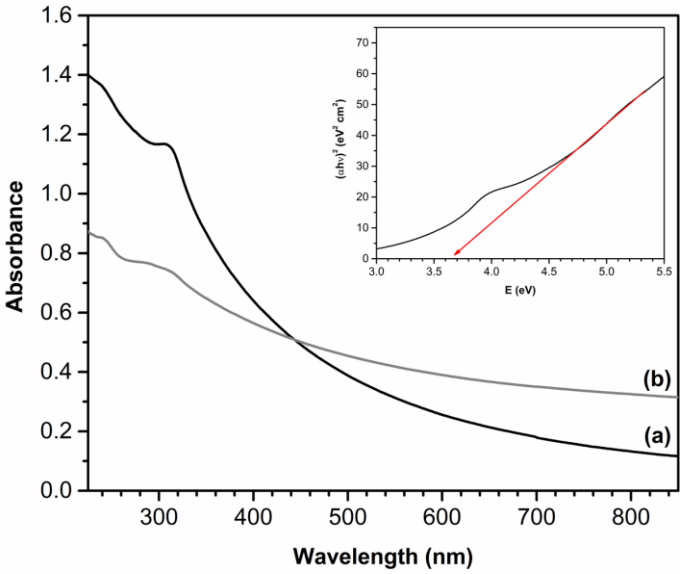


**Figure IV.4:** UV/VIS absorption spectra of ZnS nanocrystals (a) and ZnS@GO hybrid material (b). Plot of $(\alpha h\nu)^2$ vs photon energy for ZnS nanocrystals is shown in the inset.

The Raman spectra of pristine GO, ZnS@GO hybrid material and pure ZnS (**Figure IV.5**) were obtained after averaging five Raman spectra taken in different spots of the samples. The spectra of pristine GO and ZnS@GO (**Figure IV.5**-a, b) show the typical GO bands at 1350 $cm^{-1}$ (D1 band) and at 1600 $cm^{-1}$ (G band), which are assigned respectively to the $sp^3$-carbon containing moieties, due to defects introduced in the graphene lattice, and to the $sp^2$-carbons of the two-dimensional hexagonal lattice.[326] The lattice vibrational modes of ZnS have been reported as Raman shifts at 350 $cm^{-1}$ (longitudinal optical mode, LO) and at 275 $cm^{-1}$ (transverse optical mode, TO).[395,433] However, with the laser power set at 1 mW, none of these bands were observed in the ZnS@GO material, neither in a sample of pure ZnS obtained by a similar method but in the absence of the GO substrate. In order to circumvent this limitation, the use of 4-MPy for probing ZnS nanophases grown on the GO surface using Raman spectroscopic methods was investigated.

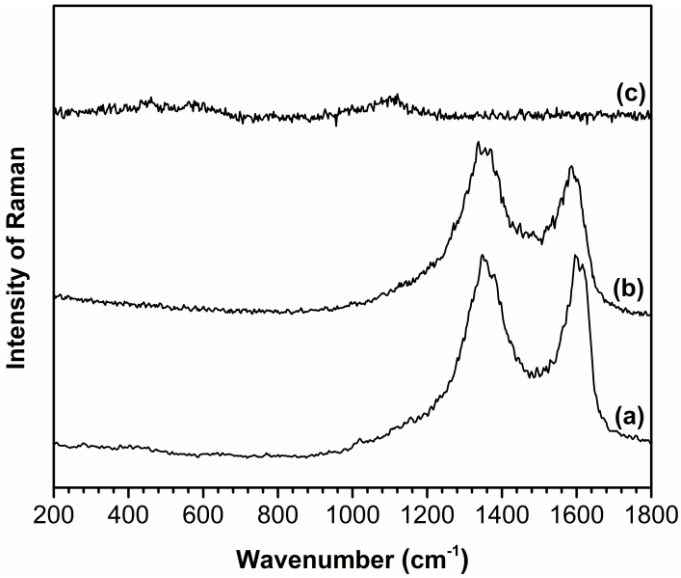


**Figure IV.5:** Average Raman spectra of GO (a), ZnS@GO (b) and ZnS (c) powders.

Wang *et al*. have reported enhancement of Raman bands for 4-MPy adsorbed onto ZnS nanocrystals and a remarkable difference in the bands' intensities, as compared with those observed in the SERS spectrum of the same analyte but using a Ag substrate.[434] Taking advantage of these observations, the ZnS@GO hybrid materials were treated with 4-MPy (molecular structure in **Figure IV.S2**) and subsequently characterized by Raman spectroscopy and Raman confocal microscopy. **Figure IV.6** shows the Raman spectra of ZnS@GO samples previously treated with 4-MPy solutions of variable concentration. For comparative purposes, the Raman spectrum of an aqueous solution of 4-MPy (0.1 M) is also shown (**Figure IV.6**-a); instead of the 4-MPy powder, because spectroscopic fingerprints due to intermolecular vibrational modes are in this case negligible. In addition, a drop of a methanolic solution containing 4-MPy (1mM) was placed on a glass slide and let it dry. In these conditions, the Raman analysis did not show any vibrational band of the analyte (data not shown), which indicates that the amount of 4-MPy deposited from a solution 1 mM is not detected by conventional Raman spectroscopy. In **Table IV.1**, the Raman bands of 4-MPy in aqueous solution have been ascribed to the respective vibrational modes based on assignments reported in the literature.[434–438] First, it should be noted that for all the samples, the Raman spectra are dominated by the bands of adsorbed 4-MPy with the exception of the spectrum shown in **Figure IV.6**-d, which corresponds to the ZnS@GO sample treated with the most diluted 4-MPy solution. In this case, the Raman spectrum shows only the GO bands at 1350 $cm^{-1}$ (D1 band) and 1600 $cm^{-1}$ (G band), because the amount of adsorbed 4-MPy is very low to allow its detection. The other spectra show significant differences in the Raman signature of 4-MPy molecules adsorbed onto the ZnS@GO surface as compared to the results obtained for a 4-MPy aqueous solution. This is a first indication that in the hybrid sample, most of 4-MPy is chemisorbed onto ZnS@GO instead of forming segregated powders over the substrates. Hence, the bands at 434 $cm^{-1}$ and 1492 $cm^{-1}$ are observed in the Raman spectrum of 4-MPy in

solution but were no longer observed in the Raman spectra of 4-MPy adsorbed on the ZnS@GO samples. On the other hand, there is strong enhancement, with concomitant downshifting of the bands at 1119 and 1627 $cm^{-1}$, assigned to the ring-breathing/(C–S) and stretching modes of the ring, respectively, and the absence of the band at 730 $cm^{-1}$ ascribed to the β(CCC)/ν(C-S) mode.

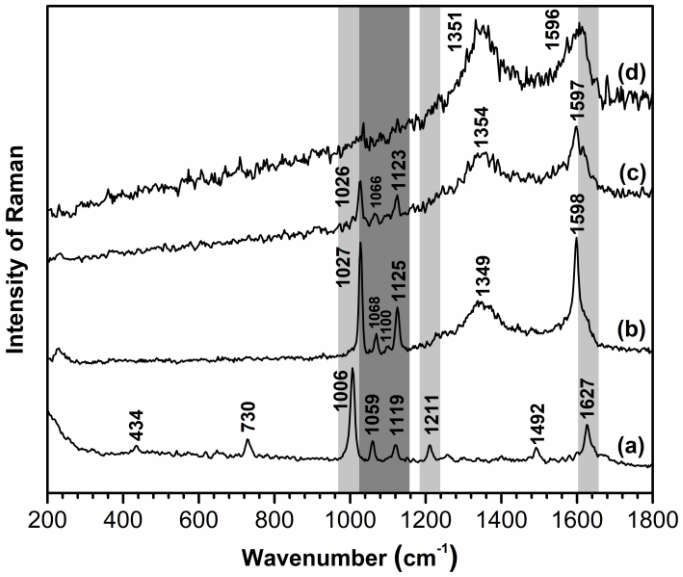


**Figure IV.6:** Raman spectrum of a 4-MPy aqueous solution (0.1 M) (a) and Raman spectra of ZnS@GO hybrid material treated with a 4-MPy solution of concentration: 1 mM (b), 100 μM (c) and 10 μM (d).

**Table IV.1:** Experimental Raman bands (wavenumber/ $cm^{-1}$) and respective assignments for 4-MPy in aqueous solution (0.1 M) and on ZnS@GO treated with 4-MPy solution (1mM).[434–438]

| **Raman band 4-MPy aqueous solution (0.1 M)** | **Raman band ZnS@GO nanostructures with 4-MPy (1 mM)** | **Assignment** |
|---|---|---|
| 434 | ----- | δ(C-S)/ γ(CCC) |
| 652 | ----- | β(CCC) |
| 730 | ----- | β(CCC)/ν(C-S) |
| 1006 | 1027 | Ring-breathing |
| 1059 | 1068 | β(CH) |
| 1119 | 1125 | Ring-breathing/C-S |
| 1211 | ----- | β(CH)/δ(NH) |
| 1492 | ----- | ν(C=C/C=N) |
| 1627 | 1598 | ν(CC) |

ν – stretching; δ – bending

Several authors have reported that the Raman band of 4-MPy at 1119 $cm^{-1}$ is particularly sensitive to chemisorption, often so-called X-sensitive mode because it is due to strongly coupled vibrational modes involving the substituent and the aromatic ring. Strong enhancement of this Raman band (1119 $cm^{-1}$) has been reported for 4-MPy chemisorbed onto metal surfaces,[439–441] as well as on semiconductors, including ZnS, CdTe and ZnO/Ag composites,[434,442,443] which was interpreted as due to coordination of 4-MPy onto surface sites through the sulfur donor atom. In addition, the bands assigned to the in-plane ring-breathing modes at 1006 $cm^{-1}$ and 1119 $cm^{-1}$ in the Raman spectrum of 4-MPy (solution) became enhanced and shifted to higher wavenumbers, respectively to 1027 $cm^{-1}$ and 1125 $cm^{-1}$, in the SERS spectrum of 4-MPy (**Figure IV.6**-b). This might be indicative of 4-MPy molecules attached to ZnS through the S atom.[435,437,442]

It has also been reported that a marked downshift of the ν(C-S) mode at 730 $cm^{-1}$ is another evidence through coordination of the sulfur atom to metal surface sites.[442] Although this has been the case for 4-MPy adsorbed onto metals,[444] a careful inspection of the Raman spectra of 4-MPy onto semiconductor substrates shows also a pronounced decrease of the respective Raman intensity or even its disappearance,[442] which is also observed in this study. On the other hand, the spectral region of the pyridine ring C=C stretching modes is very sensitive to 4-MPy N-protonation/ deprotonation.[436,438] Thus, the band observed at 1599 $cm^{-1}$ for 4-MPy molecules adsorbed onto ZnS@GO might indicate N-deprotonation, whereas for N-protonation a band at 1612 $cm^{-1}$ would be expected instead. The above discussion suggests that the 4-MPy molecules are attached to the ZnS nanophases *via* the S atoms, with the nitrogen atoms of the pyridine ring remaining non-protonated. It should be noted that the Raman spectrum of 4-MPy was recorded for an initial concentration as low as 1 mM and after the respective solution had been in contact with ZnS@GO (**Figure IV.6**-b). Indeed, the Raman signal of 4-MPy was not observed in similar experiments using neat GO substrates and pure ZnS instead of ZnS@GO (**Figure IV.7**). The results above suggest that the observation of band enhancement, in the Raman spectrum of 4-MPy adsorbed on the ZnS@GO hybrid substrate, is due to a synergistic effect that results from the presence of both GO and ZnS.

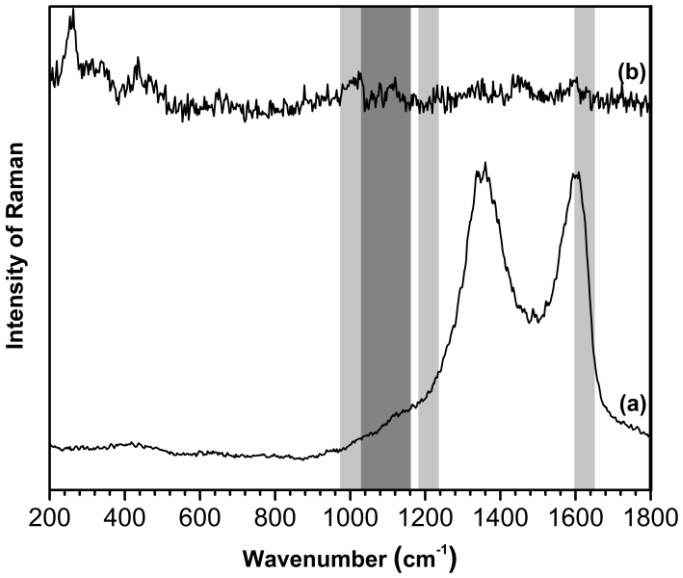


**Figure IV.7:** Average Raman spectrum of 4-MPy (1 mM) adsorbed on GO sheets (a) and on pure ZnS powder (b).

Additionally, and for comparison purposes, other hybrids containing other metal sulfides, such as $Ag_2S$@GO, $Bi_2S_3$@GO, CdS@GO and PbS@GO, were tested. TEM images of theses composites are shown in **Figure IV.S3**. Raman spectra using these composites as substrates are presented in **Figure IV.S4**. Only $Ag_2S$@GO hybrid demonstrated SERS activity towards the 4-MPy analyte at a concentration of 0.1 M, a significant lower detection limit than the one found for ZnS@GO (**Figure IV.S5**).

A charge-transfer mechanism has been used to explain Raman enhancement observed on semiconductors interacting with graphene-like substrates.[445–447] Although the theoretical framework for interpreting SERS in semiconductors is still evolving, the charge-transfer mechanism has been considered also relevant for molecules adsorbed onto semiconductor surfaces.[448] Accordingly, the molecular adsorbate on the semiconductor forms a surface complex that leads to Raman enhancement after photon incidence, because it allows photo-induced charge-transfer resonances to occur between the substrate and the adsorbed molecule. The substrates are composed of GO decorated with ZnS, that only together lead to Raman enhancement of 4-MPy present as a molecular adsorbate. Such synergistic effect likely promotes charge-transfer pathways at the interface between the ZnS@GO substrate and chemisorbed 4-MPy molecules, inducing changes on the polarizability of the adsorbed 4-MPy molecules. A plausible explanation involves the interaction of 4-MPy with ZnS through the S atoms, which results in charge-transfer assisted by electron pumping from intragap energy levels that result from the interaction of the semiconductor with GO, as schematically depicted in **Figure IV.8**.

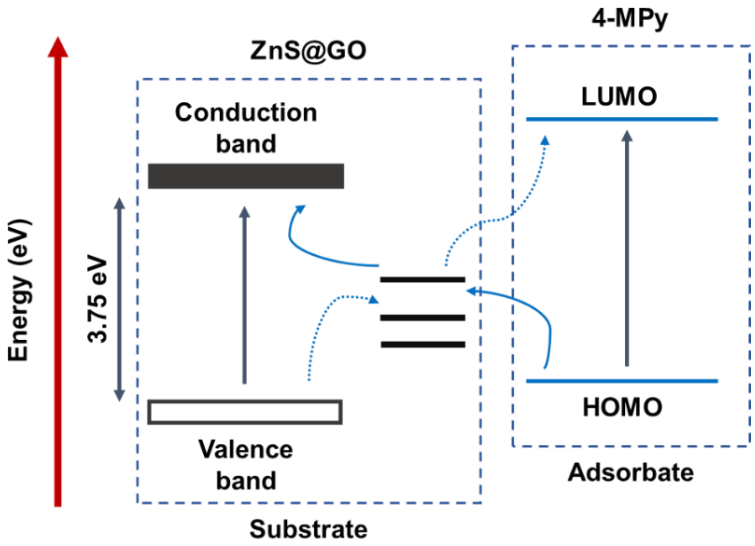


**Figure IV.8:** Schematic representation of the proposal for the charge-transfer mechanism resulting from the interaction of 4-MPy with ZnS@GO through the S atoms.

## 3.2. Density Functional Theory studies

In order to evaluate if the above hypothesis for the adsorption of 4-MPy onto ZnS is consistent with energetic criteria, DFT calculations were performed to analyze the adsorption mechanism of 4-MPy on ZnS(110) and on ZnS(110)@GO (with unit cells shown in **Figure IV.S6-S8**).

As such, it was found that the 4-MPy molecules indeed prefers to adsorb *via* its sulfur donor atom and is deprotonated in all the cases evaluated; the isolated configuration is shown in **Figure IV.S9**, the calculated vibrational spectra are shown in **Figure IV.S10**, and the frequencies of the normal vibrational modes are displayed in **Table IV.S1**. On the one hand, the molecule can only adsorb on ZnS(110) by bonding to a zinc atom on the surface, with adsorption energy $E_{ads}$ = −0.61 eV (negative $E_{ads}$ value indicates favourable adsorption; see **Appendix B**), with a S−Zn distance of 2.39 Å, comparable to the calculated bulk ZnS distance of 2.33 Å (**Figure IV.S11** and **Table IV.S2**). Bond orders (calculated using the method introduced in Ref.[449]) of 0.53 and 0.17 were found between 4-MPy and the nearest Zn and S atoms of the surface, respectively. The calculated Raman spectrum of 4-MPy adsorbed on ZnS(110) is shown in **Figure IV.S12**. On the other hand, for the ZnS(110)@GO sample, adsorption can occur either on a S atom ($E_{ads}$ = −1.01 eV) or Zn atom ($E_{ads}$ = −0.65 eV) on the surface (**Figure IV.S13**), the former being energetically advantageous by 0.36 eV, in clear contrast with the case of adsorption on ZnS(110). Although the adsorption on a Zn atom of ZnS(110)@GO yields a bond order of 0.54, very similar to the one on pure ZnS(110), the now favourable adsorption on a S atom of the surface displays a much stronger bond with the surface S atom, of order 1.13 (the bond order with the nearest Zn atom is merely 0.02). This preference for

adsorbing on a surface S atom is due to the presence of GO rather to the mechanical stress induced by the physical interaction between the surfaces.

This was confirmed by starting from the S-adsorbed configuration (**Figure IV.9**-A), deleting the GO atoms while keeping the supercell size, and optimizing the atomic positions again (**Figure IV.9**-B). After the relaxation, the molecule had moved toward a surface Zn (**Figure IV.9**-C), in a configuration similar to that adopted on pure ZnS(110), albeit with small structural differences, due to the slight disparity of lattice constants. The bond orders were also reverted to the ones found for adsorption on ZnS(110). The thickness of the considered ZnS(110) model (5 layers) was found adequate by repeating some of the calculations with 7 and 11 layers, as 10 layers were shown to be enough to describe the effects studied in Refs.[450,451] The adsorption configurations of 4-MPy on ZnS(110) or ZnS(110)@GO with 5, 7 and 11 layers are indistinguishable up to 0.01 Å, and the calculated $E_{ads}$ varied by only around 0.01 eV when more layers were added.

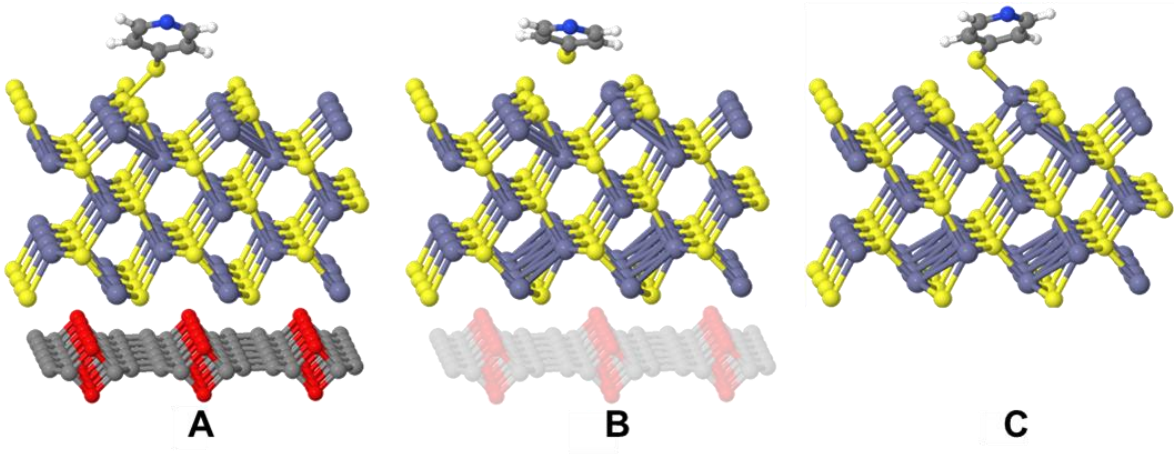


**Figure IV.9:** 4-MPy adsorbs on ZnS(110)@GO *via* a surface S atom (A). If the GO sheet is removed, the 4-MPy molecule moves away from its original adsorbed position (B) and adsorbs instead *via* a Zn atom of the surface (C). The colour code is the same as in **Figure IV.S8** and **Figure IV.S9**.

Additionally, the adsorption of two 4-MPy molecules as a dimer (the so-called 4-aldrithiol species) was considered, but it was found that the adsorption is much weaker in this scenario, as the molecule floats more than 3.5 Å away from ZnS(110)@GO and the $E_{ads}$ per molecule is around -0.18 eV (**Figure IV.S14**).

Since the 4-MPy molecule can adsorb on ZnS(110)@GO either on a surface S or on a surface Zn, it stands to reason that the co-adsorption of several nearby molecules may be possible and even energetically favourable. The co-adsorption of two molecules on neighboring surface sites was also studied (**Figure IV.S15**) and found that the $E_{ads}$ per molecule becomes -1.36 eV, which means that there is indeed a preference for several 4-MPy molecules to adsorb next to each other. The co-

adsorption of 4-MPy at high surface coverage (**Figure IV.S16**) was considered at last and modeled as an infinite array of molecules interacting with both Zn and S positions. In this situation, the $E_{ads}$ per molecule became -1.46 eV, hinting that this is the most favourable adsorption configuration.

The calculated Raman spectra of 4-MPy in the gas phase and adsorbed on ZnS(110)@GO are shown in **Figure IV.10**. Although the calculated wavenumbers are in general underestimated, the calculated spectra are able to capture the main features of the experimental Raman spectra of 4-MPy (**Figure IV.6**). Important for the discussion below are the calculated vibrations for gas-phase 4-MPy which appear at 724 $cm^{-1}$, 1107 $cm^{-1}$, and 1562 $cm^{-1}$, having correspondence with the experimental peaks determined for an aqueous solution of 4-MPy and appearing at 730 $cm^{-1}$, 1119 $cm^{-1}$, and 1627 $cm^{-1}$, respectively. It is encouraging to note that the peak at 724 $cm^{-1}$ vanishes upon adsorption, both in the experimental and calculated spectra. Having in mind that this peak corresponds to a C-S stretching mode, and that the adsorption of 4-MPy occurs *via* its S atom on ZnS(110)@GO, it makes sense that this vibrational mode changes its behaviour upon adsorption. The peaks at 1562 $cm^{-1}$ and 1107 $cm^{-1}$ appear slightly downshifted in the calculated spectrum of the adsorbed molecule, at 1547 $cm^{-1}$ and 1086 $cm^{-1}$. Note that the calculated spectrum of adsorbed 4-MPy shows only one peak at ~1100 $cm^{-1}$ and another at ~1300 $cm^{-1}$, while two peaks appear in the spectrum of gaseous 4-MPy. These differences are very probably due to the frustration of some modes upon adsorption.

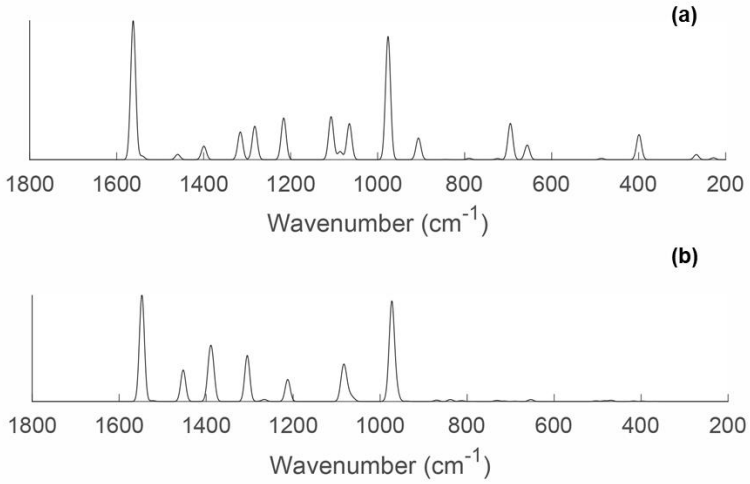


**Figure IV.10:** Calculated Raman spectra of 4-MPy in gas phase (a) and adsorbed on ZnS(110)@GO (b).

To explain the different adsorption behavior of 4-MPy molecules on ZnS(110) and on ZnS(110)@GO, structural and electronic differences between the Zn and S atoms of ZnS(110) and ZnS(110)@GO farthest from the GO sheet were pursued, because these atoms are the ones to interact more strongly with the 4-MPy molecule. However, despite the change in the lattice constant that slightly compresses ZnS, the spatial atomic arrangement of ZnS(110) does not change much with the presence of GO, with the interatomic distances remaining practically unchanged. A Bader charge

analysis showed that, in the presence of GO, the charge of the Zn and S atoms farthest from GO changes by less than one hundredth of an electron with respect to pure ZnS(110). Significant differences were only found in the calculated density of states (DOS) of the ZnS(110) and ZnS(110)@GO surfaces (**Figure IV.11**).

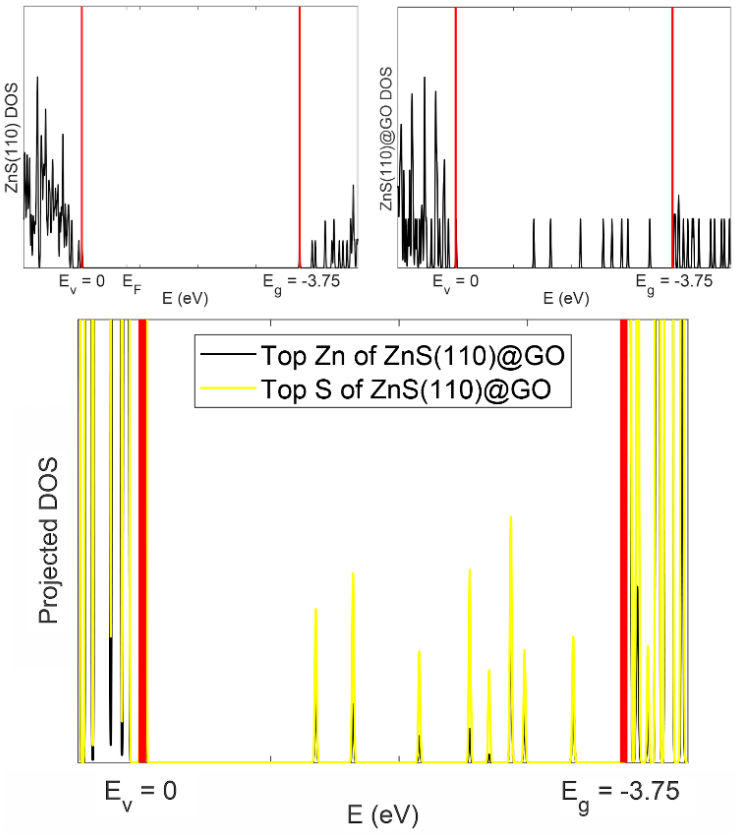


**Figure IV.11:** Calculated density of states (DOS) of the ZnS(110) (top left) and ZnS(110)@GO (top right) surfaces in the vicinity of the ZnS(110) band gap (denoted by the vertical red lines). The bottom plot is the DOS of ZnS(110)@GO, projected onto the Zn (black line) and S (yellow line) atoms farthest from GO.

In fact, in the vicinity of GO and as expected, electronic states are introduced into the bandgap of ZnS. These occupied states have a very large component on carbon and oxygen atoms of GO. However, by projecting the DOS of ZnS(110)@GO onto the Zn and S atoms farthest from GO, one realizes that the “gap states” of ZnS(110)@GO have not only a carbon/ oxygen component, but also a finite contribution from some Zn and S atoms, dominated by S. Additional confirmation of this interaction between ZnS(110) and GO was made by, again, starting from 4-MPy adsorbed on ZnS(110)@GO and increasing the distance between ZnS(110) and GO in steps of 0.5 Å. For each distance between ZnS(110) and GO, the positions of the atoms of the molecule and of the two layers of ZnS(110) closest to it (and farthest from GO) were optimized, while fixing the positions of the GO atoms and of the remaining ZnS(110) layers. As the ZnS(110)-GO distance increased, it was observed that (i) the gap states associated to Zn and S gradually disappeared (**Figure IV.S17**), and

(ii) the molecule gradually moved farther from the Zn atom on which it was initially adsorbed, and towards a surface S atom to which it ultimately became bound. The same effect was observed with 5 and with 11 layers of ZnS(110). This allowed to be certain that the change in adsorptive behaviour of 4-MPy when GO is introduced is not due to direct interaction between 4-MPy and GO; instead, the presence of GO alters the properties of ZnS(110) which, in turn, leads to a different adsorption behaviour of 4-MPy. This effect has been observed before,[452] where the sensitivity of NiFe-based layered double hydroxides (LDH) was increased by the presence of GO. The increase in sensing properties was attributed to charge contribution due to Fe orbitals near the Fermi level (within the gap of the LDH), visible in DOS plots.

## 3.3. Raman Imaging

So far, the adsorption of 4-MPy molecules onto the ZnS@GO was discussed and the effect of this substrate on the enhancement observed in the Raman bands of 4-MPy. In principle, this adsorbate can be further explored as a molecular probe for detecting GO regions with semiconducting nanophases, within the resolution of the Raman microscope. This is firstly demonstrated in this work by using confocal Raman microscopy applied to the ZnS@GO substrates. The Raman images shown in **Figure IV.12** present brighter colors for the regions with the stronger Raman signal for the 4-MPy (**Figure IV.12**-a) and for the GO sheets (**Figure IV.12**-b). For instance, **Figure IV.12**-a presents the Raman image that results from the integration of the area of the band at 1018 $cm^{-1}$, corresponding to the ring-breathing/C-S vibrational mode of 4-MPy, exhibiting a strong Raman signal at the composite surface. The combined Raman image presented in **Figure IV.13**-b was obtained based on the Raman spectra displayed in **Figure IV.13**-c, which gives the overall mapping of the 4-MPy treated ZnS@GO substrate. The spectrum corresponding to the GO (blue tracing) shows only the characteristic bands of GO sheets (1350 $cm^{-1}$ and 1600 $cm^{-1}$) while the Raman spectra corresponding to the adsorption of 4-MPy (1 mM) on the ZnS@GO substrate (red and cyan tracing) shows the enhancement of the Raman bands of the analyte. Note that the Raman spectrum (in cyan) shows vibrational bands both for the analyte (4-MPy) and the GO. A plausible explanation is that such Raman spectrum is collected from a spot containing 4-MPy adsorbed on ZnS@GO lying behind the GO, and the red spectrum is for 4-MPy adsorbed on exposed ZnS@GO. Although the extension of ZnS coverage is not homogeneous, **Figure IV.13** also shows that most of the GO surface is covered with ZnS, which accounts for the observed Raman enhancement observed in 4-MPy when using these substrates.

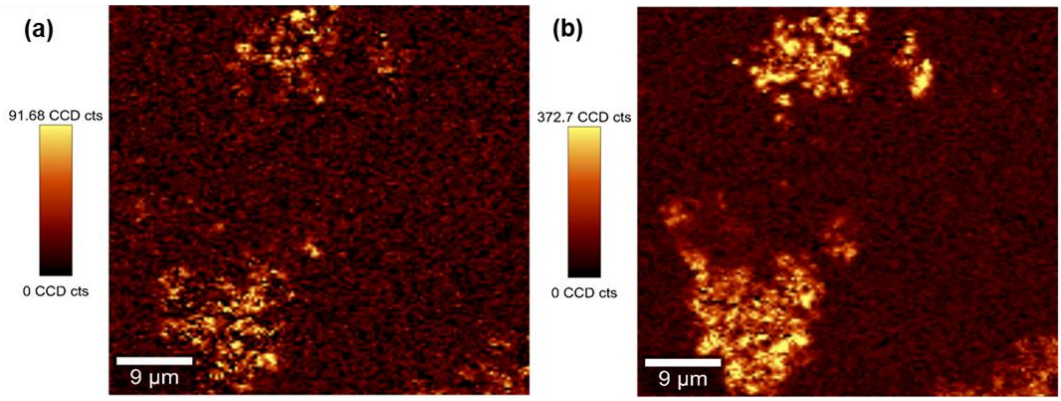


**Figure IV.12**: Raman images obtained using the integrated intensity of the Raman band at 1018 $cm^{-1}$ for 4-MPy (a) and 1353 $cm^{-1}$ for GO (b) in the SERS spectra of 4-MPy (1mM) using the ZnS@GO as substrate.

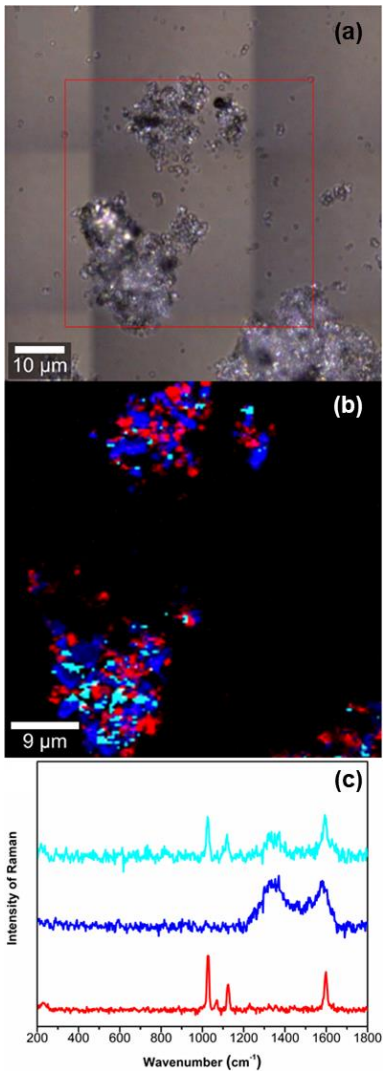


**Figure IV.13:** Optical photograph (a), combined Raman image using three different Raman spectra identified for the 4-MPy (1mM) adsorbed on the ZnS@GO used as SERS substrate (b) and Raman spectra used for the combined Raman image: GO substrate (blue) and 4-MPy adsorbed on ZnS@GO (red and cyan) (c).

# 4. Conclusions

The Raman intensities of 4-MPy adsorbed on ZnS@GO hybrid substrates were enhanced when compared to the cases where adsorption took place on the individual surface components (ZnS or GO) alone. Furthermore, the peaks at 1119 $cm^{-1}$ and 1627 $cm^{-1}$, ascribed to the ring-breathing/(C–S) and stretching modes of the ring, were strongly enhanced when compared to the Raman spectrum of a 4-MPy solution. The observed Raman enhancement is a consequence of a synergistic effect involving both ZnS and GO materials, by causing changes in the polarizability of the adsorbate. This effect might be due to charge-transfer mechanism involving intragap energy levels created in the semiconductor, due to the presence of GO, to resonant localized energy levels of the adsorbate. The DFT calculations confirmed the energetically favourable adsorption of 4-MPy on ZnS(110) and ZnS(110)@GO through the sulfur atom of the molecule. Furthermore, according to the calculations, adsorption on ZnS(110) is only possible on a surface Zn atom, while on ZnS(110)@GO it can occur on either a surface S or Zn, with preference towards the former. This subtle difference can be explained by taking into consideration the DOS of the ZnS(110)@GO surface: in the presence of GO, electronic states appear within the band gap of ZnS(110), with a finite contribution from Zn and S atoms. Finally, the potential of confocal Raman microscopy combined to the SERS effect in ZnS was demonstrated as a useful tool providing Raman maps of the hybrid nanostructures, which might be applicable to other types of semiconductors deposited on graphene-based materials.

# CHAPTER V

## *Visible-light activation of carbon supported $BiVO_4$ photocatalysts*

In this work, hybrid materials based on carbon spheres supported $BiVO_4$ phases show visible-light photocatalytic activity towards the removal of tetracycline, whose photodegradation follows a hydroxyl radical mechanism.

# CHAPTER V | "Visible-light activation of carbon supported $BiVO_4$ photocatalysts"

Bismuth vanadate ($BiVO_4$) has gained great attention for several applications including in photocatalysis applied to water purification technologies. In particular, this applies to the most stable polymorph (monoclinic scheelite) which exhibits photocatalytic activity under visible-light irradiation. On the other hand, this semiconductor also presents some limitations, namely the cost and low adsorption capacity for organic pollutants. As such, finding chemical green strategies aiming at a more sustainable use of this semiconductor remains a challenge and is the subject of the present research. By combining the hydrothermal carbonization (HTC) of κ-carrageenan, a biopolymer extracted from red seaweeds, and an aqueous chemical bath deposition (CBD) method, the preparation of monoclinic $BiVO_4$ supported on carbon spheres was described. These hybrid materials show visible-light photocatalytic activity as demonstrated by screen experiments applied to the removal of tetracycline (TC) in water, whose photodegradation follows a hydroxyl radical (•OH) mechanism. The hybrid photocatalysts feature a wider wavelength range for photon harvesting, good adsorption capacity, high durability and ability for reuse in subsequent catalytic steps. An additional benefit is the need for less amount of $BiVO_4$ for the photocatalytic process, thus making the use of this semiconductor less costly and more sustainable. [5]

*Keywords*: bismuth vanadate; carbon spheres; hydrothermal carbonization; adsorption; visible-light photocatalysis; wastewater treatment; tetracycline.

[5] This chapter is based on the submitted work: Joana L. Lopes, Ana C. Estrada, Sara Fateixa, Ana L. Daniel-da-Silva, Tito Trindade. *Visible-light activation of carbon supported $BiVO_4$ photocatalysts*. **2021**

Joana L. Lopes performed the main experimental tasks concerning the synthesis, characterization and photocatalytic studies of the materials. Sara Fateixa provided assistance to Raman characterization. Ana L. Daniel-da-Silva contributed for the hydrothermal carbonization method. Ana C. Estrada and Tito Trindade supervised all the research. All authors have made contributions in terms of results discussion and written of the final version.

Joana L. Lopes thanks the contribution of the European COST Action CA17120 supported by the EU Framework Programme Horizon 2020.

# 1. Introduction

Heterogeneous semiconductor photocatalysis has attracted great interest among available advanced oxidation processes (AOPs) applied to wastewater decontamination.[453,454] These methods have been regarded as particularly effective alternatives for eliminating certain organic pollutants, which are potentially harmful for living organisms even if present in small amounts.[455] Among the photocatalysts explored in this context, $TiO_2$ stands as the most prominent material, forming the basis of several photocatalytic technologies, which are already implemented in certain practical contexts.[456] However, the optical band gap of pure $TiO_2$ is in the UV region (anatase: 3.2 eV; rutile: 3.0 eV), and visible photons are not harvested in the photocatalytic process. Although this limitation has been tackled by several strategies that use $TiO_2$ materials, there is clear interest in developing visible-light activated photocatalysts based on alternative semiconductors with narrower band gap. In particular, $BiVO_4$ has been a prime candidate for water splitting leading to hydrogen and oxygen evolution[13,14] and also for the photocatalytic oxidation of organic compounds.[240–243] In addition, powdered $BiVO_4$ shows high photochemical stability, good dispersibility and resistance to corrosion in oxidative conditions.[457,458]

It is well-known that $BiVO_4$ exists in three natural polymorphs - *pucherite*, *dreyerite* and *clinobisvanite*. The monoclinic *clinobisvanite* (or monoclinic scheelite, *m-s*) and tetragonal *dreyerite* (or tetragonal zircon, *t-z*) are also obtained synthetically, whereas the orthorhombic polymorph *pucherite* exists only naturally.[459] In addition to these polymorphs, synthetic $BiVO_4$ is also known to crystallize in the tetragonal scheelite *t-s* structure, which shows a similar structure to *m-s* $BiVO_4$, with tetrahedrally coordinated V(V) and eight-fold coordinated Bi(III), but differing in the Bi-O polyhedron which is more distorted by the $6s^2$ lone electron pair resulting in the loss of four-fold symmetry.[240,460–462] At normal pressure and temperature conditions, the *m-s* $BiVO_4$ polymorph is thermodynamically stable, whereas the tetragonal phase is kinetically feasible by pH control of the precursor solution during the synthesis.[463] Indeed, the observed polymorphism of $BiVO_4$ powders is strongly dependent on the synthesis conditions. For instance, the monoclinic crystalline structure has been obtained through high temperature methods, while the tetragonal is typically observed in aqueous solutions at lower temperature.[464] Several synthetic routes have been employed for preparing $BiVO_4$, which include solid state,[465] microwave-assisted,[466] sol-gel,[467] co-precipitation,[468] sonochemical[469] and hydrothermal[470] methods. Concerning the photocatalytic applications, *m-s* $BiVO_4$ is the most active phase, showing higher photocatalytic activity than the *t-s* crystalline phase, with the possibility to be used as visible-light harvester due to its narrow direct band gap, $E_g$ = 2.4 eV.[462,471] The *t-s* exhibits lower photocatalytic activity under UV-light while the *t-z* phase is inactive in the whole ultraviolet/visible (UV/VIS) region of the electromagnetic spectrum.[461] Although monoclinic $BiVO_4$ shows photocatalytic activity, it has also some limitations, such as the cost, low adsorption capacity and rapid recombination of the photo-generated charged species in the conduction band (CB) and valence band (VB).[472,473] To overcome these limitations some strategies have been employed, which include (i) doping with metal/ non-metal ions; (ii) *p-n* heterojunction with *p*-type semiconductor

materials or isotype heterojunction *m-s*/*t-z* $BiVO_4$, exposed reactive facets; (iii) surface functionalization and (iv) coupling with carbonaceous materials.[473–478] Although the latter approach has been explored by using distinct carbon materials,[474,475,478] it was found just one report on the use of carbon spheres as supports for $BiVO_4$ photocatalysts and by using an approach very different from the one described here.[472]

Carbon spheres is a generic denomination related to spherical or near spherical shaped particles, which according to their size range, can be classified as graphitized spheres (2–20 nm), less graphitized spheres (50–1000 nm) and carbon beads (> 1000 nm). Typically, smaller spheres are linked together in a 2D strand extending over tens of spheres, whereas larger structures tend to aggregate, interacting *via* van der Waals forces.[479] Carbon spheres have been prepared using distinct synthetic strategies, such as adaptations of the Stöber method,[480] template methods,[481] HTC[24] and microemulsion polymerization.[482] HTC methods are particularly useful to obtain spherical, amorphous and morphological uniform carbon particles.[483] In addition, carbonaceous materials have functional oxygen groups at the surface, useful for further chemical functionalization and to explore surface modifications in aqueous medium.[12] As such, amorphous carbon spheres can be combined with other inorganic particles yielding functional composites for target applications. Several polysaccharides such as alginate, chitosan and carrageenan derived from natural sources, have been exploited as potential precursors to HTC strategies. Recently, Nogueira *et al*. has reported the use of carrageenan as a source to produce carbonaceous adsorbents,[484] which prompted the investigation of this polysaccharide as a precursor of carbon spheres for preparing supported $BiVO_4$ particles.

The synergy between $BiVO_4$ and carbon materials is expected to improve the adsorption capacity and photocatalytic activity in relation to the isolated materials. Because less photoactive material is employed, this approach is particularly relevant for a costly material such as $BiVO_4$, thus making its application more attractive.

# 2. Experimental section

## 2.1. Chemicals

The following chemicals have been used as supplied: bismuth (III) nitrate pentahydrate ($Bi(NO_3)_3.5H_2O$, Sigma-Aldrich, 98%), ethanol absolute (Fisher Chemical), ethylenediaminetetraacetic acid dissodium dihydrate (EDTA, $C_{10}H_{14}N_2O_8Na_2.2H_2O$, Fluka, 97%), formic acid ($CH_2O_2$, Sigma-Aldrich, 98%), hydrogen peroxide ($H_2O_2$, Scharlau, 30% v/v), sodium hydroxide (NaOH, JMGS, 99%), sodium monovanadate ($NaVO_3$, Sigma-Aldrich, 98%), sodium phosphate dibasic anhydrous ($Na_2HPO_4$, Aldrich, 99%), sodium phosphate monobasic ($NaH_2PO_4$, Aldrich, 99%), sulfuric acid ($H_2SO_4$, Fluka, 95-97%), *tert*-butanol ($C_4H_7O$, Riedel, 99%), tetracycline

hydrochloride ($C_{22}H_{24}N_2O_8$.HCl, Sigma-Aldrich, 95%) and κ-carrageenan (300.000 g/mol, Sigma-Aldrich).

## 2.2. Synthesis of photocatalysts

### *2.2.1. Hydrothermal synthesis and functionalization of carbon spheres*

Carbon spheres were synthetized by HTC of κ-carrageenan. In a typical procedure, κ-carrageenan (2.5 g) was dispersed into 25 ml of distilled water, placed in a 40 ml Teflon-lined stainless-steel autoclave sealed and kept at 200 ºC for 12 hours. The resulting solid sample, denominated κ-C, was isolated by filtration, thoroughly washed with water and ethanol and dried at 60 ºC overnight. Carbon spheres (κ-C) were functionalized through a strong acid treatment.[483] In a typical procedure, κ-C spheres (200 mg) were ground with a mortar and pestle and suspended in concentrated $H_2SO_4$ (10 mg/mL). The mixture was stirred overnight at room temperature, under a $N_2$ stream, in a ventilated fume-hood. Afterwards, the dark solid was slowly washed with hot deionized water under vacuum filtration using a nylon membrane with 0.2 μm pore size, until pH 5.5 was reached in the supernatant solution. The collected powder was dried overnight at 60 ºC. The functionalized carbon spheres are here identified as κ-FC.

### *2.2.2. Synthesis of hybrid $BiVO_4$@carbon spheres*

The carbon spheres were decorated with $BiVO_4$ particles by using a CBD method as follows.[485] Typically, $Bi(NO_3)_3.5H_2O$ (1.25 mmol, 605 mg) and EDTA (2.5 mmol, 730 mg) were added to 10 mL of phosphate buffer solution ($[Na_2HPO_4]$ = $[NaH_2PO_4]$ = 0.1M), and the mixture was stirred for 10 minutes. Then, 5 ml of a $NaVO_3$ (2.5 mmol, 305 mg) buffered solution was added to the white milky mixture obtained, which then changed to a yellowish orange suspension. The pH of this suspension was adjusted to 7 with aqueous NaOH 2M. For deposition of $BiVO_4$ phases on the carbon spheres, 40 mg of carbon spheres (κ-C and κ-FC) were added to the previous suspension and the mixture was then stirred at 90 ºC for 3 hours. The resultant yellow brownish suspension was centrifuged (6000 rpm, 15 minutes), and the collected brown material was thoroughly washed with water and ethanol and dried at 60 ºC. The amount of $BiVO_4$ in the hybrid photocatalysts was 65%, calculated using the content of Bi in the sample as determined by inductively coupled plasma (ICP) spectroscopy. For comparative studies, pure $BiVO_4$ powders were prepared by an analogous method but in the absence of the carbon substrates.

$BiVO_4$@κ-FC: ICP (wt.%): Found: Bi: 42; V:11

## 2.3. Photocatalytic screening studies

The photocatalytic activity of the as-prepared materials was evaluated in the degradation of aqueous solutions of TC under visible-light irradiation. The photocatalytic reactions were performed in a cylindrical quartz photochemical reactor vertically placed at 7 mm from a 120 W halogen lamp (MATEL Lineal Eco Halogen). The average intensity of irradiation was 52 mW/cm$^2$, as measured with a Laser Ophir Start Lite coupled with a Ophir 12A-V1 Power Laser Sensor 12A-V1. The reaction system was cooled by circulating water to maintain the temperature in the range 20-23 $^o$C.

In a typical photocatalytic run, the photocatalyst (7.5, 15 or 25 mg) was dispersed in 75 mL of aqueous solution of TC (5 mg/L) and stirred in the dark for 2 hours, to ensure the adsorption/ desorption equilibrium of TC molecules over the materials. Subsequently, the photoreactor was filled with the suspension, which was then light irradiated under vigorous stirring. The photoreaction was monitored at regular intervals; thus 1 mL of the reaction mixture was withdrawn, immediately centrifuged for catalyst removal and the concentration of TC was monitored by high-performance liquid chromatography with diode-array detection (HPLC-DAD) at 276 nm. The term of reaction was considered when the peak area for TC remained constant after two subsequent HPLC analysis. The photocatalytic reactions using 15 mg of hybrid photocatalyst were also performed in the presence of 1% of $H_2O_2$ (30% v/v), keeping the same reaction conditions. The TC adsorption capacity of all-prepared materials was evaluated using the same experimental procedure but keeping the mixture in the dark, under vigorous stirring.

In order to investigate the photocatalytic reaction mechanism, the degradation of TC was performed using *tert*-butanol and formic acid as $^{\bullet}$OH and hole scavengers, respectively. The photocatalytic reactions were performed under the same conditions, using a 1:100 substrate/ scavenger molar ratio. The photodegradation rate was calculated according to the **Equation V.1**, where $C_t$ and $C_0$ are the concentration of TC at time t and t = 0 (after adsorption/desorption equilibrium period), respectively. All assays were repeated thrice.

$$R = \frac{C_0 - C_t}{C_0} \times 100\% \qquad Eq.V.1$$

The TC removal was assumed to be a pseudo-first order reaction, and the rate constant values, *k* (min$^{-1}$), were estimated from the slopes of the linear ranges of the *ln*($C_t/C_0$) according to the **Equation V.2**.

$$ln(C_t/C_0) = -kt \qquad Eq.V.2$$

To further evaluate the stability and performance of the hybrid photocatalysts, the ability for recovery and recycling of materials were also assessed. The photocatalysts were recovered by centrifugation (13000 rpm, 5 minutes), dried at room temperature, and reused in new runs under identical experimental conditions.

## 2.4. Instrumentation

The UV/VIS spectra were recorded using a Jasco V-560 spectrometer. Fourier transform infrared (FTIR) spectra of the materials were obtained using a Bruker Optics Tensor 27 spectrometer (Bruker, Billerica, MA, USA) coupled to a horizontal attenuated total reflectance (ATR) cell, using 256 scans at 4 $cm^{-1}$ resolution. The FTIR spectra of the samples in KBr pellets were recorded with a Bruker Optics Tensor 27 spectrometer, using 128 scans at 4 $cm^{-1}$ resolution. The Raman spectroscopic studies were performed in a combined Raman-AFM confocal microscope WITec alpha300 RAS+. Drops of carbon spheres, $BiVO_4$ and composite solution were left to dry on glass substrates and then excited with a 532 nm line of a Nd:YAG laser (5s, 10 acquisitions, 1 mW laser power). The objective was 100x for a better laser spot area (~350 nm). Raman mappings were performed by raster-scanning the laser beam over the samples, acquiring a full Raman spectrum at each pixel of the optical image and finally integrating them to generate false color images based on the absolute area underneath specific bands at each pixel (816 $cm^{-1}$ for $BiVO_4$, 1575 $cm^{-1}$ and 1358 $cm^{-1}$ for the G band and D band, respectively, of the carbon materials). The images were created by the WITec software, WITec Project 5.0, with 100 × 100 points per grid in a 40 × 40 μm area for small areas and 100 × 100 points per grid in a 90 × 90 μm area for large areas with 0.3s each spectrum. The vertical bar in each Raman image corresponds to the relative color intensity of each selected Raman band. For the combined Raman image, the Raman spectra of κ-C, κ-FC and $BiVO_4$ were used as the basis set in the analysis using the command True Component Analysis, providing the color-coded combined Raman image. The intensity values and associated errors of the Raman bands of the carbon spheres were obtained by multi-peaks fitting using the Lorentz function, and the Raman bands related to the $BiVO_4$ were obtained by single peak fitting using the Gauss function or the multi-peaks fitting using the Lorentz function in Origin 2016. The powder X-ray diffraction (XRD) data were collected using a PAN analytical Empyrean X-ray diffractometer equipped with Cu-Kα monochromatic radiation source at 45 kV/40 mA. The samples were prepared by deposition of aliquots of the ethanolic suspensions of the samples on silicon holders. The diffraction patterns were analysed by Rietveld refinement using the HighScore Plus. Scanning electron microscopy (SEM) was performed using a scanning electron microscope Hitachi SU-70 operating at an accelerating voltage of 15 kV. The analysis of SEM images to build the particle size histograms was performed using the software ImageJ version 1.46.The surface charge of the suspended particles was assessed by zeta potential measurements performed on the respective aqueous suspensions, using a Zetasizer Nano ZS equipment from Malvern Instruments. The specific surface area of the samples was determined by nitrogen adsorption measurements at 77 K and using the Brunauer-Emmett-Teller (BET) isotherm. Before BET measurements, the samples were degassed at 80 °C under nitrogen flow overnight. The pore volume was calculated from the adsorbed $N_2$ using the Barret–Joyner–Halenda (BJH) method. The elemental analysis of Bi and V was performed by inductively coupled plasma (ICP) spectroscopy using a Jobin-Yvon JY70 Plus spectrometer. The samples collected during the photocatalytic experiments were analysed by HPLC-DAD (ThermoScientific Ultimate 3000 equipped with Ultimate

3000 DAD) at 276 nm. The HPLC system comprised a column Kromasil 100-5-C18 (250 mm of length and 4.6 mm of i.d.) coupled to a precolumn holder (imChem). The column was maintained at 35 ºC and the mobile phase consisted of formic acid 0.2% (75%) and methanol (25%) with a flow rate of 1 ml/min. The Chromeleon™ chromatography data system was used to quantify the peak areas.

# 3. Results and Discussion

## 3.1. Synthesis and characterization of the photocatalysts

**Figure V.1** shows the SEM images of carbon spheres synthesized by HTC of κ-carrageenan, used as the polysaccharide precursor. The neat κ-C spheres (**Figure V.1**-a, b) previously prepared by the HTC method were treated with a strong acid, leading to an increase of the number of oxygen functional groups at the carbonaceous surface.[479] The presence of oxygen functional groups, such as hydroxyl and carboxylic groups, enhance the materials' hydrophilic character, thereby improving water dispersion, which is required for the envisaged applications. The samples are composed predominantly of micro-sized spherical particles with the average size of the carbon particles increasing slightly from (5.8 ± 1.4) μm to (6.3 ± 1.6) μm after functionalization, still within the same size range taking into consideration the indicated size dispersion. The BET surface area ($S_{BET}$) of carbon spheres after functionalization (sample κ-FC: 2.645 $m^2/g$) was lower than that for the sample prior to the functionalization (sample κ-C: 7.117 $m^2/g$) (**Table V.S1**). This is probably due to oxidation of carbon materials after acid treatment, which increased the surface hydrophilicity *via* extensive formation of oxygen functionalities, thus reducing the measured $S_{BET}$ *via* decrease on the $N_2$ adsortion.[486]

**Figure V.2** shows the powder XRD patterns for κ-C and κ-FC samples, in which both are characterized by a broad peak at about $2\theta \approx 24^{o}$, which is more pronounced in the functionalized samples. This broad peak is attributed to the (002) diffraction planes of graphite, which is slightly shifted towards lower angles indicating a higher interlayer spacing than that of fully crystallized graphite ($d$ = 0.34 nm). Hence, the XRD data of the samples are mainly consistent with the presence of essentially amorphous carbon spheres with the presence of some crystalline graphitic domains.[483]

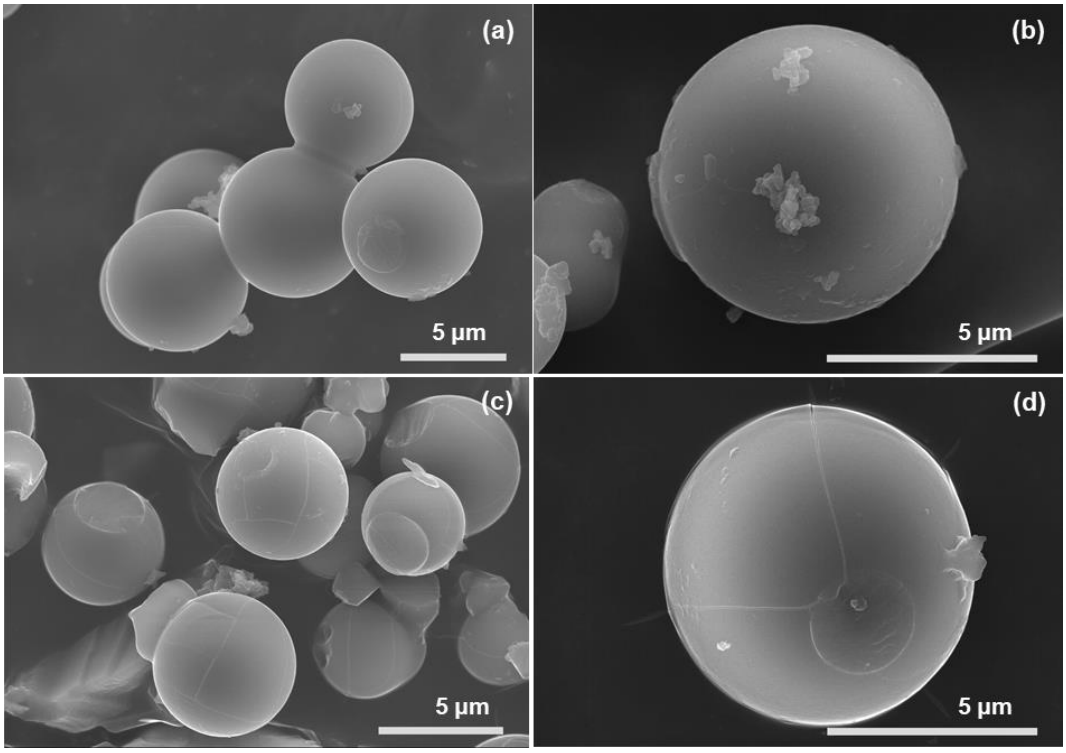


**Figure V.1:** SEM images of HTC non-functionalized carbon κ-C spheres (a, b) and functionalized carbon κ-FC spheres (c, d).

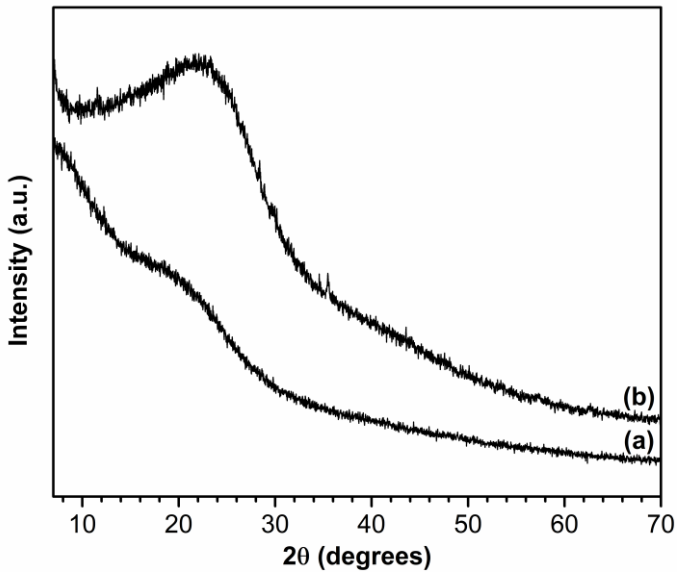


**Figure V.2:** Powder XRD patterns of HTC carbon spheres before (a) and after functionalization (b).

Aqueous suspensions of the κ-FC showed a zeta potential about -49 ± 9.8 mV (pH 7), which is a value superior (in absolute value) to the reported value for the non-functionalized samples (*ca*. -30 mV, pH 7). The higher negative value observed for the zeta potential of κ-FC suspensions, in

comparison to the non-modified samples, is in agreement with the presence of a higher number of ionizable oxygen functional groups at their surfaces. The FTIR spectra of the κ-C and κ-FC spheres are shown in **Figure V.S1** and **Table V.1**. The FTIR spectra are somewhat similar, confirming the presence of a graphitic structure functionalized with oxygen groups. Hence, the 1600-1700 $cm^{-1}$ region shows overlapping bands due to the stretching modes of C=O and C=C (aromatic) groups; the latter are also indicated by the small band at 1500 $cm^{-1}$ which is assigned to aromatic carbons.[479,487] The band at 1290 $cm^{-1}$ in the FTIR spectrum of sample κ-C and the shoulder around 1365 $cm^{-1}$ in the spectrum of κ-FC, are attributed to C-H stretching vibrations; the broad band between 1100-1200 $cm^{-1}$ is related to the presence of C-O stretching modes. The bands in the spectral regions 1020-1070 $cm^{-1}$ and 750-875 $cm^{-1}$ are characteristic of the stretching modes of C-O and bending modes of O-H vibrations, and the bending vibrations of out-of-plane C-H typical of aromatic rings resultant from the HTC process, respectively.[484,487] In the 2800-3000 $cm^{-1}$ region, the non-functionalized spheres show vibrational bands related to the asymmetric stretching modes of aliphatic groups. However, the spectra of the functionalized samples did not show these bands, perhaps indicating the effect of the acidic treatment.[488]

**Table V.1:** Experimental FTIR bands ($cm^{-1}$) and respective assignments for the samples κ-C and κ-FC.[479,484,487]

| κ-C spheres | κ-FC spheres | Assignment |
|---|---|---|
| 1690 | 1690 | ν(C=O) [487] |
| 1600 | 1590 | ν(C=C) aromatic [479] |
| 1290 | $1365^{sh}$ | ν(C-H) aromatic [484] |
| 1200-1160 | 1130 | ν(C-O) [487] |
| 1020 | 1020 | ν(C-O); δ(O-H) [484] |
| 860 | 870 | δ(C-H) aromatic [487] |
| 790 | 800 | adjacent δ(C-H) aromatic [487] |

ν – stretching; δ – bending; sh – shoulder

The Raman spectra (**Figure V.3**) of the carbon spheres show two characteristics bands attributed to the D and G bands, associated to the defects/disorder in the carbon lattice (D band) and to the in-plane vibration of graphitic carbon atoms (G band).[353,489] The D and G bands were deconvoluted into five components, which were assigned to aryl-alkyl ether (D4, 1248 $cm^{-1}$), graphene edges (D1, 1370 $cm^{-1}$), amorphous carbon structures (D3, 1546 $cm^{-1}$), graphitic carbon (G, 1578 $cm^{-1}$), and graphene sheets (D2, 1608 $cm^{-1}$).[313,353,489] The band parameters obtained from the Raman fit analysis are presented in **Table V.S2** and are similar to each other. These results can be explained

by assuming that the bulk structure of the κ-FC spheres remained unchanged after acid treatment of the starting κ-C sample, as expected from an effect that occurred mainly at the surface of the carbon spheres. This type of behaviour has also been reported for carbon nanofibers and nanotubes.[490] The intensity ratio $I_D/I_G$ was calculated as 1.4 and 1.6 for κ-C and κ-FC spheres, respectively, whose similarity is in line with this interpretation, where an increase would be expected for a situation of extensive functionalization.

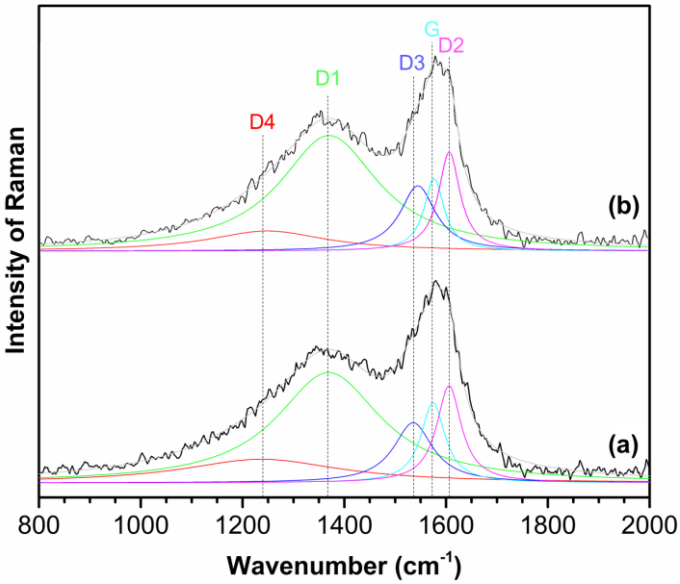


**Figure V.3:** Raman spectra of κ-FC (a) and κ-C (b) spheres showing the characteristic D and G bands. The deconvolution of Raman bands was obtained by multi-peaks fitting using the Lorentz function.[313]

Both carbon materials were analysed by confocal Raman microscopy and the respective Raman maps integrating the areas of the D1 and G bands are presented in **Figure V.S2**. The Raman maps show spherical particles with the morphological characteristics expected from the previous SEM analysis (**Figure V.1**). Note the similarity of both Raman maps when using as diagnosis bands the D1 and G features, which again support the discussion above for the Raman spectra. Hence, the vibrational data collected for the carbon samples provide information for the presence of surface oxygen groups but there is no evidence for a significant difference in the amount of these groups in both samples, i.e. before and after acid treatment of the carbon spheres. On the other hand, the better aqueous dispersibility and more negative zeta potential observed for the κ-FC spheres, as compared to the κ-C sample, agree with a more extensive functionalization of their surfaces with hydrophilic oxygen groups.

Because the acid treated carbon spheres originated more stable and homogeneous aqueous dispersions, the κ-FC samples were preferred as heterogeneous substrates for the growth of $BiVO_4$ particles using a CBD method. **Figure V.4** shows the SEM images of the non-functionalized κ-C and

the functionalized κ-FC spheres after modification with $BiVO_4$. Indeed, it was found that $BiVO_4$ particles grown either on non-functionalized or functionalized carbon spheres show distinct average sizes. The SEM images of $BiVO_4$ grown on κ-C spheres show larger $BiVO_4$ particles with fused lamellar shapes, whereas the $BiVO_4$ particles on κ-FC are considerably smaller and discrete, which is in agreement with a more extensive nucleation at the surface for $BiVO_4$ grown in the presence of acid treated carbon spheres, as compared to the non-acidic treated particles. This is because the functionalization of the carbon particles ensured their homogeneous dispersion in the reaction medium and to the higher number of surface nucleation sites available. Presumably, the cracked surfaces observed in the κ-FC spheres (**Figure V.1**), associated with an increasing number of oxygen groups on κ-FC spheres, facilitate the heterogeneous nucleation of the *in situ* generated precursor species for the $BiVO_4$ phases.

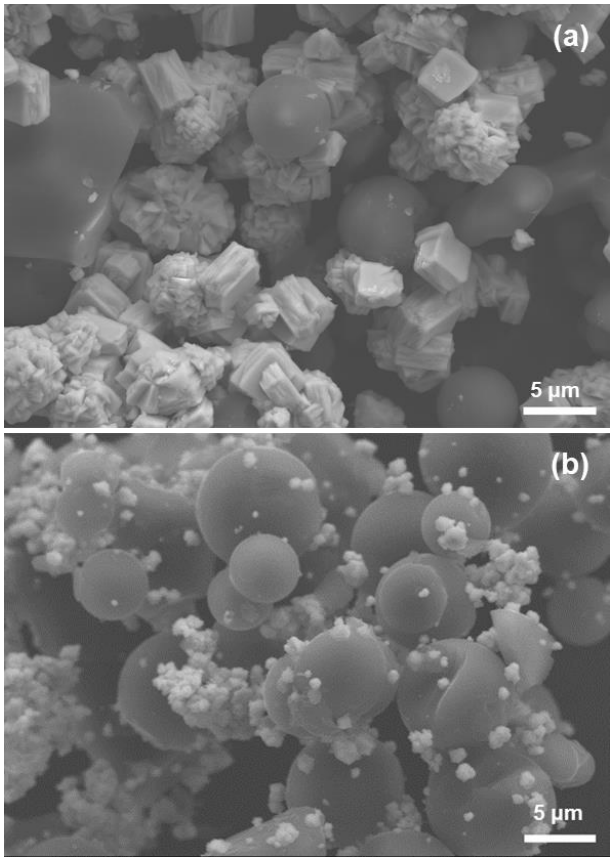


**Figure V.4:** SEM images of $BiVO_4$@κ-C (a) and $BiVO_4$@κ-FC (b) obtained by CBD method.

The *m-s* $BiVO_4$ and *t-s* $BiVO_4$ phases crystallize with the scheelite structure, having eight-fold coordinated Bi(III) and tetrahedrally coordinated V(V) polyhedral, which are connected by corner-sharing.[460,461] However, the Bi-O polyhedron in the *m-s* structure is more distorted by the stereochemically active lone electron pair of Bi(III) than that in the *t-s* $BiVO_4$ structure, which also result in differences in the respective Bi-O bond lengths. The *t-s* $BiVO_4$ phase exhibits single reflections at $2\theta$ values of 18.5°, 35° and 46° related to the Miller indices (101), (200) and (204)

(ICDDPDF No. 04-010-5710 in **Appendix D**, **Annex 8**). On the other hand, the *m-s* crystalline phase presents splitting of peaks at 18.5º, 35º and 46º corresponding to the Miller indices [(101), (011)], [(200), (002)] and [(240), (042)], respectively, and a less intense peak at 2$\theta$ of 15°, corresponding to the (020) reflection (ICDDPDF No. 00-014-0688 in **Appendix D**, **Annex 9**). Moreover, the monoclinic phase shows prominent peak splitting at 50° as well as the formation of peak clusters at ~40 and ~60°, instead of single peaks.[491] Hence, the $BiVO_4$ phases obtained in the presence of non-functionalized spheres can be well indexed to the *m-s* phase of $BiVO_4$ (**Figure V.5**-a), showing clear splitting of the peaks at 35º and 46º. The powder XRD patterns of $BiVO_4$@κ-FC hybrid is also shown in **Figure V.5**-b. The XRD patterns show splitting peaks at 18.5º, 35º and 46º related to the [(101), (011)], [(200), (002)] and [(240), (042)] reflections, respectively. The presence of monoclinic $BiVO_4$ phase was also supported by the presence of the peaks at 40º and 60º. Likely peak broadening due to amorphous carbon spheres have not been observed in this case, which is due to the high intensity of the diffraction peaks of the crystalline $BiVO_4$ phases.[472] Under these conditions, the *m-s* phase of $BiVO_4$ is indubitably formed, which is corroborated by the FTIR data. The FTIR spectrum of the $BiVO_4$@κ-FC hybrid (**Figure V.S1**-c) is dominated by a broad band around 620 $cm^{-1}$ due to the Bi-O stretching vibration mode and a weak band at 472 $cm^{-1}$ assigned to the symmetric bending mode of the $VO_4^{3-}$ units. The asymmetric ($v_3$) and symmetric ($v_1$) stretching vibrations of the V–O bond are overlapped giving rise to strong absorption at 700-900 $cm^{-1}$.[461] For both samples, the vibrational bands located in the 3000-3500 $cm^{-1}$ region are due to the characteristic stretching mode of O-H groups. For comparative purposes, the FTIR spectrum of pure $BiVO_4$ is also shown (**Figure V.S3**), showing a strong and broad absorption band located at 740 $cm^{-1}$, which is related to the asymmetric stretching vibration of the V-O group and is overlapping the band assigned to Bi-O stretching mode. The weak band at 415 $cm^{-1}$ is assigned to the bending mode of the $VO_4^{3-}$ group. Also, the cell parameters calculated from the XRD data by the least-squares method (**Table V.2**), in both cases agree with the presence of *m-s* $BiVO_4$.[492]

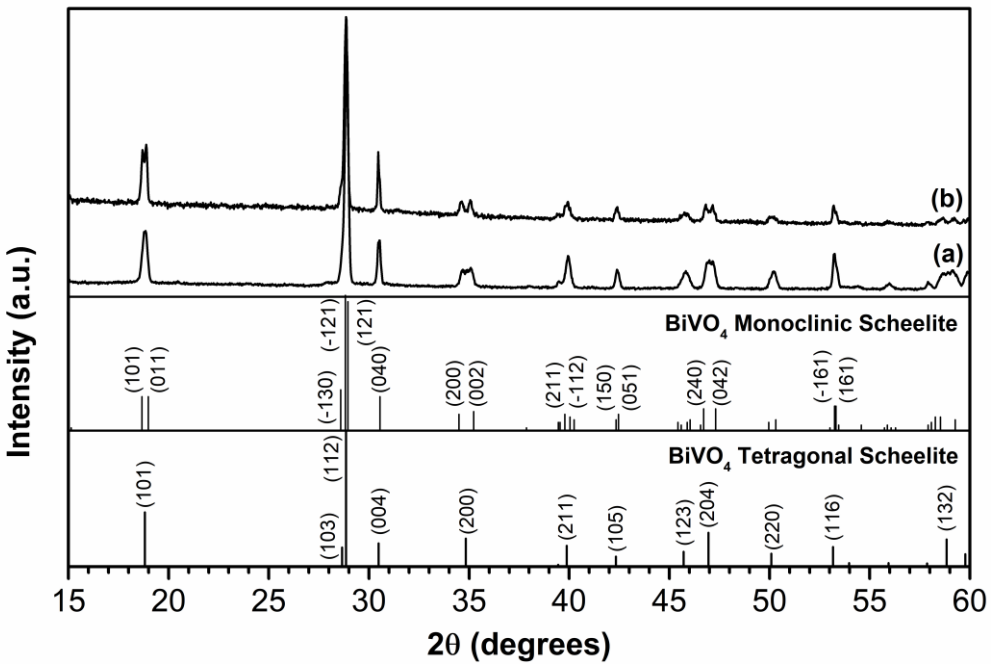


**Figure V.5:** Powder XRD patterns of $BiVO_4$@κ-C (a) and $BiVO_4$@κ-FC hybrid (b). The vertical lines correspond to the standard diffraction peaks attributed to the $BiVO_4$ monoclinic scheelite phase (ICDDPDF No. 00-014-0688) and $BiVO_4$ tetragonal scheelite phase (ICDDPDF No. 04-010-5710).

**Table V.2:** Theoretical lattice parameters of the *m-s* crystalline phase[492] and experimental lattice parameters of $BiVO_4$@κ-C (a) and $BiVO_4$@κ-FC (b), obtained by Rietveld refinement.

| Sample | *a* | *b* | *c* | β (º) |
|---|---|---|---|---|
| *m-s* [492] | 7.23 | 11.56 | 5.10 | 134.80 |
| $BiVO_4$@κ-C (a) | 7.25 | 11.70 | 5.11 | 134.62 |
| $BiVO_4$@κ-FC (b) | 7.26 | 11.79 | 5.11 | 134.56 |

As expected, the Raman spectrum of the $BiVO_4$@κ-FC hybrid shows the characteristic D1 and G bands of the carbon substrate (**Figure V.6**-a). The presence of $BiVO_4$ particles in the hybrid sample originates in the Raman spectrum a strong band at 826 $cm^{-1}$, which is ascribed to symmetric V-O stretching. The bands at 131 $cm^{-1}$ and 203 $cm^{-1}$ are associated with the lattice modes of $BiVO_4$.[472,485] The deconvolution of the Raman band at 350 $cm^{-1}$ gives two bands, at 338 and 362 $cm^{-1}$, related to the bending modes of the $VO_4^{3-}$ units.[472,485] The analysis of the Raman spectra corroborates the conclusions inferred from the XRD analysis, suggesting the formation of a slightly distorted monoclinic crystalline phase of $BiVO_4$. The Raman spectrum of the pure $BiVO_4$ particles is also shown (**Figure V.6**-b and **Table V.S3**). The deconvolution of the band around 340 $cm^{-1}$ using the Lorentz function is presented in **Figure V.S4** showing two bands, at 333 and 357 $cm^{-1}$.

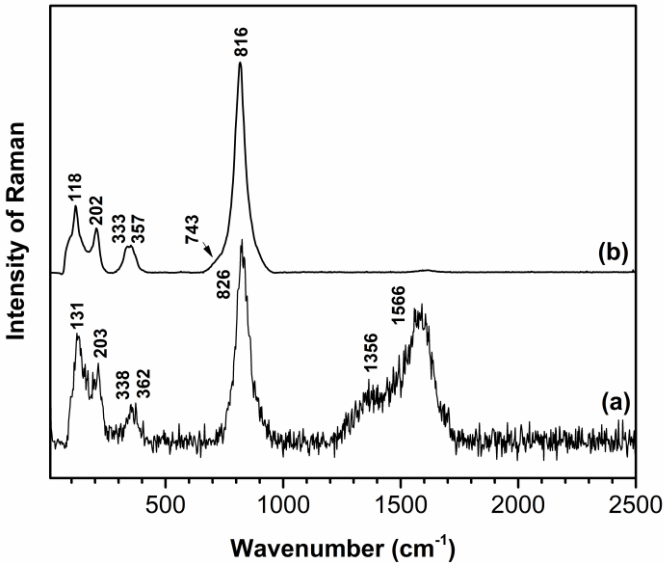


**Figure V.6:** Raman spectra of the $BiVO_4$@κ-FC hybrid (a) and pure $BiVO_4$ particles (b).

The combined Raman image of the $BiVO_4$@κ-FC hybrid particles in **Figure V.7**-A was obtained using the Raman spectra depicted in **Figure V.7**-B, which shows the $BiVO_4$ phases dispersed onto the carbon spheres' surfaces. The spectrum corresponding to the carbon spheres (blue tracing) exhibits the characteristic D and G bands, whereas the spectrum related to the $BiVO_4$ crystals (red tracing) presents the typical Raman bands of the monoclinic $BiVO_4$ phase.

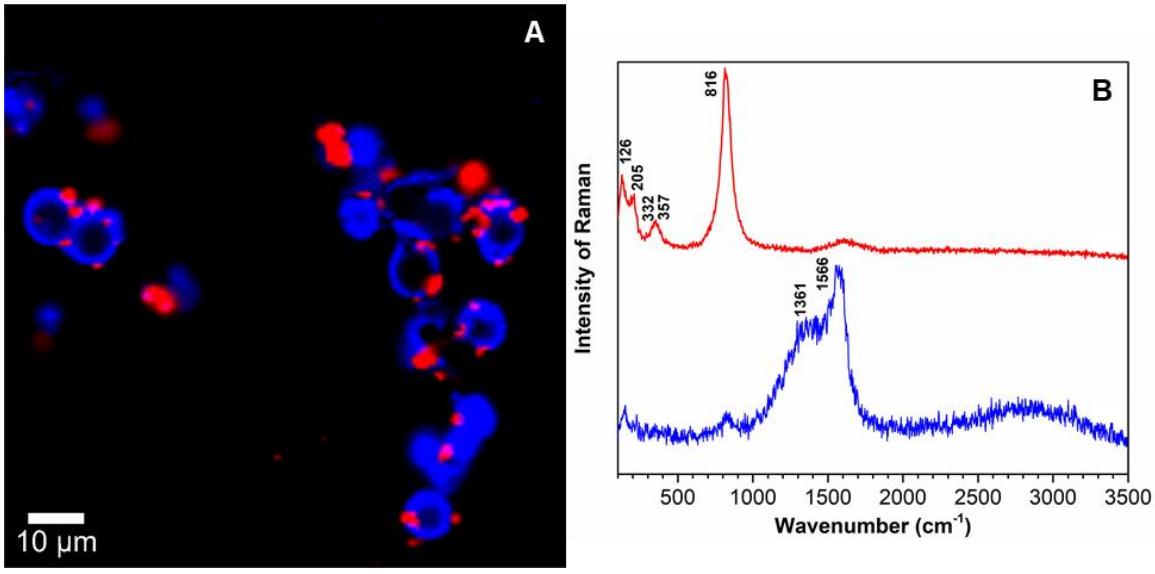


**Figure V.7:** Combined Raman image using two different Raman spectra identified on the $BiVO_4$@κ-FC hybrid (A); Raman spectra used for the combined Raman image (B): κ-FC spheres (blue) and monoclinic $BiVO_4$ (red).

The UV/VIS diffuse reflectance spectra of the hybrid sample and $BiVO_4$ particles are shown in **Figure V.8**-left panel.The spectrum of pristine $BiVO_4$ shows a strong absorption around 500 nm, which corresponds to the band gap transition involving the Bi 6s and V 3d levels, in accordance with the reported data.[493] The band gap energy of the $BiVO_4$ was estimated from the transformed Kubelka–Munk function vs. energy plot, from diffuse reflectance data, as shown in **Figure V.8**-right panel. The coupling of $BiVO_4$ particles with functionalized carbon spheres slightly extends the wavelength absorption range for photon harvesting in the hybrid photocatalyst. Indeed, a small red-shift was observed in the optical band edge of pristine $BiVO_4$ (2.11 eV) to that one observed for $BiVO_4$ grown on κ-FC spheres (2.04 eV). This observation may be related to the presence of an interfacial region between both materials that originate intragap levels in the $BiVO_4$ semiconductor.

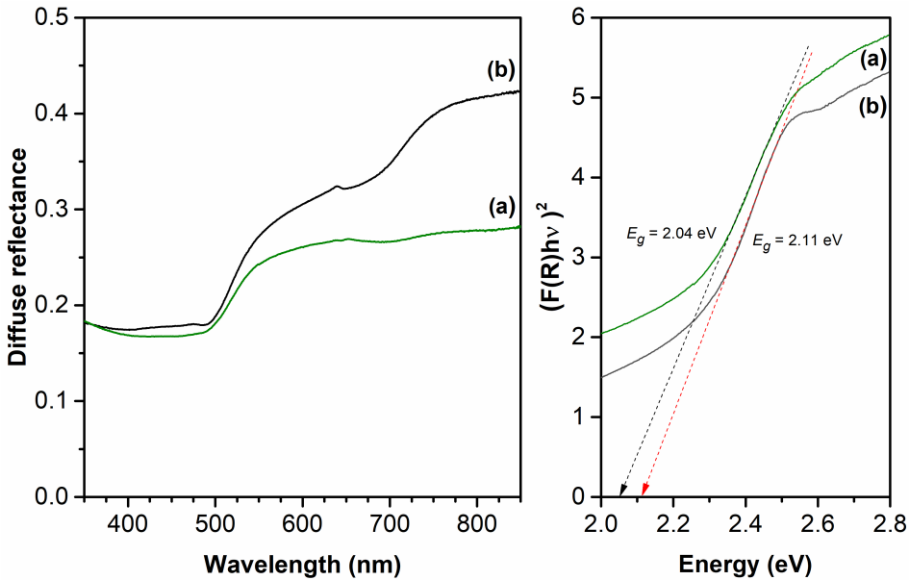


**Figure V.8:** Diffuse reflectance spectra (left) for $BiVO_4$@κ-FC hybrid (a) and $BiVO_4$ particles (b) and the respective Tauc plot (right).

## 3.2. Photocatalytic studies of the materials

The photocatalytic performance of the $BiVO_4$@κ-FC hybrid was investigated through TC degradation under visible-light irradiation. TC is one of the most used antibiotic to fight infections in humans and animals and, consequently, can also be found in municipal wastewater treatment plants.[18,494] **Figure V.9** shows the adsorption capacity for TC using the $BiVO_4$@κ-FC hybrids, pure $BiVO_4$ particles and κ-FC spheres, under dark conditions. It was found that the maximum adsorption (82%) in the conditions tested was attained in the presence of 25 mg of $BiVO_4$@κ-FC sample, and the lower adsorption value was obtained with 7.5 mg of $BiVO_4$@κ-FC sample (44%). It should be noted that almost 40% of TC was adsorbed in 15 minutes using 15 or 25 mg of the hybrid particles, and the adsorption equilibrium was reached after 240 minutes (77% and 62% for 25 mg or 15 mg,

respectively). A negligible amount of TC removal was observed in the presence of 15 mg of $BiVO_4$ or κ-FC, after 7h in the dark (6% and 11%, respectively).

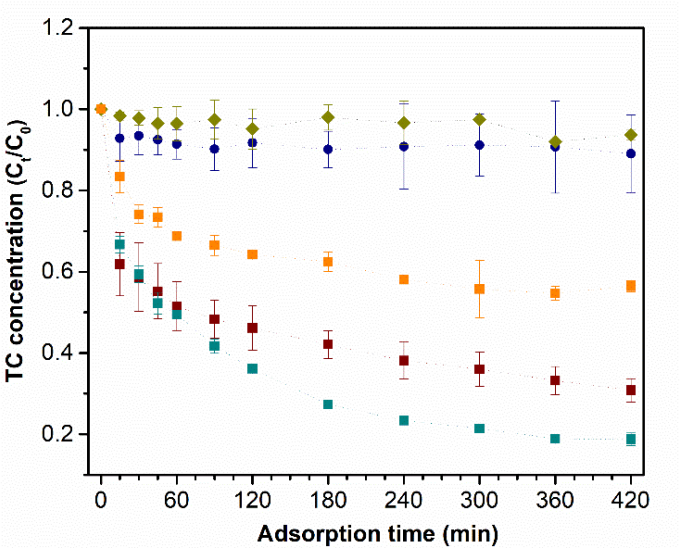


**Figure V.9:** Concentration of TC as function of contact time with 15 mg of κ-FC spheres (●); 15 mg of $BiVO_4$ particles (◆); 7.5 mg (■), 15 mg (■) and 25 mg (■) $BiVO_4$@κ-FC hybrid. Conditions: 75 mL of an aqueous solution of TC 5 mg/L; 25 ºC; 7 hours in the dark.

**Figure V.10**-A shows the concentration of TC as a function of irradiation time in the presence of three amounts of hybrid photocatalysts: 7.5, 15 and 25 mg, as well as in the presence of $BiVO_4$ and carbon spheres. The results indicate that under visible-light irradiation the photolysis of TC was negligible, i.e. in the absence of photocatalyst no significant variation of TC concentration was observed. Similarly, but in the presence of $BiVO_4$ particles or pristine κ-FC spheres only 14% and 7% of TC was removed, respectively, after 5 hours of irradiation. The $BiVO_4$@κ-FC photocatalyst shows higher visible-light photocatalytic activity, achieving almost 60% of TC removal after 5 hours of irradiation. The higher TC removal (63%) is achieved in the presence of 25 mg of the $BiVO_4$@κ-FC hybrid (5.7 mmol of $BiVO_4$ *per* g of material), while slightly lower values were obtained using 7.5 mg and 15 mg of $BiVO_4$@κ-FC (52% and 57%, respectively). Although better values of TC removal were obtained for a higher amount of photocatalyst, the subsequent studies presented here used 15 mg of the hybrid photocatalyst. In fact, by almost doubling the amount of photocatalyst, just a slight improvement of TC removal (6%) was achieved and by increasing the irradiation time for 10 hours an increase of 30% of TC removal was obtained (86% total removal) (**Figure V.S5**). The rate constant (*k*) of the photocatalytic reactions involving the photocatalysts materials (**Figure V.10**-B and **Table V.S4**) was calculated from the slope of the plot $ln(C_t/C_0)$ as function of irradiation time. The following photocatalytic degradation rate *k* constants were obtained using the κ-FC spheres, pure $BiVO_4$ and the $BiVO_4$@κ-FC hybrid, $k$ = 0.00031, 0.00046 and 0.0029 $min^{-1}$, respectively. The rate constant *k*

observed in the presence of the hybrid photocatalyst was 9 and 6 times that one obtained for κ-FC spheres and pure $BiVO_4$, respectively.

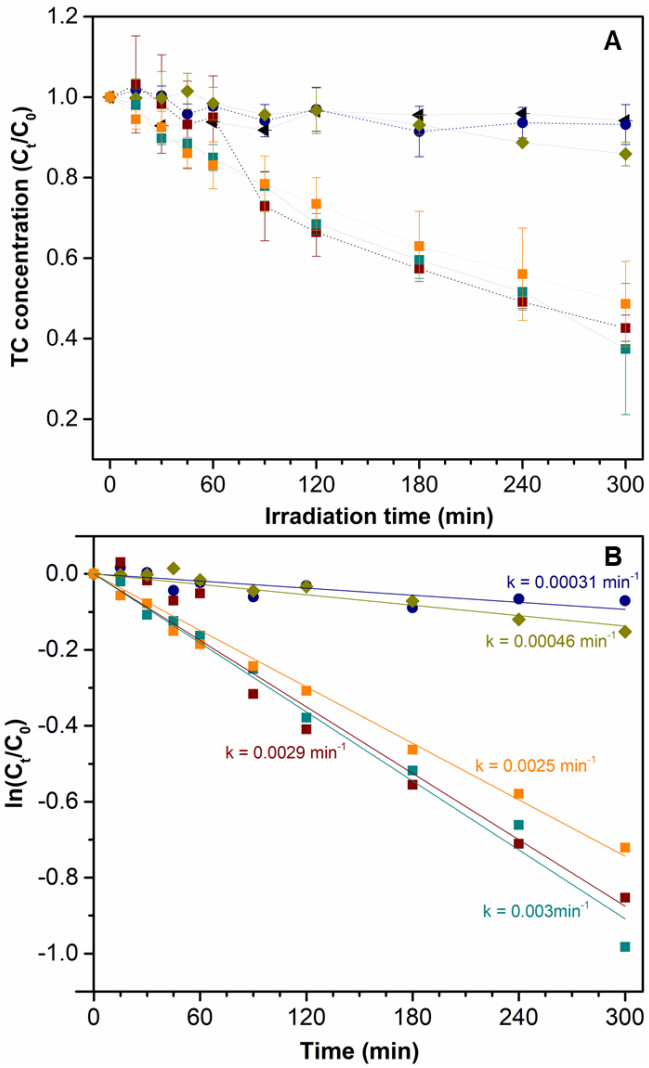


**Figure V.10:** Concentration of TC as function of light irradiation time (A) and respective pseudo-first order kinetic fitting plots (B) with 15 mg of κ-FC spheres (●); 15 mg of $BiVO_4$ particles (◆); 7.5 mg (■), 15 mg (■) and 25 mg (■) $BiVO_4$@κ-FC hybrid; photolysis (◀). Conditions: 75 mL of an aqueous solution of TC 5 mg/L; 25 °C; 5 hours of irradiation.

Overall, the hybrid samples exhibited better photocatalytic performances than their individual counterparts, which confirmed a positive synergistic effect between the two coupled components.[472] Hence, these results are in line with reports by others on the use of $BiVO_4$ photocatalysts coupled to carbon materials.[472,495] For instance, Soltani *et al*. described the use of $BiVO_4$/rGO for the complete photocatalytic degradation of methylene blue (MB) after 1 hour under visible-light irradiation.[244] Fu *et al*. prepared graphene/$BiVO_4$ photocatalysts using a hydrothermal method, and they found that the photocatalytic activity of the reported hybrid photocatalyst for the degradation of dyes was higher

than that of pure $BiVO_4$.[496] Also, Phanichphant *et al*. have described a heterojunction photocatalyst composed by monoclinic spherical-shaped $BiVO_4$ and rGO with 95% of MB degradation after 120 minutes.[497] Wang *et al*. have reported the photocatalytic properties of $BiVO_4$/carbon spheres towards the photocatalytic degradation of RhB or MB, under Xe lamp irradiation.[472] The authors described the enhanced performed of the composite when compared with pristine $BiVO_4$ particles and the potential to be used at a larger scale.[472] This improvement seems to be related with a higher capacity to adsorb pollutant molecules, more efficient harvest of incident light and separation of charge carriers, as well as to the diffusion of electrons and holes to the surface of catalyst, where the reaction takes place.

The combination of the $BiVO_4$@ κ-FC photocatalyst with 1% of $H_2O_2$ under visible-light irradiation, caused almost complete photodegradation of TC (**Figure V.11** and **Table V.S4**). In the presence of both $BiVO_4$@κ-FC and $H_2O_2$, the TC removal increased from 57% to 88%, with a kinetic rate almost three times higher ($k$ = 0.0075 $min^{-1}$) than that observed only in the presence of $BiVO_4$@κ-FC ($k$ = 0.0029 $min^{-1}$). However, $H_2O_2$ alone also degrades TC (20%) but at a slower rate ($k$ = 0.00062 $min^{-1}$). The combined action of the photocatalyst and $H_2O_2$ has also been reported for other systems as enhancing the photocatalytic process.[498] It is suggested that $H_2O_2$ is a source of additional $^{\bullet}OH$, which can explain the photocatalytic behaviour when mixed with $BiVO_4$@κ-FC in the TC photodegradation. On the other hand, the introduction of an external electron acceptor as $H_2O_2$ could suppress the recombination of photoinduced electrons and holes, enhancing the photodegradation efficiency *via* the generation of more $^{\bullet}OH$.[499]

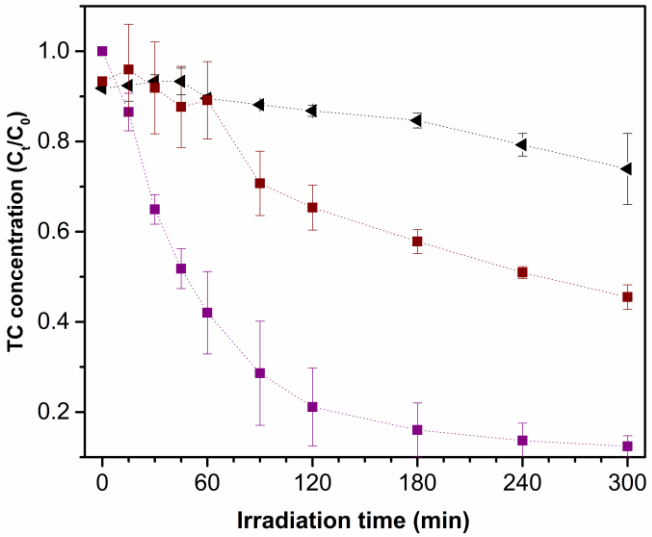


**Figure V.11:** Concentration of TC as function of light irradiation time with 15 mg of $BiVO_4$@κ-FC hybrid in absence of $H_2O_2$ (■); absence of catalyst with 1% $H_2O_2$ (◀); with 1% of $H_2O_2$ (■). Conditions: 75 mL of an aqueous solution of TC 5 mg/L; 25 ºC; 5 hours of irradiation.

Trapping experiments of •OH and holes were performed to detect the main reactive species generated in the photocatalytic system. **Figure V.12** shows the time profile for TC photodegradation in the presence of formic acid or *tert*-butanol, that provides information about the presence in the reacting system of hole and •OH species, respectively. It can be seen that the photodegradation of TC in the presence of $BiVO_4$@κ-FC was not affected by the addition of a hole scavenger. Conversely, the presence of a hole scavenger agent leads to higher values of TC removal because hole capture prevents charge carrier recombination, thus allowing enhanced degradation of TC. Nevertheless, the photodegradation of TC was markedly affected by the addition of a •OH scavenger (only 30% of TC was degraded), suggesting that TC degradation proceed mainly *via* •OH mechanism.

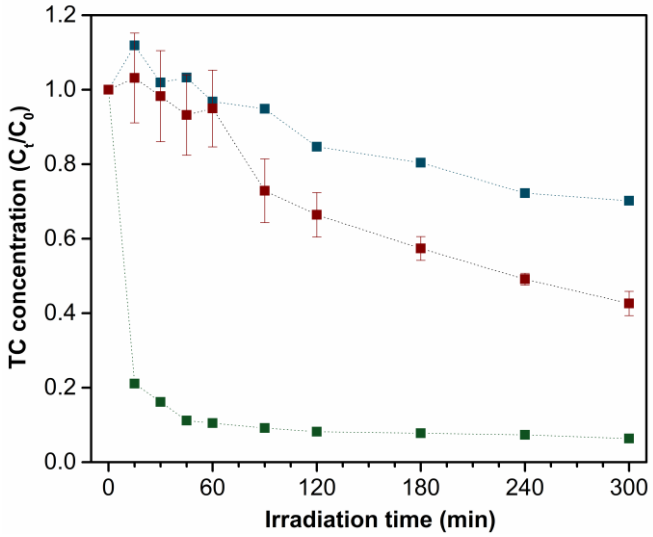


**Figure V.12:** Concentration of TC as function of light irradiation time with 15 mg of $BiVO_4$@κ-FC hybrid without scavengers (■); with presence of *tert*-butanol (■); with presence of formic acid (■). Conditions: 75 mL of an aqueous solution of TC 5 mg/L; 25 ºC; 5 hours of irradiation.

The inspection of the UV/VIS spectra of the supernatant solutions used in the photocatalytic reactions, when $BiVO_4$@κ-FC was present, show no longer the absorption band at 355 nm, corresponding to the maximum absorption of TC. This optical feature is indicative of the BCD aromatic system breakdown due to the rupture of phenolic groups attached to the aromatic ring B (**Figure V.S6**), which indicates effective photodegradation of TC. On the contrary, in the presence of pristine κ-FC spheres or $BiVO_4$ particles, either under visible-light irradiation or in the dark, the absorption bands of TC were still observed at the same wavelength, indicating that TC was adsorbed and not photodegraded (**Figure V.S7**).

Finally, to further assess the photocatalytic usefulness of the $BiVO_4$@κ-FC hybrid materials, their stability and reusability have been investigated. Therefore, the hybrid photocatalyst was recovered from the reaction medium by centrifugation and reused in subsequent cycles under similar reacting conditions, with readjustment of all quantities, without changing the reactant concentrations (**Figure**

**V.13**). The results show that the photocatalytic degradation efficiency of TC decreased (19%) after the third cycle of catalyst reuse. Although reasonable values for TC photodegradation are still observed in the second cycle (41%) they are slightly lower than those observed in the first cycle (63%), which might be due to the loss of photocatalyst mass recovered after the reaction. In fact, only 60% of the hybrid photocatalyst were recovered after the second photocatalytic run and 80% after the first cycle. The $BiVO_4$@κ-FC hybrid photocatalyst recovered after each cycle was characterized to check the stability of the photocatalyst. The powder XRD patterns of all the samples are similar, which indicates no chemical degradation of the hybrid photocatalysts, even though the slight loss of photocatalytic activity and mass loss (**Figure V.S8**).

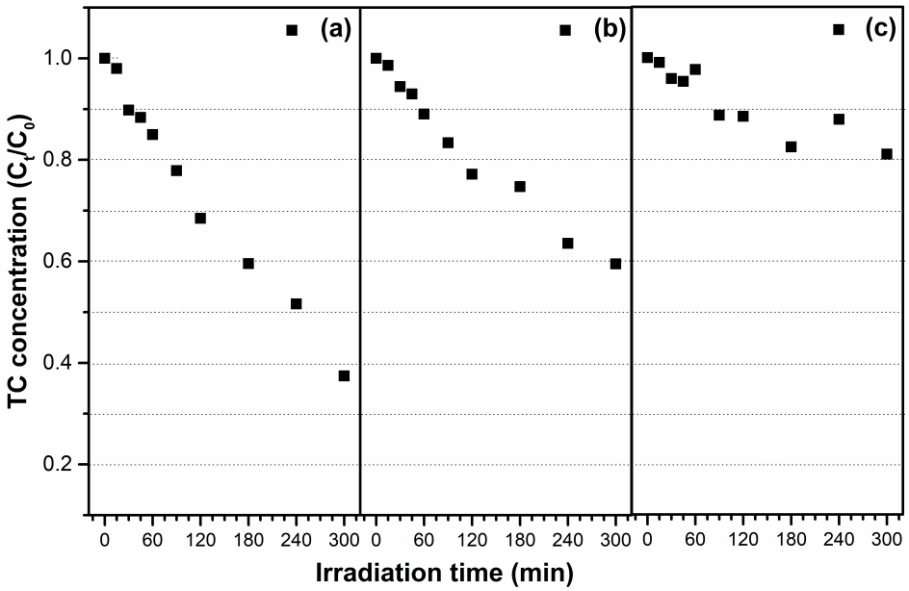


**Figure V.13:** Concentration of TC as function of light irradiation time after the first (a), second (b) and third (c) cycles with 25 mg of $BiVO_4$@κ-FC hybrid. Conditions: 75 mL of an aqueous solution of TC 5 mg/L; 25 $^oC$; 5 hours.

## 4. Conclusions

In summary, carbon spheres were prepared *via* HTC of κ-carrageenan, which have been employed successfully as powdered substrates for growing monoclinic $BiVO_4$ using a CBD method. The particles have been distributed over the carbon surfaces, and the monoclinic phase of $BiVO_4$ was assessed as the crystalline phase present. The as-prepared bi-component materials showed improved photocatalytic activity as compared to pure monoclinic $BiVO_4$, in the degradation of TC in aqueous solutions, under visible-light irradiation. This has been interpreted as due to better dispersibility in the reacting aqueous system and better photon harvesting due to slight extension of absorption wavelength range. Moreover, the $BiVO_4$ hybrids were proven to be reusable and also exhibit great adsorption capacity for TC removal, with 60% of TC removal achieved by using a

relatively low amount of $BiVO_4$ (0.43 mM). The addition of 1% $H_2O_2$ led to almost complete photodegradation of TC with a photocatalytic rate constant three times higher ($k$ = 0.0075 $min^{-1}$), as expected for a $^{\bullet}OH$ mechanism. Overall, the hybrid photocatalysts exhibited better performance than their individual counterparts, hinting a synergistic effect between the two components.

# CHAPTER VI

## *A first look on carrageenan-derived carbon dots*

This chapter describes exploratory research on the optical properties and surface chemistry of carbon dots prepared by the hydrothermal carbonization of carrageenan. This work emerges from a first look on this class of luminescent carbon materials, originating new insights for future strategies to investigate these materials.

# CHAPTER VI | “A first look on carrageenan-derived carbon dots”

Carbon dots (C-dots) are one of the many forms of carbon and particularly one of the most inspiring research nowadays. C-dots comprise nanoparticles with sizes below 10 nm and are frequently referred as nanolights due to their remarkable optical properties. They present several traditional semiconductor-based quantum dots features, such as their size and excitation wavelength ($\lambda_{exc}$) dependent photoluminescence (PL) behaviour, which has been a motivation to elucidate the origins of light emission in these materials.

There are several synthetic routes to prepare this vast class of materials; in this work, a green approach based on the hydrothermal carbonization (HTC) of polysaccharide precursors was investigated *en route* to the production of carbon-based photocatalysts. Three different carrageenan precursors, ι-, κ- and λ-carrageenan were used for the synthesis of the C-dots. In particular, there was interest to investigate if the distinct sulfur content in the precursor had impact on the PL of the as-prepared C-dots, since it is well-known that such properties depend on the dots’ surface chemistry. [6]

*Keywords*: carbon dots; carrageenan; hydrothermal carbonization; optical properties; photoluminescence.

[6] Joana L. Lopes performed the main experimental tasks concerning the synthesis and characterization of the materials. Joana Rodrigues, Sónia O. Pereira, Teresa Monteiro, Duarte Ananias and Luís D. Carlos provide all the support to the luminescence lifetime measurements of the C-dots. Joana L. Lopes has written the draft and final versions of this chapter. Ana C. Estrada and Tito Trindade supervised all the research and revised the draft version.

Joana L. Lopes thanks the contribution of the European COST Action CA17120 supported by the EU Framework Programme Horizon 2020.

# 1. Introduction

Carbon can exist in a variety of allotropes, from crystalline (diamond and graphite) to amorphous (carbon black, activated carbon and glassy carbon) carbon. In the last decades, carbon nanostructures, such as fullerenes, carbon nanotubes (CNTs), and graphene have awakened great interest due to their remarkable and extraordinary physicochemical properties.[500] However, they present as a strong disadvantage the high production cost.[500] With this in mind, carbon materials derived from natural and renewable sources present themselves as a potential attractive alternative.

C-dots are defined as 0D carbon nanostructures with sizes between 2-10 nm with graphitic or turbostratic carbon, containing mostly diamond-like $sp^3$ hybridized carbon insertions [106]. They have relevant physical properties such as their size and excitation dependent PL behaviour, which promotes their use in a variety of fields in which size, cost and bio-/eco-compatibility are critical factors.[15] At their surfaces, C-dots possess several oxygen functionalities which improves their water solubility and allows for further functionalization and surface passivation with several chemical groups, with a direct influence on their enhanced PL.[15,107]

There are two major approaches for preparing C-dots; the top-down (cutting from different pre-formed carbon structures) and the bottom-up (starting with molecular precursors) strategies.[501] Bottom-up methods enable the synthesis of C-dots from chemical precursors through combustion/thermal treatments and microwave synthetic routes.[115,117,118] In particular, pyrolysis and, more recently, HTC of biomass have attracted great attention as a sustainable and alternative route to produce carbon materials.[500] This technique presents several advantages, originating hydrothermal carbons by converting the organic matter, using aqueous media under mild temperatures (typically between 120-250 $^{o}$C) and self-generated pressures.[488,502] Typically, spherical micro-sized particles are obtained where their porosity can be controlled and the resulting particles possess oxygen groups at the surface, which are useful for further functionalization strategies. Hence, the surface chemistry of the prepared materials can be modified by additional thermal treatments or chemical functionalization.[500]

The literature on the formation mechanisms of hydrothermal C-dots is scarce. During HTC process, two distinct phases, liquid and solid, are formed, whereas the evolved gas consists mainly of carbon dioxide.[488] The resultant insoluble solid material exhibits high carbon content, show mesoporous textures and moderate calorific values; the aqueous dissolved by-products (furfural, 5-hydroxymethylfurfural 5-HMF, organic acids, aldehydes, etc.) can be efficiently separated from these carbon-rich solid materials.[487,488] The H and O content may vary due to loss of volatile compounds and decarboxylation and dehydration reactions that take place. The H/C and O/C atomic ratios are used to assess the carbonization degree; with increased temperature, H/C and O/C ratios decrease, indicating high content of aromatic compounds and high carbon stability.[502]

Carbohydrates are hydrolysed to monosaccharides glucose or fructose which in turn participate in several organic reactions. The further decomposition of the monosaccharides leads to the formation

of organic acids, such as acetic, lactic, propenoic, levulinic, and formic acid, which decreases the pH of the medium. The dehydration and fragmentation reactions (i.e., ring-opening and C=C bond-breaking) convert monosaccharides into soluble products such as furfural-like compounds (5-HMF, furfural, 5-methylfurfural), 1,2,4-benzenetriol, acids, and aldehydes. 5-HMF-related products may further decompose into acids/aldehydes and phenolic compounds. Alternatively, 5-HMF can undergo polymerization/condensation reactions (intermolecular dehydration or aldol condensation); polymerizing into small (few nm in size) polymeric nanoclusters, which be able to grow into few micrometers in size.[501] The formation of C-C double bonds is the result of intramolecular dehydration or keto-enol tautomerism. The final formation of aromatic clusters is promoted by the condensation (by intermolecular dehydration) of aromatized molecules which aggregate to hydrothermal carbonaceous spheres.[353,501] The decrease on the surface free energy of the system is the driving force for this process.[503]

As stated in literature, the growth of carbon spheres follows the LaMer model for particle formation.[504] When a critical supersaturation for the precursors is achieved, at a certain temperature and reaction time conditions, there is a burst nucleation, and the carbonization process takes place. The resultant nuclei steadily grow by diffusion of solutes toward the particles surfaces.[505] These species are linked to the surface of the microspheres through the reactive oxygen groups, while ether or quinone functionalities are formed. At the final growth step, the core is formed by less reactive oxygen groups and the outer surface contains a high level of reactive oxygen functionalities.[487] As a result, two distinct products are formed, an insoluble solid residue consisting of carbonaceous spherical micro-sized particles with a core–shell chemical structure (hydrochar microspheres) and an aqueous phase constituted by part of 5-HMF-related products and other organic compounds which are dissolved in the liquid phase.[488,503,506]

**Figure VI.1** shows an illustrative mechanism proposed for the formation of hydrothermal carbons using cellulose in the HTC process that results in particles comprising a carbonized hydrophobic core and an outer shell with hydrophilic properties.

The above information concerning the preparation of amorphous hydrothermal carbons is also important to understand the formation of C-dots with crystalline nature, which are formed together with the HTC carbon microspheres. Some reports state that the formed polymeric nuclei act as hot spots (due to temperature gradients existing in the autoclave) for the adsorption of autogenerated gases ($CO_2$, CO and $H_2$) *via* $CO_2$ reduction under autogenic pressures, leading to the formation of hydrothermal crystalline carbons. During this process a mixture of $sp^2$ and $sp^3$ carbon nanostructures formed which are then mostly converted to $sp^2$ carbons (graphitic type).[501]

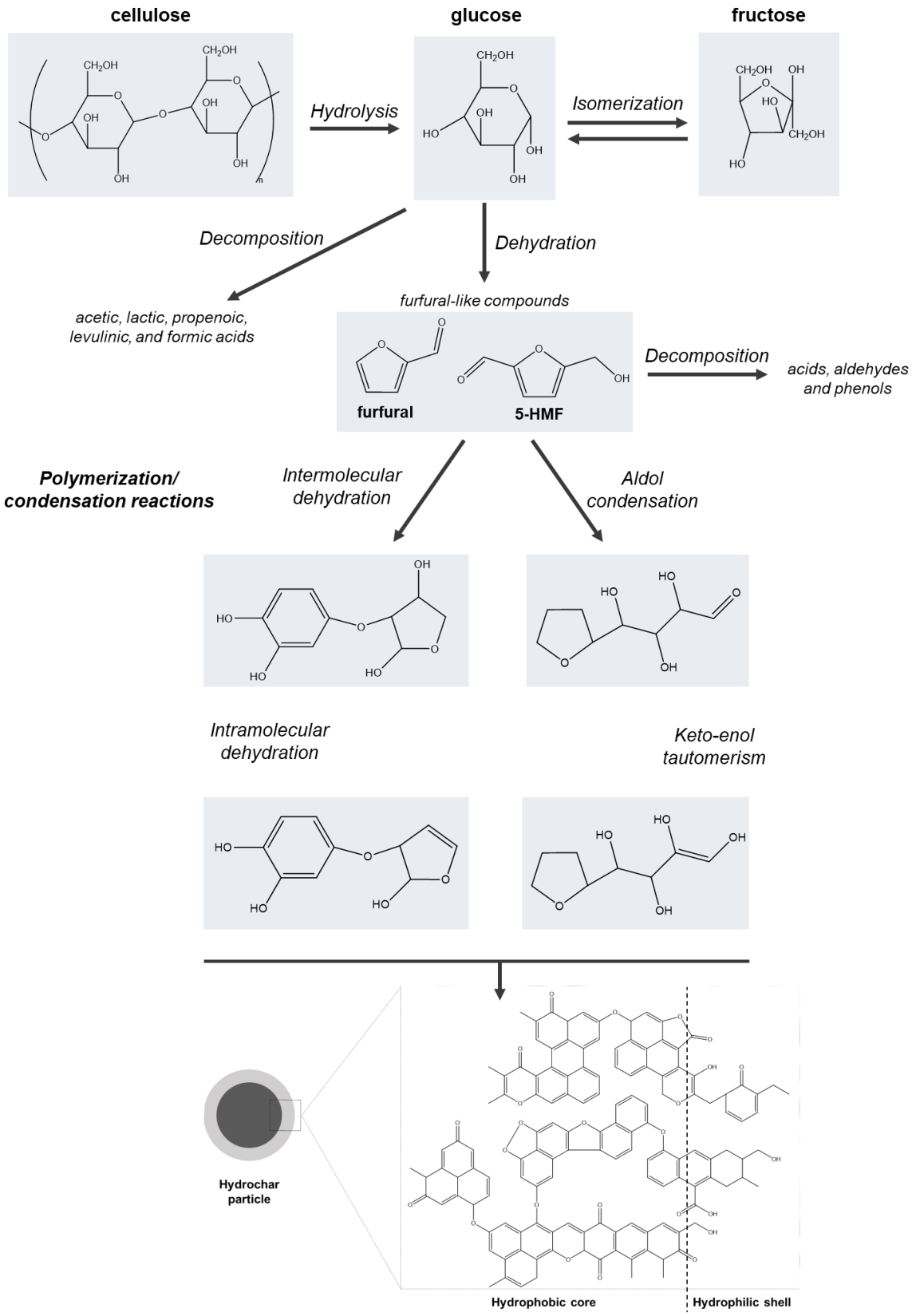


**Figure VI.1**: Proposal for a mechanism of hydrothermal carbon particles formation using cellulose as the precursor.[487]

Several types of precursors and raw materials have been used in HTC procedures, including oligomers and polymers,[479] municipal solid waste,[507] microalgae,[508] carbohydrates,[509] such as cellulose,[487] glucose,[505,510,511] fructose,[503] sucrose,[511] starch[353] or other polysaccharides such as alginate, chitosan and carrageenan.[512,513] Those precursors have distinct temperatures for the onset of HTC, related to their chemical structures, reactivity and the energetics of chemical bonds between the different functional groups.[487] Natural occurring precursors have several advantages, including relatively abundancy, low cost and high carbon content.[479] For instance, using chitosan as the precursor subjected to 180 $^{o}$C, narrow-sized 4-7 nm amino-functionalized C-dots were obtained with luminescent properties showing a strong ultraviolet/visible (UV/VIS) absorption and excitation-dependent photoluminescent properties.[121]

As mentioned above, carbohydrates are frequently used as carbon source to produce C-dots. The HTC strategies rely on hydrolysis and dehydration of the carbon precursors leading to the formation of soluble compounds which latter will follow polymerization and condensation reactions giving origin to polymeric products. The C-dots are finally formed by aromatization and carbonization reactions.[353] In this research, carrageenan precursors having distinct content on sulfate groups in their composition have been explored as sources for the hydrothermal synthesis of C-dots. Carrageenan is a family of anionic linear sulfated polysaccharides composed by galactose and anhydrogalactose units extracted from red seaweeds. These biopolymers have been used as emulsifying or gelling agents in the pharmaceutical and food industries.[514] As a result of their biodegradability, low cost, natural abundance and chemical functionality,[515] they have been widely used for the development of materials with sorption ability for the uptake of diverse ions, organic dyes, pesticides and pharmaceuticals from water.[512,515–518]

According to the sulfated groups per disaccharide unit, carrageenan may be denominated by κ-, ι- or λ-carrageenan, as they possess 1, 2 or 3 sulfated groups, respectively (**Figure VI.2**).[484,513] The three forms exhibit different linear charge density (λ > ι > κ) and solubility (λ > ι > κ), where κ-carrageenan is only soluble in hot water whereas λ-carrageenan is soluble in hot or cold water. The sulfate groups are usually neutralized by cations, such as $Na^{+}$, $K^{+}$ and $Ca^{2+}$, which also affect the solubility and promote cross-linking of the polymeric chains *via* electrostatic interactions leading to gel formation. Hence, κ- and ι-carrageenan exhibit two and one 3,6-anhydro bridges, respectively, which influence the gelation process, whereas κ-carrageenan forms brittle gels and ι-carrageenan forms softer, elastic gels or pastes [514]. The gelation process is thermally reversible, since gels start to form after cooling to about 50 $^{o}$C, and melt when heated at about 80–90 $^{o}$C.[519]

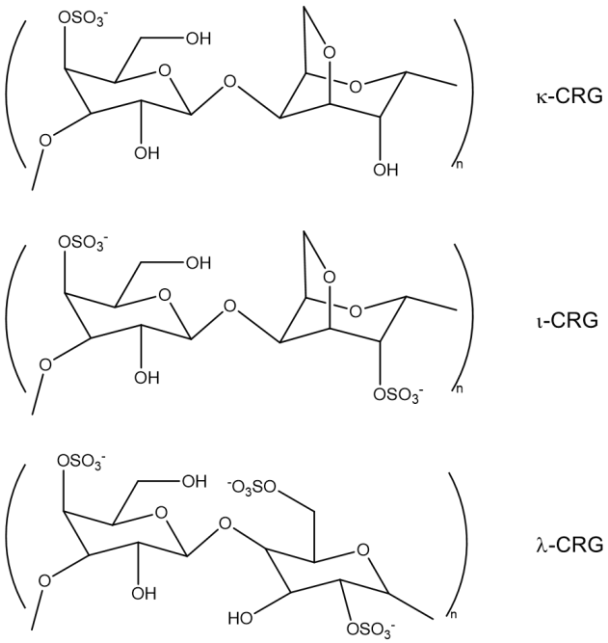


**Figure VI.2**: Chemical structure of disaccharide unit of κ-, ι- and λ-carrageenan biopolymers.

In this work, three different C-dots colloidal suspensions were prepared by HTC process at 200 ºC, using three carrageenan precursors as carbon sources. These materials were then characterized for their morphological and optical properties, in particular for their PL behaviour.

# 2. Experimental section

## 2.1. Chemicals

The following chemicals have been used as supplied: ι-carrageenan (Sigma-Aldrich), κ-carrageenan (Sigma-Aldrich) and λ-carrageenan (Sigma-Aldrich). Milli-Q water was obtained from the Synergy equipment from Millipore with a 0.22 μm filter.

## 2.2. Hydrothermal synthesis of carbon dots

C-dots were synthetized by HTC of the three carrageenan precursors (ι-, κ- and λ-carrageenan). In a typical procedure, the carrageenan precursor (2.5 g) was added to 25 ml of water (10% w/v) and placed in a 40 ml Teflon-lined stainless-steel autoclave sealed and maintained at 200 ºC for 12 hours. C-dots were separated from the precipitate through centrifugation (13000 rpm, 15 minutes). The C-dots containing suspensions were then filtered using 0.2 μm pore size nylon membranes to isolate them from the larger particles. The aqueous colloidal suspensions were stored at 4 ºC.

## 2.3. Dialysis of carbon dots colloids

To remove the excess of impurities resultant from the HTC process, 6 mL of the prepared C-dots colloids were dialysed against 600 mL Milli-Q $H_2O$ for 2 days by using regenerated cellulose membranes (flat width 14-16 mm; MW co 3500 Da) from Spectra/Por. During dialysis, the membranes were subject to constant stirring (100 rpm), and the medium was exchanged 5 times (after 2 hours, 5 hours, overnight, and then 2 hours and 5 hours on the second day). The dialyzed C-dots colloidal suspensions were recovered from the dialysis membranes, stored at 4 $^{o}$C and denominated here as ι-C, κ-C and λ-C.

## 2.4. Instrumentation

The morphology and size of the C-dots particles were analysed by scanning transmission electron microscopy (STEM), using a Hitachi HD-2700 STEM microscope operating at 200 kV. Samples for STEM analysis were prepared by evaporating the diluted suspensions of the nanoparticles on a holey copper grid coated with an amorphous carbon film. The analysis of TEM images to build the particle size histograms was performed using the software ImageJ version 1.46. Scanning electron microscopy (SEM) of the carbon microspheres was performed using a scanning electron microscope Hitachi SU-70 operating at an accelerating voltage of 15 kV. The Raman measurements were performed in a combined Raman-AFM-SNOM confocal microscope WITec alpha300 RAS. A frequency-doubled Nd:YAG laser operating at 532 nm was used as an excitation source with the power set at 1 mW, using the 100x objective. C-dots suspensions were dropped on glass slide and let it dry before measurements. The Raman spectrum of each sample was acquired by the average of 5 spectra (2s, 10 acquisition each) using the software tool WITec Project 5+. The UV/VIS spectra were recorded using a Jasco V-560 spectrometer, by placing the samples in quartz cells of 1 cm length. The C-dots samples were diluted with a dilution factor of 120. PL emission and excitation spectra were measured with a Jasco FP-8300 spectrofluorometer. The emission spectra were obtained in the range of 265−750 nm by exciting the sample at the absorption maxima range (from 255-355 nm). The excitation spectra were obtained in the range of 200-440 nm by emitting the sample at 440-460 nm and 535 nm. Excitation and emission slits were set at 5 nm with 200 nm/min scan speed and data interval of 0.5 nm. Room temperature time-resolved photoluminescence (TRPL) spectra were acquired with the same Fluorolog-3 system using a pulsed Xe lamp (operating at up to 25 Hz) coupled to the same monochromators and with the excitation fixed at 255 and 355 nm. The full-width at half-maximum of each lamp pulse is 3 μs, so that lamp interference during acquisition of decay curves is minimised. The measurement conditions were set to a sample window (duration of signal acquisition) of 5 ms, with 41 ms of time per flash (reciprocal of the repetition rate of the lamp pulses) and a flash count (number of lamp pulses contributing to each data point) of 100. Time delay after flash was employed at 0.05 ms. The nanosecond emission decay curves were acquired with a similar spectrofluorometer (Fluorolog3 Horiba Scientific; model FL3-22) coupled to a

FL1073 Horiba photomultiplier (950 V) with a pulsed NanoLED-390 (Horiba Scientific) as the excitation source. Instrumental function response for the NanoLED-390 was obtained by use of a Ludox (colloidal silica) scattering water solution.

## 3. Results and Discussion

In this work, C-dots were synthetized *via* a one-step synthetic method by the HTC of a biopolymer, carrageenan. The carrageenan precursors, ι-, κ- and λ-carrageenan were used as 10% w/v aqueous dispersions, which were then submitted to hydrothermal treatment under mild conditions. The particle size distribution and morphology of the pure C-dots were evaluated by TEM images shown in **Figure VI.3**. The resulting C-dots particles reveal a spherical morphology with average diameters of (2.94 ± 0.7) nm, (2.05 ± 0.4) nm and (3.33 ± 0.8) nm for ι-C, κ-C and λ-C samples, respectively.

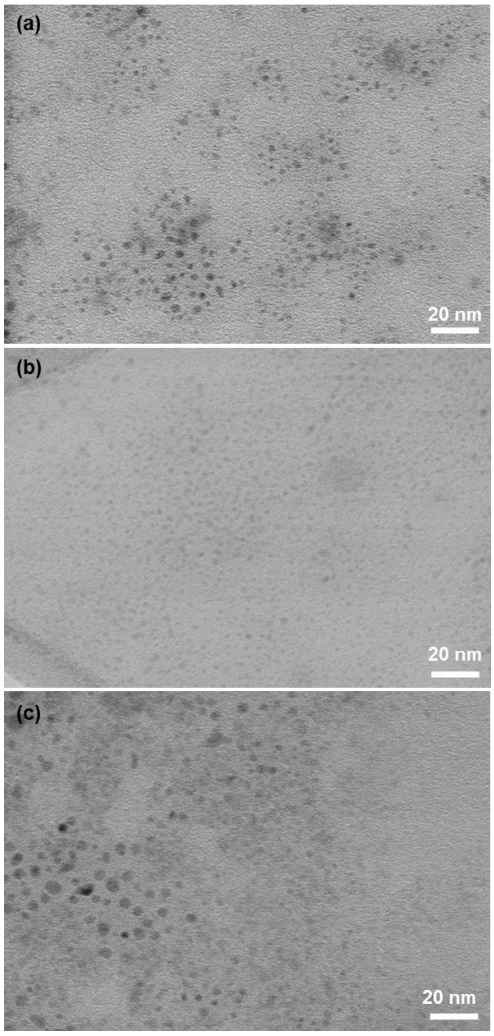


**Figure VI.3**: TEM images for pure colloidal C-dots obtained from distinct carrageenan precursors, ι-C (a), κ-C (b) and λ-C (c).

As discussed in **Chapter V** for the use of κ-carrageenan, the HTC method also yields amorphous micro-sized carbon particles that were explored as supports for semiconductor photocatalysts. Similar results have been observed when using the other carrageenan precursors (ι- and λ-carrageenan). Thus, the carbon micro-sized particles have a quasi-spherical morphology and are polydispersed, as shown by the SEM images in **Figure VI.4**. Together with individualized carbon micro-sized particles, the SEM images also show particle agglomerates which predominate for the samples obtained using the ι- and λ-carrageenan.

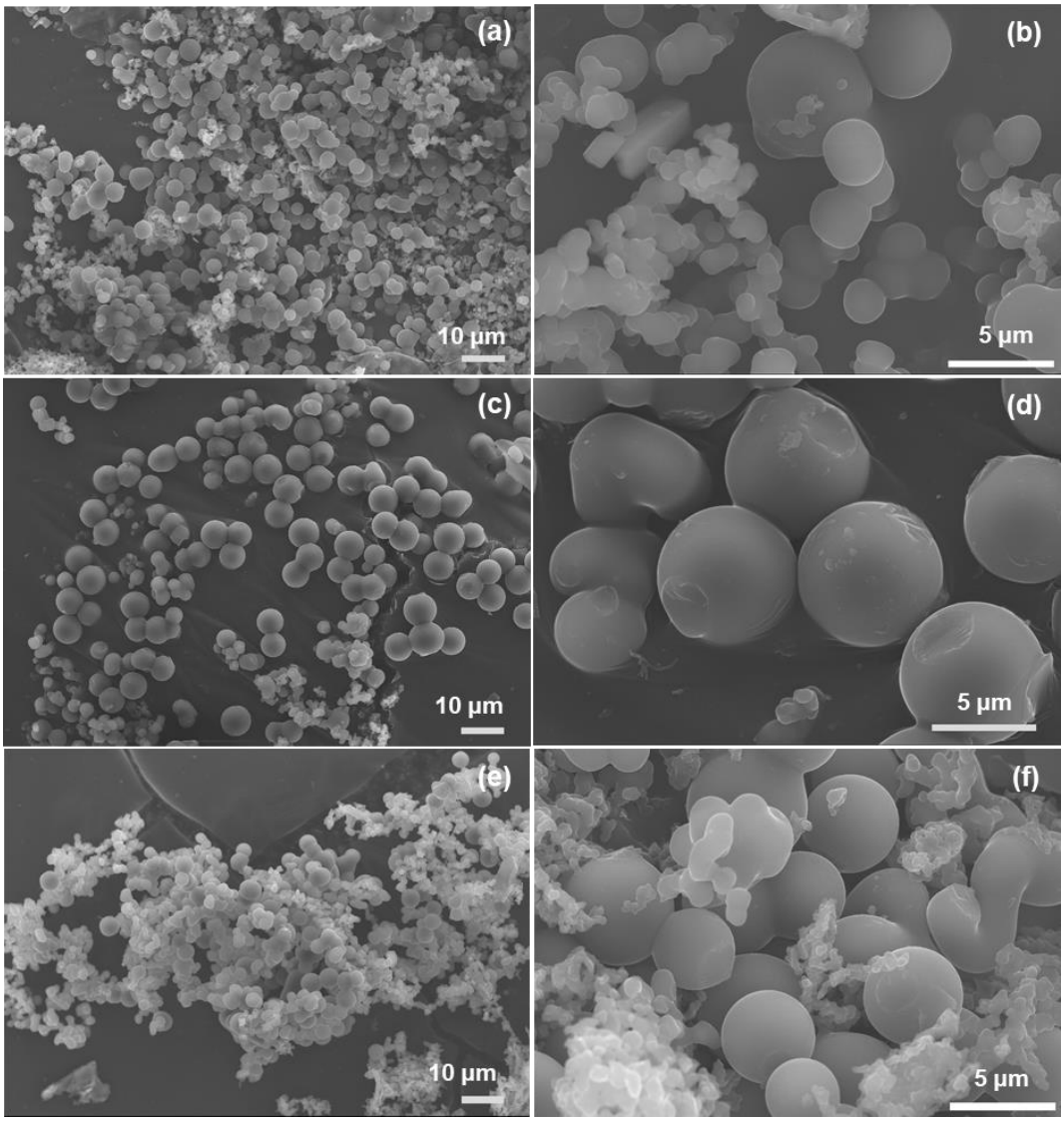


**Figure VI.4**: SEM images of HTC carbon microspheres obtained from the precursors, ι-carrageenan (a, b), κ-carrageenan (c, d) and λ-carrageenan (e, f).

**Figure VI.5** shows the UV/VIS spectra of C-dots colloids obtained from the different carrageenan precursors. The pure C-dots samples present similar UV/VIS spectra, which typically are characterized by a strong optical absorption in the UV region, with an absorption tail extending to the

visible range, but showing transparency for wavelengths longer than 500 nm. The absorption band peaked at 265 nm is ascribed to π-π* electronic transitions of the C=C bonds in the carbon core and the shoulder between 270-290 nm corresponds to n-π* transitions of C=O bonds of functional groups on the surface of the C-dots.[108] The UV/VIS spectra of the three colloidal samples before dialysis are similar, showing also the absorption band at around 255 nm, but with a second band at 290 nm, which is more noticeable for the κ-C and λ-C samples. The digital photographs show the difference between the two C-dots colloids, before and after the dialysis purification step. The synthesized C-dots suspensions were yellow and after dialysis turned light yellow, both showing no particle scattering in the UV/VIS spectra at longer wavelengths. It should be noted that the dialysis step is required to purify the C-dots colloidal suspensions from other luminescent secondary products obtained in the HTC process, such as 5-HMF-related compounds.

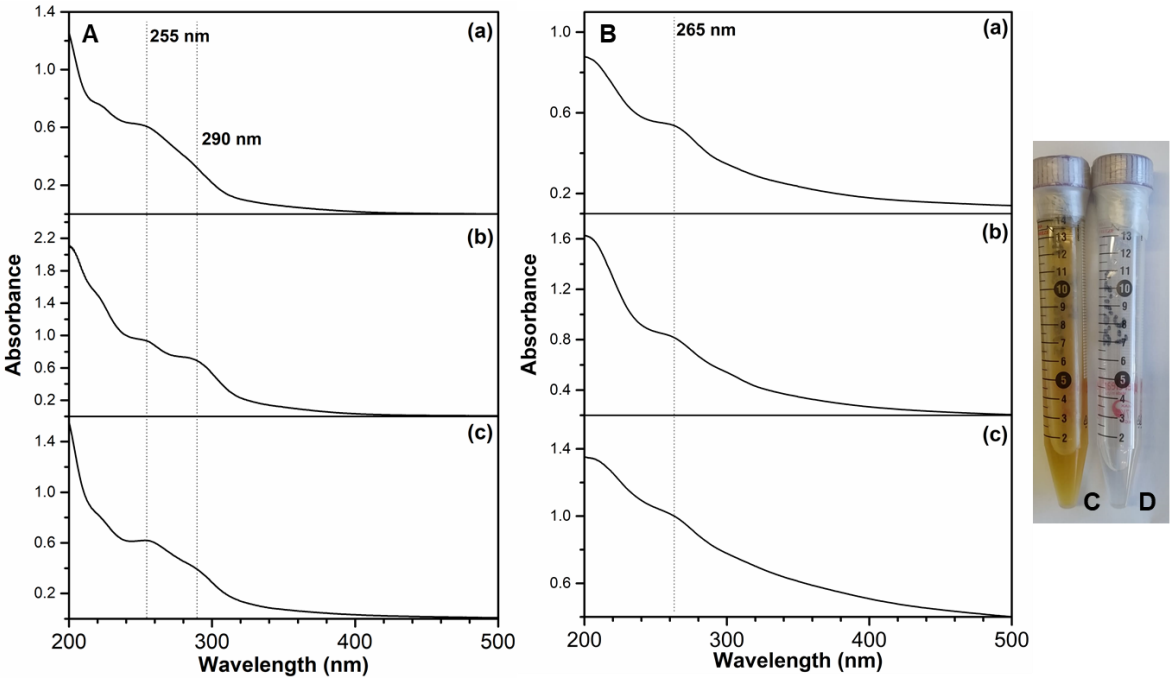


**Figure VI.5**: UV/VIS spectra of the colloids ι-C (a), κ-C (b) and λ-C (c) before (A) and after (B) dialysis. Digital photographs of the colloid κ-C before (C) and after (D) dialysis.

The optical properties of C-dots are still subject of debate and have been compared both to organic fluorophores and conventional semiconductor quantum dots.[501] C-dots are commonly referred as carbon nanolights due to their typical PL[15] and their behaviour is strongly dependent of their structural features.[501] Some reports correlate the optical properties with the band gap electronic transition affected by conjugated π-domains within the small crystalline core, whereas others attribute to the surface-localized defects.[107,501,520] Such electronic transitions display weak absorption in the near UV region but are involved in emitting processes that give rise to intense emission bands in the visible

range.[136,137] In fact, these features influence the observed multicolour PL emission, which is particularly strong in the blue-green region of the visible spectrum.[132–135]

**Figure VI.6** shows the PL and photoluminescence excitation (PLE) spectra of the three samples of pure C-dots. Upon excitation either at 275 nm and 355 nm, the PL emission spectra of the three samples of C-dots shows the presence of a broad band centred at 450-460 nm, thus emitting in the blue region of the visible spectrum, and a shoulder at 535 nm located in the green region. The $\lambda_{exc}$ were set by taking into account the respective PLE spectra of the samples, which display bands at 265 and 360 nm for all materials, in line with the UV/VIS spectra presented before (**Figure VI.5**).

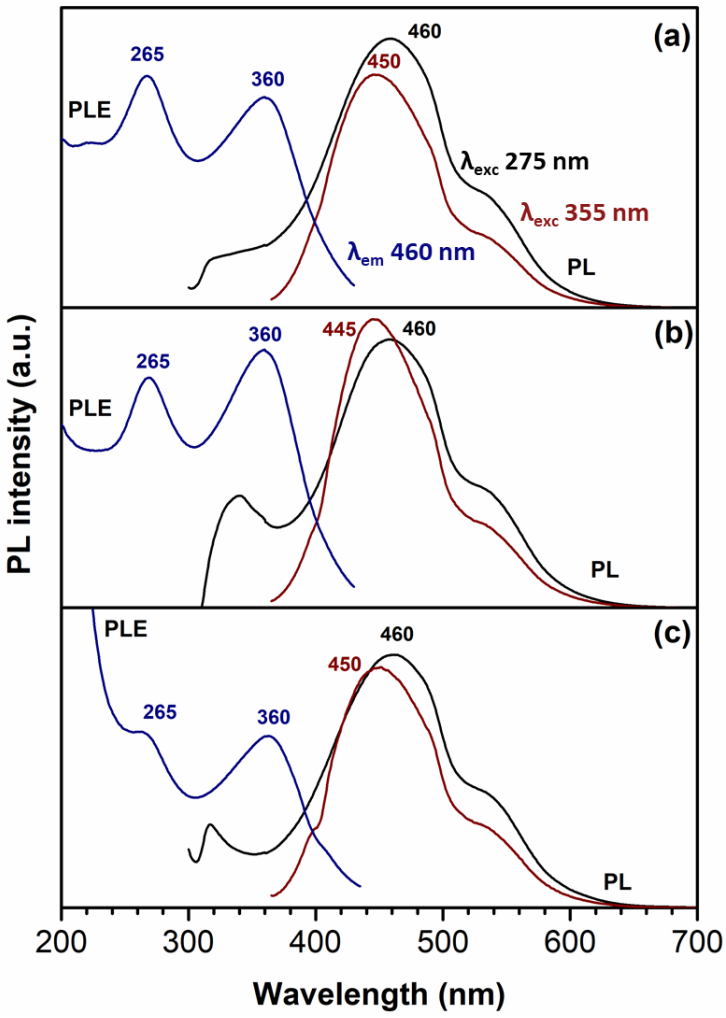


**Figure VI.6**: PL ($\lambda_{exc}$ = 275 and 355 nm) and PLE spectra ($\lambda_{em}$ = 460 nm) of the colloids ι-C (a), κ-C (b) and λ-C (c) after dialysis.

Regardless the carrageenan used as precursor, the resulting C-dots do not show emission maxima that deviate significantly among the samples, which suggest similar size effects. In fact, for the sample with the smaller average particle size (κ-C) it would be expected a blue-shift, as compared

to the PL spectra of the other samples, due to a decrease of aromatic ring conjugation. Although the respective average particle size varies slightly among the three samples analysed, as indicated in **Figure VI.3**, this variation does not cause a visible size effect. On the other hand, the small 10 nm blue-shift observed in the emission band peaked at 460 nm, when varying the $\lambda_{exc}$ from 275 nm to 355 nm, could suggest some differences on the type and/or abundance of functional groups at the surface. However, the magnitude of the observed shift and the tendency of variation do not allow a definite answer about this hypothesis.

In order to get further information about the optical properties of these samples, the PL emission spectra were collected with increasing $\lambda_{exc}$ at 20 nm intervals (from 255 to 355 nm) (**Figure VI.7**). There are several reports that relate excitation-dependent emission to the presence of surface chromophores or to quantum confinement effects due to the size of C-dots.[501] Despite the small shifts observed for the maximum emission band, the data (**Table VI.1**) do not show a clear dependence on the $\lambda_{exc}$, which is consistent with similar size effects for the C-dots obtained by the different carrageenan precursors.

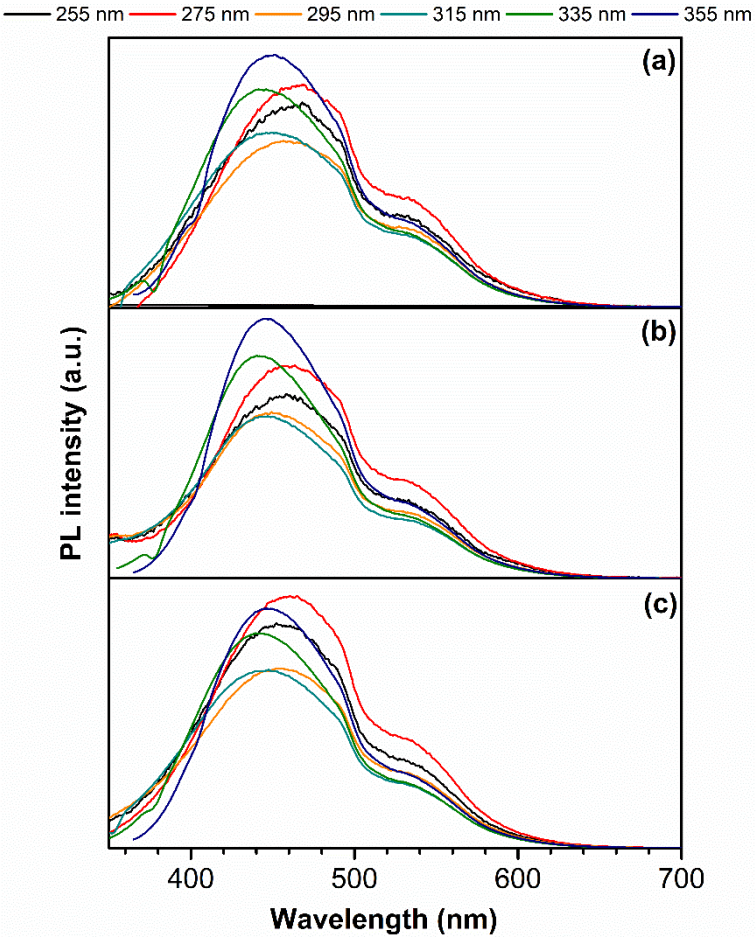


**Figure VI.7**: PL spectra ($\lambda_{exc}$ = 255, 275, 295, 315, 335 and 355 nm) of the colloids ι-C (a), κ-C (b) and λ-C (c).

**Table VI.1**: Emission band observed upon excitation at different wavelengths ($\lambda_{exc}$ = 255, 275, 295, 315, 335 and 355 nm) for the C-dots colloids ι-C, κ-C and λ-C.

| | Emission band (nm) | | |
|---|---|---|---|
| $\lambda_{exc\ (nm)}$ | **ι-C** | **κ-C** | **λ-C** |
| **255** | 460 | 460 | 460 |
| **275** | 460 | 460 | 460 |
| **295** | 460 | 450 | 450 |
| **315** | 450 | 445 | 445 |
| **335** | 445 | 445 | 445 |
| **355** | 445 | 445 | 445 |

TRPL measurements at room temperature were conducted with $\lambda_{exc}$ at 255 and 355 nm, in order to obtain further insights into the luminescent processes observed in these colloidal C-dots (**Figure VI.8**). By the steady-state PL spectra at 255 and 355 nm excitation, it was possible to identify a broad band between 460-480 nm. The PL of the C-dots covers a wide spectral range with a maximum corresponding to the emission in the blue spectral region. With this initial study, by comparing the steady-state PL with the TRPL data for 0.05 ms of delay, the emission band does not shift, matching the spectral shape and peak position, but it was observed a significant decrease in the signal to noise ratio (about one or two orders of magnitude) due to low intensity of the band when excited. This result indicates that the recombination process does not present time dependence after excitation by a short pulse. Due to the low intensity recorded for such excitations it is not possible to infer a proper value for the decay time of the different emissions for these C-dots materials. It is only possible to assume that the decay time should be very fast, probably in the order of nanoseconds, which is in accordance to the data found in literature for C-dots.[521,522]

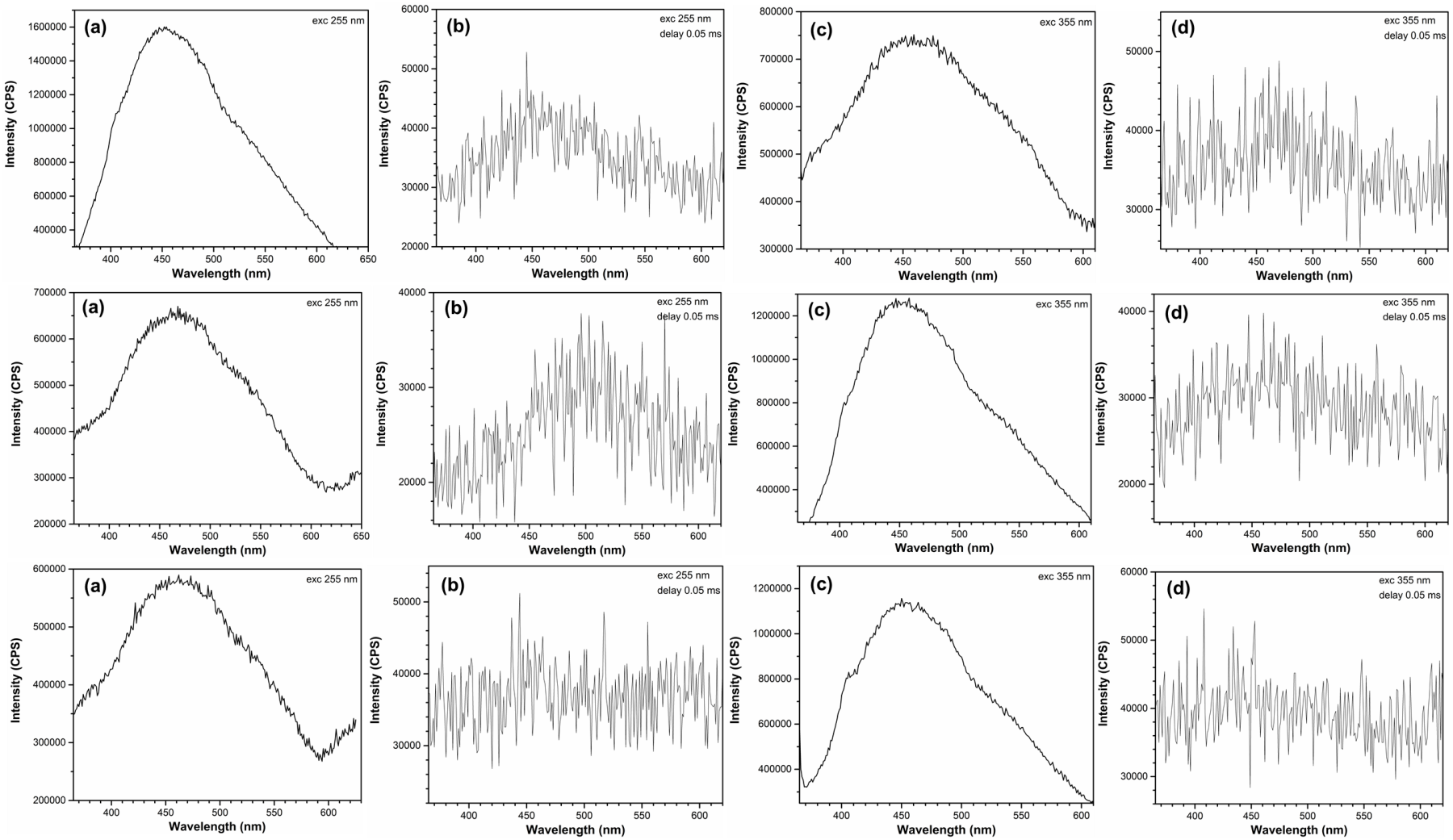


**Figure VI.8**: TRPL spectra of the colloids ι-C (top), κ-C (middle) and λ-C (bottom). $\lambda_{exc}$ = 255 nm at steady-state (a) and with 0.05 ms delay (b); $\lambda_{exc}$ = 355 nm at steady-state (c) and with 0.05 ms delay (d) with a fixed time window of 5 ms.

**Figure VI.9** shows the nanosecond emission decay curves for the three C-dots samples. The decay curves can be well fitted to a triple-exponential function ($X^2$ lower than 2), and the measured PL lifetimes (emission at 460 and 540 nm) are indicated in **Table VI.2**.

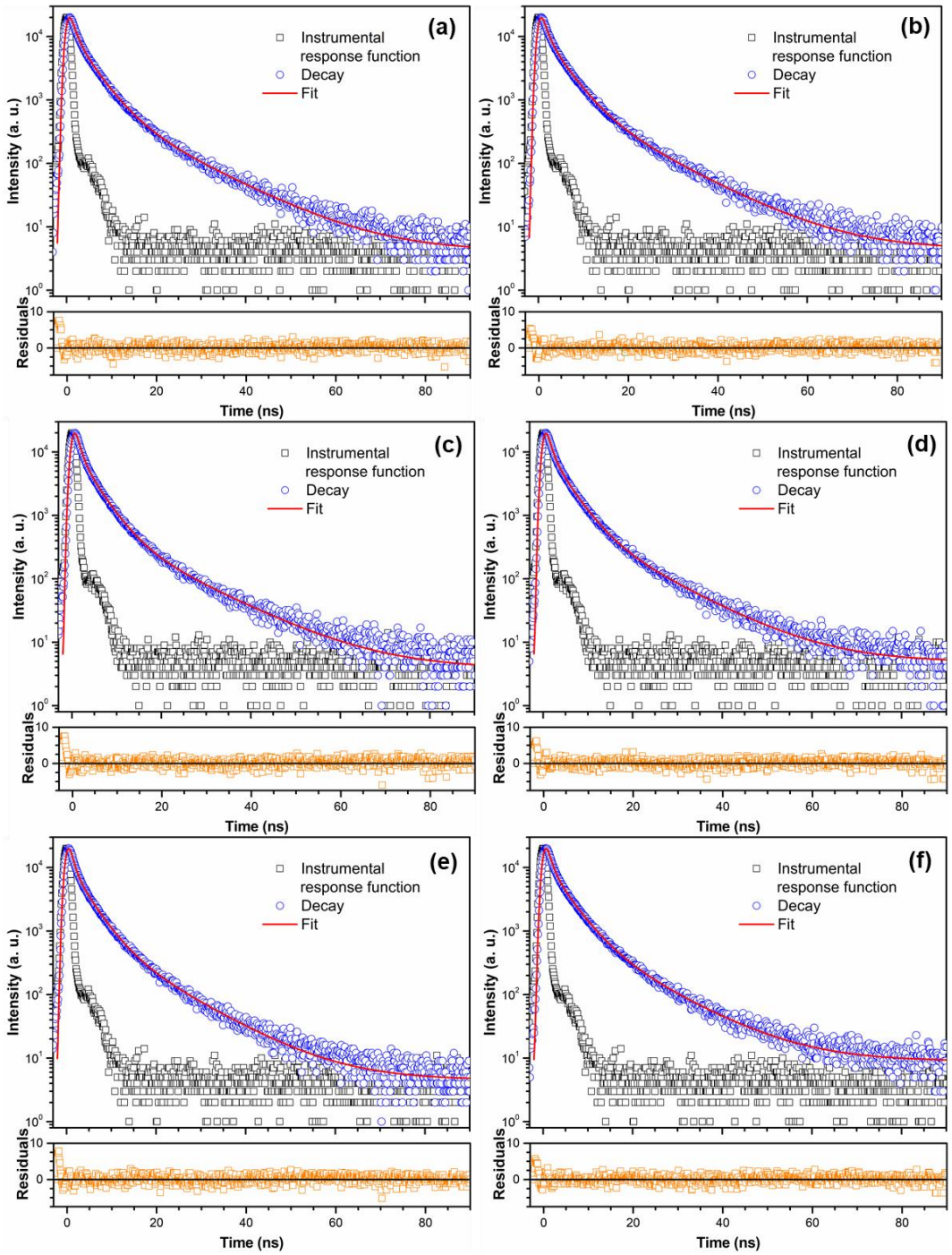


**Figure VI.9**: PL decay curves of the colloids ι-C (a and b), κ-C (c and d) and λ-C (e and f) (blue) recorded at ambient conditions. The emission was detected at 460 nm (a, c and e) and 540 nm (b, d and f) using the NanoLED-390 as excitation source. The instrumental response function (black) was measured using a LUDOX scattering water solution. The solid lines represent the best fits obtained with the DAS6 software from HORIBA, using third-order exponential function.

**Table VI.2**: Measured PL lifetimes for C-dots colloids ι-C, κ-C and λ-C with emission at 460 and 540 nm and NanoLED-390 as excitation source. (τ1, τ2 and τ3: measured lifetimes; α: relative amplitude of the lifetimes; $X^2$: chi-square statistic test).

| Sample | $\lambda_{emission}$ (nm) | Lifetime (ns) | α | $X^2$ |
|---|---|---|---|---|
| ι-C | 460 | τ1 = 1.05 ± 0.027<br>τ2 = 3.86 ± 0.042<br>τ3 = 12.16 ± 0.133 | 28.32%<br>56.17%<br>15.51% | 1.62 |
| | 540 | τ1 = 1.02 ± 0.027<br>τ2 = 3.87 ± 0.039<br>τ3 = 11.65 ± 0.104 | 26.81%<br>55.62%<br>17.57% | 1.29 |
| κ-C | 460 | τ1 = 0.90 ± 0.023<br>τ2 = 3.58 ± 0.036<br>τ3 = 12.44 ± 0.153 | 33.27%<br>53.85%<br>12.88% | 1.61 |
| | 540 | τ1 = 0.85 ± 0.020<br>τ2 = 3.61 ± 0.035<br>τ3 = 11.47 ± 0.118 | 30.48%<br>54.67%<br>14.85% | 1.32 |
| λ-C | 460 | τ1 = 0.76 ± 0.021<br>τ2 = 3.51 ± 0.039<br>τ3 = 10.75 ± 0.113 | 31.52%<br>52.87%<br>15.61% | 1.49 |
| | 540 | τ1 = 0.90 ± 0.021<br>τ2 = 3.85 ± 0.043<br>τ3 = 11.13 ± 0.114 | 28.94%<br>53.94%<br>17.12% | 1.33 |

These PL emissions display similar time dependence, not only by comparing the distinct C-dots but also by measuring the decay times conducted at different emission wavelengths (460 and 540 nm). The detection of three different lifetimes for each C-dots colloid indicates at least three distinct emission processes. This could be ascribed to distinct local environments for the emissive sites located at the surface.

Hence, the TRPL data obtained corroborate two main indications based on the previous study in steady-state PL conditions. First, the use of distinct carrageenans in the employed synthesis conditions does not result in C-dots with markedly distinct PL behaviour. Second, the C-dots samples have similar size populations precluding an observation of size effects but leading to distinct emissive surface sites.

The presence of oxygen-rich groups in C-dots is responsible for the observed water dispersibility and colloidal stability.[520] In fact, the C-dots colloidal suspensions remain stable and clear for several days but with time a black precipitate formed, leading to a clear supernatant solution. Both the solid and the aqueous solution were analysed by Raman spectroscopy. The black precipitate was dispersed in water and deposited on a glass slide, as well as the supernatant solution. The Raman spectra (**Figure VI.10**) of the precipitate show the D band related to the $sp^3$ carbons and the G band of the $sp^2$ (graphitic) carbons.[520] The deconvolution of the Raman bands using the Lorentz function shows the presence of the D1 (1368, 1372 and 1374 $cm^{-1}$) and G (1587, 155 and 1585 $cm^{-1}$) bands reported at the typical values for carbon materials, for the colloids ι-C, κ-C and λ-C, respectively. The Raman data indicate that these materials possess a significant degree of disorder, confirmed by the increased D and G peaks' width when compared with other carbon-based materials. The 2D band, typically located around 2700 $cm^{-1}$, appears as a weak signal, indicating the presence of disordered multi-layered graphite-like structures.[501] The Raman spectra of the isolated solutions did not show the characteristic D and G bands, due to the signal to noise ratio and low Raman intensity (data not shown).

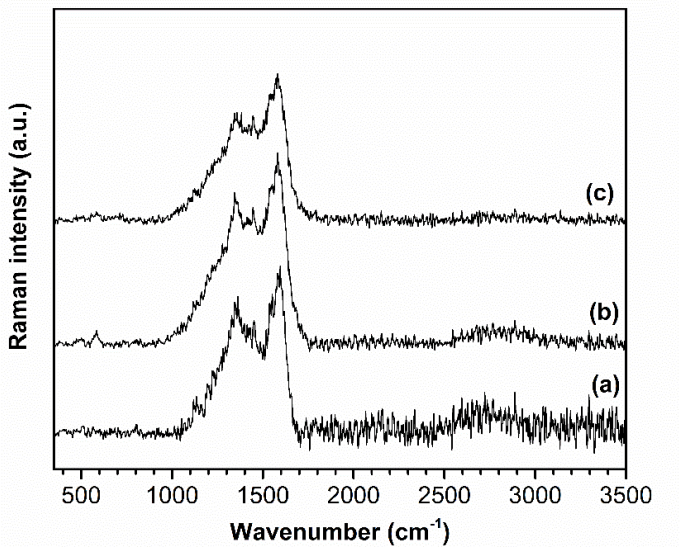


**Figure VI.10**: Raman spectra of precipitates collected from the colloids ι-C (a), κ-C (b) and λ-C (c).

The recovered solid material was redispersed in water and an aliquot of the suspension was analysed by TEM. The TEM image (**Figure VI.11**) shows the presence of nanometric particles, i.e particles bigger than the original C-dots but smaller than the micrometric HTC beads. These particles can be residues of the HTC synthesis, which due to their intermediate sizes were not detected previously. Alternatively, the nanometric particles can result from the coalescence of the most reactive C-dots, leading to submicron structures that precipitate over time, still maintaining C-dots in solution. Indeed, the UV/VIS and PL spectra of the supernatant solution retained the main optical features of the C-dots, which remained clear and stable until the present day.

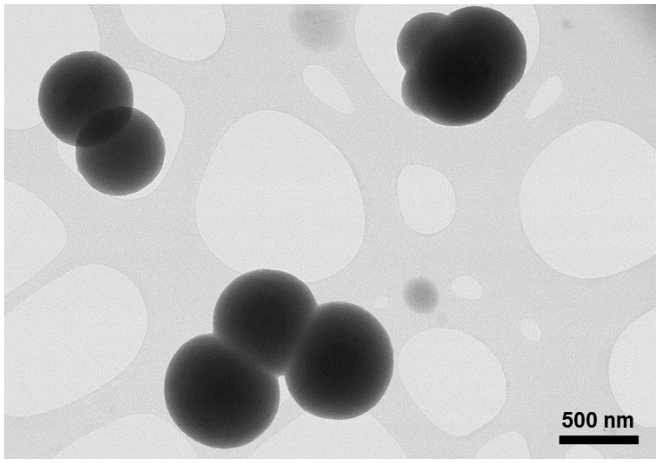


**Figure VI.11**: TEM image of the particles collected as a precipitate from the κ-C suspension.

## 4. Conclusions

A one-step HTC approach was developed to prepare C-dots using three distinct polysaccharides as precursors, ι -, κ- and λ-carrageenan. The colloids of C-dots have particle size distributions with average diameter between 2-3 nm, which is an expected size range for this type of carbon nanostructures. The optical properties of these materials were investigated by conducting absorption and PL studies. These materials possess absorption in the UV region extending until the visible. The PL studies reveal a strong emission band located at around 460 nm, and no $\lambda_{exc}$ dependent behaviour was observed in the investigated conditions. Reports show that the emission of C-dots can be tuned to cover a wider visible range by controlling certain aspects, such as the initial precursors and the surface chemistry, which can be decisive on the optical properties observed. Several reports in literature note that the optical properties of C-dots prepared by HTC and collected in colloidal suspensions are influenced by diverse parameters, such as solvent polarity and pH. Hence, additional studies are required because such effects are likely to affect the surface-light emissions due to particle-solvent interactions. On the other hand, some authors have reported solvent-free C-dots with no excitation dependence on the light emission, such as the C-dots on the present work, despite the later being investigated as colloidal suspensions. In this context, complementary XPS studies can also contribute to assess about the functional groups present. The PL decay curves of the three samples of photoluminescent C-dots indicate three lifetimes measured in the nanosecond range, which is probably due to the presence of distinct local environments for the emissive sites in the surface of C-dots. Overall, there was no evidence for size effects on the PL behaviour of the C-dots obtained from the three distinct polysaccharides. Nevertheless, other experimental conditions should be employed in the future to further confirm these observations.

# CHAPTER VII

## *Final conclusions and future perspectives*

This chapter provides a general overview of the main conclusions and summarises the most important achievements. Moreover, new perspectives for future work are proposed.

# CHAPTER VII | Final conclusions and future perspectives

This thesis was focused on distinct carbon-based materials comprising different structural dimensionalities, GO and other graphene-based materials, carbon microspheres and C-dots. The surface chemistry of such materials was explored with the main goal of developing multicomponent heterogenous photocatalysts for the photodegradation of organic pollutants in water.

**Chapter I** presented an overview on hybrid materials combining carbon-based structures and semiconductor phases that have been developed, exploring their surface chemistry and photocatalytic properties that enabled to efficient harvest visible-light. Pristine semiconductors such as metal sulfide and metal oxide nanoparticles have a small fraction absorption of photons in the visible region, low photocatalytic quantum yield and rapid electron-hole recombination. Strategies have been employed to improve photo-efficiency and performance of nanoparticles as photocatalysts, where carbon materials have been widely explored as a platform for producing hybrid materials exhibiting synergistic properties of interest in heterogeneous (photo)catalysis.

In **Chapter II** and as a first approach, a general one-step route was established to prepare hybrid GO sheets and metal sulfide materials with negligible semiconductor phase segregation. Several metal sulfides phases were explored, such as $Ag_2S$, $Bi_2S_3$, CdS, PbS, CuS and ZnS nanoparticles, where their absorption in the visible spectral region can be tuned according to the semiconductor phase deposited. This chemical route can be easily applied to other graphene-based materials, such as graphite or EGO, providing hybrid nanostructures. This is especially useful for the development of materials using cheaper carbon substrates which ultimately will allow large scale production.

This synthetic method was further investigated using CuS and ZnS as the selected metal sulfide nanophases.

In **Chapter III**, CuS nanoflower-like structures supported on GO were successfully prepared. The photocatalytic performance of the prepared materials was assessed for the removal of RhB and SMX contaminants in water. The hybrid material CuS@GO was found to present high adsorption capacity for both compounds and improved photocatalytic activity in the presence of $H_2O_2$.

Nevertheless, there has been less emphasis in demonstrating that the observed synergistic properties are intrinsic to the nature of the hybrid materials. With this in mind, in **Chapter IV**, SERS was explored as a tool to probe particular regions of GO sheets decorated with the semiconductor ZnS. These studies revealed an enhancement of the Raman signal of a molecular probe, 4-MPy, upon adsorption on the hybrid materials comprising GO sheets and ZnS phases, when compared to the cases where adsorption took place on the individual surface components. GO has a decisive role for the enhancement of the Raman signal observed for this molecular probe due to resonant energy levels generated within the ZnS gap causing changes in the polarizability of the adsorbate. These

results were corroborated by density functional theory calculations showing the adsorption mode on both S and Zn surface sites, with preference towards the sulfur atom due to the influence of GO. The potential of confocal Raman microscopy combined to the SERS effect in ZnS revealed as a useful tool providing Raman maps of the hybrid nanostructures ZnS@GO, which might be applicable to other types of semiconductors deposited on graphene-based materials.

Moving on to other type of carbon-based materials, hydrothermal carbonization methods were investigated as a green strategy to obtain spherical and morphological uniform carbon particles with functional oxygen groups at the surface. In this research work, carrageenans were used as the polysaccharide source to yield carbon microspheres and C-dots through a hydrothermal carbonization route. These materials were explored in the final two chapters of this thesis.

In **Chapter V**, upon a functionalization step to improve the aqueous dispersibility due to the increased presence of oxidized groups at the surface, carbon microspheres were used as a platform for the deposition of $BiVO_4$ phases as an attempt to explore the photocatalytic properties of such materials. The hybrid materials were successfully prepared *via* chemical bath deposition and possessed a well-defined morphology, with an overall uniform distribution at the carbon surface. The monoclinic phase was identified as the phase present in the hybrid material $BiVO_4$@κ-FC. The bi-component material showed a higher photocatalytic activity than pure $BiVO_4$ phases in the degradation of TC in aqueous solutions, which was attributed to a synergistic interaction between the functionalized carbon spheres and the $BiVO_4$ phases, influencing photon harvesting. The addition of $H_2O_2$ led to almost complete photodegradation of TC, as expected for a hydroxyl radical mechanism. The hybrid $BiVO_4$@κ-FC photocatalysts described here are particularly relevant for a costly material such as $BiVO_4$, because less amount is used for achieving good photocatalytic performance.

Finally, **Chapter VI** demonstrated that *en route* with the production of carbon microspheres for development of photocatalysts, the hydrothermal carbonization route can also be explored to produce other types of carbon structures with distinct functionalities. Hence, this chapter described exploratory research on the surface chemistry and optical properties of C-dots prepared by the hydrothermal carbonization of three distinct carrageenans, κ-, ι- and λ-. The three C-dots samples possess similar size distributions, with average sizes between 2-3 nm. Despite the difference in the sulfate groups content between the three carrageenan precursors, there was no evidence for distinct PL behaviour in the colloids obtained by such precursors. The three colloidal solutions presented a UV absorption peaked at 265 nm extending until the visible region, and a strong emission band centered at 460 nm, in the blue region of the visible spectrum. Upon excitation at different wavelengths, the PL spectra did not show significant evidence for size effects. However, distinct PL lifetimes were measured which should be ascribed to three emissions processes related to the different emissive sites at the surface of the C-dots.

Overall, the synthetic routes adopted rely on easy and eco-friendly methods, without use of toxic solvents or other additives. Nowadays, researchers need to address critical factors, namely cost-

effective production, high photostability and high photocatalytic efficiency, which will impact on its future commercialization at large scale for environmental applications, in particular for advanced water purification technologies.

The hybrid carbon-based materials investigated exhibited better performance than their individual counterparts, not only considering their adsorption capacities but also in terms of photocatalytic performances towards the photodegradation of the target pollutants considered here. These results hinted for a synergistic effect between the individual components. Nevertheless, there are still present some limitations concerning its separation after photochemical reaction and the eventual regeneration of the photocatalysts. In this context, the development of photocatalysts that can be easily magnetically separated is of major relevance due to their integration in water treatment stations for subsequent reuse. Due to their low cost and availability, magnetic iron oxides coupled with carbon nanomaterials are interesting photocatalysts for wastewater treatment applications. Among the magnetic materials available, those containing $Fe_3O_4$ nanoparticles appear as particularly relevant due to their tunable magnetic properties, high magnetic susceptibility facilitating a fast separation and eco-friendly nature. Although this strategy was also explored in the frame of a collaborative project (**Chapter III**), further research is required such as the implementation of pilot scale units that use such multifunctional photocatalysts.

Each step of the photocatalytic process, such as charge excitation, separation, transport, adsorption, and surface reaction of the semiconductor may influence the photocatalytic efficiency. Consequently, several factors should be considered and ultimately optimized when designing and manufacturing multifunctional semiconductor photocatalysts, for instance, the concentration, the pH, the temperature, the reactor, the charged nature of the pollutant, as for the light source.

Lastly, the photocatalytic performance of the materials described here should be investigated in real wastewater samples. Hence, would be interesting to study the reaction conditions, such as temperature and source of light (for instance natural sunlight exposure), subjecting these photocatalysts materials to several cycles to assess their efficiency. The photocatalytic reactions should be followed by liquid chromatography and nuclear magnetic resonance spectroscopy to be able to identify and quantify the products formed, in order to assess for adverse toxicological issues coming both from the photocatalytic reaction and the photocatalysts.

Concerning the research on C-dots, other experimental conditions for the synthesis of the colloids should be explored. In fact, it has been reported that the emission of C-dots can be tuned by the experimental conditions, such as the precursor, solvents, doping agents or pH. In particular, it would be of interest to perform the hydrothermal carbonization of the three carrageenans but with distinct degrees of reticulation. A new horizon of applications emerges by being able to tune the emission behaviour of these materials using different precursors, namely due to their potential as biocompatible fluorophores for clinical applications. Also, by coupling C-dots with semiconductor phases (e.g. $TiO_2$), the photocatalytic activity of such materials can be explored.

# REFERENCES


1. United Nations. Transforming our world: the 2030 Agenda for Sustainable Development. https://sdgs.un.org/2030agenda.

2. Savage, N. & Diallo, M. S. Nanomaterials and water purification: Opportunities and challenges. *J. Nanoparticle Res.* **7**, 331–42 (2005).

3. Feng, L., van Hullebusch, E. D., Rodrigo, M. A., Esposito, G. & Oturan, M. A. Removal of residual anti-inflammatory and analgesic pharmaceuticals from aqueous systems by electrochemical advanced oxidation processes. A review. *Chem. Eng. J.* **228**, 944–964 (2013).

4. Sim, W. J. *et al.* Occurrence and distribution of pharmaceuticals in wastewater from households, livestock farms, hospitals and pharmaceutical manufactures. *Chemosphere* **82**, 179–186 (2011).

5. Singh, S., Kumar, V., Romero, R., Sharma, K. & Singh, J. Applications of nanoparticles in wastewater treatment. *Nanotechnol. Life Sci.* **3**, 395–418 (2019).

6. Cai, Z. *et al.* Application of nanotechnologies for removing pharmaceutically active compounds from water: Development and future trends. *Environ. Sci. Nano* **5**, 27–47 (2018).

7. Gogate, P. R. & Pandit, A. B. A review of imperative technologies for wastewater treatment I: Oxidation technologies at ambient conditions. *Adv. Environ. Res.* **8**, 501–551 (2004).

8. Lin, L., Jiang, W., Chen, L., Xu, P. & Wang, H. Treatment of produced water with photocatalysis: Recent advances, affecting factors and future research prospects. *Catalysts* **10**, 924 (2020).

9. Upadhyay, R. K., Soin, N. & Roy, S. S. Role of graphene/metal oxide composites as photocatalysts, adsorbents and disinfectants in water treatment: A review. *RSC Adv.* **4**, 3823–3851 (2014).

10. Kubacka, A., Fernández-Garcia, M. & Colón, G. Advanced nanoarchitectures for solar photocatalytic applications. *Chem. Rev.* 1555–1614 (2011).

11. Sun, B., Qiao, Z., Shang, K., Fan, H. & Ai, S. Facile synthesis of silver sulfide/bismuth sulfide nanocomposites for photocatalytic inactivation of Escherichia coli under solar light irradiation. *Mater. Lett.* **91**, 142–145 (2013).

12. Titirici, M.-M. Hydrothermal carbons: Synthesis, characterization, and applications. in *Novel Carbon Adsorbents* (ed. Tascón, J. M. D.) 351–399 (Elsevier Ltd, 2012).

13. Sayama, K. *et al.* Photoelectrochemical decomposition of water into $H_2$ and $O_2$ on porous $BiVO_4$ thin-film electrodes under visible light and significant effect of Ag ion treatment. *J. Phys. Chem. B* **110**, 11352–11360 (2006).

14. Kudo, A. & Miseki, Y. Heterogeneous photocatalyst materials for water splitting. *Chem. Soc. Rev.* **38**, 253–278 (2009).

15. Baker, S. N. & Baker, G. A. Luminescent carbon nanodots: Emergent nanolights. *Angew. Chemie - Int. Ed.* **49**, 6726–6744 (2010).

16. European Environment Agency. *European waters Assessment of status and pressures 2018*. *EEA Report* (2018).

17. Crini, G. & Lichtfouse, E. Advantages and disadvantages of techniques used for wastewater treatment. *Environ. Chem. Lett.* **17**, 145–155 (2019).

18. Ren, G. *et al.* Recent advances of photocatalytic application in water treatment: A review. *Nanomaterials* **11**, 1804 (2021).

19. Chong, M. N., Jin, B., Chow, C. W. K. & Saint, C. Recent developments in photocatalytic water treatment technology: A review. *Water Res.* **44**, 2997–3027 (2010).

20. Ahmed, S. N. & Haider, W. Heterogeneous photocatalysis and its potential applications in water and wastewater treatment: A review. *Nanotechnology* **29**, (2018).

21. Kroto, H. W., Heath, J. R., O'Brien, S. C., Curl, R. F. & Smalley, R. E. C60: Buckminsterfullerene. *Nature* **318**, 62–63 (1985).

22. Novoselov, K. S. *et al.* Electric Field Effect in Atomically Thin Carbon Films. *Science.* **306**, 666–669 (2004).

23. Linares, N., Silvestre-Albero, A. M., Serrano, E., Silvestre-Albero, J. & García-Martínez, J. Mesoporous materials for clean energy technologies. *Chem. Soc. Rev.* **43**, 7681–7717 (2014).

24. Titirici, M.-M. *et al.* Sustainable carbon materials. *Chem. Soc. Rev.* **44**, 250–290 (2015).

25. Spyrou, K. & Rudolf, P. An Introduction to Graphene. in *Functionalization of Graphene* (ed. Georgakilas, V.) 1–18 (Wiley VCH, 2014).

26. Cai, M., Thorpe, D., Adamson, D. H. & Schniepp, H. C. Methods of graphite exfoliation. *J. Mater. Chem.* **22**, 24992–25002 (2012).

27. Putri, L. K., Tan, L. L., Ong, W. J., Chang, W. S. & Chai, S. P. Graphene oxide: Exploiting its unique properties toward visible-light-driven photocatalysis. *Appl. Mater. Today* **4**, 9–16 (2016).

28. Radich, J. G., Krenselewski, A. L., Zhu, J. & Kamat, P. V. Is graphene a stable platform for photocatalysis? Mineralization of reduced graphene oxide with UV-irradiated $TiO_2$ nanoparticles. *Chem. Mater.* **26**, 4662–4668 (2014).

29. Han, L., Wang, P. & Dong, S. Progress in graphene-based photoactive nanocomposites as a promising class of photocatalyst. *Nanoscale* **4**, 5814–5825 (2012).

30. Ciesielski, A. & Samorì, P. Graphene via sonication assisted liquid-phase exfoliation. *Chem. Soc. Rev.* **43**, 381–398 (2014).

31. Hontoria-Lucas, C., López-Peinado, A. J., López-González, J. de D., Rojas-Cervantes, M. L. & Martín-Aranda, R. M. Study of oxygen-containing groups in a series of graphite oxides: Physical and chemical characterization. *Carbon N. Y.* **33**, 1585–1592 (1995).

32. Zhu, Y. *et al.* Graphene and graphene oxide: Synthesis, properties and applications. *Adv. Mater.* **22**, 3906–3924 (2010).

33. Jilani, A. *et al.* Graphene and its derivatives: Synthesis, modifications and applications in wastewater treatment. *Environ. Chem. Lett.* **16**, 1301–1323 (2018).

34. Boukhvalov, D. W. & Katsnelson, M. I. Chemical functionalization of graphene with defects. *Nano Lett.* **8**, 4374–4379 (2008).

35. Khan, U. *et al.* Solvent-exfoliated graphene at extremely high concentration. *Langmuir* **27**, 9077–9082 (2011).

36. Bourlinos, A. B., Georgakilas, V., Zboril, R., Sterioti, T. A. & Stubos, A. K. Liquid-phase exfoliation of graphite towards solubilized graphenes. *Small* **5**, 1841–1845 (2009).

37. Coleman, J. N. Liquid exfoliation of defect-free graphene. *Acc. Chem. Res.* **46**, 14–22 (2013).

38. Khan, U., O'Neill, A., Lotya, M., De, S. & Coleman, J. N. High-concentration solvent exfoliation of graphene. *Small* **6**, 864–871 (2010).

39. Hernandez, Y. *et al.* High-yield production of graphene by liquid-phase exfoliation of graphite. *Nat. Nanotechnol.* **3**, 563–568 (2008).

40. Compton, O. C. & Nguyen, S. T. Graphene oxide, highly reduced graphene oxide and graphene: Versatile building blocks for carbon-based materials. *Small* **6**, 711–723 (2010).

41. Wang, H.-X. X., Wang, Q., Zhou, K.-G. G. & Zhang, H.-L. L. Graphene in light: Design, synthesis and applications of photo-active graphene and graphene-like materials. *Small* **9**, 1266–1283 (2013).

42. Lerf, A. *et al.* Hydration behavior and dynamics of water molecules in graphite oxide. *J. Phys. Chem. Solids* **67**, 1106–1110 (2006).

43. Patil, A. J., Vickery, J. L., Scott, T. B. & Mann, S. Aqueous stabilization and self-assembly of graphene sheets into layered bio-nanocomposites using DNA. *Adv. Mater.* **21**, 3159–3164 (2009).

44. Si, Y. Y., Samulski, E. E. T., Hill, C. & Carolina, N. Synthesis of water soluble graphene. *Nano Lett.* **8**, 1679–1682 (2008).

45. Liang, Y., Wu, D., Feng, X. & Müllen, K. Dispersion of graphene sheets in organic solvent supported by ionic interactions. *Adv. Mater.* **21**, 1679–1683 (2009).

46. Lomeda, J. R., Doyle, C. D., Kosynkin, D. V., Hwang, W. F. & Tour, J. M. Diazonium functionalization of surfactant-wrapped chemically converted graphene sheets. *J. Am. Chem. Soc.* **130**, 16201–16206 (2008).

47. Yang, H. *et al.* Covalent functionalization of polydisperse chemically-converted graphene sheets with amine-terminated ionic liquid. *Chem. Commun.* 3880–3882 (2009).

48. Georgakilas, V. *et al.* Noncovalent functionalization of graphene and graphene oxide for energy materials, biosensing, catalytic and biomedical applications. *Chem. Rev.* **116**, 5464–5519 (2016).

49. Hummers, W. S. & Offeman, R. E. Preparation of graphitic oxide. *J. Am. Chem. Soc.* **80**, 1339 (1958).

50. Zhao, J., Liu, L. & Li, F. *Graphene oxide: Physics and applications*. (Springer-Verlag Berlin Heidelberg, 2015).

51. Mauter, M. S. & Elimelech, M. Environmental applications of carbon-based nanomaterials. *Am. Chem. Soc.* 5843–5859 (2008).

52. Gong, X., Liu, G., Li, Y., Yu, D. Y. W. & Teoh, W. Y. Functionalized-graphene composites: Fabrication

and applications in sustainable energy and environment. *Chem. Mater.* **28**, 8082–8118 (2016).

53. Allen, M. J., Tun, V. C. & Kaner, R. B. Honeycomb carbon: A review of graphene. *Chem Soc Rev* **110**, 132–145 (2010).

54. Iijima, S. Helical microtubules of graphitic carbon. *Nature* **354**, 56–58 (1991).

55. Iijima, S. & Ichihashi, T. Single-shell carbon nanotubes of 1-nm diameter. *Nature* **363**, 603–605 (1993).

56. Liu, Z., Tabakman, S., Welsher, K. & Dai, H. Carbon nanotubes in biology and medicine: In vitro and in vivo detection, imaging and drug delivery. *Nano Res.* **2**, 85–120 (2009).

57. Dresselhaus, M. S., Dresselhaus, G. & Saito, R. Physics of carbon nanotubes. *Carbon.* **33**, 883–891 (1995).

58. Prasek, J. *et al.* Methods for carbon nanotubes synthesis - Review. *J. Mater. Chem.* **21**, 15872–15884 (2011).

59. Kouklin, N., Tzolov, M., Straus, D., Yin, a. & Xu, J. M. Infrared absorption properties of carbon nanotubes synthesized by chemical vapor deposition. *Appl. Phys. Lett.* **85**, 4463 (2004).

60. Oberlin, A., Endo, M. & Koyama, T. Filamentous growth of carbon through benzene decomposition. *J. Cryst. Growth* **32**, 335–349 (1976).

61. Mubarak, N. M., Yusof, F. & Alkhatib, M. F. The production of carbon nanotubes using two-stage chemical vapor deposition and their potential use in protein purification. *Chem. Eng. J.* **168**, 461–469 (2011).

62. Kruusenberg, I. *et al.* Effect of purification of carbon nanotubes on their electrocatalytic properties for oxygen reduction in acid solution. *Carbon N. Y.* **49**, 4031–4039 (2011).

63. Zhu, Y. *et al.* The effect of nickel content of composite catalysts synthesized by hydrothermal method on the preparation of carbon nanotubes. *Mater. Sci. Eng. B Solid-State Mater. Adv. Technol.* **127**, 198–202 (2006).

64. Soulie-Ziakovic, C., Nicolay, R., Prevoteau, A. & Leibler, L. Dispersible carbon nanotubes. *Chem. Eur. J.* **20**, 1210–1217 (2014).

65. Heister, E., Brunner, E. W., Dieckmann, G. R., Jurewicz, I. & Dalton, A. B. Are carbon nanotubes a natural solution? Applications in biology and medicine. *ACS Appl. Mater. Interfaces* **5**, 1870–1891 (2013).

66. Pantarotto, D. *et al.* Functionalized carbon nanotubes for plasmid DNA gene delivery. *Angew. Chemie - Int. Ed.* **43**, 5242–5246 (2004).

67. Singh, R. *et al.* Binding and condensation of plasmid DNA onto functionalized carbon nanotubes: Toward the construction of nanotube-based gene delivery vectors. *J. Am. Chem. Soc.* **127**, 4388–4396 (2005).

68. Bonard, J. *et al.* Purification and size-selection of carbon nanotubes. *Adv. Mater.* 827–831 (1997).

69. Richard, C., Balavoine, F., Schultz, P., Ebbesen, T. W. & Mioskowski, C. Supramolecutar self-assembly of lipid derivatives on carbon nanotubes. *Science.* **300**, 775–778 (2003).

70. Wanless, E. J. & Ducker, W. A. Organization of sodium dodecyl sulfate at the graphite-solution interface. *J. Phys. Chem.* **100**, 3207–3214 (1996).

71. Datsyuk, V. *et al.* Chemical oxidation of multiwalled carbon nanotubes. *Carbon.* **46**, 833–840 (2008).

72. Spitalsky, Z., Tasis, D., Papagelis, K. & Galiotis, C. Carbon nanotube-polymer composites: Chemistry, processing, mechanical and electrical properties. *Prog. Polym. Sci.* **35**, 357–401 (2010).

73. Campidelli, S. *et al.* Facile decoration of functionalized single-wall carbon nanotubes with phthalocyanines via 'click chemistry'. *J. Am. Chem. Soc.* **130**, 11503–11509 (2008).

74. Zhao, B., Hu, H., Yu, A., Perea, D. & Haddon, R. C. Synthesis and characterization of water soluble single-walled carbon nanotube graft copolymers. *J. Am. Chem. Soc.* **127**, 8197–8203 (2005).

75. Prevoteau, A., Soulié-Ziakovic, C. & Leibler, L. Universally dispersible carbon nanotubes. *J. Am. Chem. Soc.* **134**, 19961–19964 (2012).

76. Szleifer, I. & Yerushalmi-Rozen, R. Polymers and carbon nanotubes - Dimensionality, interactions and nanotechnology. *Polymer.* **46**, 7803–7818 (2005).

77. Estrada, A. C., Mendoza, E. & Trindade, T. Decoration of carbon nanostructures with metal sulfides by sonolysis of single-molecule precursors. *Eur. J. Inorg. Chem.* **2014**, 3184–3190 (2015).

78. Varghese, O. K. *et al.* Gas sensing characteristics of multi-wall carbon nanotubes. *Sensors Actuators, B Chem.* **81**, 32–41 (2001).

79. Merkoçi, A. *et al.* New materials for electrochemical sensing VI: Carbon nanotubes. *Trends Anal. Chem.* **24**, 826–838 (2005).

80. Gooding, J. J. Nanostructuring electrodes with carbon nanotubes: A review on electrochemistry and applications for sensing. *Electrochim. Acta* **50**, 3049–3060 (2005).

81. Bianco, A., Kostarelos, K. & Prato, M. Applications of carbon nanotubes in drug delivery. *Curr. Opin. Chem. Biol.* **9**, 674–679 (2005).

82. Liu, Z. *et al.* Drug delivery with carbon nanotubes for in vivo cancer treatment. *Cancer Res.* **68**, 6652–6660 (2008).

83. Avouris, P. Molecular electronics with carbon nanotubes. *Acc. Chem. Res.* **35**, 1026–1034 (2002).

84. Park, S., Vosguerichian, M. & Bao, Z. A review of fabrication and applications of carbon nanotube film-based flexible electronics. *Nanoscale* **5**, 1727–1752 (2013).

85. Cao, Q. & Rogers, J. A. Ultrathin films of single-walled carbon nanotubes for electronics and sensors: A review of fundamental and applied aspects. *Adv. Mater.* **21**, 29–53 (2009).

86. Onishchenko, D. V., Reva, V. P. & Kuryavyi, V. G. Hydrogen storage in multilayer carbon nanotubes. *Appl. Phys. Lett.* **76**, 2877–2879 (2000).

87. Yang, R. T. Hydrogen storage by alkali-doped carbon nanotubes-revisited. *Carbon.* **38**, 623–641 (2000).

88. Dillon, A. C. *et al.* Storage of hydrogen in single-walled carbon nanotubes. *Nature.* **386**, 377–379 (1997).

89. Yu, Y. *et al.* Enhancement of adsorption and photocatalytic activity of $TiO_2$ by using carbon nanotubes for the treatment of azo dye. *Appl. Catal. B Environ.* **61**, 1–11 (2005).

90. Yu, Y. *et al.* Enhancement of photocatalytic activity of mesoporous $TiO_2$ by using carbon nanotubes. *Appl. Catal. A Gen.* **289**, 186–196 (2005).

91. Xu, Y. J., Zhuang, Y. & Fu, X. New insight for enhanced photocatalytic activity of $TiO_2$ by doping carbon nanotubes: A case study on degradation of benzene and methyl orange. *J. Phys. Chem. C* **114**, 2669–2676 (2010).

92. Woan, K., Pyrgiotakis, G. & Sigmund, W. Photocatalytic carbon-nanotube-$TiO_2$ composites. *Adv. Mater.* **21**, 2233–2239 (2009).

93. Ding, L. *et al.* Molecular characterization of the cytotoxic mechanism of multiwall carbon nanotubes and nano-onions on human skin fibroblast. *Nano Lett.* **5**, 2448–2464 (2005).

94. Poland, C. A. *et al.* Carbon nanotubes introduced into the abdominal cavity of mice show asbestos-like pathogenicity in a pilot study. *Nat. Nanotechnol.* **3**, 423–428 (2008).

95. Cui, D., Tian, F., Ozkan, C. S., Wang, M. & Gao, H. Effect of single wall carbon nanotubes on human HEK293 cells. *Toxicol. Lett.* **155**, 73–85 (2005).

96. Cherukuri, P., Bachilo, S. M., Litovsky, S. H. & Weisman, R. B. Near-infrared fluorescence microscopy of single-walled carbon nanotubes in phagocytic cells. *J. Am. Chem. Soc.* **126**, 15638–15639 (2004).

97. Liu, Z., Winters, M., Holodniy, M. & Dai, H. siRNA delivery into human T cells and primary cells with carbon-nanotube transporters. *Angew. Chemie - Int. Ed.* **46**, 2023–2027 (2007).

98. Liu, Z., Sun, X., Nakayama-Ratchford, N. & Dai, H. Supramolecular chemistry on water-soluble carbon nanotubes for drug loading and delivery. *ACS Nano* **1**, 50–56 (2007).

99. Perepelytsina, O. M. *et al.* Influence of carbon nanotubes and its derivatives on tumor cells in vitro and biochemical parameters, cellular blood composition in vivo. *Nanoscale Res. Lett.* **13**, (2018).

100. Da Ros, T. *et al.* Carbon nanotubes as nanovectors for intracellular delivery of laronidase in mucopolysaccharidosis type I. *Nanoscale* **10**, 657–665 (2018).

101. Kavosi, A. *et al.* The toxicity and therapeutic effects of single-and multi-wall carbon nanotubes on mice breast cancer. *Sci. Rep.* **8**, 1–12 (2018).

102. Dong, X. *et al.* Thermosensitive hydrogel loaded with chitosan-carbon nanotubes for near infrared light triggered drug delivery. *Colloids Surfaces B Biointerfaces* **154**, 253–262 (2017).

103. Zhang, M. *et al.* Magnetic and fluorescent carbon nanotubes for dual modal imaging and photothermal and chemo-therapy of cancer cells in living mice. *Carbon N. Y.* **123**, 70–83 (2017).

104. Schipper, M. L. *et al.* A pilot toxicology study of single-walled carbon nanotubes in a small sample of mice. *Nat. Nanotechnol.* **3**, 216–221 (2008).

105. Xu, X. *et al.* Electrophoretic analysis and purification of fluorescent single-walled carbon nanotube fragments. *J. Am. Chem. Soc.* **126**, 12736–12737 (2004).

106. Georgakilas, V., Perman, J. A., Tucek, J. & Zboril, R. Broad family of carbon nanoallotropes: Classification, chemistry and applications of fullerenes, carbon dots, nanotubes, graphene, nanodiamonds and combined superstructures. *Chem. Rev.* **115**, 4744–4822 (2015).

107. Lim, S. Y., Shen, W. & Gao, Z. Carbon quantum dots and their applications. *Chem. Soc. Rev.* **44**, 362–

381 (2015).

108. Wang, Y. & Hu, A. Carbon quantum dots: Synthesis, properties and applications. *J. Mater. Chem. C Mater. Opt. Electron. devices* **2**, 6921–6939 (2014).

109. Liu, H., Ye, T. & Mao, C. Fluorescent carbon nanoparticles derived from candle soot. *Angew. Chemie - Int. Ed.* **46**, 6473–6475 (2007).

110. Yu, S. J., Kang, M. W., Chang, H. C., Chen, K. M. & Yu, Y. C. Bright fluorescent nanodiamonds: No photobleaching and low cytotoxicity. *J. Am. Chem. Soc.* **127**, 17604–17605 (2005).

111. Zhou, J. *et al.* An electrochemical avenue to blue luminescent nanocrystals from multiwalled carbon nanotubes (MWCNTs). *J. Am. Chem. Soc.* **129**, 744–745 (2007).

112. Zhai, X. *et al.* Highly luminescent carbon nanodots by microwave-assisted pyrolysis. *Chem. Commun.* **48**, 7955–7957 (2012).

113. Dong, Y. *et al.* Extraction of electrochemiluminescent oxidized carbon quantum dots from activated carbon. *Chem. Mater.* **22**, 5895–5899 (2010).

114. Sun, Y. P. *et al.* Quantum-sized carbon dots for bright and colorful photoluminescence. *J. Am. Chem. Soc.* **128**, 7756–7757 (2006).

115. Bourlinos, A. B. *et al.* Surface functionalized carbogenic quantum dots. *Small* **4**, 455–458 (2008).

116. Liu, R. *et al.* An aqueous route to multicolor photoluminescent carbon dots using silica spheres as carriers. *Angew. Chemie - Int. Ed.* **48**, 4598–4601 (2009).

117. Li, H. *et al.* One-step ultrasonic synthesis of water-soluble carbon nanoparticles with excellent photoluminescent properties. *Carbon.* **49**, 605–609 (2011).

118. Peng, H. & Travas-Sejdic, J. Simple aqueous solution route to luminescent carbogenic dots from carbohydrates. *Chem. Mater.* **21**, 5563–5565 (2009).

119. Zhu, S. *et al.* Highly photoluminescent carbon dots for multicolor patterning, sensors, and bioimaging. *Angew. Chemie - Int. Ed.* **52**, 3953–3957 (2013).

120. Yang, Z.-C. C. *et al.* Intrinsically fluorescent carbon dots with tunable emission derived from hydrothermal treatment of glucose in the presence of monopotassium phosphate. *Chem. Commun.* **47**, 11615–11617 (2011).

121. Yang, Y. *et al.* One-step synthesis of amino-functionalized fluorescent carbon nanoparticles by hydrothermal carbonization of chitosan. *Chem. Commun.* **48**, 380–382 (2012).

122. Zhang, Z., Hao, J., Zhang, J., Zhang, B. & Tang, J. Protein as the source for synthesizing fluorescent carbon dots by a one-pot hydrothermal route. *RSC Adv.* **2**, 8599–8601 (2012).

123. Bhunia, S. K., Saha, A., Maity, A. R., Ray, S. C. & Jana, N. R. Carbon nanoparticle-based fluorescent bioimaging probes. *Sci. Rep.* **3**, 1473 (2013).

124. Xu, Y. *et al.* Nitrogen-doped carbon dots: A facile and general preparation method, photoluminescence investigation and imaging applications. *Chem. - A Eur. J.* **19**, 2276–2283 (2013).

125. Li, H. *et al.* Fluorescent carbon nanoparticles: Electrochemical synthesis and their pH sensitive

photoluminescence properties. *New J. Chem.* **35**, 2666–2670 (2011).

126. Guo, Y., Wang, Z., Shao, H. & Jiang, X. Hydrothermal synthesis of highly fluorescent carbon nanoparticles from sodium citrate and their use for the detection of mercury ions. *Carbon.* **52**, 583–589 (2013).

127. Yang, Z.-C. C., Li, X. & Wang, J. Intrinsically fluorescent nitrogen-containing carbon nanoparticles synthesized by a hydrothermal process. *Carbon.* **49**, 5207–5212 (2011).

128. Zhang, B., Liu, C. Y. & Liu, Y. A novel one-step approach to synthesize fluorescent carbon nanoparticles. *Eur. J. Inorg. Chem.* 4411–4414 (2010).

129. Chowdhury, D., Gogoi, N. & Majumdar, G. Fluorescent carbon dots obtained from chitosan gel. *RSC Adv.* **2**, 12156–12159 (2012).

130. Li, H., Kang, Z., Liu, Y. & Lee, S.-T. T. Carbon nanodots: Synthesis, properties and applications. *J. Mater. Chem.* **22**, 24230–24253 (2012).

131. Puvvada, N. *et al.* Synthesis of biocompatible multicolor luminescent carbon dots for bioimaging applications. *Sci. Technol. Adv. Mater.* **13**, 045008 (2012).

132. Gokus, T. *et al.* Making graphene luminescent by oxygen plasma treatment. *ACS Nano* **3**, 3963–3968 (2009).

133. Shen, J., Zhu, Y., Chen, C., Yang, X. & Li, C. Facile preparation and upconversion luminescence of graphene quantum dots. *Chem. Commun.* **47**, 2580–2582 (2011).

134. Shen, J. *et al.* One-pot hydrothermal synthesis of graphene quantum dots surface-passivated by polyethylene glycol and their photoelectric conversion under near-infrared light. *New J. Chem.* **36**, 97–101 (2012).

135. Nourbakhsh, A. *et al.* Bandgap opening in oxygen plasma-treated graphene. *Nanotechnology* **21**, 435203 (2010).

136. Cao, L., Meziani, M. J., Sahu, S. & Sun, Y. P. Photoluminescence properties of graphene versus other carbon nanomaterials. *Acc. Chem. Res.* **46**, 171–182 (2013).

137. Demchenko, A. P. & Dekaliuk, M. O. Novel fluorescent carbonic nanomaterials for sensing and imaging. *Methods Appl. Fluoresc.* **1**, 042001 (2013).

138. Wang, F., Xie, Z., Zhang, H., Liu, C. Y. & Zhang, Y. G. Highly luminescent organosilane-functionalized carbon dots. *Adv. Funct. Mater.* **21**, 1027–1031 (2011).

139. Li, H., Zhang, Y., Wang, L., Tian, J. & Sun, X. Nucleic acid detection using carbon nanoparticles as a fluorescent sensing platform. *Chem. Commun.* **47**, 961–963 (2011).

140. Zhao, H. X. *et al.* Highly selective detection of phosphate in very complicated matrixes with an off-on fluorescent probe of europium-adjusted carbon dots. *Chem. Commun.* **47**, 2604–2606 (2011).

141. Sun, Y.-P. P. *et al.* Doped carbon nanoparticles as a new platform for highly photoluminescent dots. *J. Phys. Chem. C* **112**, 18295–18298 (2008).

142. Fan, R. J., Sun, Q., Zhang, L., Zhang, Y. & Lu, A. H. Photoluminescent carbon dots directly derived from polyethylene glycol and their application for cellular imaging. *Carbon N. Y.* **71**, 87–93 (2014).

143. Qian, Z. *et al.* Highly Luminescent N-doped carbon quantum dots as an effective multifunctional fluorescence sensing platform. *Chem. Eur. J.* **20**, 2254–2263 (2014).

144. Zhang, Y. L. *et al.* Graphitic carbon quantum dots as a fluorescent sensing platform for highly efficient detection of $Fe^{3+}$ ions. *RSC Adv.* **3**, 3733–3738 (2013).

145. Wee, S. S., Ng, Y. H. & Ng, S. M. Synthesis of fluorescent carbon dots via simple acid hydrolysis of bovine serum albumin and its potential as sensitive sensing probe for lead (II) ions. *Talanta* **116**, 71–76 (2013).

146. Kwon, W. *et al.* Freestanding luminescent films of nitrogen-rich carbon nanodots toward large-scale phosphor-based white-light-emitting devices. *Chem. Mater.* **25**, 1893–1899 (2013).

147. Zhang, X. *et al.* Color-switchable electroluminescence of carbon dot light-emitting diodes. *ACS Nano* 11234–11241 (2013).

148. De, M., Ghosh, P. S. & Rotello, V. M. Applications of nanoparticles in biology. *Adv. Mater.* **20**, 4225–4241 (2008).

149. Yang, S.-T. T. *et al.* Carbon dots as nontoxic and high-performance fluorescence imaging agents. *J. Phys. Chem. C* **113**, 18110–18114 (2009).

150. Sun, Y.-P. *et al.* Carbon dots for optical imaging in vivo. *J. Am. Chem. Soc.* **131**, 11308–9 (2009).

151. Ray, S. C., Saha, A., Jana, N. R. & Sarkar, R. Fluorescent carbon nanoparticles: Synthesis, characterization and bioimaging application. *J. Phys. Chem. C* **113**, 18546–18551 (2009).

152. Lim, S. F. *et al.* In vivo and scanning electron microscopy imaging of upconverting nanophosphors in Caenorhabditis elegans. *Nano Lett.* **6**, 169–174 (2006).

153. Gaya, U. I. *Heterogeneous photocatalysis using inorganic semiconductor solids*. (Springer, 2014).

154. Fresno, F., Portela, R., Suárez, S. & Coronado, J. M. Photocatalytic materials: recent achievements and near future trends. *J. Mater. Chem. A* **2**, 2863–2884 (2014).

155. Williams, G., Seger, B. & Kamat, P. V. $TiO_2$-graphene nanocomposites. UV-assisted photocatalytic reduction of graphene oxide. *ACS Nano* **2**, 1487–1491 (2008).

156. Lightcap, I. V., Kosel, T. H. & Kamat, P. V. Anchoring semiconductor and metal nanoparticles on a two-dimensional catalyst mat. storing and shuttling electrons with reduced graphene oxide. *Nano Lett.* **10**, 577–583 (2010).

157. Momma, K. & Izumi, F. VESTA 3 for three-dimensional visualization of crystal, volumetric and morphology data. *J. Appl. Crystallogr.* **44**, 1272–1276 (2011).

158. Yang, S., Feng, X. & Müllen, K. Sandwich-like, graphene-based titania nanosheets with high surface area for fast lithium storage. *Adv. Mater.* **23**, 3575–3579 (2011).

159. Sun, L., Zhao, Z., Zhou, Y. & Liu, L. Anatase $TiO_2$ nanocrystals with exposed {001} facets on graphene sheets via molecular grafting for enhanced photocatalytic activity. *Nanoscale* **4**, 613–620 (2012).

160. Zhu, C. *et al.* One-pot, water-phase approach to high-quality graphene/$TiO_2$ composite nanosheets. *Chem. Commun.* **46**, 7148–7150 (2010).

161. Li, K. *et al.* Preparation of graphene/$TiO_2$ composites by nonionic surfactant strategy and their simulated sunlight and visible light photocatalytic activity towards representative aqueous POPs degradation. *J. Hazard. Mater.* **250**–**251**, 19–28 (2013).

162. Liu, X. *et al.* Microwave-assisted synthesis of ZnO-graphene composite for photocatalytic reduction of Cr(VI). *Catal. Sci. Technol.* **1**, 1189–1193 (2011).

163. Ton, N. N. T. *et al.* One-pot synthesis of $TiO_2$/graphene nanocomposites for excellent visible light photocatalysis based on chemical exfoliation method. *Carbon.* **133**, 109–117 (2018).

164. Zhang, Z., Xiao, F., Guo, Y., Wang, S. & Liu, Y. One-pot self-assembled three-dimensional $TiO_2$-graphene hydrogel. *ACS Appl. Mater. Interfaces* **6**, 2227–2233 (2013).

165. Pan, X. *et al.* Comparing graphene-$TiO_2$ nanowire and graphene-$TiO_2$ nanoparticle composite photocatalysts. *ACS Appl. Mater. Interfaces* **4**, 3944–3950 (2012).

166. Najafi, M., Kermanpur, A., Rahimipour, M. R. & Najafizadeh, A. Effect of $TiO_2$ morphology on structure of $TiO_2$-graphene oxide nanocomposite synthesized via a one-step hydrothermal method. *J. Alloys Compd.* **722**, 272–277 (2017).

167. Safajou, H., Khojasteh, H., Salavati-Niasari, M. & Mortazavi-Derazkola, S. Enhanced photocatalytic degradation of dyes over graphene/Pd/$TiO_2$ nanocomposites: $TiO_2$ nanowires versus $TiO_2$ nanoparticles. *J. Colloid Interface Sci.* **498**, 423–432 (2017).

168. Kumar, S., Sharma, V., Bhattacharyya, K. & Krishnan, V. Synergetic effect of $MoS_2$-RGO doping to enhance the photocatalytic performance of ZnO nanoparticles. *New J. Chem.* **40**, 5185–5197 (2016).

169. Atchudan, R., Edison, T. N. J. I., Perumal, S., Karthikeyan, D. & Lee, Y. R. Facile synthesis of zinc oxide nanoparticles decorated graphene oxide composite via simple solvothermal route and their photocatalytic activity on methylene blue degradation. *J. Photochem. Photobiol. B Biol.* **162**, 500–510 (2016).

170. Rabieh, S., Nassimi, K. & Bagheri, M. Synthesis of hierarchical ZnO-reduced graphene oxide nanocomposites with enhanced adsorption-photocatalytic performance. *Mater. Lett.* **162**, 28–31 (2016).

171. Dong, X. *et al.* Hybrid structure of zinc oxide nanorods and three dimensional graphene foam for supercapacitor and electrochemical sensor applications. *RSC Adv.* **2**, 4364–4369 (2012).

172. Yein, W. T., Wang, Q., Feng, X., Li, Y. & Wu, X. Enhancement of photocatalytic performance in sonochemical synthesized ZnO–rGO nanocomposites owing to effective interfacial interaction. *Environ. Chem. Lett.* **16**, 251–264 (2018).

173. Yin, Z. *et al.* Electrochemical deposition of ZnO nanorods on transparent reduced graphene oxide electrodes for hybrid solar cells. *Small* **6**, 307–312 (2010).

174. Wu, C., Li, F., Zhang, Y. & Guo, T. Improving the field emission of graphene by depositing zinc oxide nanorods on its surface. *Carbon.* **50**, 3622–3626 (2012).

175. Xu, S. *et al.* Preparation of ZnO flower/reduced graphene oxide composite with enhanced photocatalytic performance under sunlight. *Ceram. Int.* **41**, 4007–4013 (2015).

176. Lonkar, S. P., Pillai, V. & Abdala, A. Solvent-free synthesis of ZnO-graphene nanocomposite with

superior photocatalytic activity. *Appl. Surf. Sci.* **465**, 1107–1113 (2019).

177. Guler, Ö. *et al.* Electrical and optical properties of carbon nanotube hybrid zinc oxide nanocomposites prepared by ball mill technique. *Fullerenes Nanotub. Carbon Nanostructures* **23**, 865–869 (2015).

178. Zhang, Y. *et al.* Carbon nanotube-ZnO nanocomposite electrodes for supercapacitors. *Solid State Ionics* **180**, 1525–1528 (2009).

179. Paul, R., Kumbhakar, P. & Mitra, A. K. Bluegreen luminescence by SWCNT/ZnO hybrid nanostructure synthesized by a simple chemical route. *Phys. E Low-Dimensional Syst. Nanostructures* **43**, 279–284 (2010).

180. Saleh, T. A., Gondal, M. A. & Drmosh, Q. A. Preparation of a MWCNT/ZnO nanocomposite and its photocatalytic activity for the removal of cyanide from water using a laser. *Nanotechnology* **21**, 495705 (2010).

181. Aïssa, B., Fauteux, C., Khakani, M. A. El & Therriault, D. Structural and photoluminescence properties of laser processed ZnO/carbon nanotube nanohybrids. *J. Mater. Res.* **24**, 3313–3320 (2009).

182. Mäki-Jaskari, M. A. & Rantala, T. T. Band structure and optical parameters of the $SnO_2$ (110) surface. *Phys. Rev. B - Condens. Matter Mater. Phys.* **64**, 1–7 (2001).

183. Seema, H., Christian Kemp, K., Chandra, V. & Kim, K. S. Graphene-$SnO_2$ composites for highly efficient photocatalytic degradation of methylene blue under sunlight. *Nanotechnology* **23**, 355705 (2012).

184. Wu, F. *et al.* Enhanced photocatalytic activities of $SnO_2$ by graphene oxide and its application in antibacterial. *Opt. Quantum Electron.* **50**, 1–16 (2018).

185. Sagadevan, S. *et al.* A facile hydrothermal approach for catalytic and optical behavior of tin oxide-graphene ($SnO_2$/G) nanocomposite. *PLoS One* **13**, 1–15 (2018).

186. Wu, Z. & Wang, L. Graphene oxide (GO)-doping $SnO_2$ flower-like structure to enhance photocatalytic activity. *Fullerenes Nanotub. Carbon Nanostructures* **27**, 1–9 (2019).

187. Tang, L., Nguyen, V. H., Lee, Y. R., Kim, J. & Shim, J. J. Photocatalytic activity of reduced graphene oxide/$SnO_2$ nanocomposites prepared in ionic liquid. *Synth. Met.* **201**, 54–60 (2015).

188. Kim, T. *et al.* Facile synthesis of $SnO_2$ aerogel/reduced graphene oxide nanocomposites via in situ annealing for the photocatalytic degradation of methyl orange. *Nanomaterials* **9**, 358 (2019).

189. Liang, B., Han, D., Sun, C., Zhang, W. & Qin, Q. Reduced graphene oxide-SnO nanocomposites with good visible-light photoactivity. *Int. J. Mater. Res.* **109**, 880–884 (2018).

190. Xie, Y., Yu, S., Zhong, Y., Zhang, Q. & Zhou, Y. $SnO_2$/graphene quantum dots composited photocatalyst for efficient nitric oxide oxidation under visible light. *Appl. Surf. Sci.* **448**, 655–661 (2018).

191. Chen, Y. *et al.* Photochemical fabrication of $SnO_2$ dense layers on reduced graphene oxide sheets for application in photocatalytic degradation of p-Nitrophenol. *Appl. Catal. B Environ.* **215**, 8–17 (2017).

192. Diebold, U. The surface science of titanium dioxide. *Surf. Sci. Rep.* **48**, 53–229 (2002).

193. Klingshirn, C. F. ZnO: Material, physics and applications. *ChemPhysChem* **8**, 782–803 (2007).

194. Parkinson, G. S. Iron oxide surfaces. *Surf. Sci. Rep.* **71**, 272–365 (2016).

195. L. E. Brus. Electron-electron and electron-hole interactions in small semiconductor crystallites: The size dependence of the lowest excited electronic state. *J. Chem. Phys.* **80**, 4403–4409 (1984).

196. Trindade, T., O'Brien, P. & Pickett, N. L. Nanocrystalline semiconductors: Synthesis, properties and perspectives. *Chem. Mater.* **13**, 3843–3858 (2001).

197. Smith, A. M. A. M. & Nie, S. Semiconductor nanocrystals: Structure, properties and band gap engineering. *Acc. Chem. Res.* **43**, 190–200 (2010).

198. Xiang, Q., Yu, J. & Jaroniec, M. Graphene-based semiconductor photocatalysts. *Chem. Soc. Rev.* **41**, 782–796 (2012).

199. El-Sayed, M. A. Small is different: Shape-, size-, and composition-dependent properties of some colloidal semiconductor nanocrystals. *Acc. Chem. Res.* **37**, 326–333 (2004).

200. Ayodhya, D. & Veerabhadram, G. A review on recent advances in photodegradation of dyes using doped and heterojunction based semiconductor metal sulfide nanostructures for environmental protection. *Mater. Today Energy* **9**, 83–113 (2018).

201. Chen, F. J., Cao, Y. L. & Jia, D. Z. A room-temperature solid-state route for the synthesis of graphene oxide-metal sulfide composites with excellent photocatalytic activity. *CrystEngComm* **15**, 4747–4754 (2013).

202. Manga, K. K. *et al.* High-performance broadband photodetector using solution-processible PbSe-$TiO_2$-graphene hybrids. *Adv. Mater.* **24**, 1697–1702 (2012).

203. Liu, F. *et al.* Solvothermal synthesis of graphene-CdS nanocomposites for highly efficient visible-light photocatalyst. *J. Alloys Compd.* **551**, 327–332 (2013).

204. Mo, Z. *et al.* Graphene sheets/$Ag_2S$ nanocomposites: Synthesis and their application in supercapacitor materials. *Mater. Lett.* **68**, 416–418 (2012).

205. Kaur, M., Umar, A., Mehta, S. K. & Kansal, S. K. Reduced graphene oxide-CdS heterostructure: An efficient fluorescent probe for the sensing of Ag(I) and sunset yellow and a visible-light responsive photocatalyst for the degradation of levofloxacin drug in aqueous phase. *Appl. Catal. B Environ.* **245**, 143–158 (2019).

206. Sagadevan, S. *et al.* One pot synthesis of hybrid ZnS–Graphene nanocomposite with enhanced photocatalytic activities using hydrothermal approach. *J. Mater. Sci. Mater. Electron.* **29**, 9099–9107 (2018).

207. Wei, X. N., Ou, C. L., Guan, X. X., Peng, Z. K. & Zheng, X. C. Facile assembly of CdS-reduced graphene oxide heterojunction with enhanced elimination performance for organic pollutants in wastewater. *Appl. Surf. Sci.* **469**, 666–673 (2019).

208. Yu, L., Ruan, H., Zheng, Y. & Li, D. A facile solvothermal method to produce ZnS quantum dots-decorated graphene nanosheets with superior photoactivity. *Nanotechnology* **24**, (2013).

209. Zhang, Y., Zhang, N., Tang, Z. R. & Xu, Y. J. Graphene transforms wide band gap ZnS to a visible light photocatalyst. The new role of graphene as a macromolecular photosensitizer. *ACS Nano* **6**, 9777–9789 (2012).

210. Shi, J. *et al.* Sonochemical synthesis of CuS/reduced graphene oxide nanocomposites with enhanced absorption and photocatalytic performance. *Mater. Lett.* **126**, 220–223 (2014).

211. Bai, S. *et al.* Optical properties and a simple and general route for the rapid syntheses of reduced graphene oxide-metal sulfide nanocomposites. *Eur. J. Inorg. Chem.* 256–262 (2013).

212. Hu, H., Wang, X., Liu, F., Wang, J. & Xu, C. Rapid microwave-assisted synthesis of graphene nanosheets-zinc sulfide nanocomposites: Optical and photocatalytic properties. *Synth. Met.* **161**, 404–410 (2011).

213. Liu, X. *et al.* Microwave-assisted synthesis of CdS-reduced graphene oxide composites for photocatalytic reduction of Cr(VI). *Chem. Commun.* **47**, 11984–11986 (2011).

214. Thangavel, S., Krishnamoorthy, K., Kim, S. J. & Venugopal, G. Designing ZnS decorated reduced graphene-oxide nanohybrid via microwave route and their application in photocatalysis. *J. Alloys Compd.* **683**, 456–462 (2016).

215. Chen, F., Cao, Y., Jia, D. & Liu, A. Solid-state synthesis of ZnS/graphene nanocomposites with enhanced photocatalytic activity. *Dye. Pigment.* **120**, 8–14 (2015).

216. Chen, Y. *et al.* Facile synthesis of well-dispersed $Bi_2S_3$ nanoparticles on reduced graphene oxide and enhanced photocatalytic activity. *Appl. Surf. Sci.* **378**, 231–238 (2016).

217. Hull, S., Keen, D. A., Sivia, D. S., Madden, P. A. & Wilson, M. The high-temperature superionic behaviour of $Ag_2S$. *J. Phys. Condens. Matter* **14**, 9–17 (2002).

218. Chen, A., Bian, Z., Xu, J., Xin, X. & Wang, H. Simultaneous removal of Cr(VI) and phenol contaminants using Z-scheme bismuth oxyiodide/reduced graphene oxide/bismuth sulfide system under visible-light irradiation. *Chemosphere* **188**, 659–666 (2017).

219. Lopes, J., Estrada, A., Fateixa, S., Ferro, M. & Trindade, T. A general route for growing metal sulfides onto graphene oxide and exfoliated graphite oxide. *Nanomaterials* **7**, 245 (2017).

220. Liu, F., Shao, X., Li, H., Wang, M. & Yang, S. Facile fabrication of $Bi_2S_3$-ZnS nanohybrids on graphene sheets with enhanced electrochemical performances. *Mater. Lett.* **108**, 125–128 (2013).

221. Wang, L. *et al.* Photocatalytic degradation of organic pollutants using rGO supported $TiO_2$-CdS composite under visible light irradiation. *J. Alloys Compd.* **683**, 318–328 (2016).

222. Tian, Z. *et al.* Hydrothermal synthesis of graphene/$TiO_2$/CdS nanocomposites as efficient visible-light-driven photocatalysts. *Mater. Lett.* **194**, 172–175 (2017).

223. Liu, T. *et al.* RGO/$Ag_2S$/$TiO_2$ ternary heterojunctions with highly enhanced UV-NIR photocatalytic activity and stability. *Appl. Catal. B Environ.* **204**, 593–601 (2017).

224. Ziylan, A. & Ince, N. H. The occurrence and fate of anti-inflammatory and analgesic pharmaceuticals in sewage and fresh water: Treatability by conventional and non-conventional processes. *J. Hazard. Mater.* **187**, 24–36 (2011).

225. Wang, N., Xu, J. & Guan, L. Synthesis and enhanced photocatalytic activity of tin oxide nanoparticles coated on multi-walled carbon nanotube. *Mater. Res. Bull.* **46**, 1372–1376 (2011).

226. Worajittiphon, P., Pingmuang, K., Inceesungvorn, B., Wetchakun, N. & Phanichphant, S. Enhancing the

photocatalytic activity of ZnO nanoparticles for efficient rhodamine B degradation by functionalised graphene nanoplatelets. *Ceram. Int.* **41**, 1885–1889 (2015).

227. Madima, N., Mishra, S. B., Inamuddin, I. & Mishra, A. K. Carbon-based nanomaterials for remediation of organic and inorganic pollutants from wastewater. A review. *Environ. Chem. Lett.* **18**, 1169–1191 (2020).

228. Du, A. *et al.* Hybrid graphene/titania nanocomposite: Interface charge transfer, hole doping, and sensitization for visible light response. *J. Phys. Chem. Lett.* **2**, 894–899 (2011).

229. Liang, Y., Wang, H., Casalongue, H. S., Chen, Z. & Dai, H. $TiO_2$ Nanocrystals grown on graphene as advanced photocatalytic hybrid materials. *Nano Res.* **3**, 701–705 (2010).

230. Lee, J. S., You, K. H. & Park, C. B. Highly photoactive, low bandgap $TiO_2$ nanoparticles wrapped by graphene. *Adv. Mater.* **24**, 1084–1088 (2012).

231. Zhang, H., Lv, X., Li, Y., Wang, Y. & Li, J. P25-graphene composite as a high performance photocatalyst. *ACS Nano* **4**, 380–386 (2010).

232. Chen, C. *et al.* Synthesis of visible-light responsive graphene oxide/$TiO_2$ composites with p/n heterojunction. *ACS Nano* **4**, 6425–6432 (2010).

233. Lin, C. *et al.* GO/$TiO_2$ composites as a highly active photocatalyst for the degradation of methyl orange. *J. Mater. Res.* **35**, 1307–1315 (2020).

234. Víctor-Román, S. *et al.* Controlling the surface chemistry of graphene oxide: Key towards efficient ZnO-GO photocatalysts. *Catal. Today* **357**, 350–360 (2020).

235. Azarang, M., Shuhaimi, A., Yousefi, R. & Jahromi, S. P. One-pot sol-gel synthesis of reduced graphene oxide uniformly decorated zinc oxide nanoparticles in starch environment for highly efficient photodegradation of methylene blue. *RSC Adv.* **5**, 21888–21896 (2015).

236. Qin, J. *et al.* ZnO microspheres-reduced graphene oxide nanocomposite for photocatalytic degradation of methylene blue dye. *Appl. Surf. Sci.* **392**, 196–203 (2017).

237. Xu, J., Cui, Y., Han, Y., Hao, M. & Zhang, X. ZnO-graphene composites with high photocatalytic activities under visible light. *RSC Adv.* **6**, 96778–96784 (2016).

238. Tien, H. N. *et al.* One-pot synthesis of a reduced graphene oxide-zinc oxide sphere composite and its use as a visible light photocatalyst. *Chem. Eng. J.* **229**, 126–133 (2013).

239. Bu, Y., Chen, Z., Li, W. & Hou, B. Highly efficient photocatalytic performance of graphene-ZnO quasi-shell-core composite material. *ACS Appl. Mater. Interfaces* **5**, 12361–12368 (2013).

240. Trung, D., Trinh, T., Khanitchaidecha, W. & Channei, D. Synthesis, characterization and environmental applications of bismuth vanadate. *Res. Chem. Intermed.* **45**, 5217–5259 (2019).

241. Sajid, M. M. *et al.* Hydrothermal fabrication of monoclinic bismuth vanadate (m-$BiVO_4$) nanoparticles for photocatalytic degradation of toxic organic dyes. *Mater. Sci. Eng. B Solid-State Mater. Adv. Technol.* **242**, 83–89 (2019).

242. Zhang, L., Chen, D. & Jiao, X. Monoclinic structured $BiVO_4$ nanosheets: Hydrothermal preparation, formation mechanism, and coloristic and photocatalytic properties. *J. Phys. Chem. B* **110**, 2668–2673

(2006).

243. Zhou, L. *et al.* A sonochemical route to visible-light-driven high-activity $BiVO_4$ photocatalyst. *J. Mol. Catal. A Chem.* **252**, 120–124 (2006).

244. Soltani, T., Tayyebi, A. & Lee, B. K. Enhanced photoelectrochemical (PEC) and photocatalytic properties of visible-light reduced graphene-oxide/bismuth vanadate. *Appl. Surf. Sci.* **448**, 465–473 (2018).

245. Wang, Y. *et al.* Fabrication of $BiVO_4$/$BiPO_4$/GO composite photocatalytic material for the visible light-driven degradation. *J. Clean. Prod.* **247**, 119108 (2020).

246. Liu, C. *et al.* Leaf-like $BiVO_4$ nanostructure decorated by nitrogen-doped carbon quantum dots: Binary heterostructure photocatalyst for enhanced photocatalytic performance. *Mater. Res. Bull.* **122**, 110640 (2020).

247. Liu, S. Q. Magnetic semiconductor nano-photocatalysts for the degradation of organic pollutants. *Environ. Chem. Lett.* **10**, 209–216 (2012).

248. Tahar, L. Ben, Oueslati, M. H. & Abualreish, M. J. A. Synthesis of magnetite derivatives nanoparticles and their application for the removal of chromium (VI) from aqueous solutions. *J. Colloid Interface Sci.* **512**, 115–126 (2018).

249. Tang, S. C. N. & Lo, I. M. C. Magnetic nanoparticles: Essential factors for sustainable environmental applications. *Water Res.* **47**, 2613–2632 (2013).

250. Banerjee, S. K. & Moskowitz, B. M. Ferrimagnetic properties of nagnetite. in *Magnetite biomineralization and magnetoreception in organisms* (eds. Kirschvink, J. L., Jones, D. S. & MacFadden, B. J.) 17–42 (Plenum Press - New York and London, 1985).

251. Wu, W., Wu, Z., Yu, T., Jiang, C. & Kim, W. S. Recent progress on magnetic iron oxide nanoparticles: Synthesis, surface functional strategies and biomedical applications. *Sci. Technol. Adv. Mater.* **16**, 023501 (2015).

252. Shen, Y. F. *et al.* Preparation and application of magnetic $Fe_3O_4$ nanoparticles for wastewater purification. *Sep. Purif. Technol.* **68**, 312–319 (2009).

253. Wang, F. *et al.* Removal of ciprofloxacin from aqueous solution by a magnetic chitosan grafted graphene oxide composite. *J. Mol. Liq.* **222**, 188–194 (2016).

254. Padhi, D. K., Panigrahi, T. K., Parida, K., Singh, S. K. & Mishra, P. M. Green synthesis of $Fe_3O_4$/RGO nanocomposite with enhanced photocatalytic performance for Cr(VI) reduction, phenol degradation and antibacterial activity. *ACS Sustain. Chem. Eng.* **5**, 10551–10562 (2017).

255. Nazari, Y. & Salem, S. Efficient photocatalytic methylene blue degradation by $Fe_3O_4$@$TiO_2$ core/shell linked to graphene by aminopropyltrimethoxysilane. *Environ. Sci. Pollut. Res.* **26**, 25359–25371 (2019).

256. Ma, P. *et al.* Synthesis and photocatalytic property of $Fe_3O_4$@$TiO_2$ core/shell nanoparticles supported by reduced graphene oxide sheets. *J. Alloys Compd.* **578**, 501–506 (2013).

257. Xuan, S., Jiang, W., Gong, X., Hu, Y. & Chen, Z. Magnetically separable $Fe_3O_4$/$TiO_2$ hollow spheres: Fabrication and photocatalytic activity. *J. Phys. Chem. C* **113**, 553–558 (2009).

258. Nada, A. A., Tantawy, H. R., Elsayed, M. A., Bechelany, M. & Elmowafy, M. E. Elaboration of nano titania-magnetic reduced graphene oxide for degradation of tartrazine dye in aqueous solution. *Solid State Sci.* **78**, 116–125 (2018).

259. Benjwal, P., Kumar, M., Chamoli, P. & Kar, K. K. Enhanced photocatalytic degradation of methylene blue and adsorption of arsenic(III) by reduced graphene oxide (rGO)-metal oxide ($TiO_2$/$Fe_3O_4$) based nanocomposites. *RSC Adv.* **5**, 73249–73260 (2015).

260. Lin, Y. *et al.* Ternary graphene-$TiO_2$-$Fe_3O_4$ nanocomposite as a recollectable photocatalyst with enhanced durability. *Eur. J. Inorg. Chem.* 4439–4444 (2012).

261. Li, Z. Q., Wang, H. L., Zi, L. Y., Zhang, J. J. & Zhang, Y. S. Preparation and photocatalytic performance of magnetic $TiO_2$–$Fe_3O_4$/graphene (RGO) composites under VIS-light irradiation. *Ceram. Int.* **41**, 10634–10643 (2015).

262. Tang, Y. *et al.* Synthesis of reduced graphene oxide/magnetite composites and investigation of their adsorption performance of fluoroquinolone antibiotics. *Colloids Surfaces A Physicochem. Eng. Asp.* **424**, 74–80 (2013).

263. Hao, H. & Lang, X. Metal sulfide photocatalysis: Visible-light-induced organic transformations. *ChemCatChem* **11**, 1378–1393 (2019).

264. Sharma, S. *et al. Tailoring cadmium sulfide-based photocatalytic nanomaterials for water decontamination: a review*. *Environmental Chemistry Letters* (Springer International Publishing, 2020).

265. Zhang, N., Yang, M. Q., Tang, Z. R. & Xu, Y. J. CdS-graphene nanocomposites as visible light photocatalyst for redox reactions in water: A green route for selective transformation and environmental remediation. *J. Catal.* **303**, 60–69 (2013).

266. Wang, J. *et al.* Preparation of $Bi_2S_3$/carbon quantum dot hybrid materials with enhanced photocatalytic properties under ultraviolet-, visible- and near infrared-irradiation. *Nanoscale* **9**, 15873–15882 (2017).

267. Khalid, A. *et al.* Bismuth sulfide photocatalysis water treatment under visible irradiation. *Res. Chem. Intermed.* **47**, 3395–3409 (2021).

268. Hu, W. *et al.* Preparation and photocatalytic activity of graphene-modified $Ag_2S$ composite. *J. Exp. Nanosci.* **11**, 433–443 (2016).

269. Cao, Q., Che, R. & Chen, N. Scalable synthesis of $Cu_2S$ double-superlattice nanoparticle systems with enhanced UV/visible-light-driven photocatalytic activity. *Appl. Catal. B Environ.* **162**, 187–195 (2015).

270. Srinivas, B., Kumar, B. G. & Muralidharan, K. Stabilizer free copper sulphide nanostructures for rapid photocatalytic decomposition of rhodamine B. *J. Mol. Catal. A Chem.* **410**, 8–18 (2015).

271. Ayodhya, D. *et al.* Photocatalytic degradation of dye pollutants under solar, visible and UV lights using green synthesised CuS nanoparticles. *J. Exp. Nanosci.* **11**, 418–432 (2016).

272. Li, S. *et al.* Fast synthesis of CuS and $Cu_9S_5$ microcrystal using subcritical and supercritical methanol and their application in photocatalytic degradation of dye in water. *J. Supercrit. Fluids* **123**, 11–17 (2017).

273. Wu, H., Li, Y. & Li, Q. Facile synthesis of CuS nanostructured flowers and their visible light photocatalytic

properties. *Appl. Phys. A Mater. Sci. Process.* **123**, 1–11 (2017).

274. Estrada, A. C. *et al.* An ionic liquid route to prepare copper sulphide nanocrystals aiming at photocatalytic applications. *RSC Adv.* **6**, 34521–34528 (2016).

275. Zhang, Y. *et al.* Biomolecule-assisted, environmentally friendly, one-pot synthesis of CuS/reduced graphene oxide nanocomposites with enhanced photocatalytic performance. *Langmuir* **28**, 12893–12900 (2012).

276. Hu, X. S., Shen, Y., Zhang, Y. T. & Nie, J. J. Preparation of flower-like CuS/reduced graphene oxide (RGO) photocatalysts for enhanced photocatalytic activity. *J. Phys. Chem. Solids* **103**, 201–208 (2017).

277. Saranya, M., Ramachandran, R., Kollu, P., Jeong, S. K. & Grace, A. N. A template-free facile approach for the synthesis of CuS-rGO nanocomposites towards enhanced photocatalytic reduction of organic contaminants and textile effluents. *RSC Adv.* **5**, 15831–15840 (2015).

278. Siong, V. L. E. *et al.* Removal of methylene blue dye by solvothermally reduced graphene oxide: A metal-free adsorption and photodegradation method. *RSC Adv.* **9**, 37686–37695 (2019).

279. El-Hout, S. I., El-Sheikh, S. M., Gaber, A., Shawky, A. & Ahmed, A. I. Highly efficient sunlight-driven photocatalytic degradation of malachite green dye over reduced graphene oxide-supported CuS nanoparticles. *J. Alloys Compd.* **849**, 156573 (2020).

280. Wang, Y., Zhang, L., Jiu, H., Li, N. & Sun, Y. Depositing of CuS nanocrystals upon the graphene scaffold and their photocatalytic activities. *Appl. Surf. Sci.* **303**, 54–60 (2014).

281. La Porta, F. A. *et al.* Zinc blende versus wurtzite ZnS nanoparticles: Control of the phase and optical properties by tetrabutylammonium hydroxide. *Phys. Chem. Chem. Phys.* **16**, 20127–20137 (2014).

282. Fang, X. *et al.* ZnS nanostructures: From synthesis to applications. *Prog. Mater. Sci.* **56**, 175–287 (2011).

283. Ming, F., Hong, J., Xu, X. & Wang, Z. Dandelion-like ZnS/carbon quantum dots hybrid materials with enhanced photocatalytic activity toward organic pollutants. *RSC Adv.* **6**, 31551–31558 (2016).

284. Chakraborty, K., Chakrabarty, S., Das, P., Ghosh, S. & Pal, T. UV-assisted synthesis of reduced graphene oxide zinc sulfide composite with enhanced photocatalytic activity. *Mater. Sci. Eng. B Solid-State Mater. Adv. Technol.* **204**, 8–14 (2016).

285. Zhou, X., Shi, T. & Zhou, H. Hydrothermal preparation of ZnO-reduced graphene oxide hybrid with high performance in photocatalytic degradation. *Appl. Surf. Sci.* **258**, 6204–6211 (2012).

286. Liu, F., Shao, X. & Yang, S. $Bi_2S_3$-ZnS/graphene complexes: Synthesis, characterization, and photoactivity for the decolorization of dyes under visible light. *Mater. Sci. Semicond. Process.* **34**, 104–108 (2015).

287. Lonkar, S. P., Pillai, V. V. & Alhassan, S. M. Facile and scalable production of heterostructured ZnS-ZnO/graphene nano-photocatalysts for environmental remediation. *Sci. Rep.* **8**, 1–14 (2018).

288. Cheshme Khavar, A. H. *et al.* Enhanced visible light photocatalytic degradation of acetaminophen with $Ag_2S$-ZnO@rGO core-shell microsphere as a novel catalyst: Catalyst preparation and characterization and mechanistic catalytic experiments. *Sep. Purif. Technol.* **229**, 115803 (2019).

289. Zhang, X., Liu, X., Zhang, L., Li, D. & Liu, S. Novel porous $Ag_2S$/ZnS composite nanospheres: Fabrication and enhanced visible-light photocatalytic activities. *J. Alloys Compd.* **655**, 38–43 (2016).

290. Seger, B. & Kamat, P. V. Electrocatalytically active graphene-platinum nanocomposites. Role of 2-D carbon support in pem fuel cells. *J. Phys. Chem. C* **113**, 7990–7995 (2009).

291. Yan, Q. *et al.* Intrinsic current−voltage characteristics of graphene nanoribbon transistors and effect of edge doping. *Nano Lett.* **7**, 1469–1473 (2007).

292. Yoo, E. J. *et al.* Large reversible Li storage of graphene nanosheet families for use in rechargeable lithium ion batteries. *Nano Lett.* **8**, 2277–2282 (2008).

293. Stoller, M. D., Park, S., Zhu, Y., An, J. & Ruoff, R. S. Graphene-based ultracapacitors. *Nano Lett.* **8**, 3498–3502 (2008).

294. Trindade, T. & Thomas, P. J. Solid-state materials, including ceramics and minerals. in *Comprehensive inorganic chemistry II: from elements to applications.* (eds. Reedijk, J. & Poeppelmeter, K.) 343–369 (Elsevier, 2013).

295. Narayanam, P. K. *et al.* Growth of CdS nanocrystallites on graphene oxide Langmuir-Blodgett monolayers. *Nanotechnology* **23**, (2012).

296. Gao, P., Liu, J., Sun, D. D. & Ng, W. Graphene oxide-CdS composite with high photocatalytic degradation and disinfection activities under visible light irradiation. *J. Hazard. Mater.* **250**–**251**, 412–420 (2013).

297. Lü, W. *et al.* Graphene-enhanced visible-light photocatalysis of large-sized CdS particles for wastewater treatment. *Nanoscale Res. Lett.* **9**, 148 (2014).

298. Li, G., Chen, X. & Gao, G. $Bi_2S_3$ microspheres grown on graphene sheets as low-cost counter-electrode materials for dye-sensitized solar cells. *Nanoscale* **6**, 3283–3288 (2014).

299. Tavakoli, M. M., Aashuri, H., Simchi, A., Kalytchuk, S. & Fan, Z. Quasi core/shell lead sulfide/graphene quantum dots for bulk heterojunction solar cells. *J. Phys. Chem. C* **119**, 18886–18895 (2015).

300. Tayyebi, A., Tavakoli, M. M., Outokesh, M., Shafiekhani, A. & Simchi, A. Supercritical synthesis and characterization of graphene-PbS quantum dots composite with enhanced photovoltaic properties. *Ind. Eng. Chem. Res.* **54**, 7382–7392 (2015).

301. Cao, A. *et al.* A facile one-step method to produce craphene-CdS quantum dot nanocomposites as promising optoelectronic materials. *Adv. Mater.* **22**, 103–106 (2010).

302. Wang, P. *et al.* One-step, solvothermal synthesis of graphene-CdS and graphene-ZnS quantum dot nanocomposites and their interesting photovoltaic properties. *Nano Res.* **3**, 794–799 (2010).

303. Wu, J., Bai, S., Shen, X. & Jiang, L. Preparation and characterization of graphene/CdS nanocomposites. *Appl. Surf. Sci.* **257**, 747–751 (2010).

304. Zhang, N. *et al.* Assembly of CdS nanoparticles on the two-dimensional graphene scaffold as visible-light-driven photocatalyst for selective organic transformation under ambient conditions. *J. Phys. Chem. C* **115**, 23501–23511 (2011).

305. Li, Q. *et al.* Highly efficient visible-light-driven photocatalytic hydrogen production of CdS-cluster-

decorated graphene nanosheets. *J. Am. Chem. Soc.* **133**, 10878–10884 (2011).

306. Zhang, K. & Liu, X. One step synthesis and characterization of CdS nanorod/graphene nanosheet composite. *Appl. Surf. Sci.* **257**, 10379–10383 (2011).

307. Gao, Z. *et al.* Graphene-CdS composite, synthesis and enhanced photocatalytic activity. *Appl. Surf. Sci.* **258**, 2473–2478 (2012).

308. Pan, S. & Liu, X. CdS–Graphene nanocomposite: synthesis, adsorption kinetics and high photocatalytic performance under visible light irradiation. *New J. Chem.* **36**, 1781–1787 (2012).

309. Gao, P., Liu, J., Lee, S., Zhang, T. & Sun, D. D. High quality graphene oxide-CdS-Pt nanocomposites for efficient photocatalytic hydrogen evolution. *J. Mater. Chem.* **22**, 2292–2298 (2012).

310. Chen, F., Jia, D., Jin, X., Cao, Y. & Liu, A. A general method for the synthesis of graphene oxide-metal sulfide composites with improved photocatalytic activities. *Dye. Pigment.* **125**, 142–150 (2016).

311. Ren, Z., Zhang, J., Xiao, F.-X. & Xiao, G. Revisiting the construction of graphene–CdS nanocomposites as efficient visible-light-driven photocatalysts for selective organic transformation. *J. Mater. Chem. A* **2**, 5330–5339 (2014).

312. Monteiro, O. C., Esteves, A. C. C. & Trindade, T. The synthesis of $SiO_2$@CdS nanocomposites using single-molecule precursors. *Chem. Mater.* **14**, 2900–2904 (2002).

313. López-Díaz, D., López Holgado, M., García-Fierro, J. L. & Velázquez, M. M. Evolution of the Raman spectrum with the chemical composition of graphene oxide. *J. Phys. Chem. C* **121**, 20489–20497 (2017).

314. Sharon, M. & Sharon, M. *Graphene: An introduction to the fundamentals and industrial applications*. (Wiley, 2015).

315. Saikia, B. K., Boruah, R. K. & Gogoi, P. K. A X-ray diffraction analysis on graphene layers of assam coal. *J. Chem. Sci.* **121**, 103–106 (2009).

316. Pham, T. A., Choi, B. C. & Jeong, Y. T. Facile covalent immobilization of cadmium sulfide quantum dots on graphene oxide nanosheets: Preparation, characterization and optical properties. *Nanotechnology* **21**, 465603 (2010).

317. Wang, X. *et al.* Reduced graphene oxide/CdS for efficiently photocatalystic degradation of methylene blue. *J. Alloys Compd.* **524**, 5–12 (2012).

318. Li, D., Müller, M. B., Gilje, S., Kaner, R. B. & Wallace, G. G. Processable aqueous dispersions of graphene nanosheets. *Nat. Nanotechnol.* **3**, 101–105 (2008).

319. Luo, J. *et al.* Graphene oxide nanocolloids. *J. Am. Chem. Soc.* **132**, 17667–17669 (2010).

320. Yang, Y. & Liu, T. Fabrication and characterization of graphene oxide/zinc oxide nanorods hybrid. *Appl. Surf. Sci.* **257**, 8950–8954 (2011).

321. Wu, J., Shen, X., Jiang, L., Wang, K. & Chen, K. Solvothermal synthesis and characterization of sandwich-like graphene/ZnO nanocomposites. *Appl. Surf. Sci.* **256**, 2826–2830 (2010).

322. Zhang, L. *et al.* Size-controlled synthesis of graphene oxide sheets on a large scale using chemical exfoliation. *Carbon.* **47**, 3365–3368 (2009).

323. Weller, H. Quantized semiconductor particles: A novel state of matter for materials science. *Adv. Mater.* **5**, 88–95 (1993).

324. Brus, L. Quantum crystallites and nonlinear optics. *Appl. Phys. A* **53**, 465–474 (1991).

325. Neves, M. C., Monteiro, O. C., Hempelmann, R., Silva, A. M. S. & Trindade, T. From single-molecule precursors to coupled $Ag_2S/TiO_2$ nanocomposites. *Eur. J. Inorg. Chem.* 4380–4386 (2008).

326. Ferrari, A. C. & Basko, D. M. Raman spectroscopy as a versatile tool for studying the properties of graphene. *Nat. Nanotechnol.* **8**, 235–246 (2013).

327. Dresselhaus, M. S., Jorio, A., Hofmann, M., Dresselhaus, G. & Saito, R. Perspectives on carbon nanotubes and graphene Raman spectroscopy. *Nano Lett.* **10**, 751–758 (2010).

328. Xu, T., Zhang, L., Cheng, H. & Zhu, Y. Significantly enhanced photocatalytic performance of ZnO via graphene hybridization and the mechanism study. *Appl. Catal. B Environ.* **101**, 382–387 (2011).

329. Beams, R., Gustavo Cançado, L., Novotny, L., Canç Ado, L. G. & Novotny, L. Raman characterization of defects and dopants in graphene. *J. Phys. Condens. Matter J. Phys. Condens. Matter* **27**, 83002–26 (2015).

330. Zhang, X., Rajaraman, B. R. S., Liu, H. & Ramakrishna, S. Graphene's potential in materials science and engineering. *RSC Adv.* **4**, 28987–29011 (2014).

331. Lambert, T. N. *et al.* Synthesis and characterization of titania−graphene nanocomposites. *J. Phys. Chem. C* **113**, 19812–19823 (2009).

332. Berciaud, S. *et al.* Intrinsic line shape of the Raman 2D-mode in freestanding graphene monolayers. *Nano Lett.* **13**, 3517–3523 (2013).

333. Paz, F. A. A. *et al.* Optimised hydrothermal synthesis of multi-dimensional hybrid coordination polymers containing flexible organic ligands. *Prog. Solid State Chem.* **33**, 113–125 (2005).

334. Martins, N. C. T. *et al.* N-doped carbon quantum dots/$TiO_2$ composite with improved photocatalytic activity. *Appl. Catal. B Environ.* **193**, 67–74 (2016).

335. UNICEF; WHO. *Progress on Sanitation and Drinking Water. 2015 Update and MDG Assessment*. (2015).

336. Bui, X. T., Chiemchaisri, C., Fujioka, T. & Varjani, S. Introduction to recent advances in water and wastewater treatment technologies. in *Energy, environment, and sustainability* (eds. Bui, X., Chiemchaisri, C., Fujioka, T. & Varjani, S.) 3–12 (Springer, 2019).

337. Belver, C., Bedia, J., Gómez-Avilés, A., Peñas-Garzón, M. & Rodriguez, J. J. Semiconductor photocatalysis for water purification. in *Nanoscale materials in water purification* (eds. Thomas, S., Pasquini, D., Leu, S.-Y. & Gopakumar, D. A.) 581–651 (Elsevier, 2019).

338. Zhu, D. & Zhou, Q. Action and mechanism of semiconductor photocatalysis on degradation of organic pollutants in water treatment: A review. *Environ. Nanotechnology, Monit. Manag.* **12**, 100255 (2019).

339. Rajeshwar, K. Advanced oxidation processes for water treatment. *J. Phys. Chem. Lett.* **3**, 2112–2113 (2012).

340. Liu, J. *et al.* Slow photons for photocatalysis and photovoltaics. *Adv. Mater.* **29**, 1–21 (2017).

341. Nagarajan, R. & Hatton, T. A. *Synthesis, stabilization, passivation and functionalization*. (American Chemical Society, 2008).

342. Zhao, Y. *et al.* Plasmonic $Cu_{2-x}S$ nanocrystals: Optical and structural properties of copper-deficient copper(I) sulfides. *J. Am. Chem. Soc.* **131**, 4253–4261 (2009).

343. Nam, S. W. *et al.* Adsorption characteristics of diclofenac and sulfamethoxazole to graphene oxide in aqueous solution. *Chemosphere* **136**, 20–26 (2015).

344. Jauris, I. M. *et al.* Adsorption of sodium diclofenac on graphene: A combined experimental and theoretical study. *Phys. Chem. Chem. Phys.* **18**, 1526–1536 (2016).

345. Matos, R. *et al.* Graphene@metal sulfide/oxide nanocomposites as novel photo-Fenton-like catalysts for 4-nitrophenol degradation. *Eur. J. Inorg. Chem.* (2021).

346. Oliveira-Silva, R., Da Costa, J. P., Vitorino, R. & Daniel-Da-Silva, A. L. Magnetic chelating nanoprobes for enrichment and selective recovery of metalloproteases from human saliva. *J. Mater. Chem. B* **3**, 238–249 (2015).

347. Afonso, E. L. *et al.* Can contaminated waters or wastewater be alternative sources for technology-critical elements? The case of removal and recovery of lanthanides. *J. Hazard. Mater.* **380**, 120845 (2019).

348. Jarrais, B., Guedes, A. & Freire, C. Heteroatom-doped carbon nanomaterials as metal-free catalysts for the reduction of 4-nitrophenol. *ChemistrySelect* **3**, 1737–1748 (2018).

349. Pejjai, B., Reddivari, M. & Kotte, T. R. R. Phase controllable synthesis of CuS nanoparticles by chemical co-precipitation method: Effect of copper precursors on the properties of CuS. *Mater. Chem. Phys.* **239**, 122030 (2020).

350. Ji, H. *et al.* Fabrication of CuS nanocrystals with various morphologies in the presence of a nonionic surfactant. *Mater. Lett.* **59**, 3169–3172 (2005).

351. Ding, T. Y., Wang, M. S., Guo, S. P., Guo, G. C. & Huang, J. S. CuS nanoflowers prepared by a polyol route and their photocatalytic property. *Mater. Lett.* **62**, 4529–4531 (2008).

352. Neelgund, G. M., Oki, A., Bandara, S. & Carson, L. Photothermal effect and cytotoxicity of CuS nanoflowers deposited over folic acid conjugated nanographene oxide. *J. Mater. Chem. B* **9**, 1792–1803 (2021).

353. Sevilla, M. & Fuertes, A. B. Chemical and structural properties of carbonaceous products obtained by hydrothermal carbonization of saccharides. *Chem. Eur. J.* **15**, 4195–4203 (2009).

354. Xiao, W. *et al.* One-pot solvothermal synthesis of flower-like copper sulfide/reduced graphene oxide composite superstructures as high-performance supercapacitor electrode materials. *J. Mater. Sci. Mater. Electron.* **28**, 5931–5940 (2017).

355. Sharma, D., Menon, A. V & Bose, S. Graphene templated growth of copper sulphide ‘flowers’ can suppress electromagnetic interference. *Nanoscale Adv.* **2**, 3292–3303 (2020).

356. Karikalan, N., Karthik, R., Chen, S. & Karuppiah, C. Sonochemical synthesis of sulfur doped reduced graphene oxide supported CuS nanoparticles for the non-enzymatic glucose sensor applications. *Sci. Rep.* **7**, 2494 (2017).

357. Xu, W. *et al.* Localized surface plasmon resonances in self-doped copper chalcogenide binary nanocrystals and their emerging applications. *Nano Today* **33**, 100892 (2020).

358. Xie, Y. *et al.* Tuning and locking the localized surface plasmon resonances of CuS (covellite) nanocrystals by an amorphous $CuPd_xS$ shell. *Chem. Mater.* **29**, 1716–1723 (2017).

359. Wolf, A., Kodanek, T. & Dorfs, D. Tuning the LSPR in copper chalcogenide nanoparticles by cation intercalation, cation exchange and metal growth. *Nanoscale* **7**, 19519–19527 (2015).

360. Amendola, V. Surface plasmon resonance of silver and gold nanoparticles in the proximity of graphene studied using the discrete dipole approximation method. *Phys. Chem. Chem. Phys* **18**, 2230–2241 (2016).

361. Yu, Y. *et al.* Benzene carboxylic acid derivatized graphene oxide nanosheets on natural zeolites as effective adsorbents for cationic dye removal. *J. Hazard. Mater.* **260**, 330–338 (2013).

362. Li, F., Wu, J., Qin, Q., Li, Z. & Huang, X. Controllable synthesis, optical and photocatalytic properties of CuS nanomaterials with hierarchical structures. *Powder Technol.* **198**, 267–274 (2010).

363. Deng, C. *et al.* Template-free and green sonochemical synthesis of hierarchically structured CuS hollow microspheres displaying excellent Fenton-like catalytic activities. *CrystEngComm* **16**, 2738–2745 (2014).

364. Zhao, W., Wang, Z., Zhou, L., Liu, N. & Wang, H. Natural sunlight irradiated flower-like CuS synthesized from DMF solvothermal treatment. *Front. Mater. Sci.* **10**, 290–299 (2016).

365. Tanveer, M. *et al.* Template free synthesis of CuS nanosheet-based hierarchical microspheres: An efficient natural light driven photocatalyst. *CrystEngComm* **16**, 5290–5300 (2014).

366. de Faria, D. L. A. & Lopes, F. N. Heated goethite and natural hematite: Can Raman spectroscopy be used to differentiate them? *Vib. Spectrosc.* **45**, 117–121 (2007).

367. Legodi, M. A. & de Waal, D. The preparation of magnetite, goethite, hematite and maghemite of pigment quality from mill scale iron waste. *Dye. Pigment.* **74**, 161–168 (2007).

368. Hanesch, M. Raman spectroscopy of iron oxides and (oxy)hydroxides at low laser power and possible applications in environmental magnetic studies. *Geophys. J. Int.* **177**, 941–948 (2009).

369. Ivashchenko, O. *et al.* Fourier transform infrared and Raman spectroscopy studies on magnetite/Ag/antibiotic nanocomposites. *Appl. Surf. Sci.* **364**, 400–409 (2016).

370. Ullah, S. *et al.* Advances and trends in chemically doped graphene. *Adv. Mater. Interfaces* **7**, 2000999 (2020).

371. Putri, L. K., Ong, W. J., Chang, W. S. & Chai, S. P. Heteroatom doped graphene in photocatalysis: A review. *Appl. Surf. Sci.* **358**, 2–14 (2015).

372. Lin, T. *et al.* Scotch-tape-like exfoliation of graphite assisted with elemental sulfur and graphene-sulfur composites for high-performance lithium-sulfur batteries. *Energy Environ. Sci.* **6**, 1283–1290 (2013).

373. Huang, S. *et al.* Nitrogen and fluorine co-doped graphene as a high-performance anode material for lithium-ion batteries. *J. Mater. Chem. A* **3**, 23095–23105 (2015).

374. Malesevic, A. *et al.* Synthesis of few-layer graphene via microwave plasma-enhanced chemical vapour

deposition. *Nanotechnology* **19**, (2008).

375. Pereira, C. *et al.* Multifunctional mixed valence N-doped CNT@$MFe_2O_4$ hybrid nanomaterials: From engineered one-pot coprecipitation to application in energy storage paper supercapacitors. *Nanoscale* **10**, 12820–12840 (2018).

376. Araújo, M. P., Soares, O. S. G. P., Fernandes, A. J. S., Pereira, M. F. R. & Freire, C. Tuning the surface chemistry of graphene flakes: New strategies for selective oxidation. *RSC Adv.* **7**, 14290–14301 (2017).

377. Cañizares, P., Sáez, C., Lobato, J. & Rodrigo, M. A. Electrochemical treatment of 2,4-dinitrophenol aqueous wastes using boron-doped diamond anodes. *Electrochim. Acta* **49**, 4641–4650 (2004).

378. Zhang, H., Fei, C., Zhang, D. & Tang, F. Degradation of 4-nitrophenol in aqueous medium by electro-Fenton method. *J. Hazard. Mater.* **145**, 227–232 (2007).

379. Li, J. *et al.* A graphene oxide-based electrochemical sensor for sensitive determination of 4-nitrophenol. *J. Hazard. Mater.* **201**–**202**, 250–259 (2012).

380. Jiao, X. X., Luo, H. Q. & Li, N. B. Fabrication of graphene–gold nanocomposites by electrochemical co-reduction and their electrocatalytic activity toward 4-nitrophenol oxidation. *J. Electroanal. Chem.* **691**, 83–89 (2013).

381. Masqué, N., Marcé, R. M., Borrul, F., Cormack, P. A. G. & Sherrington, D. C. Synthesis and evaluation of a molecularly imprinted polymer for selective on-line solid-phase extraction of 4-nitrophenol from environmental water. *Anal. Chem.* **72**, 4122–4126 (2000).

382. Pedrosa, V. A., Codognoto, L., Machado, S. A. S. & Avaca, L. A. Is the boron-doped diamond electrode a suitable substitute for mercury in pesticide analyses? A comparative study of 4-nitrophenol quantification in pure and natural waters. *J. Electroanal. Chem.* **573**, 11–18 (2004).

383. Nichela, D. A., Berkovic, A. M., Costante, M. R., Juliarena, M. P. & García Einschlag, F. S. Nitrobenzene degradation in Fenton-like systems using Cu(II) as catalyst. Comparison between Cu(II)- and Fe(III)-based systems. *Chem. Eng. J.* **228**, 1148–1157 (2013).

384. Barros, W. R. P., Steter, J. R., Lanza, M. R. V. & Tavares, A. C. Catalytic activity of $Fe_{3-x}Cu_xO_4$ ($0 \leq x \leq 0.25$) nanoparticles for the degradation of Amaranth food dye by heterogeneous electro-Fenton process. *Appl. Catal. B Environ.* **180**, 434–441 (2016).

385. Feng, Y., Liao, C. & Shih, K. Copper-promoted circumneutral activation of $H_2O_2$ by magnetic $CuFe_2O_4$ spinel nanoparticles: Mechanism, stoichiometric efficiency, and pathway of degrading sulfanilamide. *Chemosphere* **154**, 573–582 (2016).

386. Gao, J. *et al.* 3D mesoporous $CuFe_2O_4$ as a catalyst for photo-Fenton removal of sulfonamide antibiotics at near neutral pH. *J. Colloid Interface Sci.* **524**, 409–416 (2018).

387. Han, Z., Dong, Y. & Dong, S. Copper-iron bimetal modified PAN fiber complexes as novel heterogeneous Fenton catalysts for degradation of organic dye under visible light irradiation. *J. Hazard. Mater.* **189**, 241–248 (2011).

388. Zhang, X. *et al.* Degradation of bisphenol A by hydrogen peroxide activated with $CuFeO_2$ microparticles as a heterogeneous Fenton-like catalyst: Efficiency, stability and mechanism. *Chem. Eng. J.* **236**, 251–262 (2014).

389. Qiu, B., Li, Q., Shen, B., Xing, M. & Zhang, J. Stöber-like method to synthesize ultradispersed $Fe_3O_4$ nanoparticles on graphene with excellent photo-Fenton reaction and high-performance lithium storage. *Appl. Catal. B Environ.* **183**, 216–223 (2016).

390. Zubir, N. A., Yacou, C., Motuzas, J., Zhang, X. & Diniz Da Costa, J. C. Structural and functional investigation of graphene oxide-$Fe_3O_4$ nanocomposites for the heterogeneous Fenton-like reaction. *Sci. Rep.* **4**, 1–8 (2014).

391. Boruah, P. K., Sharma, B., Karbhal, I., Shelke, M. V. & Das, M. R. Ammonia-modified graphene sheets decorated with magnetic $Fe_3O_4$ nanoparticles for the photocatalytic and photo-Fenton degradation of phenolic compounds under sunlight irradiation. *J. Hazard. Mater.* **325**, 90–100 (2017).

392. Morales, M. V. *et al.* Development of highly efficient Cu versus Pd catalysts supported on graphitic carbon materials for the reduction of 4-nitrophenol to 4-aminophenol at room temperature. *Carbon.* **111**, 150–161 (2017).

393. Rocha, M. *et al.* L-serine-functionalized montmorillonite decorated with Au nanoparticles: A new highly efficient catalyst for the reduction of 4-nitrophenol. *J. Catal.* **361**, 143–155 (2018).

394. Ito, Y., Cong, W., Fujita, T., Tang, Z. & Chen, M. High catalytic activity of nitrogen and sulfur co-doped nanoporous graphene in the hydrogen evolution reaction. *Angew. Chemie - Int. Ed.* **54**, 2131–2136 (2015).

395. Trajić, J. *et al.* Raman spectroscopy of ZnS quantum dots. *J. Alloys Compd.* **637**, 401–406 (2015).

396. Wu, Z. *et al.* Efficient planar heterojunction perovskite solar cells employing graphene oxide as hole conductor. *Nanoscale* **6**, 10505–10510 (2014).

397. Ameen, S., Shaheer Akhtar, M., Seo, H. K. & Shik Shin, H. Advanced ZnO-graphene oxide nanohybrid and its photocatalytic Applications. *Mater. Lett.* **100**, 261–265 (2013).

398. Wu, N. Plasmonic metal-semiconductor photocatalysts and photoelectrochemical cells: A review. *Nanoscale* **10**, 2679–2696 (2018).

399. Li, S.-S., Tu, K.-H., Lin, C.-C., Chen, C.-W. & Chhowalla, M. Solution-processable graphene oxide as an efficient hole transport layer in polymer solar cells. *ACS Nano* **4**, 3169–3174 (2010).

400. Yoon, H. J. *et al.* Sensitive capture of circulating tumour cells by functionalized graphene oxide nanosheets. *Nat. Nanotechnol.* **8**, 735–741 (2013).

401. Chung, C. *et al.* Biomedical applications of graphene and graphene oxide. *Acc. Chem. Res.* **46**, 2211–2224 (2013).

402. Zhang, L., Xia, J., Zhao, Q., Liu, L. & Zhang, Z. Functional graphene oxide as a nanocarrier for controlled loading and targeted delivery of mixed anticancer drugs. *Small* **6**, 537–544 (2010).

403. Sun, X. *et al.* Nano-graphene oxide for cellular imaging and drug delivery. *Nano Res.* **1**, 203–212 (2008).

404. Kumar, S., Raj, S., Sarkar, K. & Chatterjee, K. Engineering a multi-biofunctional composite using poly(ethylenimine) decorated graphene oxide for bone tissue regeneration. *Nanoscale* **8**, 6820–6836 (2016).

405. Díez-Pascual, A. M. & Díez-Vicente, A. L. Poly(propylene fumarate)/polyethylene glycol-modified

graphene oxide nanocomposites for tissue engineering. *ACS Appl. Mater. Interfaces* **8**, 17902–17914 (2016).

406. Shuai, C. *et al.* Graphene oxide reinforced poly(vinyl alcohol): Nanocomposite scaffolds for tissue engineering applications. *RSC Adv.* **5**, 25416–25423 (2015).

407. Ng, Y. H., Iwase, A., Kudo, A. & Amal, R. Reducing graphene oxide on a visible-light $BiVO_4$ photocatalyst for an enhanced photoelectrochemical water splitting. *J. Phys. Chem. Lett.* **1**, 2607–2612 (2010).

408. Meng, F. *et al.* Photocatalytic water oxidation by hematite/reduced graphene oxide composites. *ACS Catal.* **3**, 746–751 (2013).

409. Ng, Y. H., Iwase, A., Bell, N. J., Kudo, A. & Amal, R. Semiconductor/reduced graphene oxide nanocomposites derived from photocatalytic reactions. *Catal. Today* **164**, 353–357 (2011).

410. Lv, H. *et al.* Synthesis of graphene oxide-$BiPO_4$ composites with enhanced photocatalytic properties. *Appl. Surf. Sci.* **284**, 308–314 (2013).

411. Campion, A., Kambhampati, P., Campion, A. & Harris, C. Surface-enhanced Raman scattering. *Chem. Soc. Rev.* **27**, 241–250 (1998).

412. Nie, S. & Emory, S. R. Probing single molecules and single nanoparticles by surface-enhanced Raman scattering. *Science.* **275**, 1102–1106 (1997).

413. Fateixa, S., Nogueira, H. I. S. & Trindade, T. Hybrid nanostructures for SERS: Materials development and chemical detection. *Phys. Chem. Chem. Phys.* **17**, 21046–21071 (2015).

414. Tian, Z. Q., Ren, B. & Wu, D. Y. Surface-enhanced Raman scattering: From noble to transition metals and from rough surfaces to ordered nanostructures. *J. Phys. Chem. B* **106**, 9463–9483 (2002).

415. Ding, S. Y. *et al.* Nanostructure-based plasmon-enhanced Raman spectroscopy for surface analysis of materials. *Nat. Rev. Mater.* **1**, 1–16 (2016).

416. Quagliano, L. G. Observation of molecules adsorbed on III-V semiconductor quantum dots by surface-enhanced Raman scattering. *J. Am. Chem. Soc.* **126**, 7393–7398 (2004).

417. Yang, L. *et al.* Observation of enhanced Raman scattering for molecules adsorbed on $TiO_2$ nanoparticles: Charge-transfer contribution. *J. Phys. Chem. C* **112**, 20095–20098 (2008).

418. Ji, W., Zhao, B. & Ozaki, Y. Semiconductor materials in analytical applications of surface-enhanced Raman scattering. *J. Raman Spectrosc.* **47**, 51–58 (2016).

419. Guicheteau, J., Christesen, S., Emge, D. & Tripathi, A. Bacterial mixture identification using Raman and surface-enhanced Ramanchemical imaging. *J. Raman Spectrosc.* **41**, 1632–1637 (2010).

420. Fateixa, S., Wilhelm, M., Nogueira, H. I. S. & Trindade, T. SERS and Raman imaging as a new tool to monitor dyeing on textile fibres. *J. Raman Spectrosc.* **47**, 1239–1246 (2016).

421. Fateixa, S., Nogueira, H. I. S. & Trindade, T. Surface-enhanced Raman scattering spectral imaging for the attomolar range detection of crystal violet in contaminated water. *ACS Omega* **3**, 4331–4341 (2018).

422. Stewart, S., Priore, R. J., Nelson, M. P. & Treado, P. J. Raman imaging. *Annu. Rev. Anal. Chem.* **5**, 337–360 (2012).

423. Wright, K., Watson, G. W., Parker, S. C. & Vaughan, D. J. Simulation of the structure and stability of sphalerite (ZnS) surfaces. *Am. Mineral.* **83**, 141–146 (1998).

424. Kresse, G. & Hafner, J. Ab initio molecular dynamics for liquid metals. *Phys. Rev. B* **47**, 558–561 (1993).

425. Kresse, G. & Hafner, J. Ab initio molecular-dynamics simulation of the liquid-metalamorphous-semiconductor transition in germanium. *Phys. Rev. B* **49**, 14251–14269 (1994).

426. Kresse, G. & Furthmüller, J. Efficiency of ab-initio total energy calculations for metals and semiconductors using a plane-wave basis set. *Comput. Mater. Sci.* **6**, 15–50 (1996).

427. Kresse, G. & Furthmüller, J. Efficient iterative schemes for ab initio total-energy calculations using a plane-wave basis set. *Phys. Rev. B - Condens. Matter Mater. Phys.* **54**, 11169–11186 (1996).

428. Perdew, J. P., Burke, K. & Ernzerhof, M. Generalized gradient approximation made simple. *Phys. Rev. Lett.* **77**, 3865–3868 (1996).

429. Grimme, S., Antony, J., Ehrlich, S. & Krieg, H. A consistent and accurate ab initio parametrization of density functional dispersion correction (DFT-D) for the 94 elements H-Pu. *J. Chem. Phys.* **132**, 154104 (2010).

430. Kresse, G. & Joubert, D. From ultrasoft pseudopotentials to the projector augmented-wave method. *Phys. Rev. B* **59**, 1758–1775 (1999).

431. Krukau, A. V., Vydrov, O. A., Izmaylov, A. F. & Scuseria, G. E. Influence of the exchange screening parameter on the performance of screened hybrid functionals. *J. Chem. Phys.* **125**, 224106 (2006).

432. Heyd, J., Scuseria, G. E. & Ernzerhof, M. Hybrid functionals based on a screened Coulomb potential. *J. Chem. Phys.* **118**, 8207–8215 (2003).

433. Milekhin, A. . *et al.* Optical vibrational modes in (Cd, Pb, Zn)S quantum dots embedded in Langmuir–Blodgett matrices. *Thin Solid Films* **422**, 200–204 (2002).

434. Wang, Y. *et al.* Raman scattering study of molecules adsorbed on ZnS nanocrystals. *J. Raman Spectrosc.* **38**, 34–38 (2007).

435. Baldwin, J. A., Vlčková, B., Andrews, M. P. & Butler, I. S. Surface-enhanced Raman scattering of mercaptopyridines and pyrazinamide incorporated in silver colloid−adsorbate films. *Langmuir* **13**, 3744–3751 (2002).

436. Wang, Y. *et al.* Enhanced Raman scattering as a probe for 4-mercaptopyridine surface-modified copper oxide nanocrystals. *Anal. Sci.* **23**, 787–791 (2007).

437. Wang, Y. *et al.* Direct observation of surface-enhanced Raman scattering in ZnO nanocrystals. *J. Raman Spectrosc.* **40**, 1072–1077 (2009).

438. Wang, Y. *et al.* Surface-enhanced Raman scattering on mercaptopyridine-capped CdS microclusters. *Spectrochim. Acta - Part A Mol. Biomol. Spectrosc.* **66**, 1199–1203 (2007).

439. McLellan, J. M., Xiong, Y., Hu, M. & Xia, Y. Surface-enhanced Raman scattering of 4-mercaptopyridine on thin films of nanoscale Pd cubes, boxes, and cages. *Chem. Phys. Lett.* **417**, 230–234 (2006).

440. Hu, J., Zhao, B., Xu, W., Li, B. & Fan, Y. Surface-enhanced Raman spectroscopy study on the structure changes of 4-mercaptopyridine adsorbed on silver substrates and silver colloids. *Spectrochim. Acta -*

*Part A Mol. Biomol. Spectrosc.* **58**, 2827–2834 (2002).

441. Guo, H., Ding, L. & Mo, Y. Adsorption of 4-mercaptopyridine onto laser-ablated gold, silver and copper oxide films: A comparative surface-enhanced Raman scattering investigation. *J. Mol. Struct.* **991**, 103–107 (2011).

442. Wang, Y. *et al.* Mercaptopyridine surface-functionalized CdTe quantum dots with enhanced Raman scattering properties. *J. Phys. Chem. C* **112**, 996–1000 (2008).

443. Song, W., Wang, Y., Hu, H. & Zhao, B. Fabrication of surface-enhanced Raman scattering-active ZnO/Ag composite microspheres. *J. Raman Spectrosc.* **38**, 1320–1325 (2007).

444. Saha, S., Ghosh, M. & Chowdhury, J. Infused self-assembly on Langmuir–Blodgett film: Fabrication of highly efficient SERS active substrates with controlled plasmonic aggregates. *J. Raman Spectrosc.* **50**, 330–344 (2019).

445. Stobinski, L., Peszke, J., Tomasik, P. & Lin, H. M. Decoration of carboxylated multi-wall carbon nanotubes with quantum dots. *J. Alloys Compd.* **455**, 137–141 (2008).

446. Pan, S. & Liu, X. ZnS-graphene nanocomposite: Synthesis, characterization and optical properties. *J. Solid State Chem.* **191**, 51–56 (2012).

447. Jiang, S. D., Tang, G., Ma, Y. F., Hu, Y. & Song, L. Synthesis of nitrogen-doped graphene-ZnS quantum dots composites with highly efficient visible light photodegradation. *Mater. Chem. Phys.* **151**, 34–42 (2015).

448. Wang, X. & Guo, L. SERS Activity of semiconductors: Crystalline and amorphous nanomaterials. *Angew. Chemie - Int. Ed.* **59**, 4231–4239 (2020).

449. Manz, T. A. Introducing DDEC6 atomic population analysis: Part 3. Comprehensive method to compute bond orders. *RSC Adv.* **7**, 45552–45581 (2017).

450. Long, X. *et al.* The effect of water molecules on the thiol collector interaction on the galena (PbS) and sphalerite (ZnS) surfaces: A DFT study. *Appl. Surf. Sci.* **389**, 103–111 (2016).

451. Long, X., Chen, J. & Chen, Y. Adsorption of ethyl xanthate on ZnS(110) surface in the presence of water molecules: A DFT study. *Appl. Surf. Sci.* **370**, 11–18 (2016).

452. Moolayadukkam, S. *et al.* Role of transition metals in layered double hydroxides for differentiating the oxygen evolution and nonenzymatic glucose sensing. *ACS Appl. Mater. Interfaces* **12**, 6193–6204 (2020).

453. Fan, H. *et al.* Effect of $BiVO_4$ crystalline phases on the photoinduced carriers behavior and photocatalytic activity. *J. Phys. Chem. C* **116**, 2425–2430 (2012).

454. Sun, S., Wang, W., Zhou, L. & Xu, H. Efficient methylene blue removal over hydrothermally synthesized starlike $BiVO_4$. *Ind. Eng. Chem. Res.* **48**, 1735–1739 (2009).

455. Andreozzi, R. Advanced oxidation processes (AOP) for water purification and recovery. *Catal. Today* **53**, 51–59 (1999).

456. Chen, D. *et al.* Photocatalytic degradation of organic pollutants using $TiO_2$-based photocatalysts: A review. *J. Clean. Prod.* **268**, 121725 (2020).

457. Ahmed, T., Zhang, H. ling, Xu, H. bin & Zhang, Y. m-BiVO4 hollow spheres coated on carbon fiber with superior reusability as photocatalyst. *Colloids Surfaces A Physicochem. Eng. Asp.* **531**, 213–220 (2017).

458. Lu, Y. *et al.* Preparation and efficient visible light-induced photocatalytic activity of m-$BiVO_4$ with different morphologies. *J. Phys. Chem. Solids* **85**, 44–50 (2015).

459. Ke, D., Peng, T., Ma, L., Cai, P. & Dai, K. Effects of hydrothermal temperature on the microstructures of $BiVO_4$ and its photocatalytic $O_2$ evolution activity under visible light. *Inorg. Chem.* **48**, 4685–4691 (2009).

460. Tokunaga, S., Kato, H. & Kudo, A. Selective preparation of monoclinic and tetragonal $BiVO_4$ with scheelite structure and their photocatalytic properties. *Chem. Mater.* **13**, 4624–4628 (2001).

461. Nagabhushana, G. P., Tavakoli, A. H. & Navrotsky, A. Energetics of bismuth vanadate. *J. Solid State Chem.* **225**, 187–192 (2015).

462. Martínez-De La Cruz, A., García-Pérez, U. M. & Sepúlveda-Guzmán, S. Characterization of the visible-light-driven $BiVO_4$ photocatalyst synthesized via a polymer-assisted hydrothermal method. *Res. Chem. Intermed.* **39**, 881–894 (2013).

463. Zhang, A. *et al.* Effects of pH on hydrothermal synthesis and characterization of visible-light-driven $BiVO_4$ photocatalyst. *J. Mol. Catal. A Chem.* **304**, 28–32 (2009).

464. Obregón, S., Caballero, A. & Colón, G. Hydrothermal synthesis of $BiVO_4$: Structural and morphological influence on the photocatalytic activity. *Appl. Catal. B Environ.* **117**–**118**, 59–66 (2012).

465. Sarkar, S., Garain, S., Mandal, D. & Chattopadhyay, K. K. Electro-active phase formation in PVDF-$BiVO_4$ flexible nanocomposite films for high energy density storage application. *RSC Adv.* **4**, 48220–48227 (2014).

466. Obregón, S., Lee, S. W. & Colón, G. Exalted photocatalytic activity of tetragonal $BiVO_4$ by $Er^{3+}$ doping through a luminescence cooperative mechanism. *Dalt. Trans.* **43**, 311–316 (2014).

467. Yin, C. *et al.* One step fabrication of C-doped $BiVO_4$ with hierarchical structures for a high-performance photocatalyst under visible light irradiation. *J. Mater. Chem. A* **1**, 8367–8378 (2013).

468. Yuan, Q. *et al.* $Cu_2O$/$BiVO_4$ heterostructures: Synthesis and application in simultaneous photocatalytic oxidation of organic dyes and reduction of Cr(VI) under visible light. *Chem. Eng. J.* **255**, 394–402 (2014).

469. Shang, M., Wang, W., Zhou, L., Sun, S. & Yin, W. Nanosized $BiVO_4$ with high visible-light-induced photocatalytic activity: Ultrasonic-assisted synthesis and protective effect of surfactant. *J. Hazard. Mater.* **172**, 338–344 (2009).

470. Li, G., Zhang, D. & Yu, J. C. Ordered mesoporous $BiVO_4$ through nanocasting: A superior visible light-driven photocatalyst. *Chem. Mater.* **20**, 3983–3992 (2008).

471. Dabodiya, T. S., Selvarasu, P. & Murugan, A. V. Tetragonal to monoclinic crystalline phases change of $BiVO_4$ via microwave-hydrothermal reaction: In correlation with visible-light-driven photocatalytic performance. *Inorg. Chem.* **58**, 5096–5110 (2019).

472. Wang, X., Zhou, J., Zhao, S., Chen, X. & Yu, Y. Synergistic effect of adsorption and visible-light

photocatalysis for organic pollutant removal over $BiVO_4$/carbon sphere nanocomposites. *Appl. Surf. Sci.* **453**, 394–404 (2018).

473. Duy, T. *et al.* $BiVO_4$ photocatalysis design and applications to oxygen production and degradation of organic compounds: A review. *Environ. Chem. Lett.* **18**, 1779–1801 (2020).

474. Lin, X. *et al.* Graphitic carbon nitride quantum dots and nitrogen-doped carbon quantum dots co-decorated with $BiVO_4$ microspheres: A ternary heterostructure photocatalyst for water purification. *Sep. Purif. Technol.* **226**, 117–127 (2019).

475. Lin, X. *et al.* Graphitic carbon nitride quantum dots loaded on leaf-like $InVO_4$/$BiVO_4$ nanoheterostructures with enhanced visible-light photocatalytic activity. *J. Alloys Compd.* **688**, 891–898 (2016).

476. Zhou, F. Q., Fan, J. C., Xu, Q. J. & Min, Y. L. $BiVO_4$ nanowires decorated with CdS nanoparticles as Z-scheme photocatalyst with enhanced $H_2$ generation. *Appl. Catal. B Environ.* **201**, 77–83 (2017).

477. Liu, Y. *et al.* Facet effect on the photoelectrochemical performance of a $WO_3$/$BiVO_4$ heterojunction photoanode. *Appl. Catal. B Environ.* **245**, 227–239 (2019).

478. Yan, Y. *et al.* Microwave-assisted in situ synthesis of reduced graphene oxide-$BiVO_4$ composite photocatalysts and their enhanced photocatalytic performance for the degradation of ciprofloxacin. *J. Hazard. Mater.* **250**–**251**, 106–114 (2013).

479. Deshmukh, A. A., Mhlanga, S. D. & Coville, N. J. Carbon spheres. *Mater. Sci. Eng. Reports* **70**, 1–28 (2010).

480. Liu, J. *et al.* Extension of the Stöber method to the preparation of monodisperse resorcinol-formaldehyde resin polymer and carbon spheres. *Angew. Chemie - Int. Ed.* **50**, 5947–5951 (2011).

481. White, R. J., Tauer, K., Antonietti, M. & Titirici, M.-M. Functional hollow carbon nanospheres by latex templating. *J. Am. Chem. Soc.* **132**, 17360–17363 (2010).

482. Ouyang, Y., Shi, H., Fu, R. & Wu, D. Highly monodisperse microporous polymeric and carbonaceous nanospheres with multifunctional properties. *Sci. Rep.* **3**, 1430 (2013).

483. Frusteri, L. *et al.* Carbon microspheres preparation, graphitization and surface functionalization for glycerol etherification. *Catal. Today* **277**, 68–77 (2016).

484. Nogueira, J. *et al.* Porous carrageenan-derived carbons for efficient ciprofloxacin removal from water. *Nanomaterials* **8**, 1004 (2018).

485. Neves, M. C. & Trindade, T. Chemical bath deposition of $BiVO_4$. *Thin Solid Films* **406**, 93–97 (2002).

486. El-Shafey, E. I., Ali, S. N. F., Al-Busafi, S. & Al-Lawati, H. A. J. Preparation and characterization of surface functionalized activated carbons from date palm leaflets and application for methylene blue removal. *J. Environ. Chem. Eng.* **4**, 2713–2724 (2016).

487. Sevilla, M. & Fuertes, A. B. The production of carbon materials by hydrothermal carbonization of cellulose. *Carbon.* **47**, 2281–2289 (2009).

488. He, C., Giannis, A. & Wang, J. Y. Conversion of sewage sludge to clean solid fuel using hydrothermal carbonization: Hydrochar fuel characteristics and combustion behavior. *Appl. Energy* **111**, 257–266

(2013).

489. Yousatit, S. *et al.* Natural rubber as a renewable carbon source for mesoporous carbon/silica nanocomposites. *Sci. Rep.* **10**, 12977 (2020).

490. Koskin, A. P., Larichev, Y. V., Mishakov, I. V., Mel'gunov, M. S. & Vedyagin, A. A. Synthesis and characterization of carbon nanomaterials functionalized by direct treatment with sulfonating agents. *Microporous Mesoporous Mater.* **299**, 110130 (2020).

491. Österbacka, N. & Wiktor, J. Influence of oxygen vacancies on the structure of $BiVO_4$. *J. Phys. Chem. C* **125**, 1200–1207 (2021).

492. Lardhi, S., Cavallo, L. & Harb, M. Determination of the intrinsic defect at the origin of poor $H_2$ evolution performance of the monoclinic $BiVO_4$ photocatalyst using Density Functional Theory. *J. Phys. Chem. C* **122**, 18204–18211 (2018).

493. Zhang, X. *et al.* Selective synthesis and visible-light photocatalytic activities of $BiVO_4$ with different crystalline phases. *Mater. Chem. Phys.* **103**, 162–167 (2007).

494. Magureanu, M., Mandache, N. B. & Parvulescu, V. I. Degradation of pharmaceutical compounds in water by non-thermal plasma treatment. *Water Res.* **81**, 124–136 (2015).

495. Sun, J. *et al.* Engineering the dimensional interface of $BiVO_4$-2D reduced graphene oxide (RGO) nanocomposite for enhanced visible light photocatalytic performance. *Nanomaterials* **9**, 907 (2019).

496. Fu, Y., Sun, X. & Wanga, X. $BiVO_4$-graphene catalyst and its high photocatalytic performance under visible light irradiation. *Mater. Chem. Phys.* **131**, 325–330 (2011).

497. Phanichphant, S., Nakaruk, A., Chansaenpak, K. & Channei, D. Evaluating the photocatalytic efficiency of the $BiVO_4$/rGO photocatalyst. *Sci. Rep.* **9**, 16091 (2019).

498. Saha, D. *et al.* Influence of hydrogen peroxide in enhancing photocatalytic activity of carbon nitride under visible light: An insight into reaction intermediates. *J. Environ. Chem. Eng.* **6**, 4927–4936 (2018).

499. Pham, P. T. D. *et al.* Synthesis of the $BIVO_4$ nanoparticle as an efficient photocatalyst to activate hydrogen peroxide for the degradation of methylene blue under visible light irradiation. *IOP Conf. Ser. Mater. Sci. Eng.* **479**, 012036 (2019).

500. Titirici, M. M., White, R. J., Falco, C. & Sevilla, M. Black perspectives for a green future: Hydrothermal carbons for environment protection and energy storage. *Energy Environ. Sci.* **5**, 6796–6822 (2012).

501. Papaioannou, N. *et al.* Structure and solvents effects on the optical properties of sugar-derived carbon nanodots. *Sci. Rep.* **8**, 1–10 (2018).

502. Gascó, G., Paz-Ferreiro, J., Álvarez, M. L., Saa, A. & Méndez, A. Biochars and hydrochars prepared by pyrolysis and hydrothermal carbonisation of pig manure. *Waste Manag.* **79**, 395–403 (2018).

503. Zhang, M. *et al.* Hydrophobic precipitation of carbonaceous spheres from fructose by a hydrothermal process. *Carbon.* **50**, 2155–2161 (2012).

504. LaMer, V. K. & Dinegar, R. H. Theory, Production and mechanism of formation of monodispersed hydrosols. *J. Am. Chem. Soc.* **72**, 4847–4854 (1950).

505. Sun, X. & Li, Y. Colloidal carbon spheres and their core/shell structures with noble-metal nanoparticles.

*Angew. Chemie - Int. Ed.* **43**, 597–601 (2004).

506. Falco, C., Baccile, N. & Titirici, M. M. Morphological and structural differences between glucose, cellulose and lignocellulosic biomass derived hydrothermal carbons. *Green Chem.* **13**, 3273–3281 (2011).

507. Berge, N. D. *et al.* Hydrothermal carbonization of municipal waste streams. *Environ. Sci. Technol.* **45**, 5696–5703 (2011).

508. Heilmann, S. M. *et al.* Hydrothermal carbonization of microalgae II. Fatty acid, char, and algal nutrient products. *Appl. Energy* **88**, 3286–3290 (2011).

509. Correa, C. R. & Kruse, A. Biobased functional carbon materials: Production, characterization, and applications - a review. *Materials (Basel).* **11**, (2018).

510. Wu, C. & Chang, J. Bonelike apatite formation on carbon microspheres. *Mater. Lett.* **61**, 2502–2505 (2007).

511. Wang, Q., Li, H., Chen, L. & Huang, X. Monodispersed hard carbon spherules with uniform nanopores. *Carbon.* **39**, 2211–2214 (2001).

512. Mahdavinia, G. R., Bazmizeynabad, F. & Seyyedi, B. kappa-Carrageenan beads as new adsorbent to remove crystal violet dye from water: Adsorption kinetics and isotherm. *Desalin. Water Treat.* **53**, 2529–2539 (2015).

513. Soares, S. F., Simões, T. R., Trindade, T. & Daniel-da-Silva, A. L. Highly efficient removal of dye from water using magnetic carrageenan/silica hybrid nano-adsorbents. *Water. Air. Soil Pollut.* **228**, (2017).

514. Liu, J., Zhan, X., Wan, J., Wang, Y. & Wang, C. Review for carrageenan-based pharmaceutical biomaterials: Favourable physical features versus adverse biological effects. *Carbohydr. Polym.* **121**, 27–36 (2015).

515. Soares, S. F., Simões, T. R., António, M., Trindade, T. & Daniel-da-Silva, A. L. Hybrid nanoadsorbents for the magnetically assisted removal of metoprolol from water. *Chem. Eng. J.* **302**, 560–569 (2016).

516. Fernandes, T., Soares, S. F., Trindade, T. & Daniel-Da-silva, A. L. Magnetic hybrid nanosorbents for the uptake of paraquat from water. *Nanomaterials* **7**, (2017).

517. Nanaki, S. G. *et al.* Synthesis and characterization of modified carrageenan microparticles for the removal of pharmaceuticals from aqueous solutions. *Colloids Surfaces B Biointerfaces* **127**, 256–265 (2015).

518. Papageorgiou, M. *et al.* Novel isocyanate-modified carrageenan polymer materials: Preparation, characterization and application adsorbent materials of pharmaceuticals. *Polymers (Basel).* **9**, (2017).

519. Bixler, H. J. The carrageenan connection IV. *Br. Food J.* **96**, 12–17 (1994).

520. Luo, T. *et al.* One-step microwave-assisted preparation of oxygen-rich multifunctional carbon quantum dots and their application for $Cu^{2+}$-curcumin detection. *Talanta* **205**, 120117 (2019).

521. Liang, Q., Ma, W., Shi, Y., Li, Z. & Yang, X. Easy synthesis of highly fluorescent carbon quantum dots from gelatin and their luminescent properties and applications. *Carbon.* **60**, 421–428 (2013).

522. Wang, Y. *et al.* κ-Carrageenan-derived carbon dots for highly selective and sensitive detection of $Fe^{3+}$

and oxytetracycline. *J. Mater. Sci.* **56**, 1272–1285 (2021).

# Appendices

# Appendix A | CHAPTER II

## Supporting Material

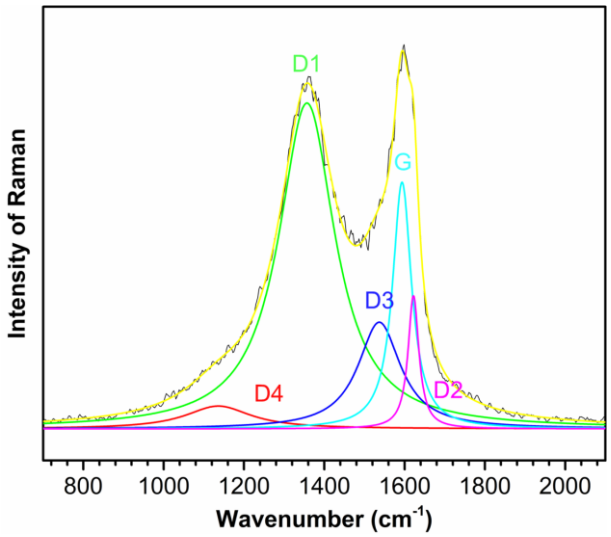


**Figure II.S1:** Deconvolution of Raman bands of pristine GO obtained by multi-peaks fitting using the Lorentz function.[313] The D and G bands were deconvoluted into five components, which were assigned to aryl-alkyl ether (D4, 1135 $cm^{-1}$), graphene edges (D1, 1356 $cm^{-1}$), amorphous carbon structures (D3, 1536 $cm^{-1}$), graphitic carbon (G, 1593 $cm^{-1}$), and graphene sheets (D2, 1622 $cm^{-1}$).[313,353,489]

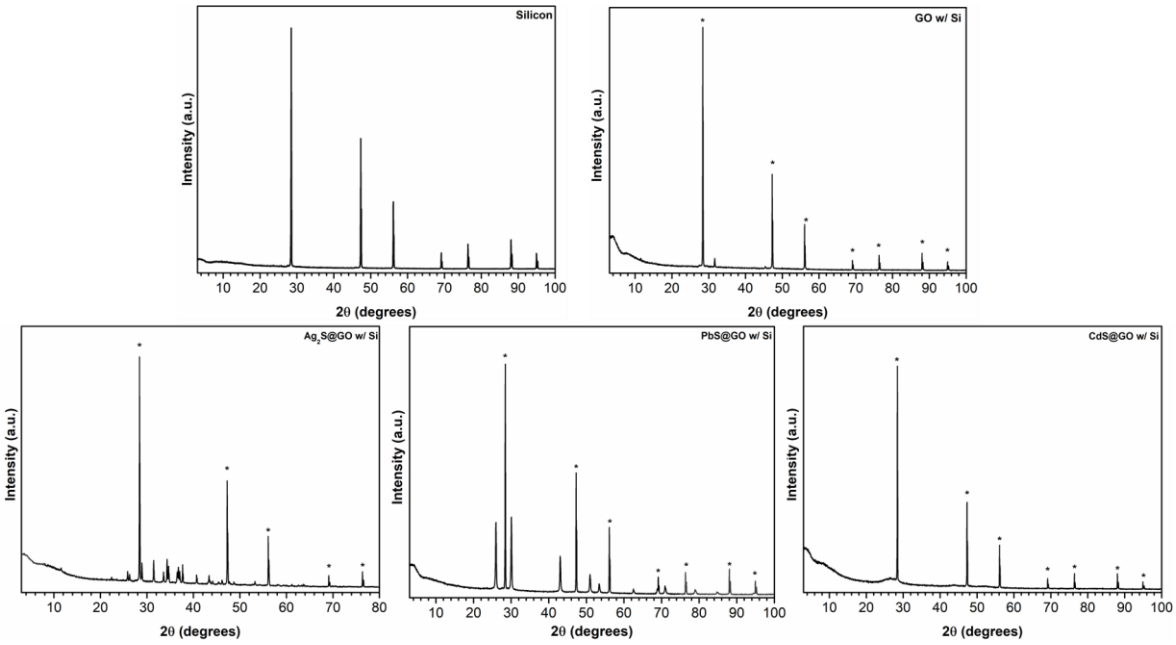


**Figure II.S2:** Powder XRD patterns for metal sulfide@GO hybrid nanostructures as indicated, with Si as internal reference (marked as *).

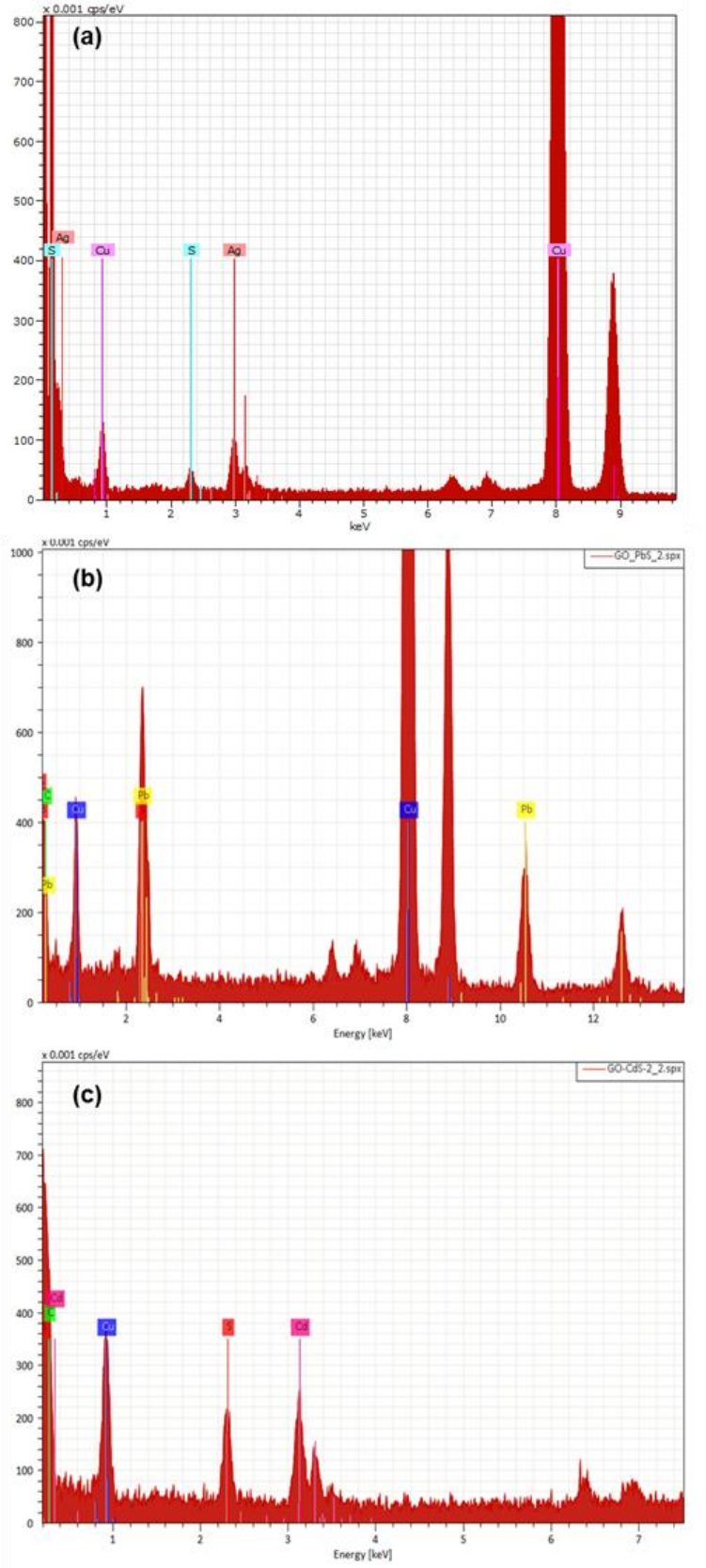


**Figure II.S3:** EDS measurements for $Ag_2S$@GO (a), PbS@GO (b) and CdS@GO (c) hybrid nanostructures indicating the respective metal.

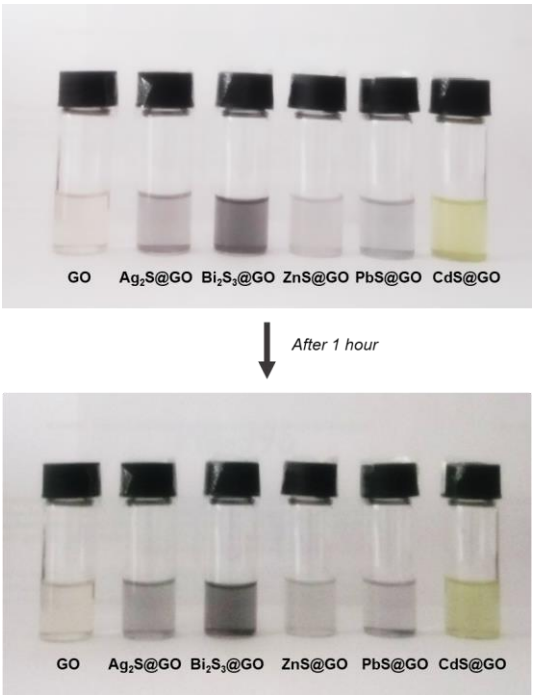


**Figure II.S4:** Ethanolic suspensions of metal sulfide@GO (0.05 mg/ mL) after preparation and 1 hour standing.

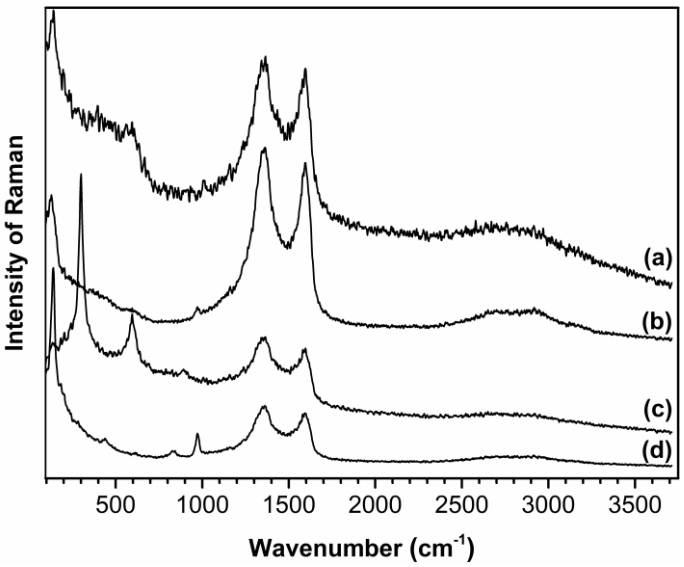


**Figure II.S5**: Raman spectra of $Ag_2S$@GO (a), $Bi_2S_3$@GO (b), CdS@GO (c) and PbS@GO (d) hybrid nanostructures.

# Appendix B | CHAPTER IV

**Supporting Material**

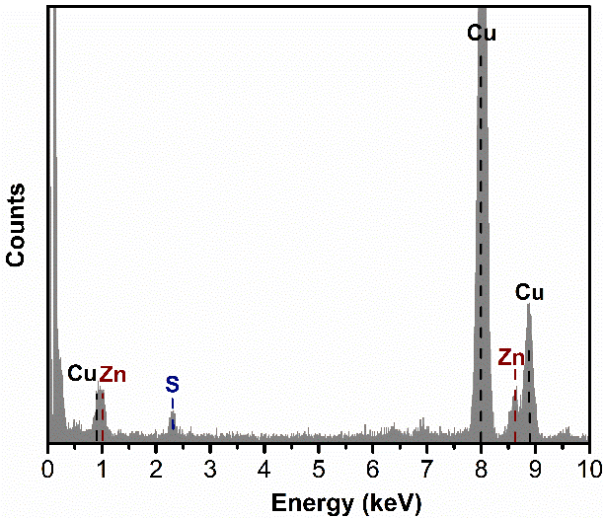


**Figure IV.S1:** EDS spectrum of the ZnS@GO hybrid material placed on a Cu grid.

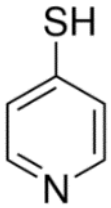


**Figure IV.S2:** Molecular structure of 4-mercaptopyridine (4-MPy).

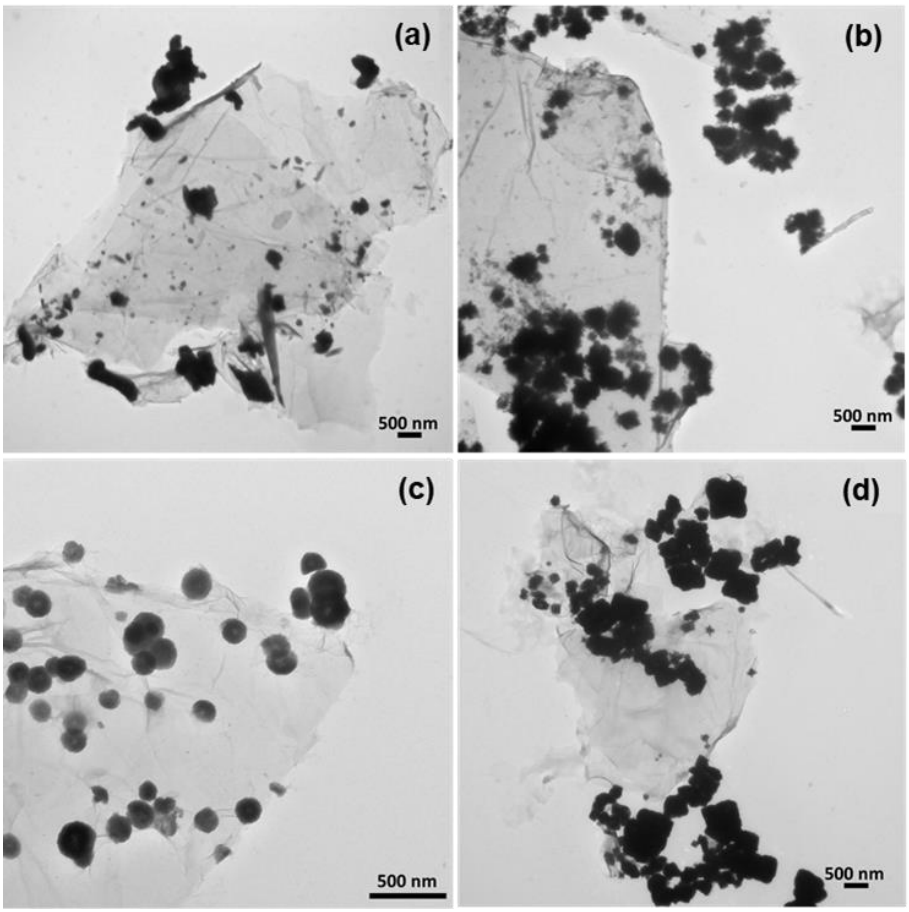


**Figure IV.S3:** TEM images of GO sheets decorated with several semiconductor nanophases $Ag_2S$ (a), $Bi_2S_3$ (b), CdS (c) and PbS (d).

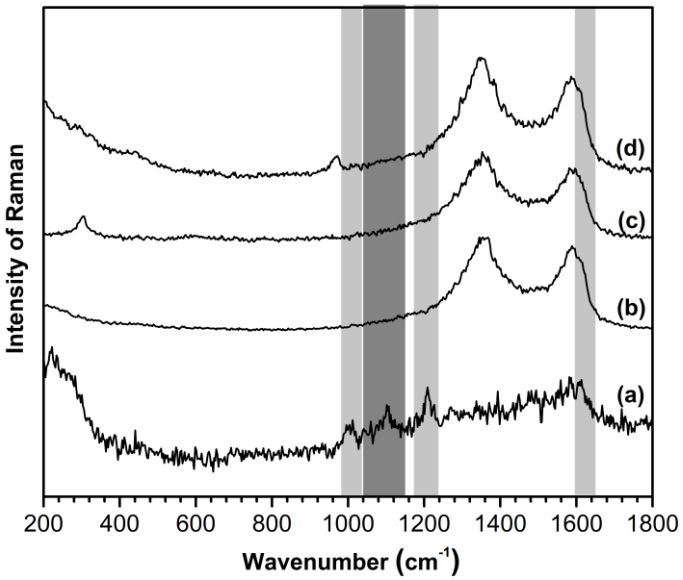


**Figure IV.S4:** Raman spectra of 4-MPy (0.1 M) using $Ag_2S$@GO (a), $Bi_2S_3$@GO (b), CdS@GO (c) and PbS@GO (d) as substrate.

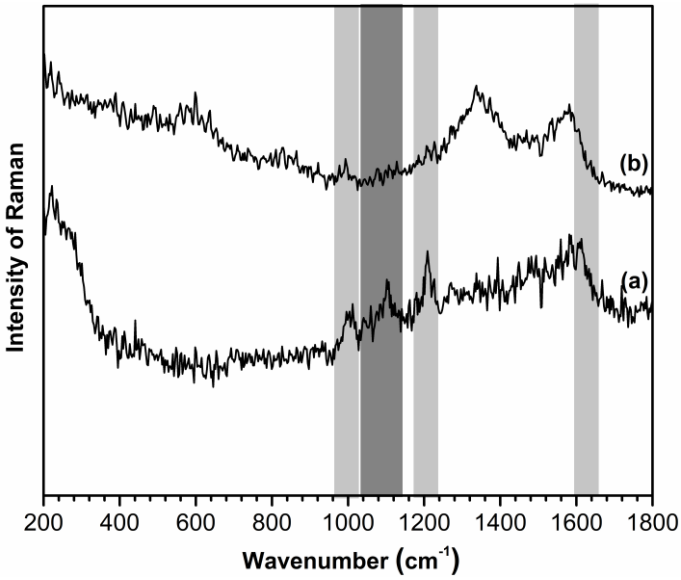


**Figure IV.S5:** Raman spectra of 4-MPy with concentration of 0.1M (a) and 0.01 M (b) using $Ag_2S$@GO as substrate.

## Computational details

The adsorption of 4-MPy on a ZnS(110) surface was investigated using the Vienna ab initio simulation package (VASP).[1] The valence electron densities were expanded in a plane-wave basis set with a cutoff for the kinetic energy of 415 eV, while the effects of the core electrons on the valence electron densities were taken into account by means of the projector-augmented wave (PAW) method.[2] The calculations were carried out using the Perdew, Burke, and Ernzerhof (PBE) exchange-correlation functional[3] within the generalized gradient approximation (GGA), including dispersion interactions through the Grimme D3 method.[4] The convergence criteria for the self-consistent energies and forces for relaxed structures were set to $10^{-6}$ eV and 0.01 eV/Å, respectively. For the calculation of band gaps and densities of states, was employed the hybrid functional known as HSE06, with Hartree-Fock exchange mixing fraction and screening parameters of 0.25 and 0.2 $Å^{-1}$, respectively.[5,6] In all calculations involving surfaces, aligned along the $x$-$y$ plane, in order to avoid interaction between replicas of the surface, due to the use of periodic boundary conditions along all three cartesian directions, the total height of the cells (in the direction perpendicular to the plane of the slabs) was set so as to leave at least 15 Å of vacuum width between the periodic copies of the surface, to be partially filled by the adsorbed 4-MPy. The Brillouin zone was sampled using Monkhorst-Pack (MP) grids of k-points,[7] with different densities depending on the size of the system, as disclosed in the following paragraphs. Normal modes of vibration were obtained by diagonalizing the Hessian matrix with elements computed as finite differences of 0.015 Å of analytical gradients.

***Bulk ZnS***

The sphalerite polymorph of ZnS, with zinc blende structure was considered and experimentally measured the lattice parameter, *a* of 5.42 Å. The calculations (with an MP 16×16×16 k-point sampling) yield similar values: 5.38 and 5.36 Å with PBE and HSE06, respectively. As often happens with most semiconductors, although the lattice constants are similar with both functionals, the band gap of ZnS is quite different: 2.16 and 3.57 eV with PBE and HSE06, respectively. The latter compares well with the experimental value of 3.7 eV. The calculated bulk Zn-S bond length is therefore $\sqrt{3}a/4$ = 2.33 Å.

***ZnS(110) surface***

For the adsorption of 4-MPy on ZnS, the ZnS(110) surface was analyzed, as it is the most likely morphology of the surface of the ZnS particles.[8] The structure is known to undergo some surface relaxation, which reflects in shorter bond lengths near the edges. In particular, the calculations on a single rectangular unit cell (**Figure IV.S6**), using an MP 12×12×1 k-point grid, indicate that the bond length between the outermost Zn and S atoms is reduced to 2.26 Å. The calculated lattice parameters are $a_{ZnS(110)}$ = 5.35 and $b_{ZnS(110)}$ = 3.81 Å. The HSE06 band gap is 3.75 eV, in agreement with the experimental value of 3.7 eV.

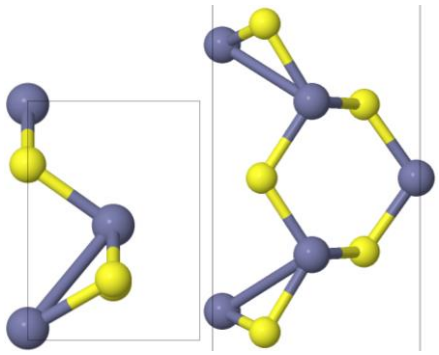

**Figure IV.S6:** Top (left) and side (right) views of the ZnS(110) surface unit cell considered in this work. Yellow and purple spheres represent sulphur and zinc atoms, respectively. The grey straight lines are boundaries of the cell.

***GO***

The experiments were conducted using GO with 70% and 30% of carbon and oxygen, respectively, the computational model of this surface comprises a rectangular GO unit cell (**Figure IV.S7**) with four carbon atoms and two oxygens, equivalent to a 67%/ 33% carbon/ oxygen stoichiometry. This unit cell is the result of comparing several positions of the oxygen atoms with respect to the baseline graphene unit cell, with the calculations done using an MP 16×16×1 grid of k-points. This unit cell is

similar to the one used in Ref.[9] but with only half as many oxygen atoms. For this reason, the shortest lattice parameter, $b_{GO}$ = 2.57 Å, is very close to the 2.53 Å found in that reference, while the longest one, $a_{GO}$ = 4.87 Å, is considerably shorter than the 5.53 Å found in the same reference, due to the lack of oxygen atoms along this direction.

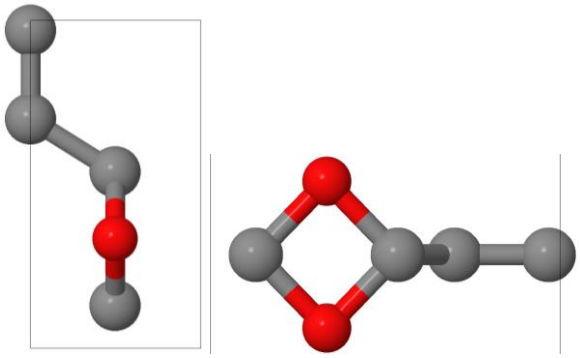

**Figure IV.S7:** Top (left) and side (right) views of the GO surface unit cell considered in this work. Red and grey spheres represent oxygen and carbon atoms, respectively. The grey straight lines are boundaries of the cell.

***ZnS@GO***

Because the lattice parameters of ZnS(110) and GO are different, a unit cell of ZnS@GO is necessarily larger than that of ZnS(110) or GO. The *a* lattice constants of both surfaces are similar (they differ by around 8%), therefore it was assumed that $a_{ZnS@GO} = a_{GO}$, as GO is likely to be less flexible to changes in bond lengths than the thicker, more spread-out ZnS(110). As for the *b* lattice parameter of ZnS@GO, note that $2b_{ZnS(110)}$ = 7.62 Å ≈ 7.72 Å = $3b_{GO}$ and, for this reason, $3b_{GO}$ should be an adequate initial guess for $b_{ZnS@GO}$. Indeed, after atomic position and cell size optimization (using MP 4×6×1), values that are between those of GO and ZnS(110), $a_{ZnS@GO}$ = 5.01 Å and $b_{ZnS@GO}$ = 7.72 Å were obtained, which differ from the predicted parameters by 0.85% and 0.02%, respectively, confirming that GO does indeed impose its lattice parameter upon the more stretchy ZnS(110); (repeating the calculation initially assuming $a_{ZnS@GO} = a_{ZnS(110)}$ gave the same result). The ensuing unit cell of ZnS@GO is shown in **Figure IV.S8**. The distance between surfaces, measured in the direction perpendicular to them, is of about 2.25 Å. Inspection of the side view of the unit cell shows that the oxygen atoms of GO attempt to occupy interstitial positions of the nearby ZnS(110) face. This contrasts with the reported findings,[9] where the 1:1 carbon:oxygen ratio assumed for GO forces the two surfaces farther apart, lying 3.43 Å away from each other. However, in agreement with the same reference, an alignment can be seen between the S atoms of ZnS(110) and the interstitials between oxygen atoms of GO.

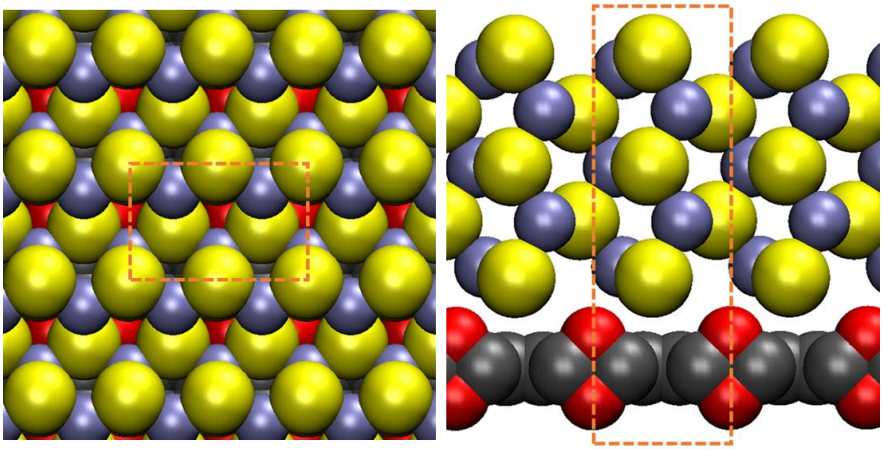

**Figure IV.S8:** Top (left) and side (right) views of the ZnS(110)@GO surface unit cell considered in this work. The dashed rectangles represent the boundaries of the unit cell. The colour code is the same as in **Figure IV.S6** and **Figure IV.S7.**

***4-MPy***

Even though the experimental results indicate that the molecule is deprotonated when adsorbed, it was found that the most stable form of isolated 4-MPy is the protonated one, with the hydrogen atom bonded to the sulphur atom (**Figure IV.S9**). The normal modes of vibration and the respective Raman and IR intensities were calculated;[10,11] the respective plots are shown in **Figure IV.S10**, while the frequencies of the normal modes of vibration are shown in **Table IV.S1**. The differences between the experimental and theoretical plots are partially due to the fact that the calculations were done for a molecule in vacuum, rather than in an aqueous solution. In both cases, the calculated plots are able to capture the main features of the experimental spectra, albeit generally with lower frequencies. Note the presence of the peak measured at 730 $cm^{-1}$ and calculated at 724 $cm^{-1}$, corresponding to a C-S stretching mode. The experimental peaks at 1627 and 1119 $cm^{-1}$ appear slightly downshifted in the calculations as well, at 1562 and 1107 $cm^{-1}$.

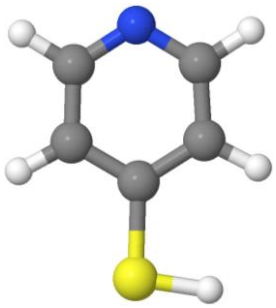

**Figure IV.S9:** Configuration of isolated 4-MPy considered in this work. The spheres represent atoms of carbon (grey), hydrogen (white), nitrogen (blue) and sulphur (yellow).

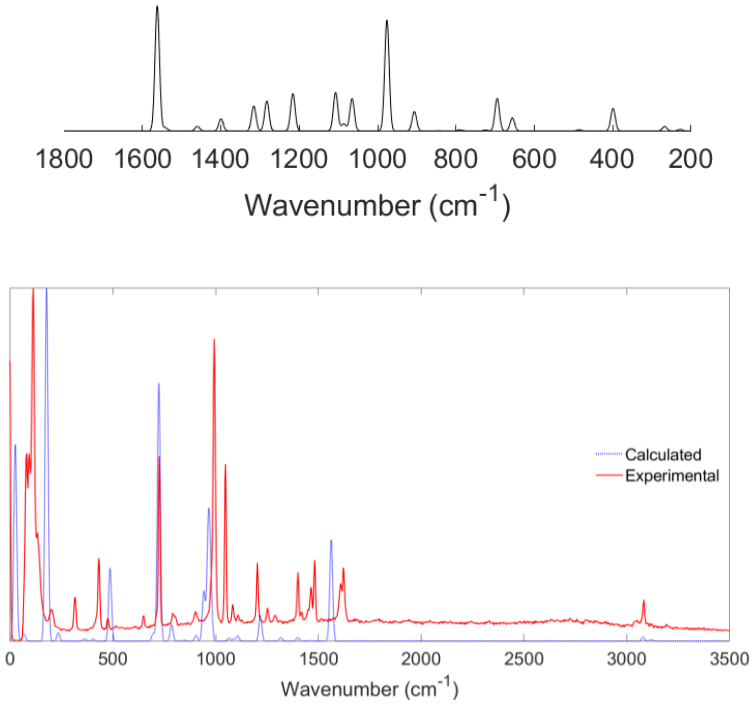


**Figure IV.S10:** Calculated Raman (top) and calculated/measured IR (bottom) plots of 4-MPy.

**Table IV.S1**: Frequencies ($cm^{-1}$) of the normal modes of vibration identified experimentally (left), the corresponding calculated modes (centre) and the percent deviation of the calculations with respect to the measurements (right).

| Measured | Calculated | Deviation (%) |
|---|---|---|
| 434 | 399 | -8 |
| 652 | 695 | 7 |
| 730 | 724 | -1 |
| 1006 | 976 | -3 |
| 1059 | 1065 | 1 |
| 1119 | 1107 | -1 |
| 1211 | 1216 | 0 |
| 1399 | 1400 | 0 |
| 1492 | 1460 | -2 |
| 1627 | 1562 | -4 |

***4-MPy@ZnS(110)***

Regardless of the surface considered, it was found that the adsorption of the molecule occurs in its deprotonated form. In order to minimize the interaction between periodic copies of the molecule, the adsorption of 4-MPy on ZnS was studied considering an approximately square *p*(3×4) supercell, with dimensions 15.22×17.35×24.00 Å$^3$, and an MP 2×2×1 special k-point grid. Given that the slab has a width of about 8 Å, this leaves 16 Å of vacuum to be partially filled by the molecule, whose largest distance between atoms was calculated at around 5.7 Å. On this surface, the calculations suggest that the molecule adsorbs preferably *via* its sulphur atom, bonded to a zinc atom of the surface, as shown in **Figure IV.S11**, with a Zn-S distance of approximately 2.39 Å, comparable to the bulk Zn-S distance of 2.33 Å. The plane of the molecule makes an angle of around 41º with the plane of the surface. On this surface, adsorption on an S atom of the surface is not stable – the molecule relaxes back to the vicinity of a surface Zn – nor is the adsorption *via* the N atom of 4-MPy. The measured Raman spectrum of 4-MPy@ZnS(110) is shown in **Figure IV.S12**.

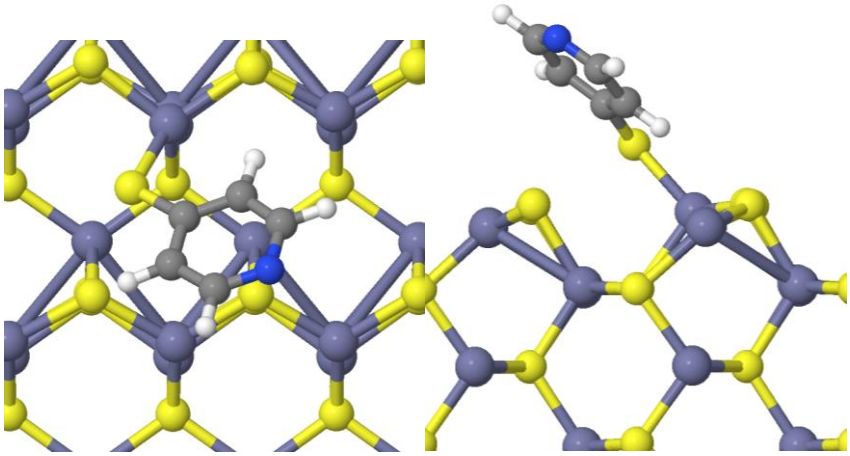

**Figure IV.S11:** Top (left) and side (right) views of the configuration of the most stable form of 4-MPy adsorbed onto a ZnS(110) surface. The colour code is the same as in **Figure IV.S6** and **Figure IV.S9**.

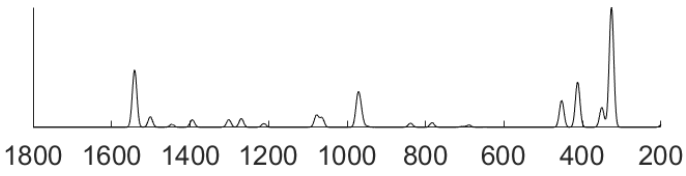


**Figure IV.S12:** Calculated Raman spectra of 4-MPy@ZnS(110), as a function of the wavenumber in cm$^{-1}$.

The adsorption energy ($E_{ads}$) can be calculated by **Equation IV.S1**, where $E_X$ on the right side of the equation stands for the total energy of a supercell containing X.

$$E_{\text{ads}} = E_{\text{surf+mol}} + E_{\text{surf+H}} - 2E_{\text{surf}} - E_{\text{mol+H}} \qquad Eq.IV.S1$$

Negative $E_{ads}$ indicate energetically favourable adsorption, while positive values occur when the adsorbent and adsorbate prefer to remain far from each other. Here, it was assumed that the molecule is protonated in aqueous solution but deprotonates as it approaches the surface, with the H atom adsorbing on a different site. All relevant calculated $E_{ads}$ and distances between the adsorbate and the closest surface atom are summarized in **Table IV.S2**.

**Table IV.S2:** Adsorption energy ($E_{ads}$) and shortest distance between the atoms of the adsorbate and those of the surface ($d$) for all the studied adsorptions. In some cases, two distances are given, corresponding to two adsorbates present in the periodic supercell, adsorbed on a surface Zn and on a surface S, respectively. H adsorptions are relative to the gas phase $H_2$, and 4-MPy adsorptions are relative to the gas phase protonated 4-MPy.

| System | $E_{ads}$ / eV | $d$ / Å |
|---|---|---|
| **H on Zn of ZnS(110)** | +1.85 | 1.62 |
| **H on S of ZnS(110)** | +0.59 | 1.35 |
| **H covering ZnS(110)** | +0.21 | 1.55 / 1.35 |
| **H on GO** | -1.12 | 0.99 |
| **4-MPy on Zn of ZnS(110)** | -0.61 | 2.39 |
| **4-MPy on Zn of ZnS(110)@GO** | -0.65 | 2.38 |
| **4-MPy on S of ZnS(110)@GO** | -1.01 | 2.10 |
| **Two nearby 4-MPy on ZnS(110)@GO** | -1.36 | 2.24 / 2.10 |
| **4-MPy covering ZnS(110)@GO** | -1.46 | 2.23 / 2.10 |

### *4-MPy@ZnS(110)@GO*

As in the case of 4-MPy@ZnS(110), a larger, $p(2\times3)$, ZnS(110)@GO supercell to study the adsorption of 4-MPy on this hybrid surface was employed. The adsorption of a single molecule occurs again *via* the S atom of 4-MPy but bonded to an S atom of the surface (**Figure IV.S13**), in clear contrast with the case of the absence of GO. The S-S bond length is about 2.10 Å, while the Zn atom closest to the S atom of the molecule is 3.55 Å away from it. In this configuration, the angle between the planes of the molecule and the surface is around 34º. Adsorption on a surface Zn is also possible, but energetically disadvantageous by 0.36 eV.

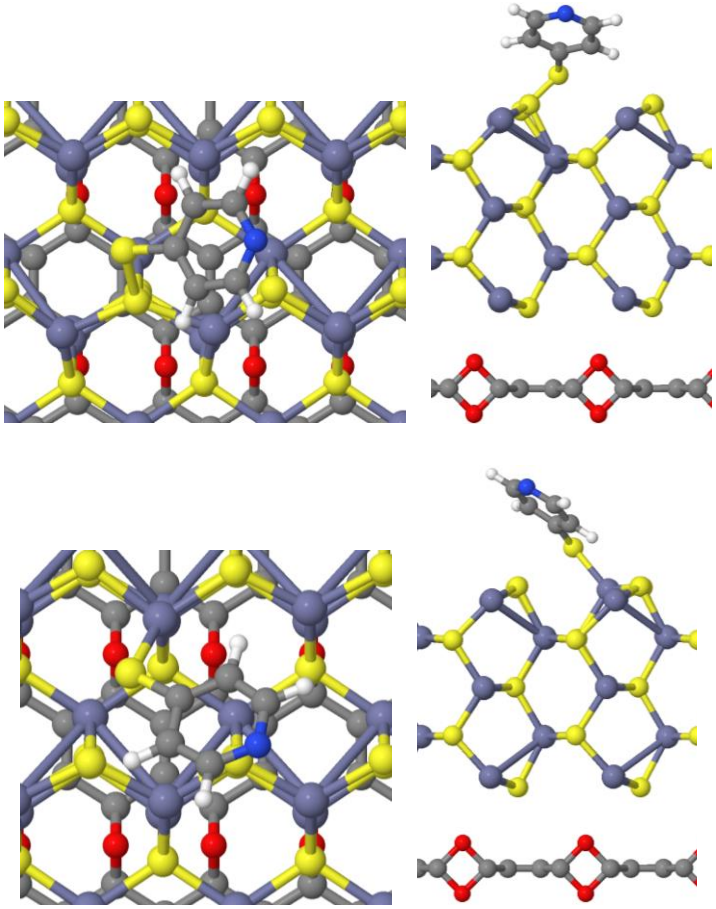

**Figure IV.S13:** Top (left) and side (right) views of the configuration of the most stable form of 4-MPy adsorbed onto a Zn (top) or S (bottom) atom of the ZnS(110)@GO surface. The colour code is the same as in **Figure IV.S8** and **Figure IV.S9**.

The $E_{ads}$ of H on ZnS(110)@GO was calculated and found that it can only adsorb (with negative $E_{ads}$) by bonding to an O atom of GO; adsorption on ZnS(110) is not stable with respect to having a hydrogen molecule isolated from the surface. Adsorption on the GO sheet is reasonable from the experimental point of view since that it is only partially covered by ZnS particles. For 4-MPy adsorbed on ZnS(110)@GO, an $E_{ads}$ of -1.01 eV was obtained. Additionally, was considered the adsorption of two 4-MPy molecules as a dimer, 4-aldrithiol species (**Figure IV.S14**).

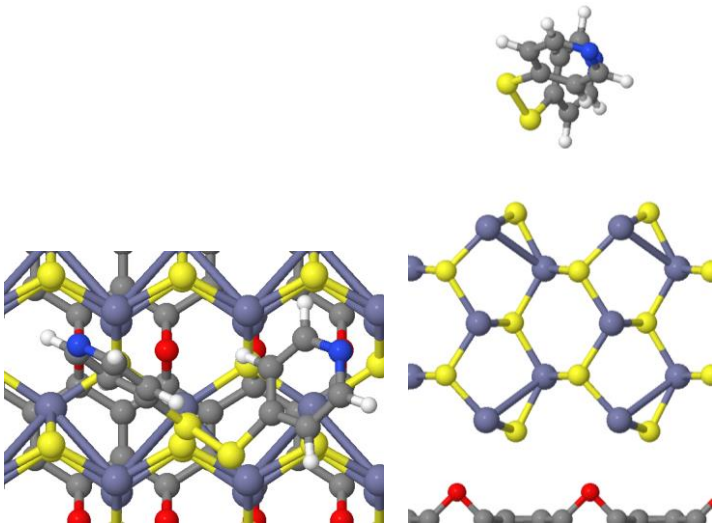

**Figure IV.S14:** Top (left) and side (right) views of the configuration of the most stable form of 4-aldrithiol adsorbed onto a ZnS(110)@GO surface. The colour code is the same as in **Figure IV.S8** and **Figure IV.S9**.

Since, on ZnS(110)@GO, the 4-MPy can adsorb either on a surface S or on a surface Zn, the co-adsorption of several nearby molecules may be possible and even favourable. The co-adsorption of two molecules occurs on neighbouring surface sites as depicted in **Figure IV.S15**.

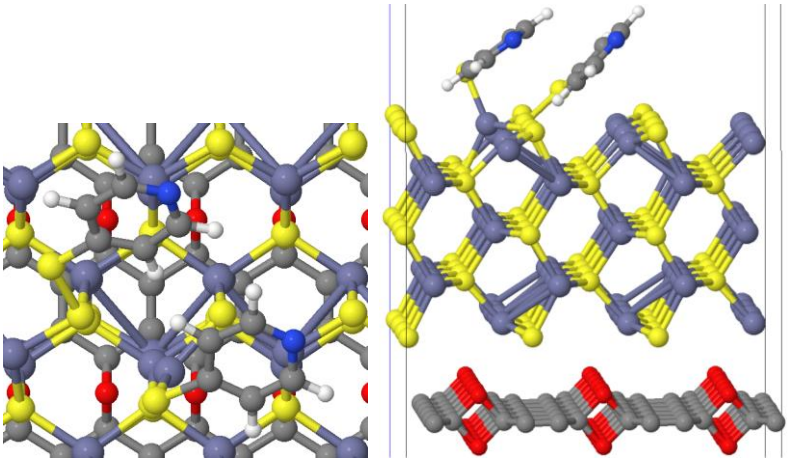

**Figure IV.S15:** Top (left) and side (right) views of the configuration of the most stable form of two 4-MPy molecules co-adsorbed onto a ZnS(110)@GO surface. The colour code is the same as in **Figure IV.S8** and **Figure IV.S9**.

Finally, the possibility of the co-adsorption of 4-MPy as an infinite array of molecules was investigated. This was done by considering a small cell of ZnS(110)@GO with two molecules adsorbed on it (the periodic boundary and the fact that the molecules lie near the boundary of the supercell produce the infinite array of molecules). The relaxed atomic positions, in **Figure IV.S16**,

show that the molecules form a hexagonal lattice (more easily seen by focusing on the blue N atoms on the top view). The $E_{ads}$ per molecule is -1.46 eV, hinting that this is the most favourable adsorption configuration. The molecules lie almost parallel to each other (with an angle of approximately 8$^{o}$ between their planes) and make angles of around 45$^{o}$ with the plane of the surface.

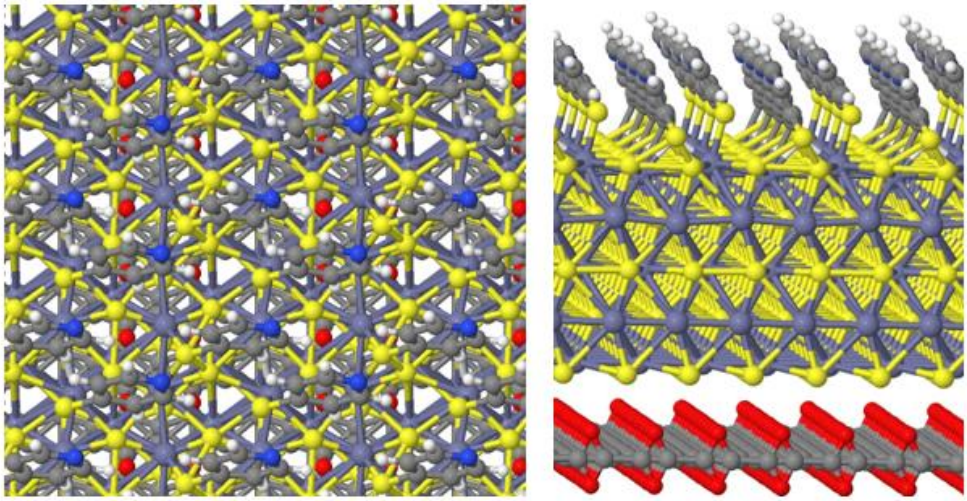

**Figure IV.S16:** Top (left) and side (right) views of the configuration of the most stable form of an infinite array of 4-MPy molecules co-adsorbed onto a ZnS(110)@GO surface. The configurations shown are in fact periodic replicas of the cell that was used for the calculations.

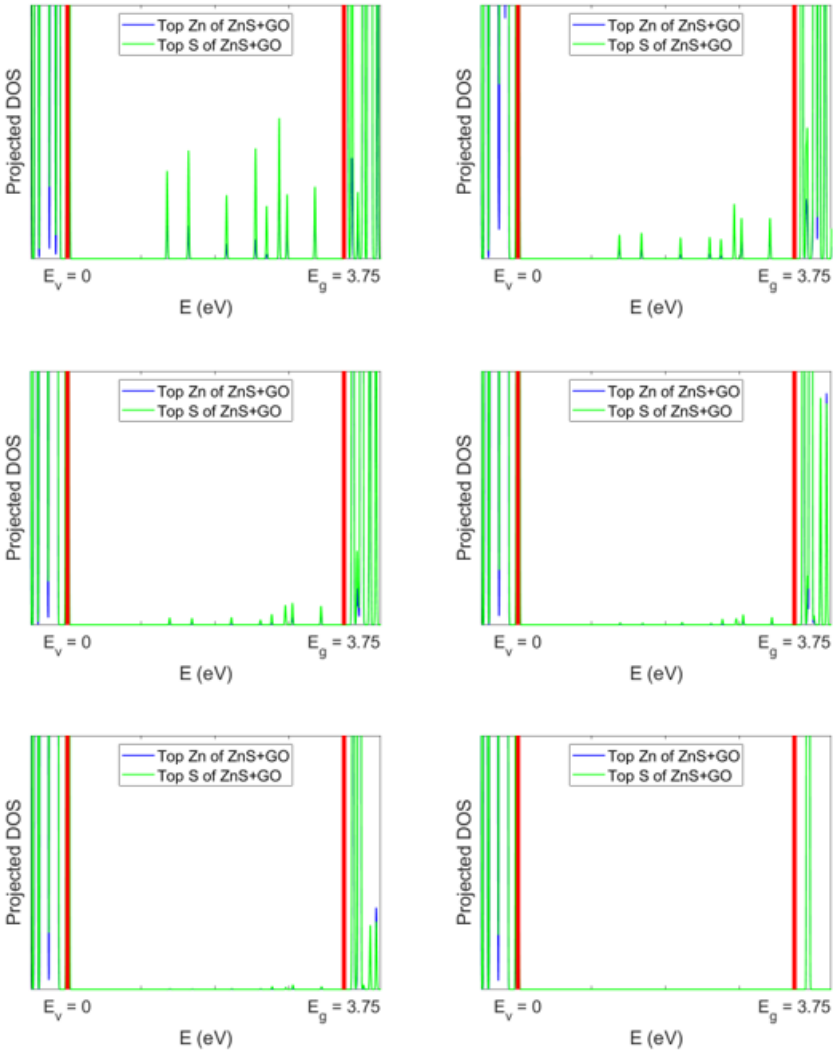


**Figure IV.S17**: Projected DOS onto the S and Zn atoms farthest from GO, in ZnS(110)@GO. The topmost image corresponds to ZnS(110) and GO separated by the optimized distance. The following four images correspond, from left to right and from top to bottom, to an extra spacing of 0.5, 1, 1.5 and 2 Å. In the last image, GO is absent, causing the band gap to contain no Zn or S electronic states.

## References

1. Kresse, G. & Furthmüller, J. Efficient iterative schemes for ab initio total-energy calculations using a plane-wave basis set. *Phys. Rev. B - Condens. Matter Mater. Phys.* **54**, 11169–11186 (1996).

2. Blöchl, P. E. Projector augmented-wave method. *Phys. Rev. B* **50**, 17953–17979 (1994).

3. Perdew, J. P., Burke, K. & Ernzerhof, M. Generalized gradient approximation made simple. *Phys. Rev. Lett.* **77**, 3865–3868 (1996).

4. Grimme, S., Antony, J., Ehrlich, S. & Krieg, H. A consistent and accurate ab initio

parametrization of density functional dispersion correction (DFT-D) for the 94 elements H-Pu. *J. Chem. Phys.* **132**, 154104 (2010).

5. Heyd, J., Scuseria, G. E. & Ernzerhof, M. Hybrid functionals based on a screened Coulomb potential. *J. Chem. Phys.* **118**, 8207–8215 (2003).

6. Krukau, A. V., Vydrov, O. A., Izmaylov, A. F. & Scuseria, G. E. Influence of the exchange screening parameter on the performance of screened hybrid functionals. *J. Chem. Phys.* **125**, 224106 (2006).

7. Pack, J. D. & Monkhorst, H. J. Special Points for Brillouin-Zone Integrations. *Phys. Rev. B* **13**, 5188–5192 (1976).

8. Wright, K., Watson, G. W., Parker, S. C. & Vaughan, D. J. Simulation of the structure and stability of sphalerite (ZnS) surfaces. *Am. Mineral.* **83**, 141–146 (1998).

9. Opoku, F., Govender, K. K., Van Sittert, C. G. C. E. & Govender, P. P. Understanding the mechanism of enhanced charge separation and visible light photocatalytic activity of modified wurtzite ZnO with nanoclusters of ZnS and graphene oxide: From a hybrid density functional study. *New J. Chem.* **41**, 8140–8155 (2017).

10. Fonari, A.; Stauffer, S. Raman off-resonant activity calculator using VASP as a back-end. 2013, https://github.com/raman-sc/VASP

11. Carrasco, J. *et al.* A one-dimensional ice structure built from pentagons. *Nat. Mater.* **8**, 427–431 (2009).

# Appendix C | CHAPTER V

## Supporting Material

**Table V.S1:** Surface properties (BET surface area ($S_{BET}$), pore volume ($V_P$) and pore size ($S_P$)) of the carbon spheres materials.

| Material | $S_{BET}$ ($m^2/g$) | $V_P$ ($cm^3/g$) | $S_P$ (Å) |
|---|---|---|---|
| **κ-C spheres** | 7.1171 | 0.002812 | 56.410 |
| **κ-FC spheres** | 2.6447 | 0.003036 | 126.587 |

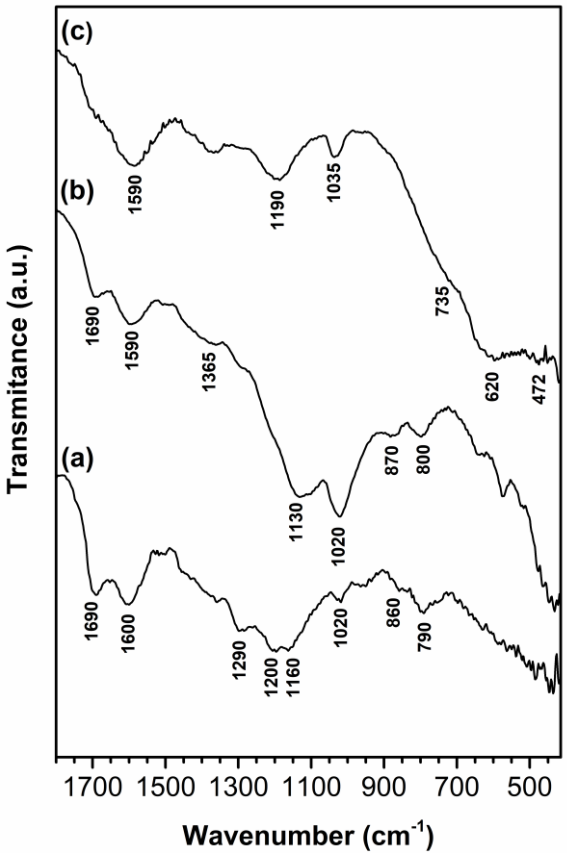


**Figure V.S1**: ATR-FTIR spectra of the κ-C spheres (a), κ-FC spheres (b) and $BiVO_4$@κ-FC hybrid (c).

**Table V.S2:** Fitting parameters obtained from Raman spectra of κ-C and κ-FC spheres in region 800-2000 $cm^{-1}$.

| Bands | Samples | κ-C spheres | κ-FC spheres |
|---|---|---|---|
| **D4** | Position $x_0/cm^{-1}$ | 1248 | 1236 |
| | FWHM/$cm^{-1}$ | 282.6 | 376.4 |
| | Area/% | 11.9 | 16.9 |
| | Intensity | 128.9 | 52.6 |
| **D1** | Position $x_0/cm^{-1}$ | 1370 | 1369 |
| | FWHM/$cm^{-1}$ | 238.3 | 249.7 |
| | Area/% | 58.1 | 52.9 |
| | Intensity | 742.2 | 246.6 |
| **D3** | Position $x_0/cm^{-1}$ | 1546 | 1535 |
| | FWHM/$cm^{-1}$ | 85.2 | 93.1 |
| | Area/% | 11.7 | 10.7 |
| | Intensity | 419.0 | 134.3 |
| **G** | Position $x_0/cm^{-1}$ | 1578 | 1574 |
| | FWHM/$cm^{-1}$ | 48.1 | 57.1 |
| | Area/% | 7.4 | 8.7 |
| | Intensity | 465.7 | 179.1 |
| **D2** | Position $x_0/cm^{-1}$ | 1608 | 1605 |
| | FWHM/$cm^{-1}$ | 51.7 | 59.0 |
| | Area/% | 10.8 | 10.9 |
| | Intensity | 634.7 | 216.9 |
| | $I_{D1}/I_G$ | 1.6 | 1.4 |
| | $I_{D4}/I_G$ | 0.3 | 0.3 |

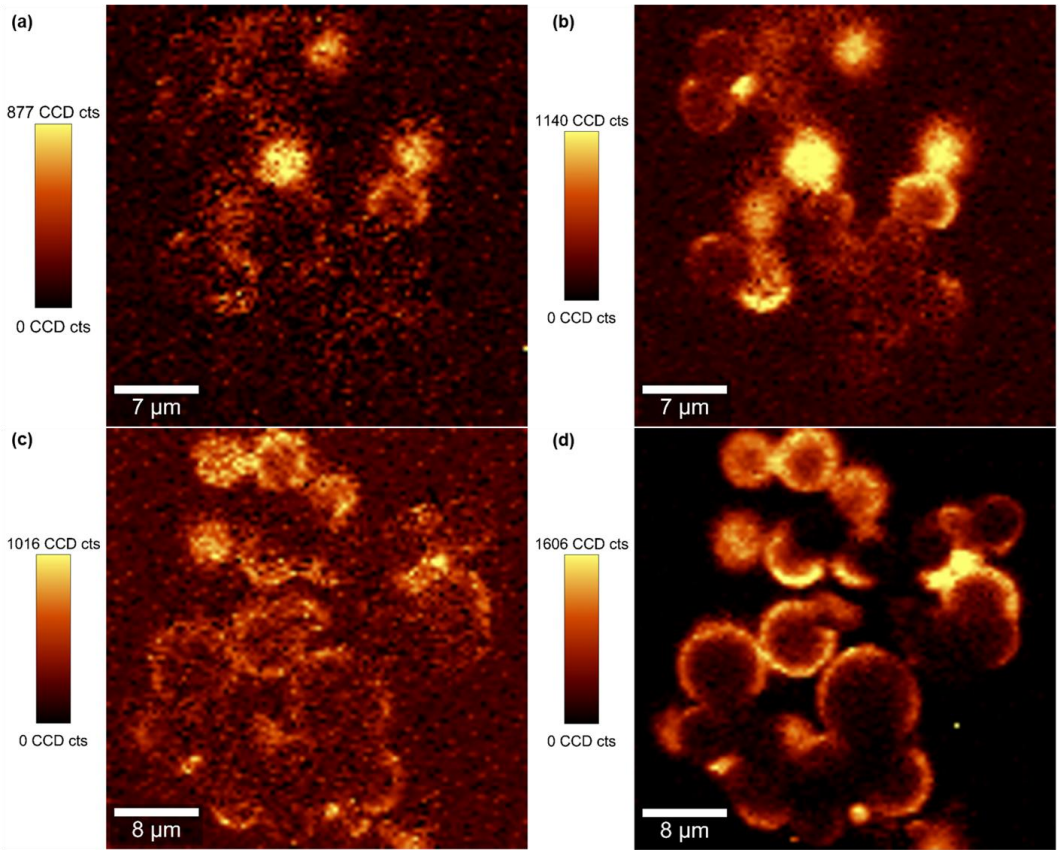


**Figure V.S2:** Raman images obtained using the integrated area of the Raman bands at 1370 $cm^{-1}$ (a) and 1578 $cm^{-1}$ (b) for κ-C and at 1369 $cm^{-1}$ (c) and 1574 $cm^{-}1$ (d) for κ-FC spheres.

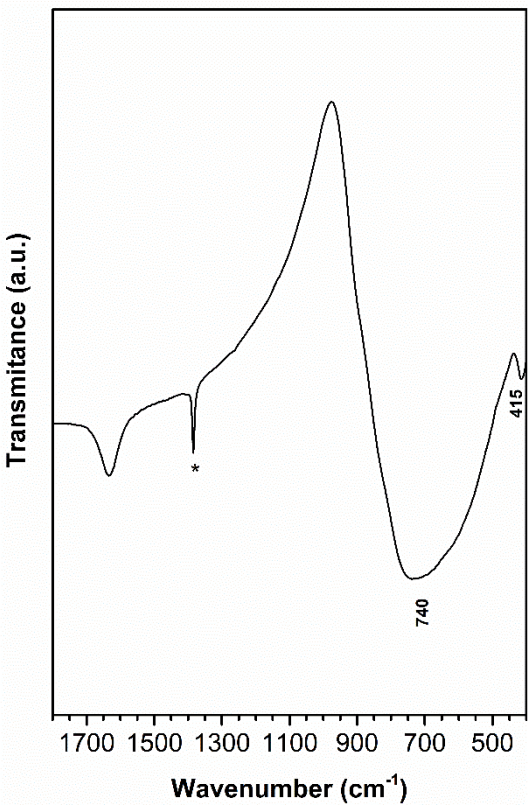


**Figure V.S3:** FTIR spectrum of $BiVO_4$ particles. Some residual KBr impurities are visible (*).

**Table V.S3:** Raman bands ($cm^{-1}$) and respective assignments of the $BiVO_4$ particles.

| Raman bands ($cm^{-1}$) | Assignment |
|---|---|
| 816 | $\nu_{sym}$(V-O) |
| 357 | $\delta_{sym}$ ($VO_4^{3-}$) |
| 333 | $\delta_{assym}$ ($VO_4^{3-}$) |
| 202 | External mode |
| 118 | External mode |

$\nu_{sym}$ – symmetric stretching; $\delta_{sym}$ – symmetric deformation; $\delta_{assym}$ – asymmetric deformation

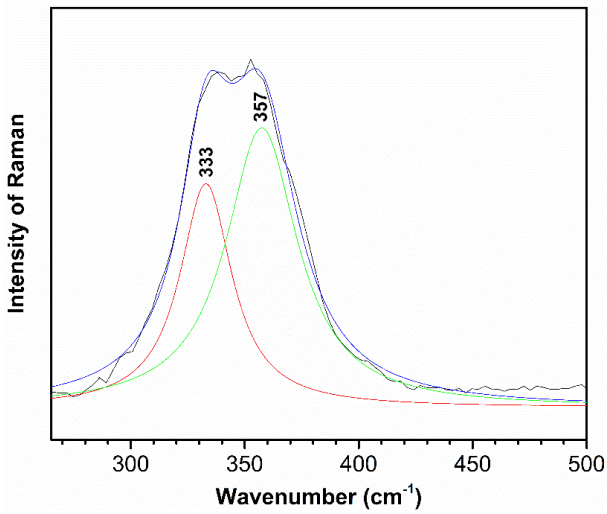


**Figure V.S4:** Deconvolution of the Raman bands (333 and 357 $cm^{-1}$) of the $BiVO_4$ particles obtained by multi-peaks fitting using the Lorentz function.

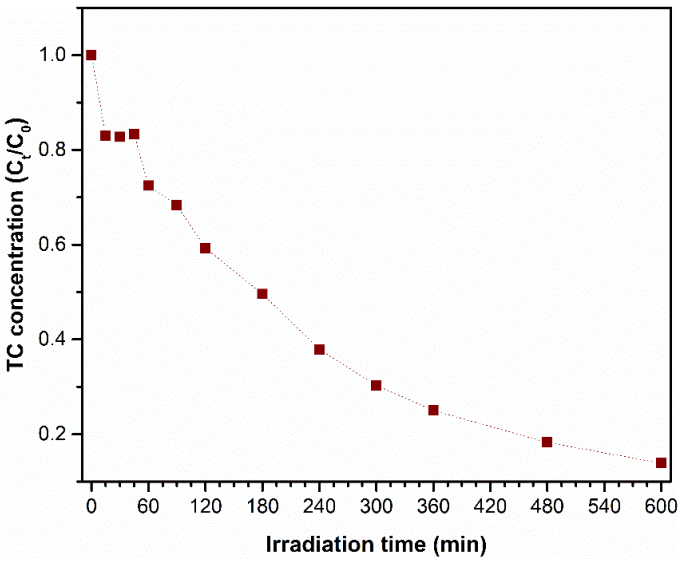


**Figure V.S5:** Concentration of TC as function of light irradiation time with 15 mg of $BiVO_4$@κ-FC hybrid (■). Conditions: 75 mL of an aqueous solution of TC 5 mg/L; 25 ºC; 10 hours of irradiation.

**Table V.S4**: TC degradation (%) obtained after 300 minutes of photocatalytic reaction (calculated by **Equation V.1**) and determined kinetic rate constant ($k$ – $min^{-1}$) of pseudo-first order with the respective $r^2$ values.

| Material | TC degradation (%) | $k$ ($min^{-1}$) ($r^2$) |
|---|---|---|
| **κ-FC** | 7 | 0.00031 (±0.826) |
| **$BiVO_4$** | 14 | 0.00046 (±0.947) |
| **$BiVO_4$@ κ-FC (7.5 mg)** | 52 | 0.0025 (±0.996) |
| **$BiVO_4$@ κ-FC (15 mg)** | 57 | 0.0029 (±0.979) |
| **$BiVO_4$@ κ-FC (25 mg)** | 63 | 0.003 (±0.993) |
| **$BiVO_4$@ κ-FC (15 mg w/ 1% $H_2O_2$)** | 88 | 0.0075 (±0.963) |

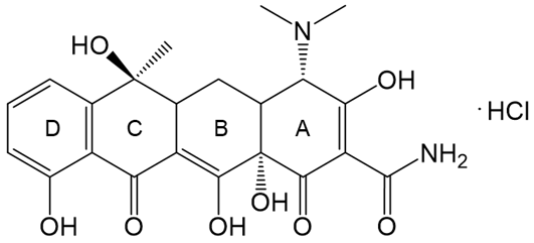


**Figure V.S6:** Chemical structure of tetracycline (TC) molecule.

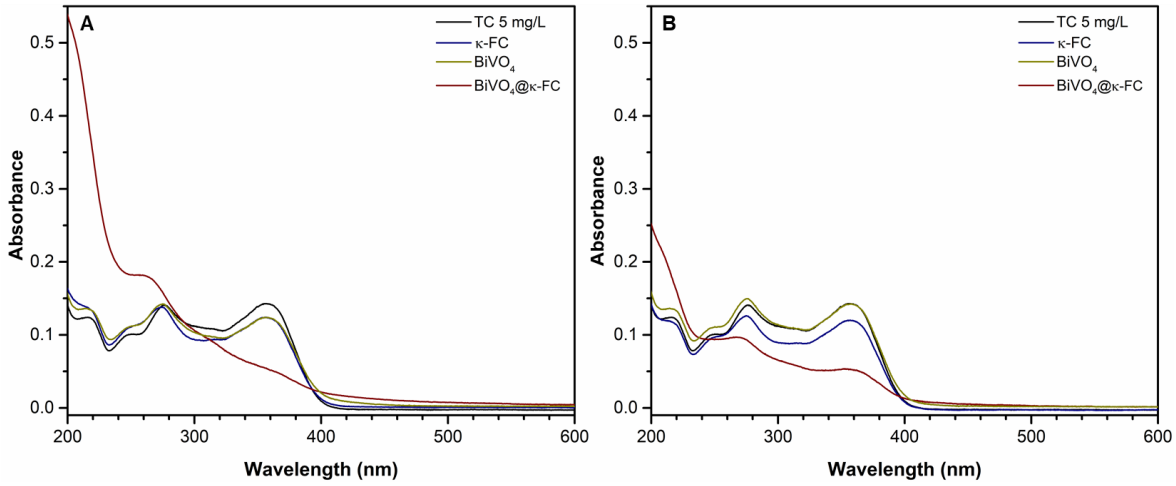


**Figure V.S7:** UV/VIS spectra of the TC 5 mg/L solution and the respective supernatants using the 3 materials (κ-FC spheres, $BiVO_4$ particles and $BiVO_4$@κ-FC hybrid) after photocatalysis (A) and adsorption (B) experiments.

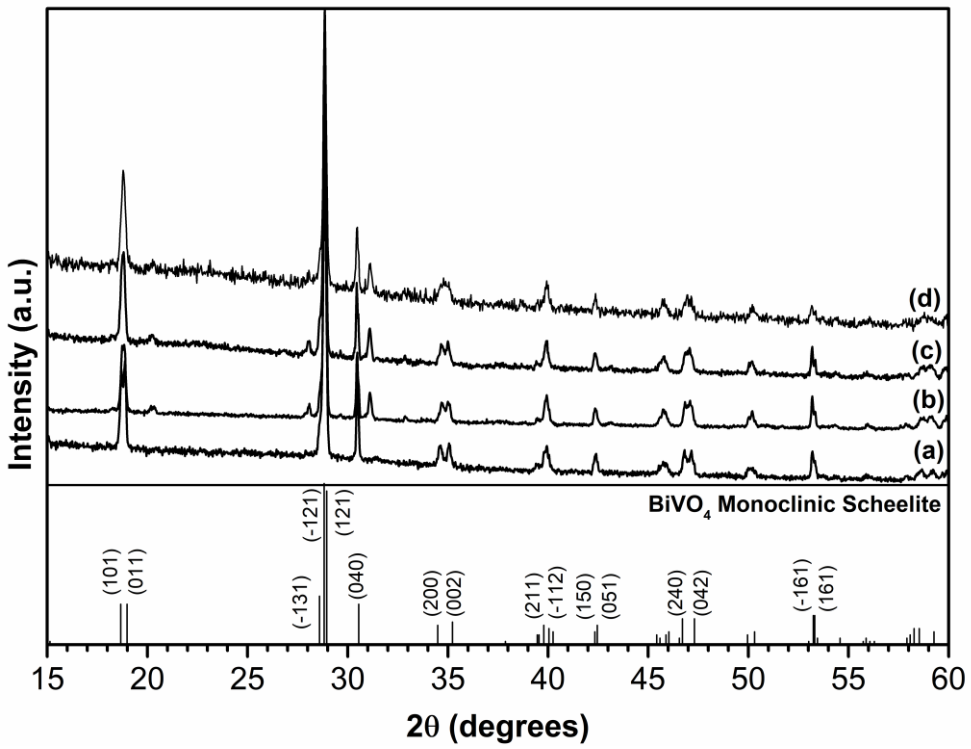


**Figure V.S8**: Powder XRD pattern of $BiVO_4$@κ-FC hybrid before photocatalysis (a) and after first (b), second (c) and third (d) photocatalytic run.

# Appendix D | Standard Powder X-ray Diffraction Data

**Annex 1:** ICDDPDF No. 00-014-0072 for the monoclinic phase of $Ag_2S$.

**00-014-0072** Nov 5, 2015 4:10 PM (rosarios)

**Status** Primary **QM:** Star **Pressure/Temperature:** Ambient **Chemical Formula:** Ag2 S
**Empirical Formula:** Ag2 S **Weight %:** Ag87.06 S12.94 **Atomic %:** Ag66.67 S33.33
**Compound Name:** Silver Sulfide **Mineral Name:** Acanthite, syn

**Radiation:** CuKα1 **λ:** 1.5405 Å **Filter:** Ni Beta **Intensity:** Diffractometer

**SYS:** Monoclinic **SPGR:** P21/n (14)
**Author's Cell [ AuthCell a:** 4.229 Å **AuthCell b:** 6.931 Å **AuthCell c:** 7.862 Å **AuthCell β:** 99.61°
**AuthCell Vol:** 227.21 Å³ **AuthCell Z:** 4.00 **AuthCell MolVol:** 56.80 ]
**Author's Cell Axial Ratio [ c/a:** 1.859 **a/b:** 0.610 **c/b:** 1.134 ]
**Density [ Dcalc:** 7.244 g/cm³ **Dmeas:** 7.2 g/cm³ ] **SS/FOM:** F(30) = 36.5(0.0147, 56)
**Temp:** 298.0 K (Author provided temperature) **Color:** Black

**Space Group:** P21/n (14) **Molecular Weight:** 247.80
**Crystal Data [ XtlCell a:** 7.862 Å **XtlCell b:** 6.931 Å **XtlCell c:** 4.229 Å **XtlCell α:** 90.00°
**XtlCell β:** 99.61° **XtlCell γ:** 90.00° **XtlCell Vol:** 227.21 Å³ **XtlCell Z:** 4.00 ]
**Crystal Data Axial Ratio [ c/a:** 0.538 **a/b:** 1.134 **c/b:** 0.610 ]
**Reduced Cell [ RedCell a:** 4.229 Å **RedCell b:** 6.931 Å **RedCell c:** 7.862 Å **RedCell α:** 90.00°
**RedCell β:** 99.61° **RedCell γ:** 90.00° **RedCell Vol:** 227.21 Å³ ]

**Atomic parameters are cross-referenced from PDF entry 04-007-8856**
**Crystal (Symmetry Allowed):** Centrosymmetric
**SG Symmetry Operators:**

| Seq | Operator | Seq | Operator | Seq | Operator | Seq | Operator |
|---|---|---|---|---|---|---|---|
| 1 | x,y,z | 2 | -x,-y,-z | 3 | x+1/2,-y+1/2,z+1/2 | 4 | -x+1/2,y+1/2,-z+1/2 |

**Atomic Coordinates:**

| Atom | Num | Wyckoff | Symmetry | x | y | z | SOF | IDP | AET |
|---|---|---|---|---|---|---|---|---|---|
| Ag | 1 | 4e | 1 | 0.733 | 0.018 | 0.305 | 1.0 | | 2#a |
| Ag | 2 | 4e | 1 | 0.285 | 0.317 | 0.432 | 1.0 | | 11-b |
| S | 3 | 4e | 1 | 0.333 | 0.233 | 0.133 | 1.0 | | 5-c |

**Subfile(s):** Common Phase, Educational Pattern, Forensic, Inorganic, Metals & Alloys, Mineral Related (Mineral , Synthetic), NBS Pattern, Thermoelectric Material

**Prototype Structure [Formula Order]:** Ag2 S **Prototype Structure [Alpha Order]:** Ag2 S
**LPF Prototype Structure [Formula Order]:** Ag2 S,mP12,14
**LPF Prototype Structure [Alpha Order]:** Ag2 S,mP12,14 **Pearson Symbol:** mP12.00
**Cross-Ref PDF #'s:** 00-011-0688 (Deleted), ✓04-001-9363 (Alternate), ✓04-006-1857 (Alternate), ✓04-006-4887 (Alternate), ✓04-007-8856 (Primary), ✓04-008-8450 (Alternate)
**Entry Date:** 09/01/1964

**References:**

| Type | DOI | Reference |
|---|---|---|
| Primary Reference | | Natl. Bur. Stand. (U. S. ), Circ. 539 10, 51 (1960). |
| Crystal Structure | | Crystal Structure Source: LPF. |
| Reflectance | | IMA Commission on Ore Microscopy QDF. |

**Database Comments:** Additional Patterns: See PDF 01-075-1061. Analysis: Spectroscopic analysis showed 0.001-0.01% Si and 0.0001-0.001% Cu. Color: Black. General Comments: Acanthite is the mineral name for this phase, most natural silver sulfide is pseudomorphous after argentite, the cubic high temperature phase. Validated by calculated pattern 00-024-0715. Sample Preparation: Sample was precipitated from the reaction of "Ag N O3" and "H2 S". Reflectance: Opaque mineral optical data on specimen from unspecified locality: R3R%=30.3-31.3, Disp.=Std. Temperature of Data Collection: Pattern taken at 298 K. Vickers Hardness Number: VHN100=23-26. Unit Cell Data Source: Powder Diffraction.

**d-Spacings (39) - Ag2 S - 00-014-0072 (Stick, Fixed Slit Intensity) - Cu Kα1 1.54056 Å**

| 2θ (°) | d (Å) | I | h | k | l | * | 2θ (°) | d (Å) | I | h | k | l | * | 2θ (°) | d (Å) | I | h | k | l | * |
|---|---|---|---|---|---|---|---|---|---|---|---|---|---|---|---|---|---|---|---|---|
| 22.4328 | 3.960000 | 10 | -1 | 0 | 1 | | 40.7387 | 2.213000 | 45 | 0 | 3 | 1 | | 52.7799 | 1.733000 | 12 | 0 | 4 | 0 | |
| 24.9137 | 3.571000 | 6 | 1 | 1 | 0 | | 43.1879 | 2.093000 | 16 | 1 | 2 | 2 | | 53.2768 | 1.718000 | 20 | -2 | 1 | 3 | |
| 25.9016 | 3.437000 | 35 | -1 | 1 | 1 | | 43.4058 | 2.083000 | 45 | 2 | 0 | 0 | | 54.1965 | 1.691000 | 6 | 0 | 4 | 1 | |
| 26.3224 | 3.383000 | 20 | 0 | 1 | 2 | | 43.6480 | 2.072000 | 16 | 0 | 2 | 3 | | 57.1665 | 1.610000 | 4 | 1 | 1 | 4 | |
| 28.9658 | 3.080000 | 60 | 1 | 1 | 1 | | 44.2090 | 2.047000 | 16 | 1 | 0 | 3 | | 58.0733 | 1.587000 | 14 | -1 | 4 | 1 | |
| 31.5199 | 2.836000 | 70 | -1 | 1 | 2 | | 45.4247 | 1.995000 | 16 | -1 | 3 | 1 | | 58.3958 | 1.579000 | 10 | -2 | 2 | 3 | |
| 33.6134 | 2.664000 | 45 | 1 | 2 | 0 | | 46.2078 | 1.963000 | 20 | -1 | 2 | 3 | | 59.4286 | 1.554000 | 8 | -2 | 0 | 4 | |
| 34.3846 | **2.606000** | 100 | -1 | 2 | 1 | | 46.9161 | 1.935000 | 4 | 0 | 0 | 4 | | 60.0241 | 1.540000 | 8 | -1 | 0 | 5 | |
| 34.7004 | 2.583000 | 70 | 0 | 2 | 2 | | 47.3572 | 1.918000 | 4 | 1 | 3 | 1 | | 61.2088 | 1.513000 | 12 | 0 | 1 | 5 | |
| 36.5565 | 2.456000 | 70 | 1 | 1 | 2 | | 47.7536 | 1.903000 | 14 | -2 | 1 | 2 | | 62.5849 | 1.483000 | 10 | 2 | 3 | 1 | |
| 36.8048 | **2.440000** | 80 | 1 | 2 | 1 | | 48.7614 | 1.866000 | 16 | 0 | 1 | 4 | | 63.2019 | 1.470000 | 10 | 2 | 1 | 3 | |
| 37.1041 | 2.421000 | 60 | 0 | 1 | 3 | | 50.1954 | 1.816000 | 4 | -1 | 1 | 4 | | 63.7342 | 1.459000 | 14 | -1 | 3 | 4 | |
| 37.7179 | **2.383000** | 75 | -1 | 0 | 3 | | 50.7333 | 1.798000 | 4 | -2 | 2 | 1 | | 67.9151 | 1.379000 | 6 | 2 | 3 | 2 | |

**Annex 2:** ICDDPDF No. 00-006-0314 for the hexagonal phase of CdS.

**00-006-0314** Oct 3, 2016 12:22 PM (ana.estrada)

**Status** Alternate **QM:** Indexed **Pressure/Temperature:** Ambient **Chemical Formula:** Cd S
**Empirical Formula:** Cd S **Weight %:** Cd77.81 S22.19 **Atomic %:** Cd50.00 S50.00
**Compound Name:** Cadmium Sulfide **Mineral Name:** Greenockite, syn **Common Name:** cadmium yellow

**Radiation:** CuKα1 **λ:** 1.5405 Å **Filter:** Ni Beta **Intensity:** Diffractometer

**SYS:** Hexagonal **SPGR:** P63mc (186)
**Author's Cell [ AuthCell a:** 4.136 Å **AuthCell c:** 6.713 Å **AuthCell Vol:** 99.45 Å³ **AuthCell Z:** 2.00
**AuthCell MolVol:** 49.73 ] **Author's Cell Axial Ratio [ c/a:** 1.623 ]
**Density [ Dcalc:** 4.824 g/cm³ **Dmeas:** 4.82 g/cm³ ] **SS/FOM:** F(30) = 70.4(0.0122, 35)
**Temp:** 298.0 K (Author provided temperature) **Avg. Melting Point:** 1053 K **Color:** Yellow

**Space Group:** P63mc (186) **Molecular Weight:** 144.47
**Crystal Data [ XtlCell a:** 4.136 Å **XtlCell b:** 4.136 Å **XtlCell c:** 6.713 Å **XtlCell α:** 90.00°
**XtlCell β:** 90.00° **XtlCell γ:** 120.00° **XtlCell Vol:** 99.45 Å³ **XtlCell Z:** 2.00 ]
**Crystal Data Axial Ratio [ c/a:** 1.623 **a/b:** 1.000 **c/b:** 1.623 ]
**Reduced Cell [ RedCell a:** 4.136 Å **RedCell b:** 4.136 Å **RedCell c:** 6.713 Å **RedCell α:** 90.00°
**RedCell β:** 90.00° **RedCell γ:** 120.00° **RedCell Vol:** 99.45 Å³ ]

**πωβ:** =2.506 **εγ:** =2.529 **Sign:** =+

**Atomic parameters are cross-referenced from PDF entry 04-002-3090**
**Crystal (Symmetry Allowed):** Non-centrosymmetric - Pyro / Piezo (p), Piezo (2nd Harm.)

**SG Symmetry Operators:**

| Seq | Operator | Seq | Operator | Seq | Operator | Seq | Operator | Seq | Operator | Seq | Operator |
|---|---|---|---|---|---|---|---|---|---|---|---|
| 1 | x,y,z | 3 | -x+y,-x,z | 5 | x,x-y,z | 7 | -x,-y,z+1/2 | 9 | x-y,x,z+1/2 | 11 | -x,-x+y,z+1/2 |
| 2 | -y,x-y,z | 4 | -y,-x,z | 6 | -x+y,y,z | 8 | y,-x+y,z+1/2 | 10 | y,x,z+1/2 | 12 | x-y,-y,z+1/2 |

**Atomic Coordinates:**

| Atom | Num | Wyckoff | Symmetry | x | y | z | SOF | IDP | AET |
|---|---|---|---|---|---|---|---|---|---|
| Cd | 1 | 2b | 3m. | 0.33333 | 0.66666 | 0.0 | 1.0 | | 4-a |
| S | 2 | 2b | 3m. | 0.33333 | 0.66666 | 0.3788 | 1.0 | | 4-a |

**Subfile(s):** Ceramic (Semiconductor), Common Phase, Forensic, Inorganic, Metals & Alloys, Mineral Related (Mineral , Synthetic), NBS Pattern, Pigment/Dye

**Prototype Structure [Formula Order]:** Zn O **Prototype Structure [Alpha Order]:** O Zn
**LPF Prototype Structure [Formula Order]:** Zn O,hP4,186 **LPF Prototype Structure [Alpha Order]:** O Zn,hP4,186
**Mineral Classification:** Wurtzite (Supergroup), 2H (Group) **Pearson Symbol:** hP4.00

**Cross-Ref PDF #'s:** 00-001-0780 (Deleted), 00-001-0783 (Deleted), 00-002-0549 (Deleted), 00-002-0563 (Deleted), 00-041-1049 (Primary), 01-070-2553 (Alternate), 01-074-9663 (Alternate), 01-075-1545 (Alternate), 01-077-2306 (Alternate), 01-080-0006 (Alternate), 01-089-2944 (Alternate), ✓03-065-3414 (Alternate), ✓04-001-6853 (Alternate), ✓04-001-7806 (Alternate), ✓04-001-8667 (Alternate), ✓04-001-9249 (Alternate), ✓04-002-3090 (Primary), ✓04-002-3139 (Alternate), ✓04-002-6790 (Alternate), ✓04-002-7261 (Alternate), ✓04-003-1457 (Alternate), ✓04-003-1516 (Alternate), ✓04-003-2268 (Alternate), ✓04-003-2992 (Alternate), ✓04-003-3805 (Alternate), ✓04-003-6705 (Alternate), ✓04-003-7134 (Alternate), ✓04-004-1240 (Alternate), ✓04-004-5012 (Alternate), ✓04-004-5103 (Alternate), ✓04-004-5283 (Alternate), ✓04-004-5848 (Alternate), ✓04-004-6592 (Alternate), ✓04-004-6658 (Alternate), ✓04-004-8521 (Alternate), ✓04-004-8642 (Alternate), ✓04-004-8895 (Alternate), ✓04-005-7864 (Alternate), ✓04-006-0809 (Alternate), ✓04-006-2554 (Alternate), ✓04-006-4886 (Alternate), ✓04-008-2191 (Alternate), ✓04-008-6543 (Alternate), ✓04-008-8223 (Alternate), ✓04-017-1120 (Alternate), ✓04-018-6894 (Alternate), ✓04-019-5137 (Alternate)

**Entry Date:** 09/01/1956

**References:**

| Type | DOI | Reference |
|---|---|---|
| Primary Reference | | Natl. Bur. Stand. (U. S. ), Circ. 539 4, 15 (1955). |
| Crystal Structure | | Crystal Structure Source: LPF. |
| Optical Data | | Dana's System of Mineralogy, 7th Ed. 1. |

**Database Comments:** Additional Patterns: To replace 00-001-0780. See PDF 00-041-1049. Analysis: Spectrographic analysis: <0.01% Al, B, Fe, Mg, Si; <0.001% Ca, Cu. Color: Yellow. Melting Point: 1053 K. Sample Preparation: Sample was heated at 400 C for 30 hours in S atmosphere to eliminate cubic phase. Sample Source or Locality: Sample from R.C.A. Temperature of Data Collection: Pattern taken at 298 K. Warning: Lines with abs(delta 2Theta)>0.06 DEG. Unit Cell Data Source: Powder Diffraction.

**d-Spacings (40) - Cd S - 00-006-0314 (Stick, Fixed Slit Intensity) - Cu Kα1 1.54056 Å**

| 2θ (°) | d (Å) | I | h | k | l | * | 2θ (°) | d (Å) | I | h | k | l | * | 2θ (°) | d (Å) | I | h | k | l | * |
|---|---|---|---|---|---|---|---|---|---|---|---|---|---|---|---|---|---|---|---|---|
| 24.8289 | **3.583000** | 75 | 1 | 0 | 0 | | 47.8873 | 1.898000 | 40 | 1 | 0 | 3 | | 58.3148 | 1.581000 | 8 | 2 | 0 | 2 | |
| 26.4497 | **3.367000** | 60 | 0 | 0 | 2 | | 50.9458 | 1.791000 | 18 | 2 | 0 | 0 | | 60.8969 | 1.520000 | 2 | 1 | 0 | 4 | |
| 28.2171 | **3.160000** | 100 | 1 | 0 | 1 | | 51.8776 | 1.761000 | 45 | 1 | 1 | 2 | | 66.8695 | 1.398000 | 16 | 2 | 0 | 3 | |
| 36.6492 | 2.450000 | 25 | 1 | 0 | 2 | | 52.8456 | 1.731000 | 18 | 2 | 0 | 1 | | 69.3694 | 1.353600 | 6 | 2 | 1 | 0 | |
| 43.7368 | 2.068000 | 55 | 1 | 1 | 0 | | 54.6159 | 1.679000 | 4 | 0 | 0 | 4 | | 70.9607 | 1.327100 | 12 | 2 | 1 | 1 | |

**Annex 3:** ICDDPDF No. 01-072-4873 for the cubic phase of PbS.

**01-072-4873** Apr 23, 2014 12:54 PM (ana.estrada)

**Status** Alternate **QM:** Indexed **Pressure/Temperature:** Ambient **Chemical Formula:** Pb S
**Empirical Formula:** Pb S **Weight %:** Pb86.60 S13.40 **Atomic %:** Pb50.00 S50.00 **ANX:** AX
**Compound Name:** Lead Sulfide **Mineral Name:** Galena

**Radiation:** CuKα **λ:** 1.5406Å **d-Spacing:** Calculated **Intensity:** Calculated **I/Ic:** 14.94

**SYS:** Cubic **SPGR:** Fm-3m (225)
**Author's Cell [ AuthCell a:** 5.94Å **AuthCell Vol:** 209.58Å$^3$ **AuthCell Z:** 4.00 **AuthCell MolVol:** 52.40 **]**
**Density [ Dcalc:** 7.583g/cm$^3$ **Dstruc:** 7.58g/cm$^3$ **]** **SS/FOM:** F(19) = 999.9(0.0002, 19)
**Temp:** 298.000K (Ambient temperature assigned by ICDD editor)

**Space Group:** Fm-3m (225) **Molecular Weight:** 239.26
**Crystal Data [ XtlCell a:** 5.940Å **XtlCell b:** 5.940Å **XtlCell c:** 5.940Å **XtlCell α:** 90.00° **XtlCell β:** 90.00°
**XtlCell γ:** 90.00° **XtlCell Vol:** 209.58Å$^3$ **XtlCell Z:** 4.00 **]**
**Crystal Data Axial Ratio [ a/b:** 1.000 **c/b:** 1.000 **]**
**Reduced Cell [ RedCell a:** 4.200Å **RedCell b:** 4.200Å **RedCell c:** 4.200Å **RedCell α:** 60.00°
**RedCell β:** 60.00° **RedCell γ:** 60.00° **RedCell Vol:** 52.40Å$^3$ **]**

**Atomic parameters are cross-referenced from PDF entry 04-004-4329** **ADP Type:** B
**Crystal (Symmetry Allowed):** Centrosymmetric

**SG Symmetry Operators:**

| Seq | Operator | Seq | Operator | Seq | Operator | Seq | Operator | Seq | Operator | Seq | Operator | Seq | Operator |
|---|---|---|---|---|---|---|---|---|---|---|---|---|---|
| 1 | x,y,z | 8 | -x,-z,-y | 15 | z,-x,-y | 22 | -y,x,z | 29 | -y,z,-x | 36 | z,-y,x | 43 | -x,-z,y |
| 2 | -x,-y,-z | 9 | y,x,z | 16 | -z,x,y | 23 | z,-y,-x | 30 | y,-z,x | 37 | -x,-y,z | 44 | x,z,-y |
| 3 | z,x,y | 10 | -y,-x,-z | 17 | y,-z,-x | 24 | -z,y,x | 31 | -x,z,-y | 38 | x,y,-z | 45 | -y,-x,z |
| 4 | -z,-x,-y | 11 | z,y,x | 18 | -y,z,x | 25 | -x,y,-z | 32 | x,-z,y | 39 | -z,-x,y | 46 | y,x,-z |
| 5 | y,z,x | 12 | -z,-y,-x | 19 | x,-z,-y | 26 | x,-y,z | 33 | -y,x,-z | 40 | z,x,-y | 47 | -z,-y,x |
| 6 | -y,-z,-x | 13 | x,-y,-z | 20 | -x,z,y | 27 | -z,x,-y | 34 | y,-x,z | 41 | -y,-z,x | 48 | z,y,-x |
| 7 | x,z,y | 14 | -x,y,z | 21 | y,-x,-z | 28 | z,-x,y | 35 | -z,y,-x | 42 | y,z,-x | | |

**Atomic Coordinates:**

| Atom | Num | Wyckoff | Symmetry | x | y | z | SOF | Biso | AET |
|---|---|---|---|---|---|---|---|---|---|
| Pb | 1 | 4a | m-3m | 0.0 | 0.0 | 0.0 | 1.0 | 1.283 | 6-a |
| S | 2 | 4b | m-3m | 0.5 | 0.5 | 0.5 | 1.0 | 1.247 | 6-a |

**Pearson:** cF8.00

**Subfile(s):** Common Phase, Forensic, Mineral Related (Mineral , Natural), Alternate Pattern, Inorganic, ICSD Pattern, Metals & Alloys

**Entry Date:** 07/27/2010 **Last Modification Date:** 01/17/2013

**Cross-Ref PDF #'s:** 00-001-0880 (Deleted), 00-002-0699 (Deleted), 00-002-1431 (Deleted), 00-003-0665 (Deleted), 00-005-0592 (Primary), 01-071-4752 (Deleted), ✓ 03-065-2935 (Alternate), ✓ 03-066-0020 (Alternate), ✓ 04-001-9338 (Alternate), ✓ 04-002-0034 (Alternate), ✓ 04-003-1798 (Alternate), ✓ 04-003-2094 (Alternate), ✓ 04-003-2095 (Alternate), ✓ 04-003-2266 (Alternate), ✓ 04-003-2271 (Alternate), ✓ 04-003-2910 (Alternate), ✓ 04-003-2980 (Alternate), ✓ 04-003-3827 (Alternate), ✓ 04-003-4310 (Alternate), ✓ 04-003-5384 (Alternate), ✓ 04-003-5502 (Alternate), ✓ 04-003-7034 (Alternate), ✓ 04-004-1952 (Alternate), ✓ 04-004-3789 (Alternate), ✓ 04-004-4276 (Alternate), ✓ 04-004-4329 (Primary), ✓ 04-004-4516 (Alternate), ✓ 04-004-5639 (Alternate), ✓ 04-004-5715 (Alternate), ✓ 04-004-5729 (Alternate), ✓ 04-004-7866 (Alternate), ✓ 04-004-7966 (Alternate), ✓ 04-005-6442 (Alternate), ✓ 04-005-9447 (Alternate), ✓ 04-006-1799 (Alternate), ✓ 04-006-4885 (Alternate), ✓ 04-015-0430 (Alternate), ✓ 04-015-2204 (Alternate), ✓ 04-015-4082 (Alternate), ✓ 04-016-4614 (Alternate), ✓ 04-016-4784 (Alternate), ✓ 04-016-6873 (Alternate)

**References:**

| Type | DOI | Reference |
|---|---|---|
| Primary Reference | | Calculated from ICSD using POWD-12++. |
| Additional Reference | | Ramsdell, L.S. An. Fis. Quim. 24, 611 (1926). |
| Additional Reference | | Ramsdell, L.S. Z. Kristallogr., Kristallgeom., Kristallphys., Kristallchem. 60, 379 (1924). |
| Crystal Structure | | Crystal Structure Source: LPF. |
| Structure | | "The crystal structure of some metallic sulfides". Ramsdell, L.S. Am. Mineral. 10, 281 (1925). |

**Database Comments:** ANX: AX. Analysis: Pb1 S1. Formula from original source: Pb S. ICSD Collection Code: 53932. Calculated Pattern Original Remarks: Cell from 2nd reference: 5.966, from 3rd ref.: 5.96. Sample Source or Locality: Galena. Minor Warning: No e.s.d reported/abstracted on the cell dimension. No R factors reported/abstracted. Wyckoff Sequence: b a(FM3-M). Unit Cell Data Source: Single Crystal.

**d-Spacings (19) - 01-072-4873 (Fixed Slit Intensity) - Cu Kα1 1.54056Å**

| 2θ | d(Å) | I | h | k | l | * | 2θ | d(Å) | I | h | k | l | * | 2θ | d(Å) | I | h | k | l | * |
|---|---|---|---|---|---|---|---|---|---|---|---|---|---|---|---|---|---|---|---|---|
| 25.9595 | **3.429460** | 935 | 1 | 1 | 1 | | 70.8918 | 1.328220 | 231 | 4 | 2 | 0 | | 116.4989 | 0.905842 | 30 | 5 | 3 | 3 | |
| 30.0634 | **2.970000** | 999 | 2 | 0 | 0 | | 78.8819 | 1.212500 | 157 | 4 | 2 | 2 | | 118.6732 | 0.895489 | 57 | 6 | 2 | 2 | |
| 43.0344 | **2.100110** | 679 | 2 | 2 | 0 | | 84.7255 | 1.143150 | 86 | 5 | 1 | 1 | | 127.9042 | 0.857365 | 17 | 4 | 4 | 4 | |
| 50.9464 | 1.790980 | 400 | 3 | 1 | 1 | | 94.3722 | 1.050050 | 44 | 4 | 4 | 0 | | 135.6629 | 0.831766 | 51 | 7 | 1 | 1 | |
| 53.3865 | 1.714730 | 219 | 2 | 2 | 2 | | 100.2028 | 1.004040 | 79 | 5 | 3 | 1 | | 138.4926 | 0.823730 | 50 | 6 | 4 | 0 | |
| 62.4911 | 1.485000 | 92 | 4 | 0 | 0 | | 102.1667 | 0.990000 | 91 | 4 | 4 | 2 | | | | | | | | |
| 68.8390 | 1.362730 | 136 | 3 | 3 | 1 | | 110.1993 | 0.939196 | 62 | 6 | 2 | 0 | | | | | | | | |

**Annex 4**: ICDDPDF No. 00-006-0464 for the hexagonal phase of CuS.

**00-006-0464** Mar 6, 2014 3:13 PM (rosarios)

**Status** Primary **QM:** Star **Pressure/Temperature:** Ambient **Chemical Formula:** Cu S
**Empirical Formula:** Cu S **Weight %:** Cu66.46 S33.54 **Atomic %:** Cu50.00 S50.00
**Compound Name:** Copper Sulfide **Mineral Name:** Covellite, syn

**Radiation:** CuKα **λ:** 1.5405Å **Filter:** Ni Beta **Intensity:** Diffractometer

**SYS:** Hexagonal **SPGR:** P63/mmc (194)
**Author's Cell [ AuthCell a:** 3.792Å **AuthCell c:** 16.344Å **AuthCell Vol:** 203.53Å³ **AuthCell Z:** 6.00
**AuthCell MolVol:** 33.92 ] **Author's Cell Axial Ratio [ c/a:** 4.310 ]
**Density [ Dcalc:** 4.68g/cm³ **Dmeas:** 4.671g/cm³ ] **SS/FOM:** F(27) = 41.8(0.0106, 61)
**Temp:** 299.000K (Author provided temperature)

**Space Group:** P63/mmc (194) **Molecular Weight:** 95.61
**Crystal Data [ XtlCell a:** 3.792Å **XtlCell b:** 3.792Å **XtlCell c:** 16.344Å **XtlCell α:** 90.00° **XtlCell β:** 90.00°
**XtlCell γ:** 120.00° **XtlCell Vol:** 203.53Å³ **XtlCell Z:** 6.00 ]
**Crystal Data Axial Ratio [ c/a:** 4.310 **a/b:** 1.000 **c/b:** 4.310 ]
**Reduced Cell [ RedCell a:** 3.792Å **RedCell b:** 3.792Å **RedCell c:** 16.344Å **RedCell α:** 90.00°
**RedCell β:** 90.00° **RedCell γ:** 120.00° **RedCell Vol:** 203.53Å³ ]

**πωβ:** =1.45 **Sign:** =+

**Atomic parameters are cross-referenced from PDF entry 04-004-8687**
**Crystal (Symmetry Allowed):** Centrosymmetric

**SG Symmetry Operators:**

| Seq | Operator | Seq | Operator | Seq | Operator | Seq | Operator | Seq | Operator | Seq | Operator |
|---|---|---|---|---|---|---|---|---|---|---|---|
| 1 | x,y,z | 5 | -x+y,-x,z | 9 | x,x-y,z | 13 | -x,-y,z+1/2 | 17 | x-y,x,z+1/2 | 21 | -x,-x+y,z+1/2 |
| 2 | -x,-y,-z | 6 | x-y,x,-z | 10 | -x,-x+y,-z | 14 | x,y,-z+1/2 | 18 | -x+y,-x,-z+1/2 | 22 | x,x-y,-z+1/2 |
| 3 | -y,x-y,z | 7 | -y,-x,z | 11 | -x+y,y,z | 15 | y,-x+y,z+1/2 | 19 | y,x,z+1/2 | 23 | x-y,-y,z+1/2 |
| 4 | y,-x+y,-z | 8 | y,x,-z | 12 | x-y,-y,-z | 16 | -y,x-y,-z+1/2 | 20 | -y,-x,-z+1/2 | 24 | -x+y,y,-z+1/2 |

**Atomic Coordinates:**

| Atom | Num | Wyckoff | Symmetry | x | y | z | SOF | IDP | AET |
|---|---|---|---|---|---|---|---|---|---|
| Cu | 1 | 2d | -6m2 | 0.33333 | 0.66666 | 0.75 | 1.0 | | 3#b |
| Cu | 2 | 4f | 3m. | 0.33333 | 0.66666 | 0.1072 | 1.0 | | 4-a |
| S | 3 | 2c | -6m2 | 0.33333 | 0.66666 | 0.25 | 1.0 | | 5-c |
| S | 4 | 4e | 3m. | 0.0 | 0.0 | 0.0611 | 1.0 | | 4-a |

**Pearson:** hP12.00 **Prototype Structure:** Cu S **Prototype Structure (Alpha Order):** Cu S
**LPF Prototype Structure:** Cu S,hP12,194 **LPF Prototype Structure (Alpha Order):** Cu S,hP12,194
**Mineral Classification:** Covellite (Group), Class Member

**Subfile(s):** Primary Pattern, Inorganic, NBS Pattern, Common Phase, Mineral Related (Mineral , Synthetic), Superconducting Material (Conventional Superconductor), Educational Pattern, Metals & Alloys, Forensic

**Last Modification Date:** 01/11/2013

**Cross-Ref PDF #'s:** 00-001-1281 (Deleted), 00-002-0820 (Deleted), 00-003-0724 (Deleted), 00-003-1090 (Deleted), ✓ 04-001-1461 (Alternate), ✓04-004-8686 (Alternate), ✓04-004-8687 (Primary), ✓04-006-9635 (Alternate), ✓04-007-1392 (Alternate), ✓04-008-8149 (Alternate)

**References:**

| Type | DOI | Reference |
|---|---|---|
| Primary Reference | | Natl. Bur. Stand. (U. S. ), Circ. 539 IV, 13 (1955). |
| Color | | Dana's System of Mineralogy, 7th Ed. I. |
| Crystal Structure | | Crystal Structure Source: LPF. |
| Density measured | | Dana's System of Mineralogy, 7th Ed. I. |
| Physical Properties | | Handbook of Chemistry and Physics, 86th Edition (2005). |

**Database Comments:** Additional Patterns: To replace 00-001-1281, 00-003-0724 and 00-003-1090 and validated by calculated pattern 00-024-0060. See PDF 01-078-2121. Analysis: Spectroscopic analysis: <0.1% Si, Zn; <0.01% Ag, Al, Ca, Fe, Mg, Ni; <0.001% B, Mn, Pb. Color: Dark blue. Opaque Optical Data: Opaque mineral optical data on specimen from unspecified locality: R1Ro=7.1, RR2Re=23.7, Disp.=16, VHN100=128-138, Color Values=o .224, .226, 6.8, e .283, .287, 23.5, Ref.: IMA Commission Ore Microscopy QDF. Physical property: Tc=1.62 K. Sample Preparation: Annealed at 400 C for several hours in sulfur atmosphere. Sample Source or Locality: Sample from Fisher Scientific Company. Temperature of Data Collection: Pattern taken at 299 K. Unit Cell Data Source: Powder Diffraction.

**d-Spacings (27) - 00-006-0464 (Fixed Slit Intensity) - Cu Kα1 1.54056Å**

| 2θ | d(Å) | I | h | k | l | * | 2θ | d(Å) | I | h | k | l | * | 2θ | d(Å) | I | h | k | l | * |
|---|---|---|---|---|---|---|---|---|---|---|---|---|---|---|---|---|---|---|---|---|
| 10.8067 | 8.180000 | 8 | 0 | 0 | 2 | | 32.8518 | 2.724000 | 55 | 0 | 0 | 6 | | 47.9409 | **1.896000** | 75 | 1 | 1 | 0 | |
| 27.1224 | 3.285000 | 14 | 1 | 0 | 0 | | 38.8347 | 2.317000 | 10 | 1 | 0 | 5 | | 52.7143 | 1.735000 | 35 | 1 | 0 | 8 | |
| 27.6807 | 3.220000 | 30 | 1 | 0 | 1 | | 43.1014 | 2.097000 | 6 | 1 | 0 | 6 | | 56.2514 | 1.634000 | 4 | 2 | 0 | 1 | |
| 29.2766 | **3.048000** | 65 | 1 | 0 | 2 | | 44.3001 | 2.043000 | 8 | 0 | 0 | 8 | | 57.2053 | 1.609000 | 8 | 2 | 0 | 2 | |
| 31.7844 | **2.813000** | 100 | 1 | 0 | 3 | | 47.7803 | 1.902000 | 25 | 1 | 0 | 7 | | 58.6812 | 1.572000 | 16 | 2 | 0 | 3 | |

| 2θ | d(Å) | I | h | k | l | * |
|---|---|---|---|---|---|---|
| 59.3446 | 1.556000 | 35 | 1 | 1 | 6 | |
| 63.5395 | 1.463000 | 6 | 1 | 0 | 10 | |
| 67.3055 | 1.390000 | 6 | 1 | 1 | 8 | |
| 69.3460 | 1.354000 | 8 | 1 | 0 | 11 | |
| 69.9965 | 1.343000 | 6 | 2 | 0 | 7 | |
| 73.9952 | 1.280000 | 10 | 2 | 0 | 8 | |
| 77.7723 | 1.227000 | 6 | 2 | 1 | 2 | |
| 79.0768 | 1.210000 | 10 | 2 | 1 | 3 | |
| 88.9153 | 1.099800 | 8 | 1 | 0 | 14 | |
| 89.4507 | 1.094600 | 10 | 3 | 0 | 0 | |
| 93.1375 | 1.060700 | 10 | 2 | 1 | 8 | |
| 98.6683 | 1.015500 | 8 | 3 | 0 | 6 | |

**Annex 5**: ICDDPDF No. 01-084-2782 for the cubic phase of $Fe_3O_4$.

**01-084-2782** Jun 8, 2018 11:46 AM (rosarios)

**Status** Alternate **Quality Mark:** Star **Environment:** Ambient **Temp:** 300.0 K **Chemical Formula:** Fe3 O4
**Empirical Formula:** Fe3 O4 **Weight %:** Fe72.36 O27.64 **Atomic %:** Fe42.86 O57.14 **Compound Name:** Iron Oxide
**Mineral Name:** Magnetite, syn **Alternate Name:** iron(II) diiron(III) tetraoxide **Entry Date:** 09/01/2016

**Radiation:** CuKα1 (1.5406 Å) **d-Spacing:** Calculated **Intensity:** Calculated - Peak **I/Ic:** 5.19 **I/Ic - CW ND:** 1.52

**Crystal System:** Cubic **SPGR:** Fd-3m (227)
**Author's Cell [ a:** 8.3582(17) Å **Volume:** 583.90 Å³ **Z:** 8.00 **MolVol:** 72.99 ] **Calculated Density:** 5.268 g/cm³
**Structural Density:** 5.27 g/cm³ **SS/FOM:** F(30) = 999.9(0.0004, 33) **R-factor:** 0.0609

**Space Group:** Fd-3m (227) **Molecular Weight:** 231.54 g/mol
**Crystal Data [ XtlCell a:** 8.358 Å **XtlCell b:** 8.358 Å **XtlCell c:** 8.358 Å **XtlCell α:** 90.00° **XtlCell β:** 90.00°
**XtlCell γ:** 90.00° **XtlCell Vol:** 583.90 Å³ **XtlCell Z:** 8.00 **a/b:** 1.000 **c/b:** 1.000 ]
**Reduced Cell [ RedCell a:** 5.910 Å **RedCell b:** 5.910 Å **RedCell c:** 5.910 Å **RedCell α:** 60.00°
**RedCell β:** 60.00° **RedCell γ:** 60.00° **RedCell Vol:** 145.97 Å³ ]

**Crystal (Symmetry Allowed):** Centrosymmetric

**Subfiles:** Battery Material, Common Phase, Forensic, Inorganic, Micro & Mesoporous, Mineral Related (Mineral, Synthetic), Pharmaceutical (Excipient)

**Mineral Classification:** Spinel (Supergroup), 1C-oxide (Group) **Pearson Symbol:** cF56.00
**Prototype Structure [Formula Order]:** Mg Al2 O4 **ANX:** AB2X4

**Cross-Ref PDF #'s:** 00-001-1111 (Deleted), 00-002-1035 (Deleted), 00-003-0862 (Deleted), 00-007-0322 (Deleted), 00-011-0614 (Deleted), 00-019-0629 (Primary), 00-065-0731 (Primary), 01-071-4918 (Alternate), 01-072-2303 (Alternate), 01-074-1909 (Alternate), 01-074-1910 (Alternate), 01-075-0449 (Alternate), 01-075-1610 (Alternate), 01-075-9710 (Alternate), 01-076-1849 (Alternate), 01-076-5948 (Alternate), 01-078-6086 (Alternate), 01-080-6402 (Alternate), 01-080-6403 (Alternate), 01-080-6404 (Alternate), 01-080-6405 (Alternate), 01-080-6406 (Alternate), 01-080-6407 (Alternate), 01-080-6408 (Alternate), 01-080-6409 (Alternate), 01-080-6410 (Alternate), 01-080-7683 (Alternate), 01-082-3507 (Alternate), 01-084-6015 (Alternate), 01-084-6684 (Alternate), 01-084-6685 (Alternate), 01-084-6686 (Alternate), 01-084-6687 (Alternate), 01-084-6688 (Alternate), 01-084-6689 (Alternate), 01-084-6690 (Alternate), 01-084-6691 (Alternate), 01-084-6692 (Alternate), 01-084-6693 (Alternate), 01-084-6694 (Alternate), 01-084-6695 (Alternate), 01-084-6696 (Alternate), 01-084-6697 (Alternate), 01-084-6698 (Alternate), 01-084-6699 (Alternate), 01-084-6700 (Alternate), 01-087-2334 (Alternate), 01-088-0866 (Alternate), 01-089-3854 (Alternate), 01-089-4319 (Alternate), ✓ 03-065-3107 (Alternate), ✓ 04-001-7822 (Alternate), ✓ 04-001-7909 (Alternate), ✓ 04-001-9000 (Alternate), ✓ 04-001-9326 (Alternate), ✓ 04-002-0264 (Alternate), ✓ 04-002-0618 (Alternate), ✓ 04-002-0643 (Alternate), ✓ 04-002-1855 (Alternate), ✓ 04-002-2487 (Alternate), ✓ 04-002-2707 (Alternate), ✓ 04-002-2709 (Alternate), ✓ 04-002-2981 (Alternate), ✓ 04-002-3194 (Alternate), ✓ 04-002-3668 (Alternate), ✓ 04-002-5310 (Alternate), ✓ 04-002-5448 (Alternate), ✓ 04-002-5632 (Alternate), ✓ 04-002-5683 (Alternate), ✓ 04-002-5903 (Alternate), ✓ 04-002-6866 (Alternate), ✓ 04-002-6955 (Alternate), ✓ 04-002-8141 (Alternate), ✓ 04-002-8629 (Alternate), ✓ 04-002-9019 (Alternate), ✓ 04-002-9635 (Alternate), ✓ 04-003-1446 (Alternate), ✓ 04-004-2838 (Alternate), ✓ 04-005-4307 (Alternate), ✓ 04-005-4319 (Primary), ✓ 04-005-4404 (Alternate), ✓ 04-005-4551 (Alternate), ✓ 04-005-5733 (Alternate), ✓ 04-005-6268 (Alternate), ✓ 04-005-9786 (Alternate), ✓ 04-005-9788 (Alternate), ✓ 04-005-9815 (Alternate), ✓ 04-006-0225 (Alternate), ✓ 04-006-0424 (Alternate), ✓ 04-006-0425 (Alternate), ✓ 04-006-1668 (Alternate), ✓ 04-006-2406 (Alternate), ✓ 04-006-2467 (Alternate), ✓ 04-006-2752 (Alternate), ✓ 04-006-4615 (Alternate), ✓ 04-006-6497 (Alternate), ✓ 04-006-6550 (Alternate), ✓ 04-006-6692 (Alternate), ✓ 04-006-8076 (Alternate), ✓ 04-007-1427 (Alternate), ✓ 04-007-2718 (Alternate), ✓ 04-007-6010 (Alternate), ✓ 04-007-8567 (Alternate), ✓ 04-007-8976 (Alternate), ✓ 04-007-9093 (Alternate), ✓ 04-008-0315 (Alternate), ✓ 04-008-0777 (Alternate), ✓ 04-008-4423 (Alternate), ✓ 04-008-4511 (Alternate), ✓ 04-008-4512 (Alternate), ✓ 04-008-8145 (Alternate), ✓ 04-008-8146 (Alternate), ✓ 04-008-8147 (Alternate), ✓ 04-008-8148 (Alternate), ✓ 04-009-4225 (Alternate), ✓ 04-009-8417 (Alternate), ✓ 04-009-8418 (Alternate), ✓ 04-009-8419 (Alternate), ✓ 04-009-8420 (Alternate), ✓ 04-009-8421 (Alternate), ✓ 04-009-8422 (Alternate), ✓ 04-009-8423 (Alternate), ✓ 04-009-8424 (Alternate), ✓ 04-009-8425 (Alternate), ✓ 04-009-8426 (Alternate), ✓ 04-009-8427 (Alternate), ✓ 04-009-8428 (Alternate), ✓ 04-009-8429 (Alternate), ✓ 04-009-8430 (Alternate), ✓ 04-009-8431 (Alternate), ✓ 04-009-8432 (Alternate), ✓ 04-009-8433 (Alternate), ✓ 04-009-8434 (Alternate), ✓ 04-009-8435 (Alternate), ✓ 04-009-8436 (Alternate), ✓ 04-009-8437 (Alternate), ✓ 04-009-8438 (Alternate), ✓ 04-009-8439 (Alternate), ✓ 04-009-8440 (Alternate), ✓ 04-009-8441 (Alternate), ✓ 04-009-8442 (Alternate), ✓ 04-009-8443 (Alternate), ✓ 04-011-5952 (Alternate), ✓ 04-013-7099 (Alternate), ✓ 04-013-7100 (Alternate), ✓ 04-013-9806 (Alternate), ✓ 04-013-9807 (Alternate), ✓ 04-013-9808 (Alternate), ✓ 04-013-9809 (Alternate), ✓ 04-013-9810 (Alternate), ✓ 04-013-9811 (Alternate), ✓ 04-014-1396 (Alternate), ✓ 04-014-9664 (Alternate), ✓ 04-015-3100 (Alternate), ✓ 04-015-3101 (Alternate), ✓ 04-015-3102 (Alternate), ✓ 04-015-8200 (Alternate), ✓ 04-015-8203 (Alternate), ✓ 04-015-8204 (Alternate), ✓ 04-015-8207 (Alternate), ✓ 04-015-8209 (Alternate), ✓ 04-015-8211 (Alternate), ✓ 04-015-8213 (Alternate), ✓ 04-015-8214 (Alternate), ✓ 04-017-1024 (Alternate), ✓ 04-020-0779 (Alternate), ✓ 04-021-0451 (Alternate)

**References:**

| Type | DOI | Reference |
|---|---|---|
| Primary Reference | | Calculated from ICSD using POWD-12++. |
| Structure | 10.1107/S1600576713032895 | "Neutron and X-ray diffraction study of ferrite nanocrystals obtained by microwave-assisted growth. A structural comparison with the thermal synthetic route". Solano, Eduardo, Frontera, Carlos, Puig, Teresa, Obradors, Xavier, Ricart, Susagna, Ros, Josep J. Appl. Crystallogr. 47, 414 (2014). |

**Database Comments:** ANX: AB2X4. Analysis: Fe3 O4. Formula from original source: Fe3 O4. ICSD Collection Code: 250540. Calculated Pattern Original Remarks: R = R(_pd_proc_ls_prof_R_factor). Temperature of Data Collection: 300 K. Wyckoff Sequence: e d a (FD3-MZ). Unit Cell Data Source: Single Crystal.

**d-Spacings (31) - Fe3 O4 - 01-084-2782 (Stick, Fixed Slit Intensity) - Cu Kα1 1.54056 Å**

| 2θ (°) | d (Å) | I | h | k | l | * | 2θ (°) | d (Å) | I | h | k | l | * |
|---|---|---|---|---|---|---|---|---|---|---|---|---|---|
| 18.37007 | 4.825610 | 51 | 1 | 1 | 1 | | 90.12543 | 1.088150 | 101 | 7 | 3 | 1 | |
| 30.21892 | **2.955070** | 279 | 2 | 2 | 0 | | 94.99795 | 1.044780 | 35 | 8 | 0 | 0 | |
| 35.59524 | **2.520090** | 999 | 3 | 1 | 1 | | 97.93689 | 1.021120 | 1 | 7 | 3 | 3 | |
| 37.23483 | 2.412800 | 74 | 2 | 2 | 2 | | 102.88663 | 0.985023 | 11 | 8 | 2 | 2 | |
| 43.26284 | 2.089550 | 203 | 4 | 0 | 0 | | 105.90127 | 0.965122 | 48 | 7 | 5 | 1 | |
| 47.37032 | 1.917500 | 14 | 3 | 3 | 1 | | 106.91594 | 0.958751 | 10 | 6 | 6 | 2 | |
| 53.67777 | 1.706110 | 84 | 4 | 2 | 2 | | 111.03350 | 0.934475 | 22 | 8 | 4 | 0 | |
| 57.22313 | 1.608540 | 247 | 5 | 1 | 1 | | 114.19675 | 0.917432 | 2 | 9 | 1 | 1 | |
| 62.84248 | **1.477540** | 356 | 4 | 4 | 0 | | 119.65688 | 0.890987 | 6 | 6 | 6 | 4 | |
| 66.07927 | 1.412790 | 6 | 5 | 3 | 1 | | 123.07697 | 0.876177 | 31 | 9 | 3 | 1 | |
| 71.30405 | 1.321550 | 27 | 6 | 2 | 0 | | 129.10154 | 0.853055 | 78 | 8 | 4 | 4 | |
| 74.36072 | 1.274610 | 67 | 5 | 3 | 3 | | 132.97302 | 0.840031 | 1 | 7 | 7 | 1 | |
| 75.36844 | 1.260050 | 27 | 6 | 2 | 2 | | 140.04837 | 0.819589 | 15 | 8 | 6 | 2 | |
| 79.35933 | 1.206400 | 22 | 4 | 4 | 4 | | 144.83979 | 0.808018 | 43 | 9 | 5 | 1 | |
| 82.31714 | 1.170380 | 2 | 7 | 1 | 1 | | 146.56730 | 0.804268 | 10 | 10 | 2 | 2 | |
| 87.20525 | 1.116910 | 25 | 6 | 4 | 2 | | | | | | | | |

**Annex 6**: ICDDPDF No. 04-013-0293 for the hexagonal phase of graphite.

**04-013-0293** Oct 21, 2021 3:04 PM (rosarios)

**Status** Alternate **Quality Mark:** Indexed **Environment:** Ambient **Temp:** 298.0 K (Assigned by ICDD editor)
**Phase:** 2H **Chemical Formula:** C **Empirical Formula:** C **Weight %:** C100.00 **Atomic %:** C100.00
**Compound Name:** Carbon **Alternate Name:** graphite **Entry Date:** 09/01/2010 **Modification Date:** 09/01/2011
**Modifications:** Reflections

**Radiation:** CuKα1 (1.5406 Å) **d-Spacing:** Calculated **Intensity:** Calculated - Peak

**Crystal System:** Hexagonal **SPGR:** P63/mmc (194)
**Author's Unit Cell [ a:** 2.463 Å **c:** 6.714 Å **Volume:** 35.27 Å³ **Z:** 4.00 **MolVol:** 8.82 **c/a:** 2.726 **]**
**Calculated Density:** 2.262 g/cm³ **Structural Density:** 2.26 g/cm³ **SS/FOM:** F(24) = 999.9(0.0001, 24) **I/Ic:** 2.33
**I/Ic - CW ND:** 3.43

**Space Group:** P63/mmc (194) **Molecular Wt:** 12.01 g/mol
**Crystal Data [ a:** 2.463 Å **b:** 2.463 Å **c:** 6.714 Å **α:** 90.00° **β:** 90.00° **γ:** 120.00° **XtlCell Vol:** 35.27 Å³
**XtlCell Z:** 4.00 **c/a:** 2.726 **a/b:** 1.000 **c/b:** 2.726 **]**
**Reduced Cell [ a:** 2.463 Å **b:** 2.463 Å **c:** 6.714 Å **α:** 90.00° **β:** 90.00° **γ:** 120.00° **RedCell Vol:** 35.27 Å³ **]**

**AC Space Group:** P63/mmc (194)
**AC Unit Cell [ a:** 2.463 Å **b:** 2.463 Å **c:** 6.714 Å **α:** 90° **β:** 90° **γ:** 120° **]**

**Space Group Symmetry Operators:**

| Seq | Operator | Seq | Operator | Seq | Operator | Seq | Operator | Seq | Operator |
|---|---|---|---|---|---|---|---|---|---|
| 1 | x,y,z | 6 | x-y,x,-z | 11 | -x+y,y,z | 16 | -y,x-y,-z+1/2 | 21 | -x,-x+y,z+1/2 |
| 2 | -x,-y,-z | 7 | -y,-x,z | 12 | x-y,-y,-z | 17 | x-y,x,z+1/2 | 22 | x,x-y,-z+1/2 |
| 3 | -y,x-y,z | 8 | y,x,-z | 13 | -x,-y,z+1/2 | 18 | -x+y,-x,-z+1/2 | 23 | x-y,-y,z+1/2 |
| 4 | y,-x+y,-z | 9 | x,x-y,z | 14 | x,y,-z+1/2 | 19 | y,x,z+1/2 | 24 | -x+y,y,-z+1/2 |
| 5 | -x+y,-x,z | 10 | -x,-x+y,-z | 15 | y,-x+y,z+1/2 | 20 | -y,-x,-z+1/2 | | |

**Atomic Coordinates:**

| Atom | Num | Wyckoff | Symmetry | x | y | z | SOF | IDP | AET |
|---|---|---|---|---|---|---|---|---|---|
| C | 1 | 2c | -6m2 | 0.33333 | 0.66666 | 0.25 | 1.0 | | |
| C | 2 | 2b | -6m2 | 0.0 | 0.0 | 0.25 | 1.0 | | |

**Crystal (Symmetry Allowed):** Centrosymmetric

**Subfiles:** Battery Material, Common Phase, Forensic, Inorganic, Metal & Alloy **Pearson Symbol:** hP4.00
**Prototype Structure (Alpha Order):** C **LPF Prototype Structure (Formula Order):** C-a,hP4,194
**LPF Prototype Structure (Alpha Order):** C,hP4,194 **ANX:** N **Wyckoff Sequence:** c b

**Cross-Ref PDF #'s:** 01-071-3739 (Alternate), 01-077-7164 (Alternate), 01-083-6084 (Alternate), 01-084-9339 (Alternate), 01-086-2721 (Alternate), 01-086-7889 (Alternate), 01-086-8296 (Alternate), 01-086-8298 (Alternate), 04-006-5764 (Alternate), 04-007-2081 (Alternate), 04-007-8496 (Alternate), 04-014-0337 (Alternate), 04-014-0347 (Alternate), 04-014-0362 (Primary), 04-015-0267 (Alternate), 04-015-2405 (Alternate), 04-015-2406 (Alternate), 04-015-2407 (Alternate), 04-015-2432 (Alternate), 04-016-0554 (Alternate), 04-016-4291 (Alternate), 04-016-6288 (Alternate), 04-018-7559 (Alternate), 04-020-4354 (Alternate)

**References:**

| Type | DOI | Reference |
|---|---|---|
| Primary Reference | | Calculated from LPF using POWD-12++. |
| Structure | | Xiong Y.H., Yang S., Xiong C.S., Pi H.L., Zhang J., Ren Z.M., Mai Y.T., Xu W., Dai G.H., Song S.J., Xiong J., Zhang L., Xia Z.C., Yuan S.L. "Preparation and characterization of CBN ternary compounds with nano-structure". Physica B 2006, 382, 151-155. |

**Database Comments:** ANX: N. LPF Collection Code: 1014683. Calculated Pattern Original Remarks: editor deduced probable site occupation from nominal composition. Minor Warning: No R factors reported/abstracted. Minor warning from the LPF Editor exist. No e.s.d reported/abstracted on the cell dimension. Wyckoff Sequence: c b. Unit Cell Data Source: Powder Diffraction.

**d-spacings (24) - C - 04-013-0293 (Stick, Fixed Slit Intensity) - X-ray (Cu Kα1 1.54056 Å)**

| 2θ (°) | d (Å) | I | h | k | l | * | 2θ (°) | d (Å) | I | h | k | l | * |
|---|---|---|---|---|---|---|---|---|---|---|---|---|---|
| 26.530 | **3.357000** | 1000 | 0 | 0 | 2 | | 83.555 | 1.156160 | 53 | 1 | 1 | 2 | |
| 42.338 | 2.133020 | 32 | 1 | 0 | 0 | | 85.351 | 1.136370 | 9 | 1 | 0 | 5 | |
| 44.532 | **2.032890** | 152 | 1 | 0 | 1 | | 87.002 | 1.119000 | 8 | 0 | 0 | 6 | |
| 50.663 | 1.800340 | 28 | 1 | 0 | 2 | | 92.480 | 1.066510 | 1 | 2 | 0 | 0 | |
| 54.634 | **1.678500** | 53 | 0 | 0 | 4 | | 93.991 | 1.053300 | 7 | 2 | 0 | 1 | |
| 59.851 | 1.544050 | 40 | 1 | 0 | 3 | | 98.544 | 1.016450 | 2 | 2 | 0 | 2 | |
| 71.459 | 1.319070 | 6 | 1 | 0 | 4 | | 101.751 | 0.992918 | 29 | 1 | 1 | 4 | |
| 77.435 | 1.231500 | 35 | 1 | 1 | 0 | | 102.035 | 0.990920 | 3 | 1 | 0 | 6 | |

| 2θ (°) | d (Å) | I | h | k | l | * | 2θ (°) | d (Å) | I | h | k | l | * |
|---|---|---|---|---|---|---|---|---|---|---|---|---|---|
| 106.272 | 0.962777 | 5 | 2 | 0 | 3 | | 134.539 | 0.835145 | 4 | 2 | 0 | 5 | |
| 117.676 | 0.900168 | 1 | 2 | 0 | 4 | | 136.899 | 0.828175 | 20 | 1 | 1 | 6 | |
| 123.417 | 0.874773 | 4 | 1 | 0 | 7 | | 145.662 | 0.806206 | 1 | 2 | 1 | 0 | |
| 133.219 | 0.839250 | 3 | 0 | 0 | 8 | | 148.435 | 0.800456 | 8 | 2 | 1 | 1 | |

**Annex 7:** ICDDPDF No. 01-071-5971 for the cubic phase of ZnS.

**01-071-5971** Nov 14, 2018 3:38 PM (rosarios)

**Status** Alternate **Quality Mark:** Indexed **Environment:** Ambient **Temp:** 295.0 K **Phase:** β
**Chemical Formula:** Zn S **Empirical Formula:** S Zn **Weight %:** S32.91 Zn67.09 **Atomic %:** S50.00 Zn50.00
**Compound Name:** Zinc Sulfide **Mineral Name:** Sphalerite, syn **Entry Date:** 09/01/2005
**Modification Date:** 09/01/2015 **Modifications:** Update

**Radiation:** CuKα1 (1.5406 Å) **d-Spacing:** Calculated **Intensity:** Calculated - Peak **I/Ic:** 8.36 **I/Ic - CW ND:** 0.29

**Crystal System:** Cubic **SPGR:** F-43m (216)
**Author's Unit Cell [ a:** 5.409 Å **Volume:** 158.25 Å$^3$ **Z:** 4.00 **MolVol:** 39.56 **] Calculated Density:** 4.09 g/cm$^3$
**Structural Density:** 4.09 g/cm$^3$ **SS/FOM:** F(16) = 999.9(0.0001, 16) **R-factor:** 0.014

**Space Group:** F-43m (216) **Molecular Weight:** 97.44 g/mol
**Crystal Data [ a:** 5.409 Å **b:** 5.409 Å **c:** 5.409 Å **α:** 90.00° **β:** 90.00° **γ:** 90.00° **XtlCell Vol:** 158.25 Å$^3$
**XtlCell Z:** 4.00 **a/b:** 1.000 **c/b:** 1.000 **]**
**Reduced Cell [ a:** 3.825 Å **b:** 3.825 Å **c:** 3.825 Å **α:** 60.00° **β:** 60.00° **γ:** 60.00° **RedCell Vol:** 39.56 Å$^3$ **]**

**Atomic parameters are cross-referenced from PDF entry 04-001-6857**

**Space Group Symmetry Operators:**

| Seq | Operator | Seq | Operator | Seq | Operator | Seq | Operator | Seq | Operator | Seq | Operator |
|---|---|---|---|---|---|---|---|---|---|---|---|
| 1 | x,y,z | 5 | y,x,z | 9 | y,-z,-x | 13 | -x,y,-z | 17 | -y,x,-z | 21 | -y,-z,x |
| 2 | z,x,y | 6 | z,y,x | 10 | x,-z,-y | 14 | -z,x,-y | 18 | -z,y,-x | 22 | -x,-z,y |
| 3 | y,z,x | 7 | x,-y,-z | 11 | y,-x,-z | 15 | -y,z,-x | 19 | -x,-y,z | 23 | -y,-x,z |
| 4 | x,z,y | 8 | z,-x,-y | 12 | z,-y,-x | 16 | -x,z,-y | 20 | -z,-x,y | 24 | -z,-y,x |

**Atomic Coordinates:**

| Atom | Num | Wyckoff | Symmetry | x | y | z | SOF | IDP | AET |
|---|---|---|---|---|---|---|---|---|---|
| Zn | 1 | 4a | -43m | 0.0 | 0.0 | 0.0 | 1.0 | | 4-a |
| S | 2 | 4c | -43m | 0.25 | 0.25 | 0.25 | 1.0 | | 4-a |

**Crystal (Symmetry Allowed):** Non-centrosymmetric - Piezo (2nd Harm.) **AC Space Group:** F-43m (216)
**AC Unit Cell [ a:** 5.4 Å **b:** 5.4 Å **c:** 5.4 Å **α:** 90° **β:** 90° **γ:** 90° **]**

**Subfiles:** Ceramic (Semiconductor), Common Phase, Forensic, Inorganic, Metal & Alloy, Mineral Related (Mineral, Synthetic), Thermoelectric Material

**Mineral Classification:** Diamond (supergroup), 2C-chalcogenide (group) **Pearson Symbol:** cF8.00
**Prototype Structure [Formula Order]:** Zn S **Prototype Structure [Alpha Order]:** S Zn
**LPF Prototype Structure [Formula Order]:** Zn S,cF8,216 **LPF Prototype Structure [Alpha Order]:** S Zn,cF8,216
**ANX:** AX

**Cross-Ref PDF #'s:** 00-001-0792 (Deleted), 00-002-0564 (Deleted), 00-002-0565 (Deleted), 00-003-0570 (Deleted), 00-005-0566 (Primary), 00-065-0723 (Primary), 00-065-0724 (Primary), 00-066-0173 (Primary), 00-066-0174 (Primary), 01-071-4763 (Alternate), 01-071-5976 (Alternate), 01-072-4841 (Alternate), 01-074-6110 (Alternate), 01-077-2100 (Alternate), 01-077-8756 (Alternate), 01-079-6260 (Alternate), 01-079-7039 (Alternate), 01-080-4383 (Primary), 01-080-4442 (Alternate), 01-084-3993 (Alternate), 01-084-3994 (Alternate), 03-065-1691 (Alternate), 04-001-6857 (Primary), 04-001-8671 (Alternate), 04-002-0080 (Alternate), 04-002-0425 (Alternate), 04-002-2761 (Alternate), 04-003-2990 (Alternate), 04-003-5472 (Alternate), 04-003-6940 (Alternate), 04-003-6961 (Alternate), 04-004-2829 (Alternate), 04-004-3804 (Alternate), 04-004-4216 (Alternate), 04-004-5157 (Alternate), 04-004-5727 (Alternate), 04-004-6555 (Alternate), 04-004-6656 (Alternate), 04-006-0807 (Alternate), 04-006-2561 (Alternate), 04-007-1615 (Alternate), 04-007-9710 (Alternate), 04-008-2758 (Alternate), 04-008-8187 (Alternate), 04-008-8483 (Alternate), 04-012-0803 (Alternate), 04-012-6328 (Alternate), 04-012-7581 (Alternate), 04-013-0120 (Alternate), 04-013-4811 (Alternate), 04-013-5612 (Alternate), 04-014-0083 (Alternate), 04-015-2412 (Alternate), 04-016-4810 (Alternate), 04-016-6340 (Alternate), 04-016-6868 (Alternate), 04-019-7927 (Alternate), 04-022-7429 (Alternate)

**References:**

| Type | DOI | Reference |
|---|---|---|
| Primary Reference | | Calculated from ICSD using POWD-12++. |
| Crystal Structure | | Crystal Structure Source: LPF. |
| Structure | | Rabadanov, M.Kh. "Anharmonic temperature factors and charge density in Zn S". Kristallografiya 1995, 40, 21. |
| Structure | | Rabadanov, M.Kh. Crystallogr. Rep. 1995, 40, 17. |
| Structure | | Rabadanov, M.Kh. Golden Book of Phase Transitions, Wroclaw 2002, 1, 1. |

**Database Comments:** ANX: AX. Analysis: S1 Zn1. Formula from original source: Zn S. ICSD Collection Code: 77082. Calculated Pattern Original Remarks: AE: Zn: 4t S4; S: 4t Zn4; anion packing: S: 12co S12. Alias type name: sphalerite; SB: B3. B-values at 723 K: 3.378, 2.350, R=0.0246, R(anharmonic)=0.0210. Stable up to 1297 K (2nd ref., Tomaszewski), above P63mc. R(anharmonic)=0.0141. Subgroup relation to aristotype diamond C(cF8): Fd3-m -t2(-1/8,1/8,1/8)- F4-3m (Literatur: Dissertation Andreas Meyer, 1981, Universt„t Karlsruhe). B-values at 423 K: 1.869, 1.325; at 573 K: 2.653, 1.875, R=0.0199. Temperature of Data Collection: 295 K. Minor Warning: No e.s.d reported/abstracted on the cell dimension. Wyckoff Sequence: c a (F4-3M). Unit Cell Data Source: Powder Diffraction.

**d-Spacings (16) - Zn S - 01-071-5971 (Stick, Fixed Slit Intensity) - Cu Kα1 1.54056 Å**

| 2θ (°) | d (Å) | I | h | k | l | * | 2θ (°) | d (Å) | I | h | k | l | * |
|---|---|---|---|---|---|---|---|---|---|---|---|---|---|
| 28.55946 | **3.122890** | 1000 | 1 | 1 | 1 | | 88.47719 | 1.104110 | 94 | 4 | 2 | 2 | |
| 33.09549 | 2.704500 | 87 | 2 | 0 | 0 | | 95.45786 | 1.040960 | 51 | 5 | 1 | 1 | |
| 47.50519 | **1.912370** | 520 | 2 | 2 | 0 | | 107.33190 | 0.956185 | 26 | 4 | 4 | 0 | |
| 56.36900 | **1.630870** | 305 | 3 | 1 | 1 | | 114.80835 | 0.914288 | 48 | 5 | 3 | 1 | |
| 59.11725 | 1.561440 | 16 | 2 | 2 | 2 | | 117.39642 | 0.901500 | 2 | 6 | 0 | 0 | |
| 69.44863 | 1.352250 | 60 | 4 | 0 | 0 | | 128.49033 | 0.855238 | 39 | 6 | 2 | 0 | |
| 76.74010 | 1.240910 | 87 | 3 | 3 | 1 | | 138.07845 | 0.824865 | 18 | 5 | 3 | 3 | |
| 79.11666 | 1.209490 | 12 | 4 | 2 | 0 | | 141.68580 | 0.815437 | 1 | 6 | 2 | 2 | |

**Annex 8:** ICDDPDF No. 04-010-5710 for the tetragonal-scheelite phase of $BiVO_4$.

**04-010-5710** Apr 20, 2021 3:22 PM (rosarios)

**Status** Alternate **Quality Mark:** Star **Environment:** Non-ambient Temperature **Temp:** 566.0 K
**Chemical Formula:** Bi ( V O4 ) **Empirical Formula:** Bi O4 V **Weight %:** Bi64.52 O19.76 V15.73
**Atomic %:** Bi16.67 O66.67 V16.67 **Compound Name:** Bismuth Vanadate **Entry Date:** 09/01/2007
**Modification Date:** 09/01/2020 **Modifications:** Update

**Radiation:** CuKα1 (1.5406 Å) **d-Spacing:** Calculated **Intensity:** Calculated - Peak

**Crystal System:** Tetragonal **SPGR:** I41/a (88)
**Author's Unit Cell [ a:** 5.1470(4) Å **c:** 11.7216(12) Å **Volume:** 310.52 Å³ **Z:** 4.00 **MolVol:** 77.63 **c/a:** 2.277 **] Calculated Density:** 6.929 g/cm³ **Structural Density:** 6.927 g/cm³ **SS/FOM:** F(30) = 999.9(0.0001, 35)
**R-factor:** 0.061 **I/Ic:** 12.87 **I/Ic - CW ND:** 0.2

**Space Group:** I41/a (88) **Molecular Wt:** 323.92 g/mol
**Crystal Data [ a:** 5.147 Å **b:** 5.147 Å **c:** 11.722 Å **α:** 90.00° **β:** 90.00° **γ:** 90.00° **XtlCell Vol:** 310.52 Å³
**XtlCell Z:** 4.00 **c/a:** 2.277 **a/b:** 1.000 **c/b:** 2.277 **]**
**Reduced Cell [ a:** 5.147 Å **b:** 5.147 Å **c:** 6.899 Å **α:** 111.90° **β:** 111.90° **γ:** 90.00° **RedCell Vol:** 155.26 Å³ **]**

**AC Space Group:** I41/a (88)
**AC Unit Cell [ a:** 5.1470(4) Å **b:** 5.1470(4) Å **c:** 11.7216(12) Å **α:** 90° **β:** 90° **γ:** 90° **]**

**Space Group Symmetry Operators:**

| Seq | Operator | Seq | Operator | Seq | Operator | Seq | Operator |
|---|---|---|---|---|---|---|---|
| 1 | x,y,z | 3 | -x+1/2,-y,z+1/2 | 5 | -y+3/4,x+1/4,z+1/4 | 7 | y+3/4,-x+3/4,z+3/4 |
| 2 | -x,-y,-z | 4 | x+1/2,y,-z+1/2 | 6 | y+1/4,-x+3/4,-z+3/4 | 8 | -y+1/4,x+1/4,-z+1/4 |

**ADP Type:** B **Origin:** O2

**Atomic Coordinates:**

| Atom | Num | Wyckoff | Symmetry | x | y | z | SOF | Biso | AET |
|---|---|---|---|---|---|---|---|---|---|
| Bi | 1 | 4b | -4.. | 0.0 | 0.25 | 0.625 | 1.0 | 1.43 | |
| V | 2 | 4a | -4.. | 0.0 | 0.25 | 0.125 | 1.0 | 0.3 | |
| O | 3 | 16f | 1 | 0.1375 | 0.4985 | 0.2034 | 1.0 | 1.67 | |

**Crystal (Symmetry Allowed):** Centrosymmetric

**Subfiles:** Inorganic **Pearson Symbol:** tI24.00 **LPF Prototype Structure (Formula Order):** Ca ( W O4 ),tI24,88
**LPF Prototype Structure (Alpha Order):** Ca O4 W,tI24,88 **ANX:** ABX4 **Wyckoff Sequence:** f b a

**Cross-Ref PDF #'s:** 04-008-8592 (Primary), 04-008-8593 (Alternate) **Former PDF Numbers:** 01-074-4892

**References:**

| Type | DOI | Reference |
|---|---|---|
| Primary Reference | | Calculated from LPF using POWD-12++. |
| Structure | 10.1016/0025-5408(72)90227-9 | Sleight A.W., Chen H.Y., Ferretti A., Cox D.E. "Crystal growth and structure of BiVO4". Mater. Res. Bull. 1979, 14, 1571,1581. |

**Database Comments:** ANX: ABX4. LPF Collection Code: 1411659. Sample Preparation: STARTING MATERIALS: BiVO4. COMPOUND PREPARATION: crystals grown by Czochralski method. ATMOSPHERE: oxygen. Temperature of Data Collection: 566 K. Wyckoff Sequence: f b a. Unit Cell Data Source: Powder Diffraction.

**d-spacings (82) - Bi ( V O4 ) - 04-010-5710 (Stick, Fixed Slit Intensity) - X-ray (Cu Kα1 1.54056 Å)**

| 2θ (°) | d (Å) | I | h | k | l | * | 2θ (°) | d (Å) | I | h | k | l | * |
|---|---|---|---|---|---|---|---|---|---|---|---|---|---|
| 18.814 | **4.712680** | 400 | 1 | 0 | 1 | | 63.433 | 1.465200 | 14 | 0 | 0 | 8 | |
| 28.661 | 3.112080 | 141 | 1 | 0 | 3 | | 65.855 | 1.417050 | 20 | 3 | 2 | 1 | |
| 28.852 | **3.091840** | 1000 | 1 | 1 | 2 | | 67.608 | 1.384510 | 6 | 3 | 0 | 5 | |
| 30.479 | 2.930400 | 171 | 0 | 0 | 4 | | 69.044 | 1.359190 | 1 | 1 | 1 | 8 | |
| 34.833 | 2.573500 | 207 | 2 | 0 | 0 | | 69.340 | 1.354110 | 13 | 1 | 2 | 7 | |
| 38.161 | 2.356340 | 4 | 2 | 0 | 2 | | 70.126 | 1.340830 | 12 | 2 | 3 | 3 | |
| 39.446 | 2.282490 | 14 | 1 | 1 | 4 | | 73.543 | 1.286750 | 21 | 4 | 0 | 0 | |
| 39.880 | 2.258670 | 154 | 2 | 1 | 1 | | 74.451 | 1.273290 | 46 | 2 | 0 | 8 | |
| 42.329 | 2.133440 | 75 | 1 | 0 | 5 | | 75.189 | 1.262610 | 6 | 1 | 0 | 9 | |
| 45.709 | 1.983240 | 110 | 1 | 2 | 3 | | 75.596 | 1.256820 | 2 | 4 | 0 | 2 | |
| 46.950 | **1.933680** | 250 | 2 | 0 | 4 | | 76.047 | 1.250490 | 76 | 3 | 1 | 6 | |
| 50.085 | 1.819740 | 96 | 2 | 2 | 0 | | 76.711 | 1.241310 | 11 | 1 | 4 | 1 | |
| 53.167 | 1.721290 | 145 | 1 | 1 | 6 | | 78.360 | 1.219260 | 15 | 2 | 3 | 5 | |
| 53.969 | 1.697580 | 26 | 3 | 0 | 1 | | 79.999 | 1.198350 | 4 | 3 | 0 | 7 | |
| 55.937 | 1.642450 | 27 | 1 | 2 | 5 | | 80.841 | 1.187980 | 31m | 3 | 3 | 2 | |
| 57.859 | 1.592360 | 24 | 1 | 0 | 7 | | 80.841 | 1.187980 | 31m | 4 | 1 | 3 | |
| 58.834 | 1.568270 | 201 | 1 | 3 | 2 | | 81.656 | 1.178170 | 29 | 4 | 0 | 4 | |
| 59.771 | 1.545920 | 92 | 2 | 2 | 4 | | 84.024 | 1.150900 | 29 | 2 | 4 | 0 | |

| 2θ (°) | d (Å) | I | h | k | l | * | 2θ (°) | d (Å) | I | h | k | l | * |
|---|---|---|---|---|---|---|---|---|---|---|---|---|---|
| 84.901 | 1.141240 | 24 | 2 | 2 | 8 | | 117.457 | 0.901212 | 3 | 4 | 1 | 9 | |
| 85.616 | 1.133530 | 9 | 1 | 2 | 9 | | 118.396 | 0.896776 | 22 | 1 | 5 | 6 | |
| 87.322 | 1.115720 | 22 | 1 | 1 | 10 | | 120.292 | 0.888137 | 1 | 1 | 0 | 13 | |
| 88.706 | 1.101850 | 9 | 4 | 1 | 5 | | 120.994 | 0.885045 | 3 | 5 | 2 | 5 | |
| 90.317 | 1.086340 | 9 | 2 | 3 | 7 | | 122.892 | 0.876947 | 4 | 5 | 0 | 7 | |
| 91.952 | 1.071250 | 36 | 4 | 2 | 4 | | 123.886 | 0.872859 | 20 | 3 | 5 | 2 | |
| 95.155 | 1.043470 | 3 | 1 | 0 | 11 | | 124.862 | 0.868947 | 11 | 4 | 4 | 4 | |
| 95.896 | 1.037360 | 3 | 3 | 0 | 9 | | 127.017 | 0.860647 | 10 | 2 | 2 | 12 | |
| 96.732 | 1.030610 | 16 | 3 | 3 | 6 | | 127.776 | 0.857833 | 5 | 6 | 0 | 0 | |
| 97.382 | 1.025450 | 8 | 5 | 0 | 1 | | 128.857 | 0.853925 | 3 | 3 | 2 | 11 | |
| 100.643 | 1.000830 | 6 | 4 | 1 | 7 | | 131.760 | 0.843965 | 3 | 1 | 6 | 1 | |
| 101.490 | 0.994763 | 31 | 5 | 1 | 2 | | 132.065 | 0.842964 | 10 | 3 | 3 | 10 | |
| 104.105 | 0.976800 | 4 | 0 | 0 | 12 | | 133.125 | 0.839548 | 3 | 2 | 1 | 13 | |
| 105.632 | 0.966839 | 17m | 1 | 2 | 11 | | 136.239 | 0.830077 | 3 | 5 | 2 | 7 | |
| 105.632 | 0.966839 | 17m | 4 | 0 | 8 | | 137.316 | 0.826991 | 3 | 6 | 1 | 3 | |
| 106.374 | 0.962135 | 3 | 2 | 3 | 9 | | 138.657 | 0.823283 | 9 | 6 | 0 | 4 | |
| 107.918 | 0.952612 | 5 | 2 | 5 | 1 | | 141.481 | 0.815945 | 9 | 1 | 1 | 14 | |
| 108.157 | 0.951173 | 25 | 1 | 3 | 10 | | 142.350 | 0.813812 | 9 | 6 | 2 | 0 | |
| 109.619 | 0.942536 | 4 | 5 | 0 | 5 | | 143.760 | 0.810473 | 2 | 1 | 4 | 11 | |
| 112.133 | 0.928400 | 3 | 5 | 2 | 3 | | 145.028 | 0.807599 | 4 | 5 | 0 | 9 | |
| 115.016 | 0.913230 | 10 | 2 | 0 | 12 | | 146.503 | 0.804403 | 18 | 5 | 3 | 6 | |
| 115.684 | 0.909870 | 4 | 4 | 4 | 0 | | 147.692 | 0.801943 | 3 | 5 | 4 | 1 | |
| 116.656 | 0.905074 | 22 | 4 | 2 | 8 | | 149.629 | 0.798150 | 1 | 3 | 0 | 13 | |

**Annex 9:** ICDDPDF No. 00-014-0688 for the monoclinic-scheelite phase of $BiVO_4$.

**00-014-0688** Feb 10, 2020 10:28 AM (rosarios)

**Status** Primary **Quality Mark:** Indexed **Environment:** Ambient **Temp:** 299.0 K **Chemical Formula:** Bi V O4
**Empirical Formula:** Bi O4 V **Weight %:** Bi64.52 O19.76 V15.73 **Atomic %:** Bi16.67 O66.67 V16.67
**Compound Name:** Bismuth Vanadium Oxide **Mineral Name:** Clinobisvanite, syn **Entry Date:** 09/01/1964

**Radiation:** CuKα1 (1.5405 Å) **Filter:** Ni Beta **Intensity:** Diffractometer - Peak

**Crystal System:** Monoclinic **SPGR:** I2/a (15)
**Author's Unit Cell [ a:** 5.195 Å **b:** 11.701 Å **c:** 5.092 Å **β:** 90.38° **Volume:** 309.52 Å³ **Z:** 4.00
**MolVol:** 77.38 **c/a:** 0.980 **a/b:** 0.444 **c/b:** 0.435 **]** **Calculated Density:** 6.951 g/cm³ **Color:** Orange-yellow
**SS/FOM:** F(30) = 49.5(0.0178, 34)

**Space Group:** I2/a (15) **Molecular Wt:** 323.92 g/mol
**Crystal Data [ a:** 5.195 Å **b:** 11.701 Å **c:** 5.092 Å **α:** 90.00° **β:** 90.38° **γ:** 90.00° **XtlCell Vol:** 309.52 Å³
**XtlCell Z:** 4.00 **c/a:** 0.980 **a/b:** 0.444 **c/b:** 0.435 **]**
**Reduced Cell [ a:** 5.092 Å **b:** 5.195 Å **c:** 6.883 Å **α:** 112.02° **β:** 111.56° **γ:** 90.38° **RedCell Vol:** 154.76 Å³
**]**

**Atomic parameters are cross-referenced from PDF entry 04-010-5713** **AC Space Group:** I112/b (15)
**AC Unit Cell [ a:** 5.1956(1) Å **b:** 5.0935(1) Å **c:** 11.7044(2) Å **α:** 90° **β:** 90° **γ:** 90.383(1)° **]**
**Space Group Symmetry Operators:**

| Seq | Operator | Seq | Operator | Seq | Operator | Seq | Operator |
|---|---|---|---|---|---|---|---|
| 1 | x,y,z | 2 | -x,-y,-z | 3 | -x,-y+1/2,z | 4 | x,y+1/2,-z |

**ADP Type:** B
**Atomic Coordinates:**

| Atom | Num | Wyckoff | Symmetry | x | y | z | SOF | Biso | AET |
|---|---|---|---|---|---|---|---|---|---|
| Bi | 1 | 4e | 2 | 0.0 | 0.25 | 0.6341 | 1.0 | 0.36 | |
| V | 2 | 4e | 2 | 0.0 | 0.25 | 0.1315 | 1.0 | 0.13 | |
| O | 3 | 8f | 1 | 0.143 | 0.512 | 0.211 | 1.0 | 1.9 | |
| O | 4 | 8f | 1 | 0.252 | 0.362 | 0.446 | 1.0 | 2.0 | |

**Crystal (Symmetry Allowed):** Centrosymmetric

**Subfiles:** Common Phase, Inorganic, Mineral Related (Mineral, Synthetic), NBS Pattern **Pearson Symbol:** mC24.00
**Prototype Structure [Formula Order]:** La Nb O4 **Prototype Structure [Alpha Order]:** La Nb O4
**LPF Prototype Structure [Formula Order]:** La Nb O4,mS24,15
**LPF Prototype Structure [Alpha Order]:** La Nb O4,mS24,15

**Cross-Ref PDF #'s:** 04-010-5711 (Alternate), 04-010-5712 (Alternate), 04-010-5713 (Primary), 04-012-7973 (Alternate)

**References:**

| Type | DOI | Reference |
|---|---|---|
| Primary Reference | | Natl. Bur. Stand. (U. S. ) Monogr. 25 1964, 3, 14. |
| Crystal Structure | | Crystal Structure Source: LPF. |

**Database Comments:** Additional Patterns: See PDF 01-083-1698, 01-083-1699 and 01-075-1866. Analysis: Spectrographic analysis: 0.001 to 0.01% each of Al and Si. Sample Preparation: Sample was prepared at NBS, Gaithersburg, Maryland, USA, by heating stoichiometric mixtures of bismuth oxide and vanadium oxide at 895 C for 16 hours. Temperature of Data Collection: 299 K. Warning: Lines with abs(delta 2Theta)>0.06 DEG. Unit Cell Data Source: Powder Diffraction.

**d-spacings (40) - Bi V O4 - 00-014-0688 (Stick, Fixed Slit Intensity) - Cu Kα1 1.54056 Å**

| 2θ (°) | d (Å) | I | h | k | l | * | 2θ (°) | d (Å) | I | h | k | l | * | 2θ (°) | d (Å) | I | h | k | l | * |
|---|---|---|---|---|---|---|---|---|---|---|---|---|---|---|---|---|---|---|---|---|
| 15.140 | 5.8470 | 2 | 0 | 2 | 0 | | 40.245 | 2.2390 | 8 | 1 | 1 | 2 | | 53.310 | 1.7170 | 18 | 1 | 6 | 1 | |
| 18.669 | 4.7490 | 25 | 1 | 1 | 0 | | 42.339 | 2.1330 | 8 | 1 | 5 | 0 | | 53.445 | 1.7130 | 4 | 3 | 1 | 0 | |
| 18.988 | 4.6700 | 25 | 0 | 1 | 1 | | 42.464 | 2.1270 | 12 | 0 | 5 | 1 | | 54.581 | 1.6800 | 4 | 0 | 1 | 3 | |
| 28.586 | **3.1200** | 30 | -1 | 3 | 0 | | 45.425 | 1.9950 | 6 | -2 | 3 | 1 | | 55.732 | 1.6480 | 2 | -2 | 5 | 1 | |
| 28.822 | **3.0950** | 100 | -1 | 2 | 1 | | 45.594 | 1.9880 | 4 | 2 | 3 | 1 | | 55.879 | 1.6440 | 4 | 2 | 5 | 1 | |
| 28.947 | **3.0820** | 95 | 1 | 2 | 1 | | 45.886 | 1.9760 | 6 | -1 | 3 | 2 | | 56.065 | 1.6390 | 2 | -1 | 5 | 2 | |
| 30.548 | 2.9240 | 25 | 0 | 4 | 0 | | 46.034 | 1.9700 | 8 | 1 | 3 | 2 | | 56.289 | 1.6330 | 2 | 1 | 5 | 2 | |
| 34.494 | 2.5980 | 12 | 2 | 0 | 0 | | 46.559 | 1.9490 | 4 | 0 | 6 | 0 | | 57.913 | 1.5910 | 4 | 1 | 7 | 0 | |
| 35.221 | 2.5460 | 14 | 0 | 0 | 2 | | 46.711 | 1.9430 | 16 | 2 | 4 | 0 | | 58.073 | 1.5870 | 6 | 0 | 7 | 1 | |
| 37.866 | 2.3740 | 2 | 2 | 2 | 0 | | 47.305 | 1.9200 | 16 | 0 | 4 | 2 | | 58.274 | 1.5820 | 10 | -3 | 2 | 1 | |
| 39.455 | 2.2820 | 6 | -1 | 4 | 1 | | 49.960 | 1.8240 | 6 | -2 | 0 | 2 | | 58.530 | 1.5757 | 10 | 3 | 2 | 1 | |
| 39.545 | 2.2770 | 6 | 1 | 4 | 1 | | 50.314 | 1.8120 | 8 | 2 | 0 | 2 | | 59.261 | 1.5580 | 8 | 1 | 2 | 3 | |
| 39.782 | 2.2640 | 12 | 2 | 1 | 1 | | 53.011 | 1.7260 | 2 | 2 | 2 | 2 | | | | | | | | |
| 40.040 | 2.2500 | 10 | -1 | 1 | 2 | | 53.243 | 1.7190 | 18 | -1 | 6 | 1 | | | | | | | | |